

DOTTORATO DI RICERCA IN FISICA  
Ciclo XXXII

Settore Concorsuale: 02/D1  
Settore Scientifico Disciplinare: FIS/07

**Applications of metrological techniques for  
clinical implementation of dosimetry and  
radiobiology in molecular radiotherapy**

Presentata da: Domenico Finocchiaro

Coordinatore Dottorato:  
Prof.ssa Silvia Arcelli

Supervisore:  
Dott.ssa Elisa Grassi  
  
Co-supervisore:  
Prof. Gastone Castellani

Esame finale anno 2020



# Abstract

Molecular radiotherapy (MRT) is a fast developing and promising treatment for metastasised neuroendocrine tumours (NETs). Efficacy of MRT is based on the capability to selectively “deliver” radiation to tumour cells, minimizing administered dose to normal tissues. Outcome of MRT varies from patient to patient depending on the individual characteristics. For that reason, personalized treatment planning is important to improve outcomes of therapy. Dosimetry plays a key role in this setting, as it is the main physical quantity related to radiation effects on cells. Dosimetry in MRT consists in a complex series of procedures ranging from imaging quantification to dose calculation. This doctoral thesis focused on several aspects concerning the clinical implementation of absorbed dose calculations in MRT. Accuracy of SPECT/CT quantification was assessed in order to determine the optimal reconstruction parameters. A model of PVE correction was developed in order to improve the activity quantification in small volume, such as lesions in clinical patterns. Advanced dosimetric methods were compared with the aim of defining the most accurate modality, applicable in clinical routine. Also, for the first time on a large number of clinical cases, the overall uncertainty of tumour dose calculation was assessed. As part of the MRT Dosimetry project, protocols for calibration of SPECT/CT systems and implementation of dosimetry were drawn up in order to provide standard guidelines to the clinics offering MRT. To estimate the risk of experiencing radio-toxicity side effects and the chance of inducing damage on neoplastic cells is crucial for patient selection and treatment planning. In this thesis, the NTCP and TCP models were derived based on clinical data as help to clinicians to decide the pharmaceutical dosage in relation to the therapy control and the limitation of damage to healthy tissues. Moreover, a model for tumour response prediction based on Machine Learning analysis was developed.



# Contents

<b>Introduction</b>	<b>23</b>
<b>1 MRT in the treatment of cancer</b>	<b>25</b>
1.1 Brief introduction to Nuclear Medicine . . . . .	25
1.2 Molecular Radionuclide Therapy . . . . .	27
1.3 Neuroendocrine tumours . . . . .	28
1.4 Peptide Receptor Radionuclide Therapy . . . . .	30
1.5 Treatment planning . . . . .	32
1.6 The MIRD schema . . . . .	33
1.7 Clinical trial . . . . .	35
1.7.1 Trial A . . . . .	37
1.7.2 Trial B . . . . .	37
<b>2 Quantification of activity</b>	<b>39</b>
2.1 Impact of commercial 3D OSEM . . . . .	40
2.1.1 Material and methods . . . . .	41
2.1.2 Results . . . . .	45
2.1.3 Discussion . . . . .	48
2.2 Partial volume effect . . . . .	54
2.2.1 Materials and methods . . . . .	56
2.2.2 Results . . . . .	62
2.2.3 Discussion . . . . .	64
2.3 Impact of two non-rigid registration workflows . . . . .	67
2.3.1 Material and methods . . . . .	67
2.3.2 Results . . . . .	70
2.3.3 Discussion . . . . .	71

<b>3</b>	<b>Calculation of absorbed dose</b>	<b>75</b>
3.1	Internal dosimetry . . . . .	76
3.1.1	Organ dosimetry . . . . .	76
3.1.2	Voxel dosimetry . . . . .	77
3.2	VoxelMed: a home-made software for dosimetry in MRT . . . . .	79
3.3	Comparison of different calculation techniques . . . . .	88
3.3.1	Material and methods . . . . .	90
3.3.2	Results . . . . .	94
3.3.3	Discussion . . . . .	98
<b>4</b>	<b>MRTDosimetry Project</b>	<b>103</b>
4.1	Validation of the Commissioning Protocol: Comparison Exercise	105
4.1.1	Material and methods . . . . .	106
4.1.2	Results . . . . .	111
4.1.3	Discussion . . . . .	113
4.2	Surrogate sources for QI . . . . .	115
4.2.1	Material and methods . . . . .	116
4.2.2	Results . . . . .	119
4.2.3	Discussion . . . . .	121
4.3	Cross comparison of dosimetry calculations . . . . .	122
4.3.1	Material and methods . . . . .	123
4.3.2	Results . . . . .	125
4.3.3	Discussion . . . . .	126
<b>5</b>	<b>Correlation of dose with organ toxicity in PRRT</b>	<b>131</b>
5.1	Background . . . . .	132
5.1.1	Radiobiology aspects . . . . .	132
5.1.2	Evaluation of toxicity . . . . .	135
5.2	Material and methods . . . . .	140
5.2.1	Clinical trial . . . . .	140
5.2.2	Image acquisition and dose calculation . . . . .	140
5.2.3	Assessment of toxicity . . . . .	141
5.2.4	Data analysis and statistics . . . . .	141
5.3	Results . . . . .	141

<i>CONTENTS</i>	7
5.3.1 Evaluation of toxicity . . . . .	142
5.3.2 Correlation between dose and red marrow toxicity . . . . .	144
5.3.3 Correlation between dose and renal toxicity . . . . .	144
5.4 Discussion . . . . .	149
<b>6 Tumour Control Probability</b>	<b>151</b>
6.1 Background . . . . .	153
6.2 Material and methods . . . . .	155
6.2.1 Patients and therapy . . . . .	155
6.2.2 Image acquisition and Dosimetry . . . . .	155
6.2.3 Evaluation of response . . . . .	155
6.2.4 Machine Learning analysis . . . . .	157
6.2.5 Data analysis and statistics . . . . .	158
6.3 Results . . . . .	158
6.3.1 <sup>68</sup> Ga-PET for assessment of response . . . . .	160
6.3.2 Prediction of response: a Machine Learning approach . . . . .	161
6.4 Discussion . . . . .	163
<b>7 Evaluation of dose uncertainty on clinical cases</b>	<b>169</b>
7.1 Background . . . . .	170
7.2 Material and methods . . . . .	170
7.2.1 Dose and uncertainty calculation . . . . .	172
7.2.2 Data analysis . . . . .	173
7.3 Results . . . . .	174
7.4 Discussion . . . . .	176
<b>Conclusion and future perspectives</b>	<b>181</b>
<b>Appendices</b>	<b>191</b>
<b>A Machine Learning</b>	<b>193</b>
A.1 Decision Tree . . . . .	193
A.2 Ensemble RUSBoosted Tree . . . . .	194
A.3 Performance of classification . . . . .	194

<b>B Calculation of uncertainty</b>	<b>197</b>
B.1 The law of propagation of uncertainty (LPU) . . . . .	197
B.2 Application of LPU . . . . .	199
<b>References</b>	<b>205</b>



# List of Figures

1.1	External beam therapy and targeted radionuclide therapy for the treatment of brain tumor. SOURCE: Courtesy of Michael Zalutsky, Duke University. . . . .	27
2.1	Phantom with the six radioactive sphere inserts, on the SPECT/CT scanner table. . . . .	42
2.2	Total measured counts in the phantom is plotted against the real total activity injected in the phantom to evaluate the dead time effect.	47
2.3	Measured counts in each sphere versus the number of iterations (x-axis) and subsets (marker symbol). Data are arranged according to the sphere diameter: (a) 36mm, (b) 28mm, (c) 22mm, (d) 17mm, (e) 13mm. . . . .	51
2.4	Recovery coefficients versus the number of iterations (x-axis) and subsets (marker symbol). Data are arranged according to the sphere diameter: (a) 36mm, (b) 28mm, (c) 22mm, (d) 17mm, (e) 13mm.	52
2.5	Weighted Root Mean Squared Error (wRMSE) normalized to the true activity as a function of equivalent iterations (EI). . . . .	53
2.6	Circular source (diameter of 10 mm) of uniform activity (100 arbitrary units). Part of the signal inside the object is displaced outside of it, causing reduction of measured signal in the object. SOURCE: Soret M et al. J Nucl Med 2007. . . . .	55
2.7	Influence of image sampling on PVE. Pixels on edges of VOI do not match the object contours. Part of signal emanating from the object is seen outside the VOI. SOURCE: Soret M et al. J Nucl Med 2007. . . . .	55

2.8	Axial CT slice of the Sphere phantom (a) and Anthropomorphic phantom (b). . . . .	59
2.9	Axial CT slice for different insert-shape of the Geometrical phantom. . . . .	60
2.10	Calculated RCs for the spherical inserts (a) and the organ-shape inserts (b) as a function of the insert volume. Data points were fitted using exponential curves ( $R^2$ and RMSE are reported in the graph). Note: RCs for the left kidney and the right kidney are too close to be distinguished in the graph. . . . .	62
2.11	Error (%) of measured activity in each insert of the Geometrical phantom. Both corrected and non-corrected activities for PVE were evaluated. . . . .	63
2.12	Error (%) of measured activity in each insert of the Anthropomorphic phantom. Both corrected and non-corrected activities for PVE were evaluated. . . . .	64
2.13	Error (%) of corrected activity for PVE is plotted against the ASP. The Pearson correlation coefficient ( $R^2$ is reported in the graph. A different data point format was used for inserts with different shape or equivalent diameter. . . . .	64
2.14	Schema of the image registrations. Co-registered CT and NM images for each multi-modal acquisition (a) and non-rigidly registered sequential CT images to the first CT image (b). . . . .	68
2.15	The Activity deformation workflow (on the left) and the Dose deformation workflow (on the right). . . . .	69
2.16	SSIM between the sequential scan and the reference one (CT1). For each patient, the average value of all the sequential scans, and the corresponding error bar, are reported. . . . .	71
2.17	Distribution of percentage difference between the mean absorbed dose calculated with the AD and the DD workflows for OARs and lesions. . . . .	72
2.18	Distribution of percentage difference between the mean absorbed dose calculated with the AD and the DD workflows for OARs and lesions. . . . .	73

3.1	The Cristy-Eckerman computational phantom (A) and a realistic voxel-based phantoms (B). Source: Stabin MG et al., J Nucl Med 2018. . . . .	77
3.2	Screen capture of VoxelMed GUI. The user can enter the patient and treatment informations into the boxes on the left. The axial, coronal and sagittal slices of the fused images are shown. . . . .	80
3.3	In the <i>Patient Planning Treatment</i> GUI user can enter the values of administered activities to calculate renal BED. . . . .	82
3.4	Liver absorbed dose map of a slice in axial, sagittal and coronal viewer. Using the colorbar in the left panel it is possible to set the dose-display range, colorbar display range and to adjust the scan contrast. . . . .	88
3.5	Comparison of mean absorbed dose (Gy) calculated using OLINDA1.1, VoxelMed and RAYDOSE. . . . .	96
3.6	Comparison of DVHs calculated using VoxelMed (continuous line) and RAYDOSE (dotted line) for the Cylindrical phantom. . . . .	97
3.7	Comparison of DVHs calculated using VoxelMed (continuous line) and RAYDOSE (dotted line) for inserts of Geometrical phantom and Anthropomorphic phantom. . . . .	97
3.8	Comparison of OLINDA1.1 and VoxelMed calculated mean absorbed dose per unit of injected activity (Gy/GBq). . . . .	98
3.9	Comparison of RAYDOSE, VoxelMed and VoxelMed <sup>(<math>\lambda</math> RD)</sup> calculated mean absorbed dose per unit of injected activity (Gy/GBq). . . . .	98
4.1	Countries directly or indirectly involved in the project. On the top of the picture the logos of the main partners. . . . .	104
4.2	Siemens Symbia T2 (site: AUSL di Reggio Emilia) <sup>177</sup> Lu peaking. . . . .	107
4.3	Design and 3D printed 2-organs anthropomorphic phantom. The baseplate for attachment is also included. . . . .	110
4.4	Siemens Symbia T2 (site: AUSL di Reggio Emilia) SPECT/CT fusion images for a) the homogeneous cylindrical Jaszczak phantom, b) the IEC NEMA body phantom and c) the MRTDosimetry 2- Organs anthropomorphic phantom. . . . .	111

- 4.5 ICF values for each system and reconstruction. The red bars shows the mean and standard deviation over all 2 Siemens TEW RR and all 4 GE TEW RR reconstructions (only 3/8" crystals). . . . . 112
- 4.6 Lu-177 RC curves for each system and reconstruction. The Siemens systems are indicated in red, the GE systems in green and the Mediso system is in blue. . . . . 113
- 4.7 Lu-177 RCs and fitted curves for each participating system. The black crosses are the RCs, the solid blue lines are the weighted fits, the dotted blue lines the 95% confidence intervals and the dashed black lines the non-weighted fits. . . . . 114
- 4.8 Ratio between SPECT-based activity and radionuclide calibrator-based activity for the 2-Organ phantom. In orange the kidney's results and in green the spleen's results. The mean and standard deviation is indicated by a darker color. . . . . 115
- 4.9 Captures of (a) phantom with  $^{131}\text{I}$  cylinders during assembly and (b) phantom with  $^{133}\text{Ba}$  during the SPECT/CT acquisition. . . . . 117
- 4.10 Siemens Symbia T2 (site: AUSL di Reggio Emilia) peaking of a)  $^{131}\text{I}$  point-like source and b)  $^{133}\text{Ba}$  small source. . . . . 119
- 4.11 Siemens Symbia T2 (site: AUSL di Reggio Emilia) SPECT/CT fusion of a)  $^{131}\text{I}$  cylinders and b)  $^{133}\text{Ba}$  sources. . . . . 120
- 4.12 Pseudo-ICF of  $^{131}\text{I}$  (dashed lines) and  $^{133}\text{Ba}$  (solid lines). Color shades indicate different systems and reconstructions (Green: GE TEW RR; Red: Siemens TEW RR; Blue: Hermes) . . . . . 121
- 4.13 Mean value of the ratios between  $^{133}\text{Ba}$  and  $^{131}\text{I}$  based ICFs of all sources, for each imaging setup. The red bar is the overall average value. . . . . 122
- 4.14 Regression analysis of the pseudo ICFs of  $^{133}\text{Ba}$  and  $^{131}\text{I}$ , with a) intercept set to zero and b) intercept fitted. . . . . 123
- 4.15 Image captures of hybrid SPECT/CT axial slices of patients for the cross comparison of dosimetry calculation systems. . . . . 125

4.16 Results for each software of TIACs (h) for kidneys (sum of both kidneys) in the 2 patients. In bracket the integration and registration: 1. Voxel-based TAC fitting. 2. Organ-based TAC fitting. A: SPECR registration by the site. B: Pre-registered data were used. The mean data and the standard deviations are shown in the last columns. . . . . 127

4.17 Results for each software of TIACs (h) for total liver (both health and tumours) in the 2 patients. In bracket the integration method and image registration: 1. Voxel-based TAC fitting. 2. Organ-based TAC fitting. A: Image registration provided by the site. B: Pre-registered images were used. The mean data and the standard deviations are shown in the last columns. . . . . 128

4.18 Results for each software of TIACs (h) for spleen in the 2 patients. In bracket the integration and registration: 1. Voxel-based TAC fitting. 2. Organ-based TAC fitting. A: Image registration provided by the site. B: Pre-registered images were used. The mean data and the standard deviations are shown in the last columns. . . . . 129

5.1 Linear and quadratic components of the survival fraction as a function of absorbed dose. Source: Basic Radiation Oncology, Springer-Verlag Berlin Heidelberg 2010. . . . . 133

5.2 BED for different values of  $\alpha/\beta$  ratio (A) and  $T_{rep}$  (B). . . . . 135

5.3 Renal toxicity rates reported in several studies of PRRT with  $^{90}\text{Y}$ -DOTATOC,  $^{90}\text{Y}$ -DOTATATE,  $^{177}\text{Lu}$ - DOTATATE and the combination of  $^{90}\text{Y}$ -DOTATOC and  $^{177}\text{Lu}$ -DOTATATE. Source: Cremonesi et al. Eur J Nucl Med Mol Imaging. 2018 . . . . . 137

5.4 Dose–response curve for kidneys after ERBT and  $^{90}\text{Y}$  PRRT, as a function of the absorbed dose on the left and the BED on the right. Adapted from MIRD No. 20, J Nucl Med 2008. . . . . 140

5.5 Hemoglobin level as a function of time after injection in a representative patient (Case A). The red and blue lines are the minimum and maximum interval of ordinary values (i.e. no toxicity). . . . . 143

5.6	Platelets level as a function of time after injection in a representative patient (Case B). The red line is the minimum level of ordinary values (i.e. no toxicity). . . . .	143
5.7	Creatinine level as a function of time after injection in a representative patient (Case C). The red and green lines are the minimum and maximum interval of ordinary values (i.e. no toxicity). Dotted lines indicate the interval corresponding to toxicity effect with grade 1. . . . .	144
5.8	PLTs toxicity grade as a function of red marrow absorbed dose. . . . .	145
5.9	Hgb toxicity grade as a function of red marrow absorbed dose. . . . .	145
5.10	Final/basal Cr ratio as a function of renal BED. . . . .	146
5.11	CrCl loss (CCL) as a function of months after the end of the treatment. Patients with RF (red line) and patients with No-RF (blue line) were separately considered. . . . .	147
5.12	Frequencies of chronic renal toxicity grades. . . . .	147
5.13	Probability of developing chronic renal toxicity during the treatment as a function of renal absorbed dose. No-RF on the left and RF on the right. The green area indicates the grade 0 of toxicity, yellow area grade 1 and red area grade 2 or higher. . . . .	148
5.14	Normal Tissue Complication Probability as a function of renal BED. Dotted lines indicate the confidence intervals. . . . .	148
5.15	Distribution of absorbed dose and BED in patients who developed toxicity and patients who did not. Patients with RF, all patients and patient with No-RF were separately considered. A t-test was used to compare the median values of the distribution (p-values below the box-plots). . . . .	149
6.1	Tumour response in relation to tumour absorbed dose (A) for lesions with a diameter larger than 2.2 cm and (B) for lesions with a diameter larger than 4.0 cm. Source: Ilan et al. 2015. . . . .	153
6.2	Relationship between (A) cumulative lesion absorbed dose and radiological response (i.e. relative lesion size variation) and (B) cumulative maximum tumour absorbed dose and relative chromogranin A variation on the right. Source: Del Prete et al. 2017. . . . .	154

6.3	Frequency distribution of MTV (on the left) and absorbed dose (on the right) for all tumours. . . . .	159
6.4	Response rate (%) based on the PERCIST-like criteria for MTV, SUVmax, SUVmean and TLSR. . . . .	161
6.5	Box-plot analysis of the cumulative absorbed dose for “Responder” and “Non-Responder” lesions according to MTV, SUVmax, SUVmean and TLSR variations. . . . .	163
6.6	Rate of response (%) for each marker within intervals of absorbed dose. . . . .	164
6.7	Predicted TCP (Tumour Control Probability) against absorbed dose. . . . .	165
6.8	Confusion Matrix showing the performance of the Ensemble RUS-Boosted classifier in the prediction of response to PRRT. . . . .	166
6.9	ROC curve showing the performance of the Ensemble RUSBoosted classifier in the prediction of response to PRRT. . . . .	167
7.1	Chronological sequence of the dosimetry schema. Source: Gear et al., Eur J Nucl Med Mol Imaging 2018. . . . .	171
7.2	Distribution of uncertainty (%) for each step of the dose calculation schema. . . . .	174
7.3	Relationship between dose uncertainty (y-axis) and volume, RC, counts, CF, activity, curve fitting, cumulated activity and S-factor uncertainty (x-axis). The graph at the bottom right shows absorbed dose (Gy) against the dose uncertainty. . . . .	175
7.4	Dose uncertainty (%) against Volume (mL). Points were fitted with a Power function, $R^2$ and RMSE are reported into the graph. . . . .	176
7.5	Dose uncertainty (%) against Volume (mL) calculated for all the lesions, assuming four different spatial resolution values of the imaging system (FWHM: 0.1, 0.5, 1 and 2 cm). . . . .	177
7.6	Dose uncertainty (%) as a function of the imaging system spatial resolution (cm) in four lesions. Lesions were chosen to fill a range of different values of volume. . . . .	178
7.7	Dose uncertainty (black points) and the volume uncertainty (blue line) as a function of the delineated VOI volume. . . . .	179

B.1 S-factors for unit density spheres versus mass fitted by power model. 203



# List of Tables

2.1	Results of resolution measurements performed with three hot capillary tubes placed at 0cm, 3cm and 6cm respectively from the central axis. . . . .	46
2.2	Description of phantoms and inserts used to calculate RCs. Each sphere was named as his diameter (i.e. the sphere with 10 cm of diameter as “Sphere10”) . . . . .	58
2.3	Legend of the insert acronyms for the Geometrical phantom. . .	61
2.4	Description of phantoms and inserts used to evaluate RCs. Each sphere was named as his diameter (i.e. the sphere with 10 cm of diameter as “Sphere10”) . . . . .	61
3.1	Description of phantoms used to test the dosimetry tools. . . . .	91
3.2	Summary of phantoms and patients studies performed. . . . .	93
3.3	Mean absorbed dose (Gy) calculated with OLINDA1.1, VoxelMed, and RAYDOSE for each phantom. . . . .	94
3.4	Kidney, liver and spleen mean absorbed dose (Gy/GBq) calculated with OLINDA1.1 and VoxelMed for patients of Sample A .	95
3.5	Kidney, liver and spleen mean absorbed dose (Gy/GBq) calculated with OLINDA1.1, VoxelMed, VoxelMed <sup>(λ RD)</sup> and RAYDOSE for patients of Sample B . . . . .	99
4.1	Participating systems for the Comparison Exercise. . . . .	106
4.2	Activity and carrier solution for the commissioning and QC of SPECT. . . . .	107
4.3	SPECT/CT acquisition and reconstruction parameters for commissioning and QC. . . . .	108

4.4	Filling volume of the Two-Organ Phantom, target volume and activities for the stock solutions. . . . .	111
4.5	SPECT/CT acquisition and reconstruction parameters for $^{131}\text{I}$ and $^{133}\text{Ba}$ sources. . . . .	118
4.6	Specifications of the cylindrical solid $^{133}\text{Ba}$ sources. . . . .	118
4.7	Input image type and calculation modality of the software used by partners. . . . .	124
5.1	CTCAE Common Terminology Criteria for Adverse Event versions 4.03 for acute and chronic renal disorders after PRRT. . .	136
5.2	CTCAE Common Terminology Criteria for Adverse Event versions 4.03 for bone marrow disorders after PRRT. . . . .	138
5.3	Treatment administered activities and number of cycles. . . . .	141
5.4	Patients characteristics concerning the kidneys risk factors. . . .	142
6.1	Administered activities and number of cycles of $^{177}\text{Lu}$ - and $^{90}\text{Y}$ -DOTATATE for the patient cohort. . . . .	155
6.2	PERCIST-derived criteria adopted to evaluate therapy response for each tumour by $^{68}\text{Ga}$ -DOTATATE PET/CT images. . . . .	156
6.3	Indicators used for Machine Learning classifiers. . . . .	157
6.4	Patients characteristics. . . . .	159
6.5	Association between absorbed dose and marker percentage variation by LRT. . . . .	160
6.6	Association between absorbed dose and response. . . . .	162
6.7	Performance of classification for several supervised classifiers. . .	162
A.1	Confusion Matrix. . . . .	195

# List of Abbreviations

AD	Activity Deformation
ASP	Asphericity
AUC	Area Under the Curve
BAR	Balanced Accuracy Rate
BED	Biological Effective Dose
CA	Cumulated Activity
CERR	Computational Environment for Radiotherapy Research
CF	Calibration Factor
CT	Computed Tomography
CTCAE	Common Terminology Criteria for Adverse Events
DD	Dose Deformation
DEW	Dual Energy Window
DICOM	Digital Imaging and COmmunications in Medicine
DNA	DeoxyriboNucleic Acid
DOTATATE	[DOTA0,Tyr3]-ocreo <sup>ti</sup> de
DOTATOC	[DOTA0,Tyr3]-ocreo <sup>ti</sup> de
DVH	Dose Volume Histogram
EANM	European Association of Nuclear Medicine

EBRT	External Beam Radiation Therapy
ECOG	Eastern Cooperative Oncology Group
EI	Equivalent Iterations
EW	Energy Window
FBP	Filtered Back Projection
FWHM	Full Width at Half Maximum
GUI	Graphical User Interface
Hgb	Heboglobin
ICF	Image Calibration Factor
ICRP	International Commission on Radiological Protection
LC	Lin's Coefficient
LPU	Law of Propagation of Uncertainty
LQM	Linear Quadratic Model
MC	Monte Carlo
MELP	Medium Energy Low Penetration
MIRD	Medical Internal Radiation Dose
MRI	Magnetic Resonance Imaging
MRT	Molecular Radionuclide Therapy
MTV	Metabolic Tumour Volume
NET	Neuroendocrine Tumour
NTCP	Normal Tissue Complication Probability
OAR	Organ at Risk
OSEM	Ordered Subset Expectation Maximization

PERCIST	PET Response Criteria in Solid Tumors
PET	Positron Emission Tomography
PLT	Platelets
PVC	Partial Volume Correction
QC	Quality Control
QI	Quantitative Imaging
RC	Recovery Coefficient
RECIST	Response Evaluation Criteria in Solid Tumors
RMSD	Root Mean Square Deviation
RMSE	Root Mean Square Error
ROC	Receiver Operating Characteristics
RPC	Reproducibility Coefficient
RR	Resolution Recovery
SD	Standard Deviation
SF	Surviving Factor
SPECT	Single Photon Emission Computed Tomography
SSIM	Structural Similarity Index
SST	Somatostatine
SSTR	Somatostatine Receptor
SUV	Standardized Uptake Value
TCP	Tumour Control Probability
TEW	Triple Energy Window
TIAC	Time Integrated Activity Curve

TLSR	Total Lesion Somatostatine Receptor
TRT	Targated Radionuclide Therapy
VOI	Volume Of Interest
WBC	White Blood Cells

# Introduction and aims

Cancer is the second leading cause of death and is responsible for an estimated 9.6 million deaths in 2018. Globally, about 1 in 6 deaths is due to cancer. This ratio rises to 1 in 4 in the most developed countries. Today, cancer is not considered just one disease, but it is a collection of related diseases. There are many types of cancer, and different treatment options depending on tumour and patient characteristics. Common cancer treatments include chemotherapy, surgery, brachytherapy and external beam radiation therapy (EBRT). However, these treatments are not ideal. For example, conventional chemotherapeutical agents act by creating toxic effects on all dividing cells, both healthy and cancerous. On the other hand surgery and EBRT treat only a small portion of the body and they are not incisive if cancer is disseminated in the entire body or in several areas. Ideally, an optimum treatment affects only malignant cells, causes few or no side effects.

This doctoral thesis focuses on the treatment of neuroendocrine tumours (NETs) and, in particular, on Molecular Radionuclide Therapy (MRT), which has been demonstrated in the last years to be highly effective to treat this type of cancer. The overall aim of this thesis is to investigate several aspects concerning the application of MRT, ranging from the activity quantification to the evaluation of the treatment response, in order to improve PRRT efficacy. The specific aims are:

- To determine the optimal acquisition parameters for SPECT/CT quantitative imaging.
- To evaluate different algorithms of SPECT/CT image deformable registration and to establish a model for PVE correction.
- To compare different advanced techniques of absorbed dose calculation,

with consideration about accuracy and feasibility in clinical practice.

- To evaluate the side effects of therapy on healthy organs in a sample of patients and to study the possible correlations between toxicity and absorbed dose.
- To analyse the biological response of tumours and to study the possible correlations between response to therapy and absorbed dose.
- To develop an automatized method to evaluate uncertainty related to the absorbed dose calculation and to identify those parameters which mostly affect accuracy of calculation.

Chapter 1 gives an overview of MRT and PRRT current state. In Chapter 2 issues related to imaging quantification are addressed and a method for PVE correction is described and tested. In Chapter 3 the optimal modality of dose calculation is evaluated. Chapter 4 depicts results of the joint European MRTDosimetry project. Chapter 5 and 6 provide relations between absorbed dose and response in healthy organs and in tumours, which allow to evaluate efficacy of therapy. Chapter 7 affords to deal with calculation of uncertainty in MRT dose calculations.



# Chapter 1

## MRT in the treatment of cancer

### 1.1 Brief introduction to Nuclear Medicine

Nuclear Medicine is a branch of medicine that uses unsealed radioactive substances for diagnosis and therapy of many types of cancers, endocrine, neurological, gastrointestinal disorders, heart disease, and other abnormalities within the body. Diagnostic procedures are non-invasive and involve the use of radioactive materials called radiopharmaceuticals or radiotracers to image or measure the function of an organ. The uptake and distribution of the tracer substance is then studied with Single Photon Emission Computed Tomography (SPECT) scanner, Positron Emission Tomography (PET) camera or other devices, such as a stationary radiation detector. These radiopharmaceuticals are used to investigate disorders of metabolism and most often work at molecular level, under physiological and patho-physiological conditions.

The history of nuclear medicine contains contributions from scientists across different disciplines in physics, chemistry, engineering and medicine. The multidisciplinary nature of nuclear medicine makes it difficult to determine the birthdate of nuclear medicine. This can probably be best placed with the discovery of X-rays in November 1895 by the German physicist Wilhelm Conrad Röntgen (1845-1923)[1]. Röntgen was working on Crook's Vacuum tube when he suddenly realized that shadows of his wife's finger bones and ring in her finger appeared on the palette. X-ray discovery was a scientific bombshell, and was received with extraordinary interest by both scientist and laymen. Within a month after the announcement of the discovery, several medical ra-

diographs had been made in Europe and the United States. There were lots of improvements to this initial technique over the first half of the 20th century, culminating with digital imaging techniques. In the 1970s, G.N. Hounsfield and A.M. Cormack were given the Nobel Prize in medicine for the development of Computed Tomography (CT). Today there are lots of imaging techniques, daily used for diagnosis purpose in medicine. The most widely used are radiography, CT, MRI (Magnetic Resonance Imaging), PET and SPECT. The birth of the therapeutic nuclear medicine can be associated with the discovery of natural radioactivity on March 1896 by the French Antoine Henri Becquerel (1852-1908). He found that some minerals would glow or fluoresce when exposed to sunlight. By using photographic plates, he was able to capture this fluorescence on film. One of the early minerals Becquerel worked with was uranium. Relatively few scientists were interested in Becquerel's findings. It was not until the discovery of radium by the Curies two years later that interest in radioactivity became widespread. In 1898 Marie and Pierre Curie discovered another radioactive element and named it 'polonium'. Later that year, the Curies discovered another radioactive element which they named radium. Their studies with radium led to identify, for the first time, three different type of radiation. These different rays were named as the three first Greek letters:  $\alpha$ ,  $\beta$ , and  $\gamma$ . Since these discoveries, many other radioactive elements have been discovered and used to cure several pathologies. In 1957 the first  $^{99m}\text{Tc}$  was invented at the Brookhaven National Laboratory. Capability to provide radionuclide with short halflife transform nuclear medicine [2]. In the same years Edith Quimby and Leonidas Marinelli elaborated a model of absorbed dose. It was 1958 when H. Anger developed a ionization chamber, that is the foundation of the imaging techniques. In 1953 G. Brownell and H.H. Sweet created a system to detect photons emitted by electron-positron annihilation. However, only by the 1999 radiopharmaceuticals emitting positrons were routinely used in clinics and the use of PET became widespread.

## 1.2 Molecular Radionuclide Therapy

Due to their ability to ionize atoms, ionizing radiations have many industrial, military and medical uses. The medical applications of nuclear technology are divided into diagnostics and radiation treatment. The former is the use of radiation particles, and in particular x-rays, to produce images of human body. The latter uses ionizing radiation to kill tumour cells by damaging the cell's DNA. The most common type of radiation therapy used for cancer treatment is the EBRT. With this approach, only a limited area of the body is irradiated by delivering high-energy rays (photons, electrons, protons or positive ions) from outside the body into the tumour. However, depending on where the tumour is located, it is often difficult to irradiate it without damaging healthy tissues.

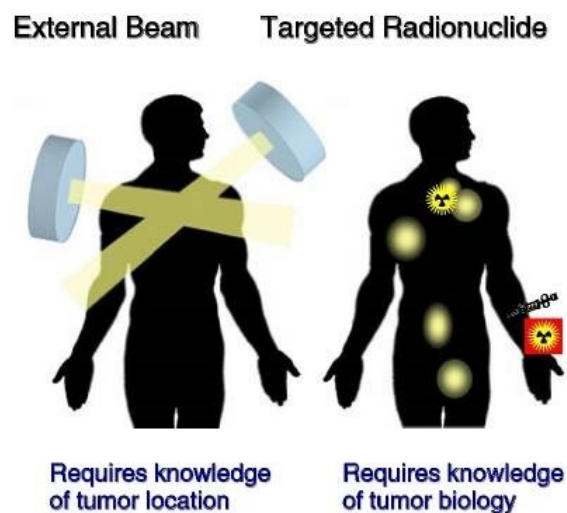


Figure 1.1: External beam therapy and targeted radionuclide therapy for the treatment of brain tumor. SOURCE: Courtesy of Michael Zalutsky, Duke University.

Molecular Radionuclide Therapy (MRT) can be more effective when disease sites are disseminated in the body. Figure 1.1 illustrates and contrasts the differences between EBRT and MRT. Molecular Radionuclide Therapy, also called Targeted Radionuclide Therapy (TRT), consists in the administration of radiolabelled vectors (called radiopharmaceuticals) that specifically binds to tumour cells. Radionuclides are directly injected into the patient to deliver a toxic level of radiation to disease sites. Radiopharmaceuticals are introduced into the body by various means (injection or ingestion are the two most commonplace). Vector allows to transport the radionuclide to the organs/tissues

of interest, while the radionuclide emits radiation that can be used both for diagnostic and therapeutic purpose. Different vectors (antibodies, peptides or organic molecules) and several radionuclides (e.g.  $^{131}\text{I}$ ,  $^{177}\text{Lu}$ ,  $^{223}\text{Ra}$ ) can be used, depending on the characteristics of the tumour. Among the types of cancer treated with this methodology there are thyroid cancer, neuroendocrine tumours and other solid tumours. Efficacy of MRT is based on the capability to selectively “deliver” radiation to tumour cells minimizing administered dose to normal organs. Unlike tumour-directed drugs and toxins, which kill only the directly targeted cells, a unique feature of radionuclides is that they can exert a “crossfire” effect, potentially destroying adjacent tumour cells even if they lack the specific tumour-associated antigen or receptor. MRT is usually a non-invasive treatment and does not produce serious and acute side effects if absorbed dose is below appropriate values. Efficacy of the treatment is mainly related to the radiation absorbed dose. Understanding the relation between the non-uniform energy deposition on tissues and the effects of the treatment is an important issue in different areas, including EBRT, brachithery and radionuclide therapy. In case of MRT relation between response to the therapy and absorbed dose is particularly relevant. Therefore, it is clear the importance to plan the therapy based on the specific characteristic of the patient.

### 1.3 Neuroendocrine tumours

Neuroendocrine tumours (NETs) are relatively rare neoplasms, that originate from neuroendocrine cells situated in various tissues in the body [3]. Neuroendocrine cells have the typical characteristics of both endocrine cells, which produce hormones, and nervous cells. These cells can be found throughout the body, but they are most often found in the abdomen, especially in the gastrointestinal tract. Neuroendocrine cells have many functions, which include controlling and setting the release of digestive enzymes, the air and blood flow through the lungs, blood pressure and heart rate, the amount of glucose in the blood and to regulate the bone and muscle growth.

The incidence of NETs is about 5.25 cases per year out of 100'000 people [4] and they account for only 0.1% [5] of all malignances, hence NETs are

considered as rare. However, the prevalence is much higher due to their mostly slow growing nature, which give the patients a fairly long survival. Interestingly, the incidence has been reported to be markedly increased in Canada [6], United States [7] and Europe [8]. This is probably due to the increased availability of advanced radiological imaging and diagnostic methods.

Symptoms and outcomes vary strongly among patients, depending on several factors that include the type of neuroendocrine tumour and where the tumour is located. NETs can occur in children and young adults, being diagnosed as early as at the age of 5 years, while their incidence increase with age. The majority of people diagnosed with NETs are over age 50. The 5-year survival rate of people is about 60% [9]. The clinical presentation may vary depending on the site of tumour origin. The most frequent are tumours affecting the gastro-entero-pancreatic tract (72%), followed by those which affect the lungs and respiratory system (25%) and less than 5% arise at other sites as skin, thyroid, parathyroid, adrenal glands, thymus breast and genitourinary system [10] [11].

Until the 1980s, chemotherapy was the standard treatment for NETs, even if usually NETs do not respond to common chemotherapeutic treatments. The objective response rates ranged from 0 to 33% [12]. Later, therapies with  $\alpha$ -Interferon and somatostatin analogs significantly improved clinical management. However, in these treatments as well, the objective response rate was rather disappointing.

Multiple treatment approaches are now available for patients suffering from NET: surgery, SSA, interferon, chemotherapy molecularly targeted agents, locoregional therapies and PRRT (Peptide Receptor Radionuclide Therapy). For the choice of the most appropriate treatment, information regarding anatomical location, tumour functionality, sstr status, histological grading and staging are required. Currently the only curative treatment for NETs is surgery. Unfortunately, over 80% of NETs are diagnosed at a relatively late stage, with metastatic spread present at the time of diagnosis and curative surgery is no longer an option [13] [14]. PRRT using radiolabelled somatostatin analogs has proven to be an effective therapeutic option for NET patients with metastases, as it allows targeted delivery radionuclides to tumour cells [15]-[18].

## 1.4 Peptide Receptor Radionuclide Therapy

Peptide Receptor Radionuclide Therapy (PRRT) is one of the most common MRT treatment.

The first experience of PRRT date back to the 1990s with the  $^{111}\text{In}$ -octreotide [19]. In Europe,  $^{111}\text{In}$ -octreotide was abandoned as a therapy option in favour of the more efficient  $\beta$  emitters  $^{90}\text{Y}$  and  $^{177}\text{Lu}$ . PRRT using  $^{90}\text{Y}$  was first used in 1996 in Switzerland. The combination of treatments involving the administration of peptides labelled with  $^{90}\text{Y}$  and  $^{177}\text{Lu}$  were the subject of many clinical trials for the greatest therapeutic potential derived from the combined characteristics of the two radio-isotopes [20]-[25].

In PRRT tumours cells are targated with radiolabelled peptides. Peptides are molecules consisting of two or more aminoacids linked together with peptide bond, and that regulates many phisiological processes in the human body, acting at some sites as endocrine or paracrine signals and, at others, as neurotransmitters or growth factor. Peptides usually display favorable pharmacokinetics characterised by high concentration in the target tissue and rapid clearance from the blood and non-target tissues. PRRT with somatostatin analogs is one of the most innovative tools in the treatment of neuroendocrine tumours, as most of them over-express receptors that binds to somatostatin, a peptide hormone that regulates the endocrine system. Ocreatide and octreotate are somatostatin analogues that binds to somatostatin receptors on neuroendocrine tumours. In PRRT they are combined with a  $\beta$ -emitting radionuclide to deliver a lethal radiation to the tumour. The most common radionuclides used in PRRT are  $^{90}\text{Y}$  and  $^{177}\text{Lu}$ . They are usually alternated during the treatment cycles. The advantage of using both the alternated radionuclides is due to the different physical characteristics:

**Yttrium-90**  $^{90}\text{Y}$  is a high energy  $\beta$ -emitter ( $E_{max} = 2.28 \text{ MeV}$  and  $E_{mean} = 0.934 \text{ MeV}$ ) with physical half-life ( $T_{1/2} = 64.1 \text{ h}$ ) compatible with the pharmacokinetics of peptides, and a long penetration range in tissue ( $R_{max} = 11.3 \text{ mm}$  and  $R_{mean} = 3.9 \text{ mm}$ ). Therefore,  $^{90}\text{Y}$  is suitable for radionuclide therapy, considering the non homogeneous distribution of peptides in solid tumours. The probability of killing the majority of

neoplastic cells is related to the so called cross-fire effect. However, there is a relative high radiation exposure to normal tissues, such as liver, kidneys and spleen.

**Lutetium-177**  $^{177}\text{Lu}$  is a  $\beta$ - and  $\gamma$ -emitting radionuclide with a long physical half-life of 162 h (6.73 days). Compared to  $^{90}\text{Y}$ ,  $^{177}\text{Lu}$  has lower maximum and mean  $\beta$ -particle energies ( $E_{max} = 0.498 \text{ MeV}$  and  $E_{mean} = 0.133 \text{ MeV}$ ). These translate to maximum and mean soft-tissue penetration depths of 1.7 mm and 0.23 mm, respectively. This indicates a lower cross-fire effect partially compensated by a higher percentage of the radiation energy absorbed in very small volumes. This makes  $^{177}\text{Lu}$  a good candidate nuclide for the treatment of small tumours (< 2 cm) and micrometastases.  $^{177}\text{Lu}$  is also a  $\gamma$ -emitter of low emission abundance, with two main emission lines: 113 keV (6% relative abundance) and 208 keV (11% relative abundance). These characteristics enable imaging and therapy with the same complex, and allow dosimetry to be carried out before and during treatment as well.

To date, the two compounds most often used in PRRT are DOTATOC and DOTATATE:

**DOTATOC** is the abbreviated form of [DOTA0,Tyr3]-ocreoide. It is a derivatized somatostatine analogue peptide. DOTA stands for the bifunctional chelating molecule 1, 4, 7, 10-tetraazacyclo-dodecane-1, 4, 7, 10-tetraacetic acid and Tyr3-preotide is the modified ocreotide. DOTATOC is usually labelled with  $^{68}\text{Ga}$  for PET diagnostic purpose ( $^{68}\text{Ga}$ -DOTATOC) and with  $^{177}\text{Lu}$  or  $^{90}\text{Y}$  for therapeutic purpose ( $^{177}\text{Lu}$ -DOTATOC or  $^{90}\text{Y}$ -DOTATOC).

**DOTATATE** is the abbreviated form of [DOTA,Tyr3, Thr8]-ocreoide. It is also a derivatized somatostatine analogue peptide. DOTA stands for the bifunctional metal chelating molecule.

Both analogues share a quite similar sst binding profile. However, the affinity of DOTATATE in binding the sst subtype 2 (sstr2) is approximately a six- to nine fold higher than that of DOTATOC. On the other, DOTATATE has no

affinity for either the sst subtypes 3 and 5 (sstr3 and sstr5), while low affinity is observed for DOTATOC.

## 1.5 Treatment planning

Standard clinical protocols of PRRT consist of the administration of a radiolabelled pharmaceutical. Radiopharmaceutical is administered to patient by injection or infusion. Treatment is commonly fractionated in sequential cycles every 6-9 weeks (usually four or five cycles), allowing for the recovery of healthy tissues. Since renal and red marrow side effect represent one of the main clinical concerns, the renal and red marrow uptake often determines how much radiation can be delivered. In this clinical setting, dosimetry plays a role of primary importance since the administered activity involves deterministic effects at the level of the tumour (target), while it should save as much as possible the healthy tissues. Hence, the purpose of the dosimetric study is to provide patient-specific information, considering the maximum activity that can be administered to the patient in order to maximize the dose to the tumour while minimize the dose to healthy organs.

Therapy can be basically distinguished into two phases:

- Diagnostic and treatment planning dosimetry: patient undergoes a series of planar scintigraphy or SPECT imaging to study distribution and biokinetics of radiopharmaceuticals. Because the radiopharmaceutical is distributed heterogeneously within the body, kinetics of the radionuclide should be resolved temporally to calculate the absorbed dose to tumours and organ at risks (OARs). Usually multiple acquisitions are performed to quantify activity as a function of time. Then, absorbed doses to organs and tumours may be calculated using dedicated software. Dosimetry, when well performed, provides patient specific information that guides the choice of radiopharmaceutical, administered activity and number of treatment cycles to achieve an adequate dose to tumour without serious normal tissue toxicity.
- Treatment, normally, consists of the systematic administration of radio-



pharmaceuticals, fractioned in sequential cycles (usually four or five), every 6-9 weeks. During all cycles the same isotope can be used, or a tandem between different radionuclides.

## 1.6 The MIRD schema

The Committee on Medical Internal Radiation Dose (MIRD) is a committee within the Society of Nuclear Medicine. The MIRD Committee was established in 1965 within the aim to standardize internal dosimetry calculations, improve the published emission data for radionuclides and enhance the data on pharmacokinetics for radiopharmaceuticals [26]. A unified approach to internal dosimetry was published by the MIRD Committee in 1968, MIRD Pamphlet No. 1, which was updated several times thereafter. The formalism presented in MIRD Pamphlet No. 21 will be used here [27].

The MIRD formalism gives a framework for the calculation of the absorbed dose to a certain region, called the target region, from activity in a source region. The absorbed dose  $D$  to a target region is defined as:

$$D = \frac{E}{m} \quad (1.1)$$

where  $E$  is the energy released by the radiation in the target with mass  $m$ . Absorbed dose is expressed in Gray ( $1 \text{ Gy} = 1 \text{ J/Kg}$ ). In the MIRD formalism the absorbed dose is expressed as the product between the cumulated activity  $\tilde{A}$  and the  $S$  value:

$$D = \tilde{A} \cdot S \quad (1.2)$$

the cumulated activity  $\tilde{A}$ , expressed in units of  $Bq \cdot s$ , represents the number of disintegrations occurring in a source regions and depends on the half life of the radionuclide and its spatial and temporal distribution in the source.  $S$  is the mean absorbed dose per unit of cumulated activity ( $Gy/Bq \cdot s$ ) and it is characteristic of the radionuclide and the specific anatomic model chosen to represent the patient or the tissue of interest. If  $r_S$  is the source region and  $r_T$

is the target region, the previous formula is expressed as:

$$D(r_T) = \tilde{A}(r_S) \cdot S(r_S \rightarrow r_T) \quad (1.3)$$

The amount of activity contained in a source region changes with time. If the time-activity curve is known, the cumulated activity  $\tilde{A}$  for a source region  $r_S$  is obtained by measuring the area under this curve:

$$\tilde{A}(r_S) = \int A(r_S, t) dt \quad (1.4)$$

The time interval of integration is theoretically from the injection time up to infinity. However, this is equivalent to integrate up to a time  $T_D$  large enough to include the physical decay of the radionuclide and the biokinetics of the pharmaceuticals:

$$\tilde{A}(r_S, T_D) = \int_0^{T_D} A(r_S, t) dt \quad (1.5)$$

It is often defined the quantity  $\tau$  as the ratio between the cumulated activity and the injected activity  $A_0$ :

$$\tau(r_S) = \frac{\tilde{A}(r_S)}{A_0} \quad (1.6)$$

$\tau$  is known as residence time, and it is expressed in unit of time (h). Sometimes, to avoid any misinterpretation, it is expressed as  $MBq \cdot h/MBq$ . The residence time represents the total number of decays occurring in the source region  $r_S$  per unit of injected activity. Eq 1.3 can be expressed in terms of mean dose per unit of injected activity:

$$\frac{D}{A_0} = \tau \cdot S \quad (1.7)$$

In this way the absorbed dose is normalized to the injected activity and it depends only on the biokinetics and on the physical factors (S).

The total mean absorbed dose to the target tissue  $r_T$  is obtained as the sum of the contribution from all source regions  $r_S$ :

$$D(r_T) = \sum_{r_S} \tilde{A}(r_S) S(r_S \rightarrow r_T) \quad (1.8)$$

Using Eq B.24 this can be written as:

$$D(r_T) = \sum_{r_S} \int_0^{T_D} \dot{D}(r_T, t), dt = \sum_{r_S} \int_0^{T_D} A(r_S, t)S(r_S \rightarrow r_T, t), dt \quad (1.9)$$

## 1.7 Clinical trial

This thesis is focused on the clinical application of MRT. The studies described in the next chapters are based either on phantom acquisitions or on clinical data. All patients were recruited at Azienda USL-IRCCS of Reggio Emilia (Italy) and enrolled in a PRRT clinical trial. Each patient gave the informed consent for the conduction of each study, which has been approved by the ethics committee.

All patients were affected by inoperable or metastatic NETs and met the following inclusion criteria:

- Age >18 years;
- Cyto-histological diagnosis of NET or other SSTR-positive tumours; inoperable or metastatic disease;
- Presence of at least one measurable lesion > 1 cm;
- Positive expression of somatostatine receptors in the  $^{68}\text{Ga}$ -SST PET/CT in lesions (ratio  $\text{SUV}_{max}$  tumour /
- CT with contrast medium or MRI scan within 2 months from recruitment date;
- Adequate haematological parameters: hemoglobin level (Hgb) > 9 g/dL; leukocytes (WBC) >  $2.5 \cdot 10^3/\mu\text{L}$ ; platelets (PLT) >  $90 \cdot 10^3/\mu\text{L}$
- Adequate liver and renal function: bilirubin levels < 2.5 mg/dL; creatinine levels < 2 mg/dL;
- The Eastern Cooperative Oncology Group (ECOG) performance status  $\leq 2$ ;

- Life expectancy longer 6 months;

The exclusion criteria were as follows:

- Pregnancy or lactation;
- Surgery, chemotherapy, radiation therapy or biological pharmaceuticals within 4 weeks preceding the PRRT (except radiotherapy with palliative intent of lesions in symptomatic patients pluri-metastatis);
- Participation in any therapeutic trial within 4 weeks before the PRRT;
- Bone marrow involvement  $> 25\%$ ;
- Other therapeutic option validated as effective;

Additionally, before each PRRT cycle the following inclusion criteria should be maintained:

- Hgb  $> 9$  g/dL, WBC  $> 2.5 \times 10^3$ /L;
- PLT  $> 90 \times 10^3$ /L;
- Creatinine levels  $< 2$ mg/dL;
- Bilirubin levels  $< 2.5$ mg/dL;

Clinical protocol consisted of an intra-venous administration of  $^{177}\text{Lu}$ - or  $^{90}\text{Y}$ -labelled somatostatine analogues, fractioned in sequential cycles up to a maximum of 5 infusions. At least one administration of  $^{90}\text{Y}$  is performed. In the first cycle  $^{177}\text{Lu}$  is injected for dosimetry purpose. The number of cycles, the isotope and the activity chosen for every injection are planned by an expert physician, on the basis of the dosimetry results. The cumulative dose limit to kidneys is set to 46 Gy of BED for patients with no risk factors (hypertension, diabetes, renal failure are considered risk factors for this therapy ) and at 28 Gy for patients with risk factors.

Absorbed doses for liver, spleen, kidneys and lesions are calculated using the organ level dosimetry software OLINDA/EXM 1.1. Red marrow absorbed dose calculation is based on the blood measurements.  $^{177}\text{Lu}$  dosimetry is used to extrapolate  $^{90}\text{Y}$  dosimetry.

In this thesis patients enrolled in two different clinical trial (here named as “Trial A” and “Trial B”) at AUSL - Reggio Emilia were considered. Dosimetry after the first administration is mandatory in both the trials. The only differences between them are the radio-compounds and the number of SPECT/CT acquisitions. Which of the two clinical trials will be from time to time specified in each Chapter.

### 1.7.1 Trial A

Patients were enrolled in a prospective study (EudraCT number 2013-002605-65) between 2014 and 2015. They underwent a sequence of  $^{177}\text{Lu}$ -DOTATOC or  $^{90}\text{Y}$ -DOTATOC administrations. Each patients undergoes to 5 sequential SPECT/CT scans at 1, 4, 24, 44 and 72 h post injection, at the first cycle of therapy.

### 1.7.2 Trial B

Patients were enrolled in a prospective study (EudraCT number 2015-005546-63) between 2016 and 2018. They underwent a sequence of  $^{177}\text{Lu}$ -DOTATATE or  $^{90}\text{Y}$ -DOTATATE administrations. Each patients undergoes to 4 sequential SPECT/CT scans at 1, 24, 44 and 72 h post injection, at the first cycle of therapy.



## Chapter 2

# Quantification of activity

In this chapter three issues related with SPECT imaging quantification are discussed. In nuclear medicine SPECT modality is widely used both for diagnostics and therapy imaging with dosimetry purpose. SPECT allows the visualization of the distribution of radioactivity within the human body and the quantification of the concentration of activity within a given volume of interest (VOI). Since the radiopharmaceutical distribution changes over time in the patient, the activity distribution is assessed using serial quantitative SPECT/CT scans. For radionuclide therapy dosimetry, the activity quantification is essential, because activity is proportional to dose rate at a given time point. Activity quantification for dosimetry has mainly been done using planar scans for decades. Although planar imaging method is the fastest and easiest dosimetry scenario due to the simple pre-processing and ROI drawing, the multi-SPECT-CT scenario provides more accurate data. In 2D, the overlapping of regions (e.g. organs), the non-attenuation corrected imaging data and the neglecting additional individual factors (e.g. organ mass) lead to incorrect determination of the ROI uptake, resulting in an overestimation of the absorbed dose in the corresponding region [25]. Unfortunately, also SPECT imaging system is affected by photon attenuation, photon scatter and limited spatial resolution, hence SPECT is not inherently quantitative. In recent years, developments in image reconstruction compensation methods have been done [28] and, nowadays, hybrid SPECT/CT imaging systems are available for daily practice.

Although nowadays reconstruction algorithms mostly incorporate correc-

tion methods for the confounding variables previously mentioned, current SPECT quantification requires multiple interlinked corrections which may have different performances throughout a typical clinical image. In order to quantify the activity in patients the imaging system must be calibrated to relate the detected count rate to activity. Partial volume effect correction, especially in case of small VOI, needs to be evaluated to prevent underestimation of measured activity. Performance of reconstruction algorithm should be tested and parameters need to be chosen depending on the specific object of acquisition. It is therefore essential to perform home-made tests to investigate the performances of the system acquisition and to validate quantitative imaging. Another issue related to the use of sequential images for dosimetry is the need to co-register the scans in a single frame of reference, so that cumulative activity can be calculated. Different registration algorithms and methods can be used and comparisons of the performances of the methods need to be evaluated.

## **2.1 Impact of commercial 3D OSEM reconstruction algorithm on the $^{177}\text{Lu}$ activity quantification of SPECT/CT imaging in a Molecular Radiotherapy trial**

In general, two main families of reconstruction techniques are commonly used in clinical SPECT/CT images: non-iterative (e.g. filtered back-projection, FBP) and iterative methods. Despite its higher demands on computation, iterative reconstruction seems to be superior for quantification than non-iterative methods. In principle this is mainly due to the ability to implement corrections and system modelling methods more readily in iterative reconstruction than in non-iterative methods. Hence, iterative reconstruction algorithms [29] are the state of the art and they are generally recommended. However, iterative reconstruction is computationally expensive. Block-iterative algorithms are commonly used to accelerate the reconstruction. The Ordered Subset Expectation Maximization (OSEM) algorithm [30] is the most widely used among the various iterative reconstruction methods. Here, the projection data are divided into



subsets which are sequentially operated on during each OSEM iteration. The higher the number of subsets, the shorter the calculation time (one iteration of OSEM with N subsets provides an image roughly similar to that from N iterations of MLEM [31] [32]). However, a large number of subsets results in more noise and artefacts in the final image [33].

In this study it was evaluated the optimum combination of the iterations and subsets employed in a commercial OSEM algorithm, with the aim to establish the quantitative accuracy of the SPECT system. This study was performed using  $^{177}\text{Lu}$ -DOTATOC. The tomographic SPECT phantom images were reconstructed using a commercial 3D OSEM algorithm (Flash 3D, Siemens Medical Solution, Germany), with collimator specific resolution recovery, CT-based attenuation and energy window-based scatter correction.

### 2.1.1 Material and methods

#### SPECT/CT acquisition and reconstruction

SPECT/CT scans were acquired on a Symbia T2 gamma-camera (Siemens Medical System, Germany) with a 3/8 inch NaI(Tl) detector and medium-energy low-penetration (MELP) collimator, with a sensitivity of about 13.9 cps/MBq (from factory data sheet). The energy windows (EW) of  $^{177}\text{Lu}$  photopeaks were set at  $113 \text{ keV} \pm 7.5\%$  and  $208.4 \text{ keV} \pm 7.5\%$ . The tomographic projection images were acquired in step and shoot mode, for 64 views over  $360^\circ$  and 30 sec/frame. Zoom of 1, circular radius of rotation of 330 mm (around the phantom surface) and image matrix of 128x128 pixels were set, resulting in a 4.8 mm pixel size image. For the lower EW, the TEW scatter correction was employed (lower scatter window was set in the range from 87.58 keV to 104.53 keV with the default window weight of 0.5, while the upper scatter window from 121.47 keV to 130.51 keV with the default window weight of 0.9375). For the higher EW, the DEW scatter correction was employed (lower scatter window ranged from 171.60 keV to 192.40 keV with the default window weight of 0.75). The CT acquisition was performed with the following parameters: 130 kV and 30 mAs. The reconstructed slice thickness was 5 mm and a smooth reconstruction kernel was used (B08s; Siemens Medical Solution, Germany).

Reconstruction of SPECT/CT images and imaging analysis were performed

in Siemens E-Soft workstation (Syngo MI, Application version 32B, Siemens Medical Solution, Germany). The images were reconstructed with the proprietary iterative Flash 3D reconstruction algorithm which includes correction for attenuation (based on energy extrapolation of the CT values from the automatically registered SPECT/CT image), compensation for scatter (estimated by means of the multiple energy windows method, and incorporated into the reconstruction) and a full collimator-detector response.

This study was performed using phantoms only. The acquisition set up of the camera is shown in Figure 2.1.



Figure 2.1: Phantom with the six radioactive sphere inserts, on the SPECT/CT scanner table.

Images were reconstructed using a number of iterations ranging from 1 to 20, in step of two iterations, using 2, 4, 8 and 16 number of subsets. A 3-D Gaussian filter with a full width at half maximum of 1 pixel (4.8 mm) on the reconstructed images was used.

## Phantoms

Three different phantoms were used in order to evaluate the dead time, to test the spatial resolution and to study the impact of the reconstruction algorithm.

- A Jaszczak type phantom (Data Spectrum Corporation, USA) with spherical inserts was used to investigate the dead time effect of detectors. This phantom consisted of a cylindrical phantom with a internal volume of 5640 ml and a set of six hollow spheres with decreasing volumes of 98, 27, 19, 11.5, 5.6, 2.57 ml. Each sphere was filled with the same  $^{177}\text{Lu}$  3.44 MBq/ml activity concentration (that is 337, 93, 65, 40, 19, 9 Mbq respectively), while cavity of phantom was filled with a non-radioactive solution. This phantom was acquired several times while decaying, until a time about 3.5 half-lives. For each sphere a spherical VOI was drawn directly on its CT image. The total counts measured in each sphere and the total body reconstructed counts were plotted in function of the known activity injected in the phantom and the time after phantom preparation.
- A cylindrical phantom with three capillary tubes (length 75 mm and internal diameter 1.2 mm) was used to test the system's tomographic spatial resolution. A tube was arranged in central position, while the remaining two tubes were placed at a distance of 3 and 6 cm from the cylinder axis. Each capillary tube was filled with 30 MBq of  $^{177}\text{Lu}$  activity. Acquisitions were performed for different OSEM updates and the spatial resolution was evaluated as average of FWHM (Full Width at Half Maximum) values on three counting profiles across each capillary tube.
- The NEMA IEC Body Phantom™(Data Spectrum Corporation, USA) was used to study the impact of the reconstruction algorithm updates on the quantification. This phantom consisted of a body shaped cavity and a set of five fillable spherical inserts with decreasing volumes of 22.46, 11.46, 5.56, 2.56, 1.15 ml. Each sphere was filled with a different  $^{177}\text{Lu}$  activity concentration ranging between 7.5 and 8.8 MBq/ml. Phantom cavity was filled with non-radioactive water. Activity in each sphere were accurately measured using a dose calibrator.

Whilst NEMA suggests leaving the 2 largest spheres cold in PET applications, we filled with a radioactive solution each sphere since the inferior system spatial resolution of SPECT system.

### Data analysis

Activities for each sphere were estimated using the volumetric analysis tool supplied by Siemens Workstation. For this purpose, a spherical VOI with a diameter equal to the nominal volume of the sphere was drawn on the CT image for each insert. In order to minimize the spill out of recorded counts from the sphere and spill in from neighboring spheres and to optimize the residual misregistration of SPECT and CT images, each VOI was manually shifted by one voxel in each coordinate direction (x, y and z). Then, for each combination of iterations and subsets considered, it was calculated the mean value of the measured data. In particular, for each VOI the total counts ( $C_m$ ), mean ( $C_{mean}$ ) and also the standard deviation ( $C_{std}$ ) of pixel counts were measured. Counts extrapolated from the SPECT images were converted to activity values using the calibration factor (CF) previously calculated. CF for the SPECT/CT scanner was obtained using a cylindrical Jaszczak phantom and the same acquisition protocol adopted for this study. In order to establish the relationship between the choice of OSEM parameters and partial volume effects on recovered concentrations in SPECT reconstruction, Recovery Coefficients (RCs) [34] were calculated using the following expression:

$$RC(V_i, j) = \frac{A_m(V_i, j)}{A_t(V_i)} \quad (2.1)$$

where  $A_m(V_i, j)$  is the reconstructed activity, obtained by the CF value, of the  $i$ -th sphere of volume  $V$ , for the particular combination ( $j$ ) of OSEM update, and  $A_t(V_i)$  is the true activity for the same  $i$ -th sphere.  $A_t(V_i)$  was decay corrected as follows:

$$A_t(V_i) = A_0(V_i) \exp\left(\frac{T_0 - T_{cal}}{T_{1/2}} \ln 2\right) \left(\frac{T_{acq}}{T_{1/2}} \ln 2\right) \left(1 - \exp\left(-\frac{T_{acq}}{T_{1/2}} \ln 2\right)\right)^{-1} \quad (2.2)$$

where  $A_0$  is the initial activity in the sphere volume  $V_i$ ,  $T_0$  the acquisition start time,  $T_{cal}$  the time of activity calibration,  $T_{1/2}$  the half-life of  $^{177}\text{Lu}$  and

$T_{acq}$  is the acquisition time. The first term in brackets corrects for the radioactive decay from the time of calibration to the acquisition start time. The second term corrects for the acquisition time, while the third term calculates the mean counts considering an exponential decay during acquisition. Here, the  $A_0$  for each sphere was determined by a direct measurement in a dose calibrator. Accuracy of quantification was evaluated using the root mean square error (RMSE):

$$RMSE(V_i, j) = \sqrt{\sum (A_m(V_i, j) - A_t(V_i, j))^2} \quad (2.3)$$

The average fractional error in activity estimation over all spheres, named as wRMSE (weighted RMSE) was calculated as:

$$wRMSE(V_i, j) = \sqrt{\sum f_k (A_m(V_i, j) - A_t(V_i, j))^2} \quad (2.4)$$

Here,  $k$  refers to the product of subsets and iterations set in the reconstructed images, and  $f_k$  is its weighting factor.

### 2.1.2 Results

Figure 2.2 shows correlation between the total measured counts and the true total activity injected into the phantom. Since activity in the phantom decreased due to physical decay between one measurement and the other one, poor correlation is an evidence of dead time effect. High linear correlation (Pearson coefficient  $R^2 = 0.99$ ) was obtained, hence no dead time effect was detected.

In Table 2.1 the estimated tomographic spatial resolution is reported for different numbers of subsets and iterations (from 4 to 16 subsets and from 4 to 18 iterations respectively).

Figure 2.3 shows the number of measured counts in the SPECT images, for increasing values of iterations and subsets. As described in the previous section, counts were obtained as the average value of the shifted six VOIs to all directions. Increasing the number of iterations and subsets resulted in increased counts. However, counts converge towards an asymptote differently according to the size of the sphere: convergence is obtained with 10 iterations

Table 2.1: Results of resolution measurements performed with three hot capillary tubes placed at 0cm, 3cm and 6cm respectively from the central axis.

		<b>Capillary tubes</b>		
		<b>central</b>	<b>3cm</b>	<b>6cm</b>
4S4I	average	17.92	15.12	14.73
	st. dev.	0.02	0.11	0.26
	noise%	0.10	0.73	1.77
4S10I	average	13.44	11.40	10.97
	st. dev.	0.06	0.06	0.07
	noise%	0.44	0.53	0.61
4S18I	average	10.27	9.99	9.49
	st. dev.	0.16	0.07	0.19
	noise%	1.57	0.72	1.95
8S4I	average	12.87	11.73	11.39
	st. dev.	0.09	0.04	0.28
	noise%	0.67	0.32	2.47
8S10I	average	10.41	9.81	9.18
	st. dev.	0.75	0.46	1.10
	noise%	7.16	4.73	11.94
8S18I	average	9.73	8.55	8.27
	st. dev.	0.92	1.32	0.94
	noise%	9.48	15.43	11.39
16S4I	average	12.15	10.46	9.33
	st. dev.	0.47	0.92	0.40
	noise%	3.86	8.75	4.34
16S10I	average	8.94	8.50	8.01
	st. dev.	0.65	1.14	1.09
	noise%	7.29	13.42	13.58
16S18I	average	8.78	8.40	8.04
	st. dev.	0.60	1.41	1.40
	noise%	6.84	16.80	17.38

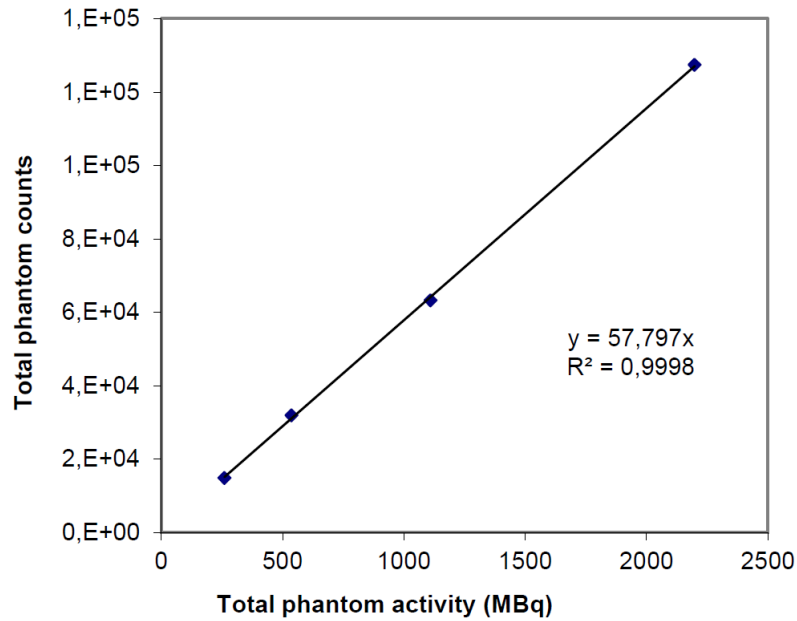


Figure 2.2: Total measured counts in the phantom is plotted against the real total activity injected in the phantom to evaluate the dead time effect.

for the largest sphere, while larger number of iterations is required in case of the smaller spheres (Figure 2.3 b,c). No convergence was observed in case of the smallest spheres (Figure 2.3 d,e), even for large number of iterations ( $> 20$ , results not shown).

Figure 2.4 shows results for RC as a function of the number of iterations and subsets. This plot allows to evaluate the lack of true activity in the reconstructed images. It is evident only in the case of the three largest spheres (diameters 36, 28 and 22 mm) it is possible to reach  $RC = 1$  (i.e. measured activity is equal to true activity) setting opportunely the number of iterations and subsets, whereas even using high number of iterations and subsets measured activity underestimates the true activity in case of the smallest spheres (diameters 17 and 13 mm).

The wRMSE, i.e. the RMSE normalized to the true activity, was plotted as a function of the product between the number of subsets and iteration (EI) in Figure 2.5. In this graph, data for each sphere refer to the highest factor obtained by the OSEM updates considered in this study, that is  $EI = 64, 80, 132$  and  $160$ . For a fixed choice of EI, the wRMSE is sphere volume dependant

because of the PVE.

### 2.1.3 Discussion

In this study the influence of the OSEM updates on the  $^{177}\text{Lu}$  SPECT reconstruction was investigated. The intention of these experiments was, in particular, to quantify the error associated with the choice of OSEM parameters, as a function of the object volume using the PET NEMA IEC body phantom.

Results showed that the choice of OSEM impacts on the quantification of activity in SPECT imaging for clinical purpose. As reported in Table 2.1, spatial resolution is strictly related to the number of iterations and subsets. For a fixed number of subsets, as iterations rise up, spatial resolution improves, but noise increase too. The same is true if the iterations number is fixed, while subsets varying. The best spatial resolution is achieved with the highest iteration and subset values (16 subsets and 18 iterations in our case), in spite of a higher noise level in reconstructed images. Indeed, the overall best spatial resolution (8 mm) can be obtained when spheres are nearest to detectors (6 cm from central position in our case). Thus, detectability of an object (for example a lesion in clinical patterns) is dependent on the OSEM updates and on the distance between the object and the detector.

Therefore, the choice of a fixed number of iterations and subsets might be a drawback for dosimetric purpose. As shown in Figure 2.2, the choice of the same OSEM updates for all lesions could be inadequate in reaching the total count convergence inside the considered volume.

Objects with different volume need different numbers of OSEM updates to be the activity correctly quantified, that is the choice for OSEM updates is object size dependent. Hence, in a potential situation where patient lesions of different volume and different geometries are dealt with, using only one reconstructed image might be not the best solution. OSEM updates might be specifically chosen for each lesion. For volumes larger than 5.5 ml (that is the volume of the median sphere Figure 2.3c), the number of subsets and iterations to be used shouldn't be lower than 4 and 8, respectively.

In case of objects with a volume smaller than 5.5 ml, such as the two smallest sphere in this study, partial volume effect is predominant and quantified activity



underestimate the real activity regardless of the OSEM parameters used. In this situation, the quantification becomes anyway challenging and particularly critical because of the limited spatial resolution of SPECT modality. This is clear in Figure 2.3: using, for example, a value of  $EI = 64$  (this can be 8 subsets and 8 iterations, or also 16 subsets and 4 iterations) RC will be lower than 1 for the smallest spheres. Intrinsic error in quantification of activity is not recoverable with the reconstruction process, in case of small VOIs. Our results show that smaller the sphere (hence, bigger the spread in total counts), bigger the error in activity estimation (Figure 5), ranging from 3.7% (biggest volume) to 35% (sphere volume of 5.56 ml) and 85% (smallest volume) at small values for subsets and iterations and from 3.7% (biggest volume) to 20% (sphere volume of 5.56 ml) and 79% (smallest volume) at higher values for subsets and iterations. Even if the EI quantity is very high, no additional gain for the  $wRMSE / (\text{true activity})$  ratio for spheres smaller than 4-5ml is detected.

There are some limitations in our study that should be highlighted. In this study we only considered spherical volumes and inserts were placed in a fixed position inside the phantom. Inserts had similar distance from the SPECT/CT detectors and were placed in a cold background. These choices are clearly distant from a clinical situation where organ motion and, consequently, unfixed lesion positions are present, together with background activity surrounding tissues responsible for the spill in effect. However, the assumptions represent a simplification that is essential in the investigation of their influence on the activity quantification. Finally, it should be noted that these results are scanner specific, i.e. they depend on the collimator, crystal detector, source-to-detector distance, energy window, system spatial resolution etc. Hence, to establish the best OSEM update similar experiments should be carried out by each specific centres.

The current study showed the need for PVE compensation to gain an accurate quantification of  $^{177}\text{Lu}$  for dosimetry purpose in a MRT trial focussed on lesions and organs dosimetry. This is particularly true when lesions or small organs should be drawn on SPECT images. A good compromise between spatial resolution, noise of the image and clinical reasons lead us to identify the EI value of 80 with 8 subsets and 10 iterations in abdomen exams, like the most

appropriate in our  $^{177}\text{Lu}$  dosimetry trials.

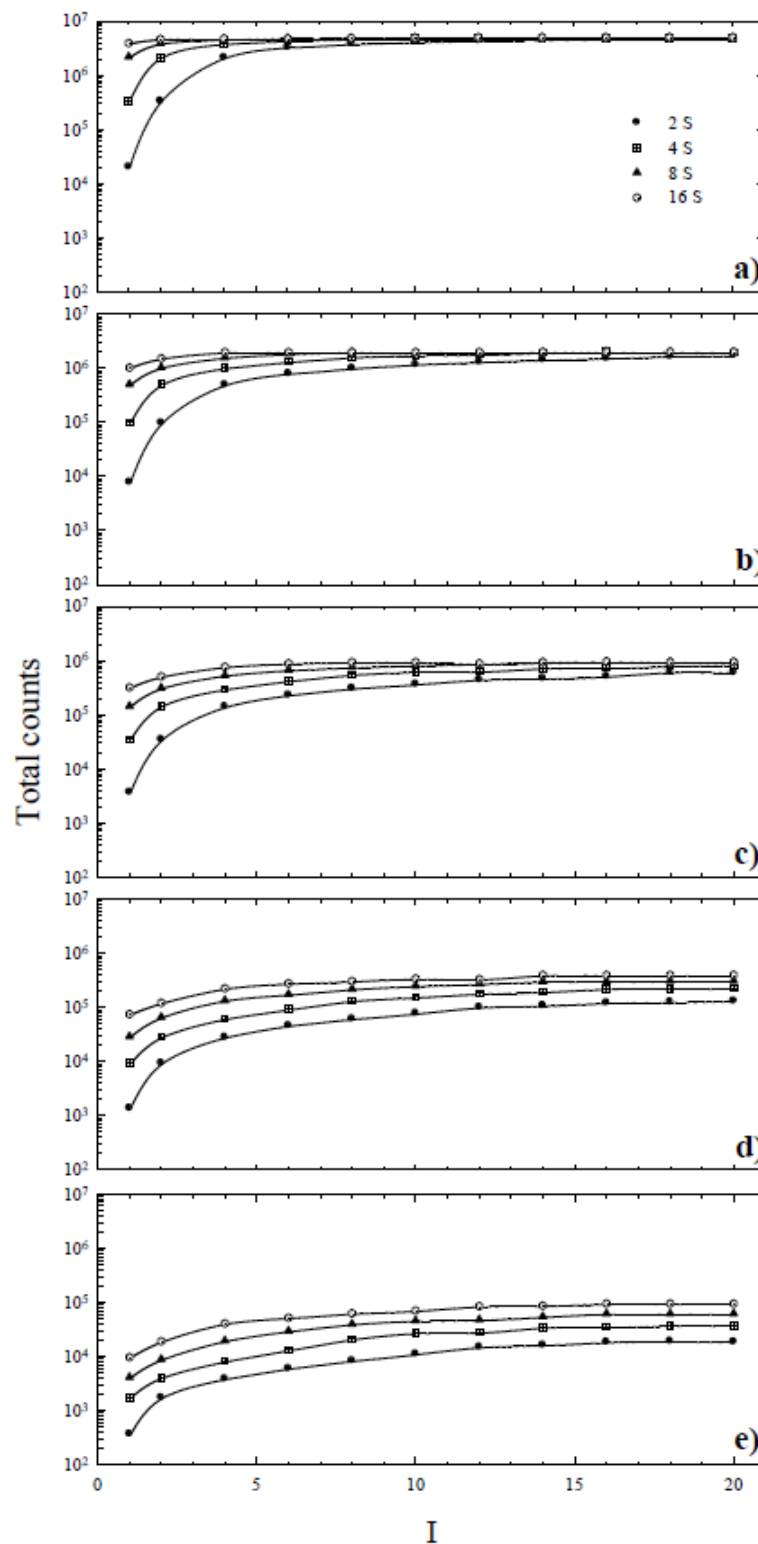


Figure 2.3: Measured counts in each sphere versus the number of iterations (x-axis) and subsets (marker symbol). Data are arranged according to the sphere diameter: (a) 36mm, (b) 28mm, (c) 22mm, (d) 17mm, (e) 13mm.

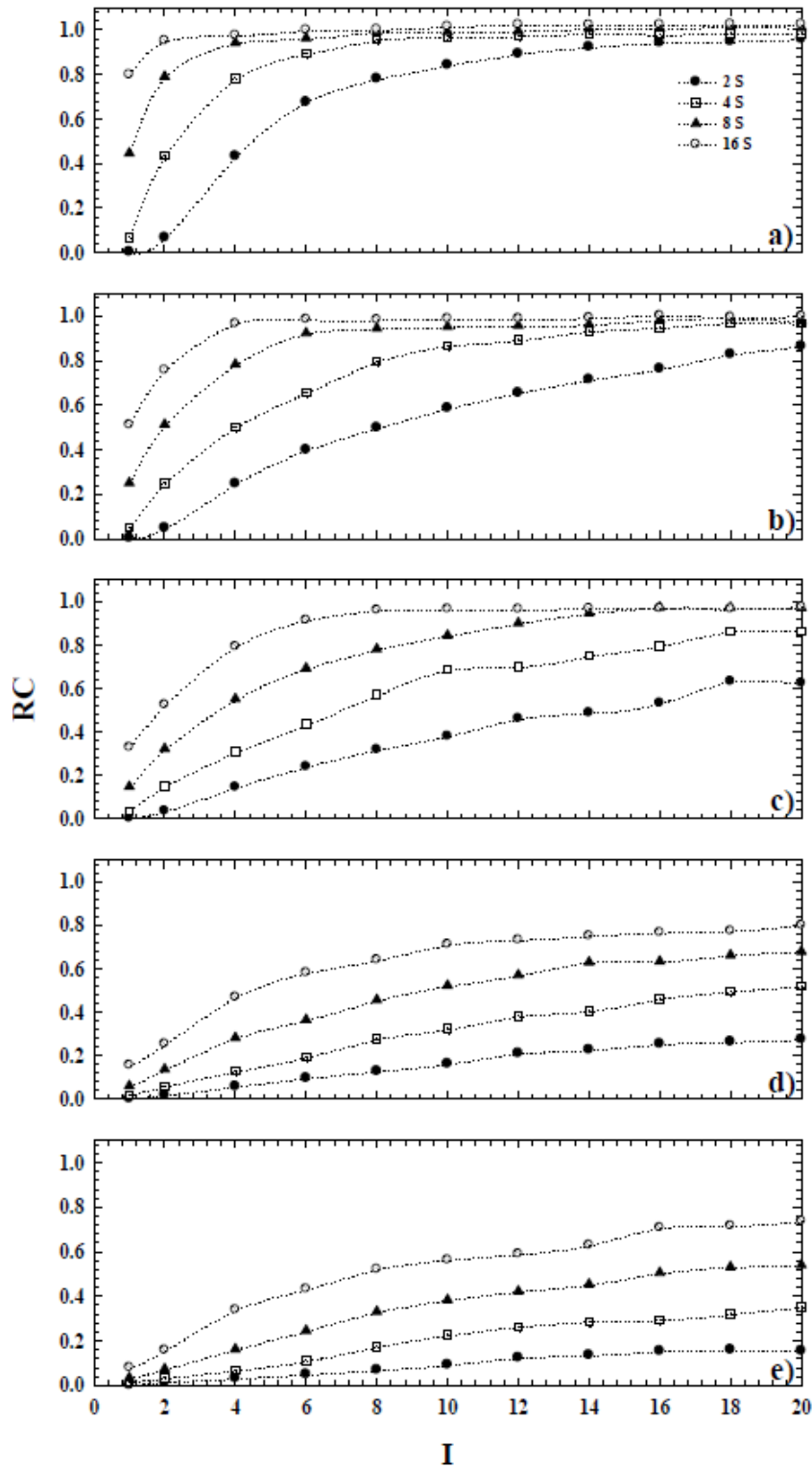


Figure 2.4: Recovery coefficients versus the number of iterations (x-axis) and subets (marker symbol). Data are arranged according to the sphere diameter: (a) 36mm, (b) 28mm, (c) 22mm, (d) 17mm, (e) 13mm.

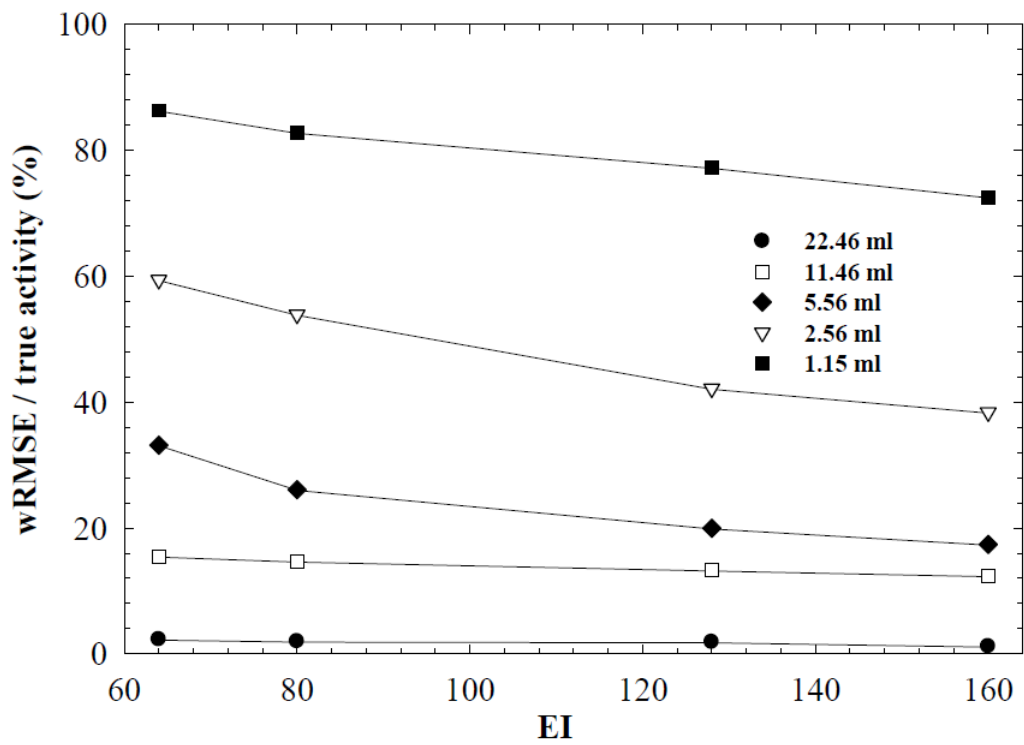


Figure 2.5: Weighted Root Mean Squared Error (wRMSE) normalized to the true activity as a function of equivalent iterations (EI).

## 2.2 Partial volume effect of SPECT images in PRRT with $^{177}\text{Lu}$ labelled somatostatin analogues

As it was highlighted in the previous section, Partial Volume Correction (PVC) is essential when imaging quantification is performed. Even if using optimal number of iterations and subsets while state-of-the-art reconstruction algorithm is used to compute 3D multi-modal imaging, PVC is essential for small object quantification. For that reason understanding PVE is foremost importance in the context of MRT, both for quantification using SPECT and for evaluation of response using PET.

### What is PVE?

The term “partial volume effect” refers to the loss of apparent intensity in small object of images. The finite spatial resolution of imaging system and the image sampling cause a distortion of activity concentration and seriously affect the possibility for accurate quantitative analysis. A small object in this context is approximatively smaller than 2-3 times the FWHM of the PSF (Point Spread Function). For larger objects, there will be full recovery of the counts in the central parts of the object. The limited spatial resolution of the imaging system, and the resulting 3-dimensional image blurring, causes spillover between regions, as illustrated in 2 dimensions in Figure 2.6. This effect results in reduction of measured activity into the VOI.

Another phenomena involved in PVE is the discretization of image. In SPECT images the fundamental level of signal is voxel. Of course, voxels do not match the actual contours of the object, hence the signal intensity in each voxel is the mean of the signal intensities of the underlying regions included in that voxel. This effect is illustrated in 2 dimension in Figure 2.7.

PVE is often viewed as two separate effects: spill-in and spill-out, which make sense when focusing on a volume of interest (VOI) in which the activity needs to be quantified. Adjacent regions are then considered as background regions and are taken into consideration only for their relation with the VOI.

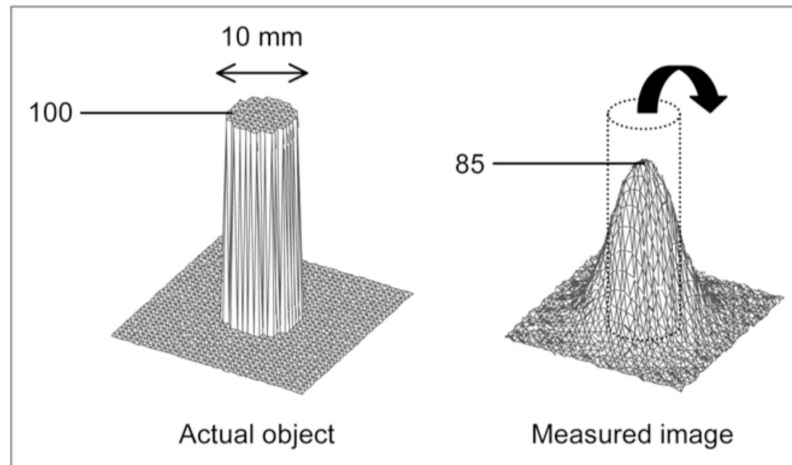


Figure 2.6: Circular source (diameter of 10 mm) of uniform activity (100 arbitrary units). Part of the signal inside the object is displaced outside of it, causing reduction of measured signal in the object. SOURCE: Soret M et al. J Nucl Med 2007.

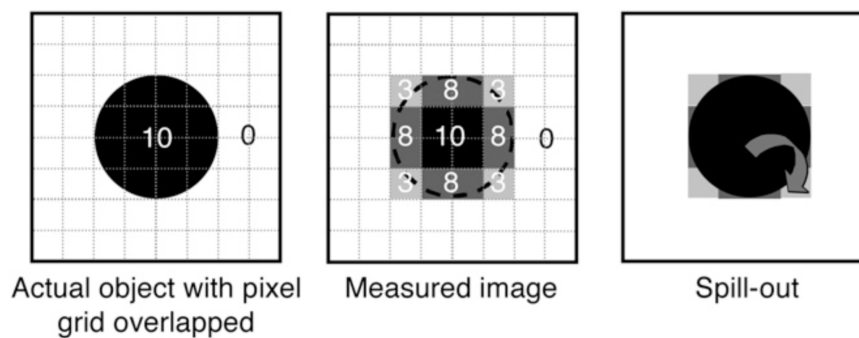


Figure 2.7: Influence of image sampling on PVE. Pixels on edges of VOI do not match the object contours. Part of signal emanating from the object is seen outside the VOI. SOURCE: Soret M et al. J Nucl Med 2007.

### Parameters affecting PVE

PVE depends on numerous parameters [35]. Firstly, it has a strong dependence on the size of the object. Objects with the same activity, but different size yield images with different degree of intensity. Furthermore, relation between PVE and size of the object is not linear. Another parameter that affects PVE is the shape of the object. Objects with the same activity and the same volume, yields different activities if the shape of the objects is different. In particular, it depends how much “compact” it is. The term “compact” refers to the ratio be-

tween the surface area and the volume. The largest the ratio, the less compact the object. Spherical volumes are the most compact, so they are less affected by PVE. Essentially, objects far from a spherical geometry are susceptible to spilling-in and spilling-out since a large part of inner points is close to the edge. PVE depends also on the activity on the surrounding regions, which determines spill-in.

### **PVC method**

PVE in a phantom with known activity can be estimated by dividing the SPECT/CT-based activity by the known activity, as described in 2.1.1. This procedure allows to use the calculated RC (Eq. 2.1) to correct quantified activity for PVE. This implies the same camera and reconstruction protocol used to estimate RC is adopted. Moreover, since PVE is strictly affected by the object size and geometry, phantoms should be as similar as possible to the object on which PVE correction is performed to.

The aim of this work is to point out the most critical issues related to PVE in SPECT images of  $^{177}\text{Lu}$  SPECT images. To this aim a model based upon phantoms that simulate a clinical context was used.

## **2.2.1 Materials and methods**

### **Image acquisition and reconstruction**

All activity measurements were performed with an accurate activity calibrator (Aktivimeter Isomed 1010, Nuklear Medizintechnik, Germany) with a traceable geometry calibration and acquisition of all images through a SPECT/CT scanner (Symbia T2, Siemens Medical, Germany). The same acquisition protocol used in the previous part and described in 2.1.1. The SPECT projections were reconstructed using Flash 3D iterative algorithm: 10 iterations, 8 subsets, Gaussian filter cut-off = 4.8 mm). These parameters were chosen based on the results of the previous section 2.1 to obtained the best compromise between spatial resolution and image noise.

To convert measured counts to activity a partial volume calibration factor (CF) was determined using a cylindrical Jaszczak phantom filled with a radioactive



$^{177}\text{Lu}$  solution. A cylindrical VOI with a radius equal to the reconstructed SPECT image FOV size was used. Once obtained the CF (equal to 28.5 Bq/cts), counts to activity conversion was obtained as:

$$\text{Measured activity} = CF \cdot \text{Counts} \quad (2.5)$$

Contours for each insert were manually drawn on the CT using Velocity 3.2.0 (Varian Medical System, Palo Alto, USA). VOIs were transferred onto the SPECT image using the CERR platform [36].

### Determination of Recovery Coefficients

Two different phantoms were used to determine RCs:

1. A Jaszczak type phantom (Data Spectrum Corporation, USA) with spherical inserts to mimic isotropic activity distribution (hereafter referred to as “Sphere phantom”). This phantom consisted of a cylindrical phantom filled with a radionuclide solution, in which seven spheres and two ellipsoidal inserts with increasing volume were placed. Each insert was filled with the same activity concentration. A capture of an axial CT slice of the phantom is shown in Figure 2.8a.
2. A Liqui-Phill phantom (The Phantom Laboratory, USA) to mimic organ-shape activity distribution (hereafter referred to as “Anthropomorphic phantom”). This phantom consisted of a human body phantom with organ-shaped inserts (liver, spleen, pancreas and kidney). These organ inserts were hand-designed to be as close as possible to real ones. Each organ-insert was filled with a specific activity concentration chosen from clinical values. A capture of an axial CT slice of the phantom is shown in Figure 2.8b.

The volumes and activity concentrations are shown in Table 2.2.

Volume for each phantom was estimated based on the contour on the CT image, while volume of inserts was derived measuring the weight of the inserts before and after the refilling using a calibrated scale (assuming the concentration of the radioactive solution is 1 g/ml).

Table 2.2: Description of phantoms and inserts used to calculate RCs. Each sphere was named as his diameter (i.e. the sphere with 10 cm of diameter as “Sphere10”)

Phantom	Phantom volume (ml)	Insert name	Insert inner Volume (ml)	Background activity concentration (MBq/ml)	Insert activity concentration (MBq/ml)
Sphere phantom	4225	Sphere10	0.6	0.032	0.905
		Sphere13	1.2		
		Sphere17	2.6		
		Sphere22	5.7		
		Sphere28	11.6		
		Sphere37	26.8		
		Sphere57	98.6		
		Falcon48a	58.5		
		Falcon48b	58.9		
Anthropomorphic phantom 1	8153	Pancreas	92	0.0035	0.12
		Right Kidney	142		0.10
		Left Kidney	142		0.10
		Spleen	156		0.14
		Liver	1470		0.07

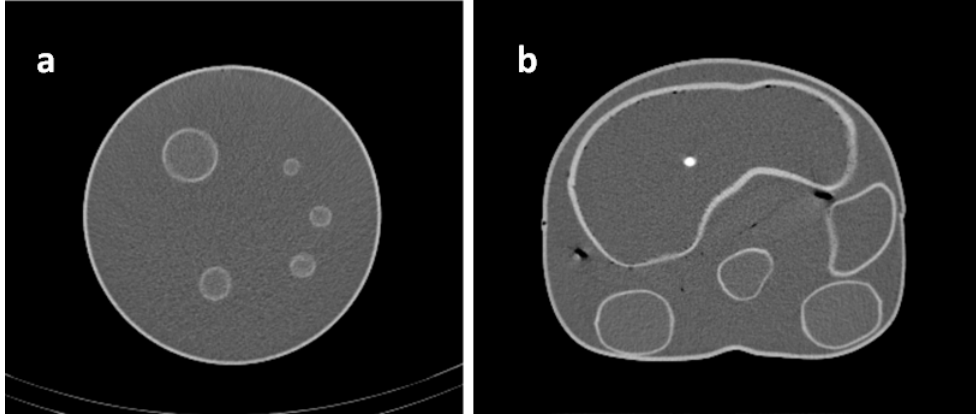


Figure 2.8: Axial CT slice of the Sphere phantom (a) and Anthropomorphic phantom (b).

For each insert RC was estimated using the following formula:

$$RC = \frac{\text{Measured activity}}{\text{True activity}} \quad (2.6)$$

Measured activity was obtained using Eq. 2.5, where CF was previously calculated and Counts were detected in a VOI precisely following the contours of the object in the CT image. True activity was measured using an activity calibrator. Uncertainty associated with RC was estimated using the law of propagation of uncertainty. The accuracy of measured activity was 10%, as reported by [37], whereas accuracy of true activity was 5%, as reported in the user manual of the activity calibrator. Partial volume corrected activity is achieved, once the RC is known, using the following expression:

$$PVC \text{ activity} = \frac{\text{Measured activity}}{RC} = CF/RC \cdot \text{Counts} \quad (2.7)$$

### Accuracy of partial volume correction

Two phantoms were used to evaluate accuracy of partial volume correction method previously described:

1. A cylindrical phantom and a set of 11 inserts were arranged in two different configurations to originate two phantoms (hereafter referred to as “Geometrical phantom”). Each insert consisted in a fillable hollow cavity with a specific geometrical shape (toroidal, pear-shape, tubular or

ellipsoidal). Inserts take the name from the shape and the equivalent diameter (i.e. the diameter for a sphere with the same volume), as shown in Table 2.3. Captures of an axial CT slice for each geometrical shape of the inserts are shown in Figure 2.9. More details are reported by Berthod et al. [38].

2. The same anthropomorphic phantom used for determination of RCs, described above in 2.2.1. This phantom was filled with a different activity concentration and scanned a second time.

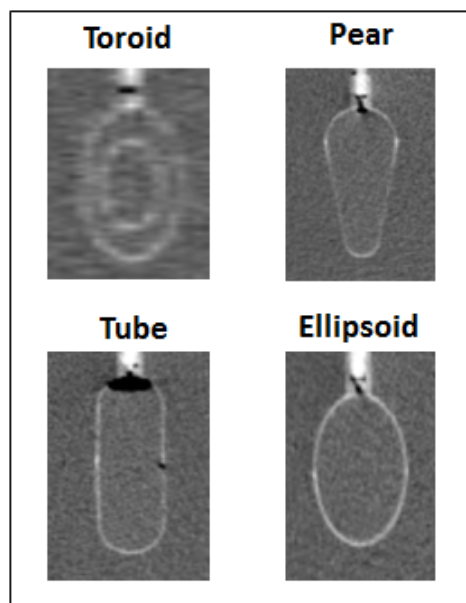


Figure 2.9: Axial CT slice for different insert-shape of the Geometrical phantom.

Details of inserts, volumes and activity concentrations are collected in Table 2.4.

Percentage difference (Error (%)) between the quantified activity the true activity was calculated to estimate accuracy of PVC method:

$$Error(\%) = \frac{Quantified\ activity - True\ activity}{True\ activity} \cdot 100 \quad (2.8)$$

Quantified activity was obtained from SPECT images, using Eq. 2.5 in caso of no PVC or using Eq. 2.7 in case of PVC.

Relation between accuracy of PVE correction and the geometrical shape of the object was then investigated. To this end “compactness” for each insert shape

Table 2.3: Legend of the insert acronyms for the Geometrical phantom.

Insert geometry	Equivalent diameter (mm)	Insert name
<b>Torus</b>	17	To17a
	17	To17b
	26	To26
<b>Ellipsoid</b>	20	E20
	30	E30
	38	E38
<b>Pear</b>	38	P38
	39	P39a
	39	P39b
<b>Tube</b>	38	Tu38a
	38	Tu39b

Table 2.4: Description of phantoms and inserts used to evaluate RCs. Each sphere was named as his diameter (i.e. the sphere with 10 cm of diameter as “Sphere10”)

Phantom	Phantom volume (ml)	Insert name	Insert inner Volume (ml)	Background activity concentration (MBq/ml)	Insert activity concentration (MBq/ml)
Geometrical phantom	6713	To17a	2.8	no background	1.53
		To26	9.7		
		E22	5.5		
		E30	14.8		
		E38	28.5		
		To17b	2.8		
		P38	29.2		
		P39a	30.1		
		P39b	31.2		
		Tu38a	28.6		
Tu39b	28.8				
Anthropomorphic phantom 2	8153	Pancreas	92	0.03	0.99
		Right Kidney	142		0.82
		Left Kidney	142		0.81
		Spleen	156		1.10
		Liver	1470		0.53

was estimated using the parameter asphericity (ASP), defined by Apostolova et al. [39] as follows:

$$ASP = 100 \cdot (\sqrt[3]{H} - 1) \quad \text{with } H = \frac{1}{36\pi} \cdot \frac{S^3}{V^2} \quad (2.9)$$

where S and V are the surface and the volume of the insert, respectively. ASP measures the deviation of a particular non-spherical VOI from the shape of a sphere with the same equivalent volume.

## 2.2.2 Results

### Determination of the Recovery Coefficients

Figure 2.10 shows the calculated RCs for the Sphere and the Anthropomorphic phantoms.

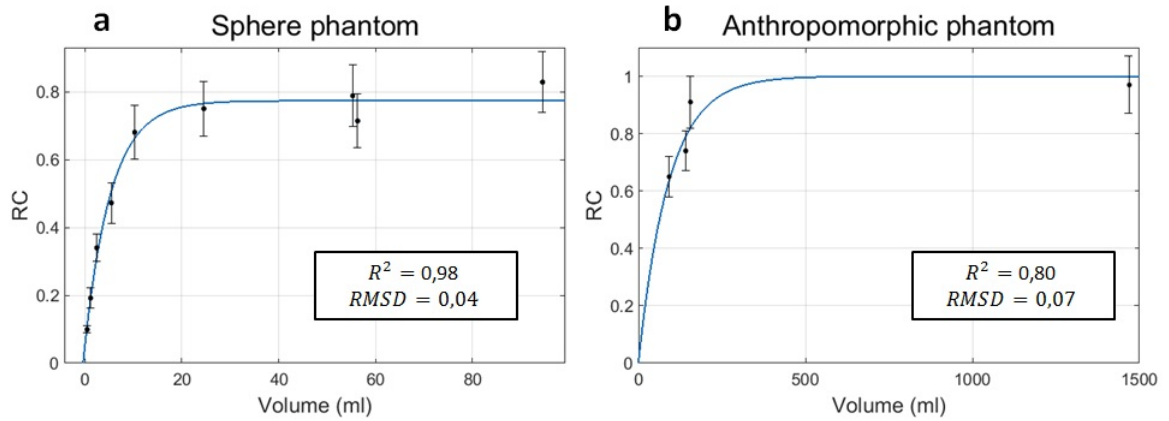


Figure 2.10: Calculated RCs for the spherical inserts (a) and the organ-shape inserts (b) as a function of the insert volume. Data points were fitted using exponential curves ( $R^2$  and RMSE are reported in the graph). Note: RCs for the left kidney and the right kidney are too close to be distinguished in the graph.

RCs vs volume data points were fitted using Eqs. 2.10 and 2.11 for the Sphere phantom and the Anthropomorphic phantom respectively.

$$RC = a \cdot e^{-b \cdot Volume} + c \quad (2.10)$$

$$RC = a \cdot e^{-b \cdot Volume} + 1 \quad (2.11)$$

where  $a$ ,  $b$  and  $c$  are the fitting parameters, Volume and RC the independent and dependent variables respectively. Eq. 2.11 was used to obtain convergence toward the asymptote ( $RC = 1$ ).

The Bravais-Pearson correlation coefficient ( $R^2$ ) and the Root Mean Square Deviation (RMSD) were used to evaluate accuracy of the best fitting curves. These values are reported in Figure 2.10.

### Accuracy of partial volume correction

Partial volume corrected activities were obtained using Eq. 2.7 and RC from curves in Figure 2.10. More in detail, the curve in Figure 2.10a was used for the Geometrical phantom inserts, whereas the curve Figure 2.10b was used for the organ-shaped inserts placed in the Anthropomorphic phantom. Figure show the Error (%) in the activity quantification.

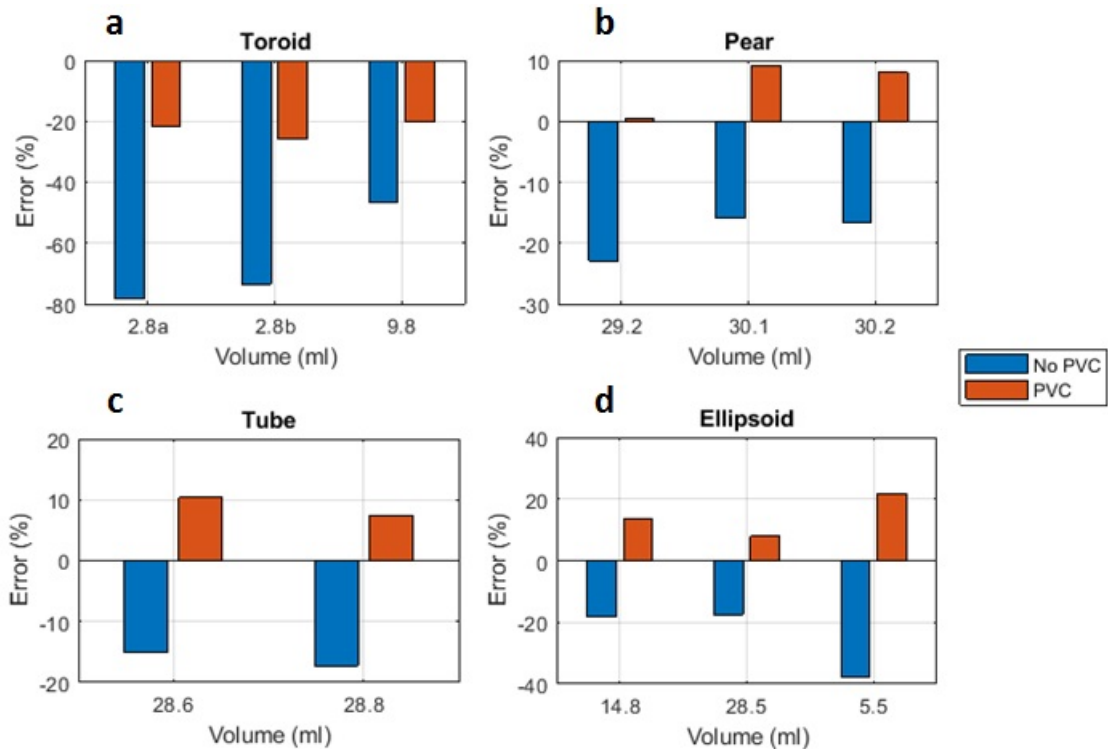


Figure 2.11: Error (%) of measured activity in each insert of the Geometrical phantom. Both corrected and non-corrected activities for PVE were evaluated.

Figure 2.13 shows the Error (%) of PVC activity as a function of the ASP for each inserts of the Geometrical phantom.

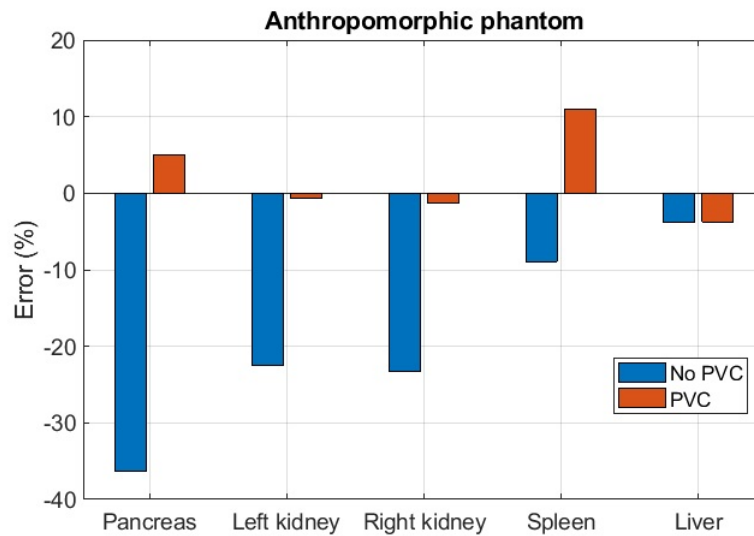


Figure 2.12: Error (%) of measured activity in each insert of the Anthropomorphic phantom. Both corrected and non-corrected activities for PVE were evaluated.

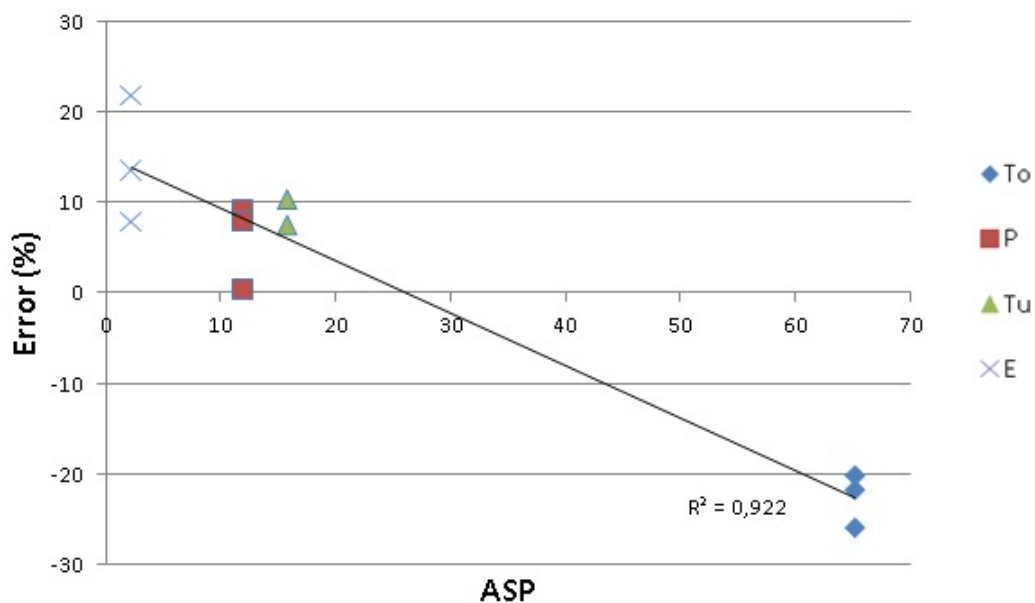


Figure 2.13: Error (%) of corrected activity for PVE is plotted against the ASP. The Pearson correlation coefficient ( $R^2$  is reported in the graph. A different data point format was used for inserts with different shape or equivalent diameter.

### 2.2.3 Discussion

The aim of this study was to generate a model to be easily applied in the clinical practice when activity quantification is required and partial volume correction



is necessary. This model is based on RC and has been chosen because it is one of the simplest method of PVE correction, suitable to be used in the clinics. The procedure to calculate RCs was described in section 2.2.1 and can be used as a guide to obtain a model for PVC in each institute. The RC method was demonstrated by Tran-Gia et al. [40] to be the most accurate, compared to other methods based on enlarged VOI, peak-ml and fixed threshold.

Phantoms used in this study were chosen in view of the clinical implementation of RCs for partial volume effect compensation. In clinics quantification of activity is usually required for organs and tumours, which have different shapes. Each organ has a typical shape and PVE can be evaluated using phantoms properly designed to mimic that geometry. On the other hand, tumours are a different matter. Generally, tumours are not characterized by a specific shape. Thus, it is very difficult to obtain RC specifically for the real shape of the lesion and they are usually approximated as spheres. For this reason in this work we studied the influence of the asphericity on RC.

A marked improvement in quantification of activity was observed when PVE corrected activities were used. Average percentage error over all inserts passed from -26% to 1.3% when activities were corrected for PVE. However, improvement of quantification depends on the specific insert. Error (%) is negative and large in case of toroids (Figure 2.11a), while it is positive and small in case of the other inserts (Figure 2.11b-d). This result suggests to calculate RCs using inserts with geometrical shape as similar as possible with the object to be quantified. Dependence on the shape of the object is quantitatively evaluated in Figure 2.13. Error (%) was plotted against the ASP, and high relation between these was observed ( $R^2 = 0.922$ ). Inserts with the same shape (vertically in the graph) showed higher value of Error (%) for larger volume (see the Toroids (To) and the Pears (P)), even if this trend was not observed in case of the Ellipsoid (E). It is possible the relation between PVE and volume depends on the shape of the object (for example it is exponential in case of spheres). Hence, relation between Error(%) and volume depends on the shape of the insert. Further studies should be performed to investigate this relation. Figure 2.12 shows results obtained with the Anthropomorphic phantom. Similarly to the Geometrical phantom, Error(%) depends on the insert. Probably

different RC curves should be used for each organ-geometry, as it was suggested by Robinson et al. [41], but it would be necessary to have several inserts with ranging between different volumes for each organ. However, this is not easy in practice on a large scale at present. Nevertheless, using a single RC curve for all organs increase quantification of activity into organs, though it has some limits. Quantification of Anthropomorphic phantom's inserts was probably also affected by spill-over effect between organs. This is, for example, the case of the spleen, which is close to the liver and the left kidney. Figure 2.10 shows that RC value calculated for the spleen is far from the RC curve and consequently compensation for PVE is too large.

Results of this work might be improved if the signal/background ratio was considered. As reported by Shyam et al. [42] spill-in depends on this ratio and affects PVE. However, in this experiment this ratio was very low and contribute of spill-in was negligible.

One of the main limitation of RC method is that not all anatomical structures can be well approximated by simple geometrical shapes, and anatomical variability between different patients is not easy to account for. The implicit assumption that the VOI is placed into a homogeneous surrounding background activity is usually not true in clinical patterns, and signal/background ratio is not easily to be defined to. PVE depends also on several factors: the tomographic scanner, the image acquisition settings and reconstruction algorithms, the scatter correction, VOI definition technique and the measurement procedure. For that reason, it is necessary the RC curve to be calculated individually in each centre, eventually following standard procedures validated by the scientific community.

## 2.3 Impact of two non-rigid registration workflows

Calculation of absorbed dose requires acquisition of multiple images to quantify the activity distribution within the patient as a function of time (see Paragraph 1.5). Both planar and tri-dimensional acquisitions can be used, however the latter provides more accurate quantification [43]. When dealing with sequential functional imaging, the misalignment of sequential scans is a critical aspect. Misregistration errors can derive from changes in patient repositioning, organ deformation, tumour progression/regression between different scans and respiratory motion, as reported also by [44]. These errors may lead to incorrect quantification of activity, compromising the absorbed dose calculation. As a consequence, registration of images is one of the main source of uncertainty in dose calculation.

Rigid registration of images has been commonly used in PRRT. However, organs can be changed in both location and shape over time, and simple roto-translation may not capture the full extent of anatomical change. Non-rigid registration algorithms were developed to improve the correspondence of anatomical and functional locations in the relevant scans. Non-rigid registration involves voxel-dependent modeling in addition to the three displacement and three rotation parameters of rigid registration. The superiority of non-rigid registration compared to rigid registration has been recently demonstrated [45]-[48]. Hence, in this work only non-rigid registration techniques were considered. Two different workflows of image registrations were compared and the best approach to use in practice was proposed.

This work was carried out in collaboration with the Cardiff University (Cardiff, UK).

### 2.3.1 Material and methods

#### Clinical protocol and data

A sample of 20 patients enrolled in a PRRT trial at AUSL di Reggio Emilia - IRCCS was considered in this study. The clinical trial (Trial A) was described

in Paragraph 1.7. Each patient underwent SPECT/CT scan of abdomen as described in 2.2.1. The mean administered activity for the cohort was  $4.27 \pm 0.97$  GBq, with activity ranging from 3.7 to 5.5 GBq. The dosimetry assessment involved the segmentation of both lesions and OARs (kidneys, liver and spleen). Contours of OARs were drawn on the first CT scan. The lesions were manually outlined on the SPECT scan acquired at about 24h p.i., when lesion uptake is maximal [49]. In total, 57 lesions were outlined, with a maximum of 6 lesions per patient.

### Image registration workflows

The CT and the corresponding NM (that is for Nuclear Medicine, i.e. SPECT) image were co-registered by default (Figure 2.14a).

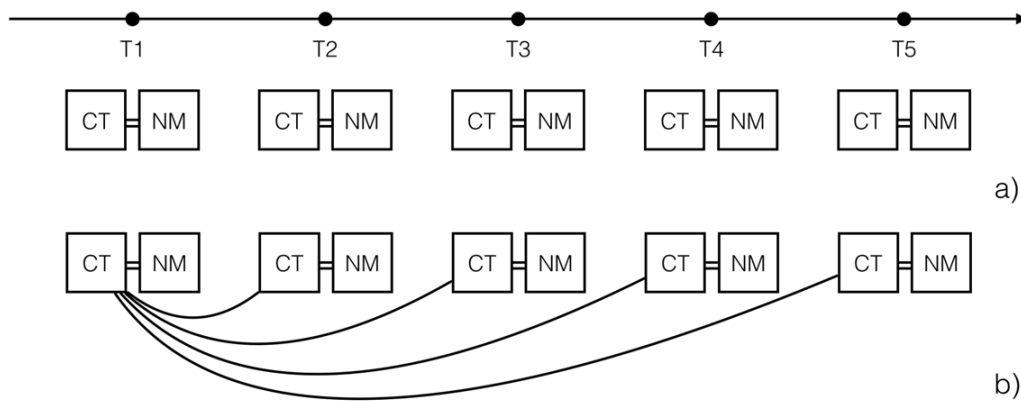


Figure 2.14: Schema of the image registrations. Co-registered CT and NM images for each multi-modal acquisition (a) and non-rigidly registered sequential CT images to the first CT image (b).

For each patient enrolled in this study, the sequential CT scans were registered to the first CT scan (Figure 2.14b). As a consequence, all sequential CT and NM images were in the same reference of the first acquisition. The image registration process involved two steps: firstly a rigid registration with bony anatomy matching and then a non-rigid registration using a 3-pass algorithm. All image registrations were carried out using the Velocity advanced imaging workstation version 3.2.

Two different non-rigid registration workflows were compared in this study:

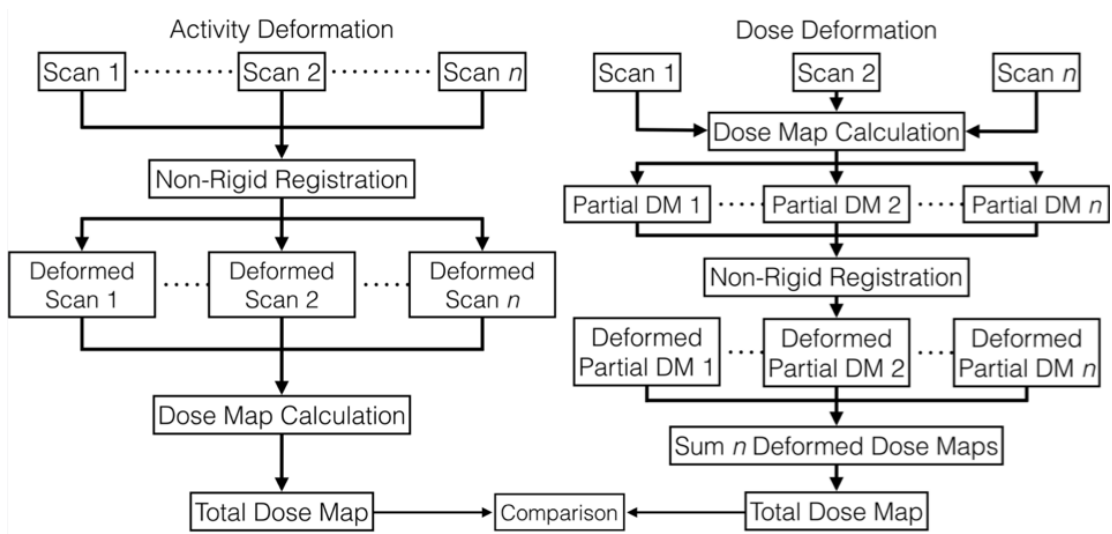


Figure 2.15: The Activity deformation workflow (on the left) and the Dose deformation workflow (on the right).

**Activity deformation workflow (AD):** in this workflow the activity map from each sequential SPECT/CT scan was deformed on the same frame of reference as the first CT scan. Then, the dose map was calculated using a Monte Carlo (MC) based 3D dose calculation engine.

**Dose deformation workflow (DD):** in this workflow, the original activity scans were first used to calculate time-point 3D dose maps (partial dose maps (DMs)). Then, each partial DM was registered to the first CT scan, and the cumulative dose map was calculated.

Figure 2.15 shows the two registration workflows.

All absorbed doses were calculated using the software RAYDOSE. RAYDOSE provides 3D absorbed dose maps based on MC simulations. A description of the software RAYDOSE is provided in Section 3.3.1.

Both workflows applied an exponential tail to the last scan point. The effective constant decay was calculated with a mono-exponential fit of the time activity curve.

## Data analysis

The quality of the image registration was evaluated using the Structural Similarity Index (SSIM) [50] as implemented in the MATLAB platform. SSIM was designed to provide an objective metric for comparing a distorted image to a distortion-free (reference) image and is calculated as a combination of pixel intensity, contrast and structural information. SSIM has been calculated in the range  $[0, 1]$  where 0 and 1 respectively indicate no match or perfect match between the first CT (taken as reference) and sequential registered CT scans.

In order to evaluate quantitative differences between the total dose distributions obtained with the two workflows, the relative percentage differences between mean doses were calculated as follows:

$$R_{\%} = \frac{D_{DD} - D_{AD}}{D_{AD}} \cdot 100 \quad (2.12)$$

where  $D_{DD}$  is the dose calculated using the Dose deformation workflow and  $D_{AD}$  is the dose calculated using the Activity deformation workflow.

In this study, AD workflow was arbitrary chosen as reference. Further analysis was performed using a Bland-Altman plot [51].

### 2.3.2 Results

Figure 2.16 shows the SSIM values calculated for all the patients.

The SSMI values range between 0.9446 and 0.9771, with total average value of 0.9781.

Distribution of percentage difference between the absorbed dose calculate with the AD and DD workflows are shown in the Box-plots in Figure 2.17. Box-plots show range from first to third quartiles as box and median as horizontal line. Whiskers denote data range. Outliers are denoted using the “+” symbol. It can be noted that the median values of the differences are positive for all the OARs, while it is negative for the lesions.

A paired samples Wilcoxon test did not show any statistical difference between the dose values computed with the two algorithms (p-value: 0.8181 for left kidney; 0.9138 for right kidney; 0.5161 for liver; 0.9138 for spleen; 0.8341 for lesions).

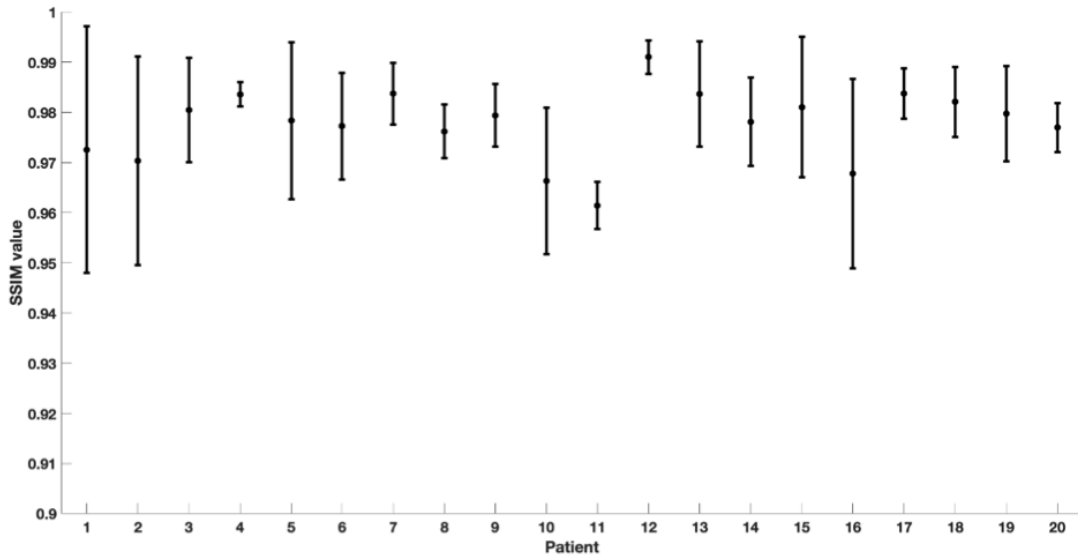


Figure 2.16: SSIM between the sequential scan and the reference one (CT1). For each patient, the average value of all the sequential scans, and the corresponding error bar, are reported.

Agreement between the two workflows was also evaluated by means of the Bland-Altman analysis (Figure 2.18). The average between the two procedures is reported on the x-axis, while the difference is reported in the y-axis. The solid line indicates the mean difference and the dotted lines are the upper and the lower limit of agreement (LoA), equivalent at 1.96 times the standard deviation. The plot also reports the reproducibility coefficient (RPC), defined as the LoA, and its percentage value. Coefficient of variation (CV) is also reported, defined as the standard deviation of the mean values in percentage.

### 2.3.3 Discussion

In this work two different workflows for implementing image registration for the calculation of patient-specific 3D dose distribution in PRRT therapy were compared. It is worth that although the two workflows used the same non-rigid registration maps, two different integration methods were used. For the AD workflow, a single absorbed dose map was calculated by fitting the time-activity curve using a trapezoidal method and a linear fit between each scan point. For the DD workflow, since only one activity map was supplied for each time point, the dose was calculated using an exponential decay model from the

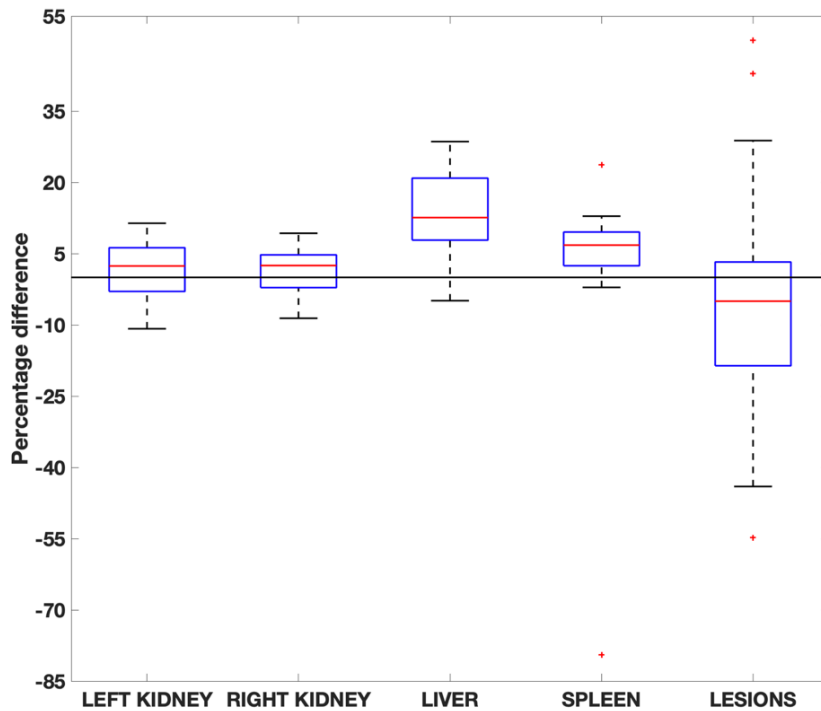


Figure 2.17: Distribution of percentage difference between the mean absorbed dose calculated with the AD and the DD workflows for OARs and lesions.

current scan time to the next time with an effective decay constant.

The SSIM confirmed the good performance of the non-rigid registration algorithm used in this study.

The mean absorbed dose calculated with the DD workflow was generally higher than the dose calculated with the AD workflow, with the exception of the lesions. However, these difference were found to be non statistically significant, with the exception of the liver. Liver contained, in most of the patient, lesions. Hence, this probably contribute to significantly widen the gap of results between the two workflows.

In conclusion, as no statistically difference was demonstrated, but the DD workflow requires multiple calculations to be performed (5 dose maps), in contrast with only 1 dose map of the AD workflow, the latter is preferable to be used in clinics.



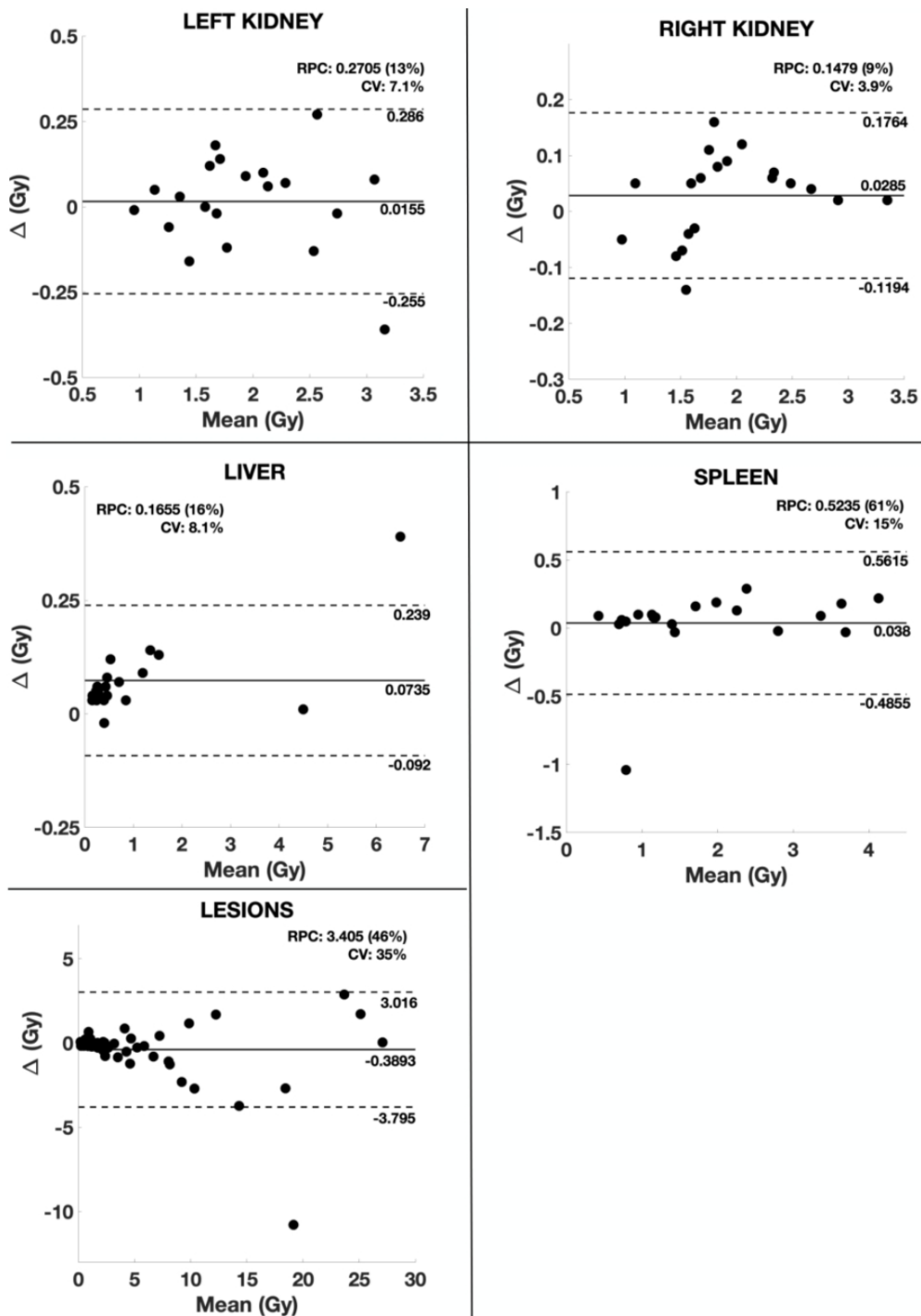


Figure 2.18: Distribution of percentage difference between the mean absorbed dose calculated with the AD and the DD workflows for OARs and lesions.



# Chapter 3

## Calculation of absorbed dose

Despite in the nuclear medicine community there is a wide consensus that patient-specific treatment based on pre-therapeutic dose estimate is likely to improve the efficacy of molecular radiotherapy, MRT is often prescribed to patients based on a fixed amount of activity, sometimes tailored to patient weight or body surface area. While this enables therapy to be performed with minimal resourcing or planning, it is probably that the development of personalized prescription alternatives based on dosimetry are likely to improve the outcome and cost-benefit of radionuclide therapies. Absorbed dose is the main physical quantity able to estimate the efficacy of the treatment. There is increasing evidence that treatment outcome correlates with the absorbed doses delivered to tumors and to healthy organs [52][53]. Furthermore, to avoid treatment-related side effects, dosimetry is mandatory for PRRT: the European Council Directive 2013/59 [54] states that “for all medical exposure of patients for radiotherapeutic purposes, exposures of target volumes shall be individually planned and their delivery appropriately verified taking into account that doses to non-target volumes and tissues shall be as low as reasonably achievable and consistent with the intended radiotherapeutic purpose of the exposure”. Thus, doses to critical tissues must be individually planned and verified for all radiotherapy techniques and accurate personalized MRT planning is required.

## 3.1 Internal dosimetry

The MIRD schema described in Paragraph 1.6 makes only two basic assumptions: the activity distribution in the source region is assumed to be uniform and the mean absorbed dose to the target region is calculated. That scheme does not set any restrictions on either the volume or the shape of the source or target. The source and target regions  $r_S$  and  $r_T$ , respectively, are those defined within the anatomic model and may represent the full range of configurations including whole organs, suborgan tissue regions, voxels from SPECT or PET images, tumours and cell clusters, individual cells, or cell components. Depending on the anatomic model used, the determination of S values may take place at the macroscopic level (i.e. organ level) or with a more refined spatial resolution (i.e. voxel dosimetry).

### 3.1.1 Organ dosimetry

Dosimetry at organ level was first developed thanks to their simplicity of implementation and have been used for many years. Pre-defined mathematical models are often employed to establish organ S factors. The current generation of anthropomorphic phantoms began in 1969 with the development of the Fisher-Snyder phantom [55]. This phantom used a combination of spheres, cylinders and cones to create a reasonably anatomically accurate representation of the body. Since then, model development has seen a systematic improvement, with the generation of models with increasing complexity of anatomical detail (Figure 3.1). In 1987 the development of the series of phantoms by Cristy and Eckerman [56] marked the beginning of the contemporary stylized models and allowed dose calculations for individuals of different size and age. The ICRP (International Commission on Radiological Protection) has been very active for many decades in providing models for the calculation of internal doses. The newest ICRP model is described in the ICRP Publication 89 [57].

Despite its widely diffusion, Organ dosimetry approach demonstrated two main limitations. Firstly, the assumption of uniform activity in the organ may affect accuracy of calculations. Evidence indicates that deterministic biological effects including tumour response and normal tissue toxicity may not be well

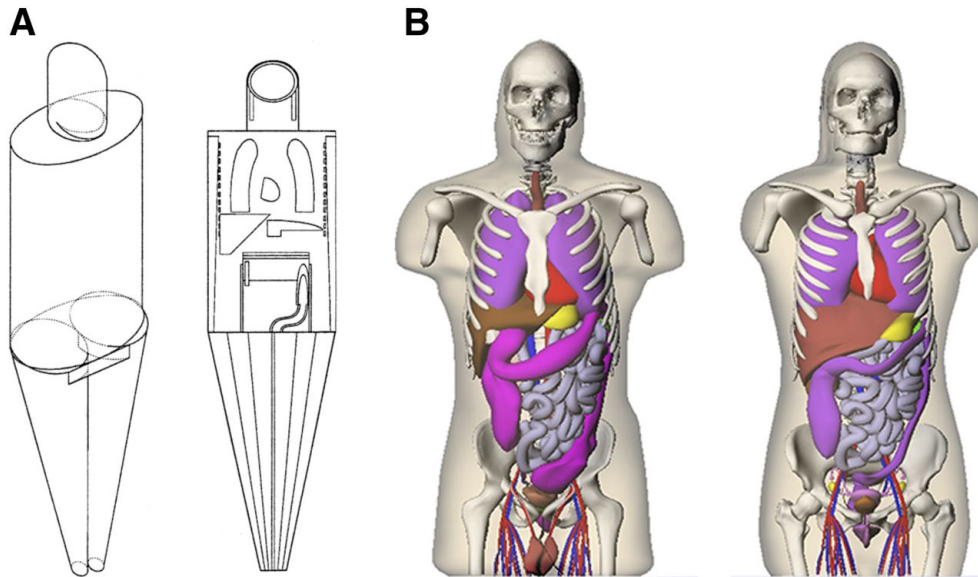


Figure 3.1: The Cristy-Eckerman computational phantom (A) and a realistic voxel-based phantoms (B). Source: Stabin MG et al., J Nucl Med 2018.

predicted by the mean absorbed dose in the organ, and may be significantly influenced by non-uniform doses [58]. Secondly, the anthropomorphic models do not guarantee that the model matches patient morphology. Furthermore, these models do not include tumours. S factors for spheres of the correct mass are used to calculate the absorbed dose to the tumour, assuming spherical geometry and no contribution from the cross-absorbed dose from activity in the surrounding tissues.

### 3.1.2 Voxel dosimetry

In order to resolve limitations imposed by organ-level dosimetry, voxel-based techniques were developed. Dosimetry at the voxel level is possible by the increasing availability of anatomical and functional imaging. Three dimensional physiologic imaging devices (PET and SPECT) provide 3D images and allow to display the distribution of radiopharmaceuticals into the patient within a resolution depending on the gamma camera characteristics. The MIRDO-17 describe three main methods to calculate voxel-level dosimetry: Dose-Point Kernel Convolution, voxel S values and Monte Carlo radiation transport.

**Dose-Point Kernel** represents the radial distribution of absorbed dose around an isotropic point source of radiation in an infinite homogeneous medium

(i.e. water). Absorbed dose as a function of the radial distance from the source can be calculated analytically or using Monte Carlo techniques, in both cases assuming a punctual source. This approach consists in assuming the source located at the center of the source voxel, and the absorbed dose is calculated at the center of the target voxel. The absorbed dose at a target point is calculated as a superposition of contributions from all point sources surrounding this target point. This superposition is a mathematical process called convolution.

**Voxel S values** is the application of the MIRD formalism (described in 1.6) to calculate the absorbed dose. Absorbed dose to the target voxel is obtained from the contribute of all the surrounding source voxels and the target voxel itself. This process is calculated by convolution between the cumulated activity map and the S values matrix. Voxel S value is defined as the mean absorbed dose to the target voxel per unit of cumulated activity in the source voxel, both of which are contained in an infinite homogeneous tissue medium. S values are usually calculated using Monte Carlo simulation. A necessary condition for the application of this method is to use S values that match with the cumulated activity map voxel size. Several groups [59] [60] have published S values for the most radionuclides commonly used the typical voxel size of imaging devices. The main drawback of voxel S values technique is that it is only valid in a homogeneous medium. In situation in which tissue inhomogeneities must be considered, Monte Carlo transport method may be used.

**Monte Carlo radiation transport** is nowadays considered the most accurate method for dosimetry in MRT. The MC simulations permit the treatment of multimaterial media during both electron and photon transport. Anatomical information provided by CT image permits to include tissue heterogeneities in dose calculations. The main limitation to the practical use of MC radiation transport in the clinical routine is due to the high time consuming requested for a complete patient dose process. Nevertheless, progresses on computer performances have permitted to progressively increase the use of these simulation codes for absorbed dose calculations.

## 3.2 VoxelMed: a home-made software for dosimetry in MRT

VoxelMed is a home-made software for dose calculations developed at Azienda USL-IRCCS research hospital of Reggio Emilia (Italy). VoxelMed allows to calculate voxel-level absorbed dose using S values convolution method. It uses the CERR platform (Computational Environment for Radiotherapy Research) [61] to import the multi-modal SPECT/CT images and to analyse and visualize the treatment planning. VoxelMed was developed in the Matlab (The Mathworks, Natick, MA). A detailed description of the previous version of VoxelMed, including all the necessary steps to perform dose calculations and the available tools for data analysis and image visualization, was reported on the academical Master thesis [62]. Here it is reported a short description of the functionality and the characteristics of Voxelmed. In particular, the improvements and the functionalities implemented in the new version of the software (VoxelMed2.0) are emphasized.

### Input data

Import of images (CT and SPECT) is supported by the CERR platform. Using the appropriate command on the Matlab Command Prompt it is possible to import images in DICOM format or files in *.mat* format. For each type of treatment planning object (image scans, informations of DICOM header, dose distributions, treatment informations, etc) a Matlab structure is created. The entire plan archive is stored in a single file with *.mat* binary format.

Once CT image is imported, it is possible to contour the VOIs (i.e. organs or tumours) using the appropriate contouring tool. Segmentation is manually performed for each slice and the final VOI is the result of interpolation between the contoured slices.

The outlined VOIs on the CT are transposed onto the SPECT voxel grid using the VoxelMed code. If voxel dimension of SPECT image does not match with the voxel dimension of CT image (this is usually the condition), VoxelMed performs a linear interpolation between the CT and SPECT coordinates to select the SPECT voxels to include into each VOI. Preliminary to this operations,

CT and SPECT images need to be registered. Registration of images can be performed using the CERR tool, or importing registration DICOM map from other software. Figure 3.2 shows the main VoxelMed Graphical User Interface (GUI).

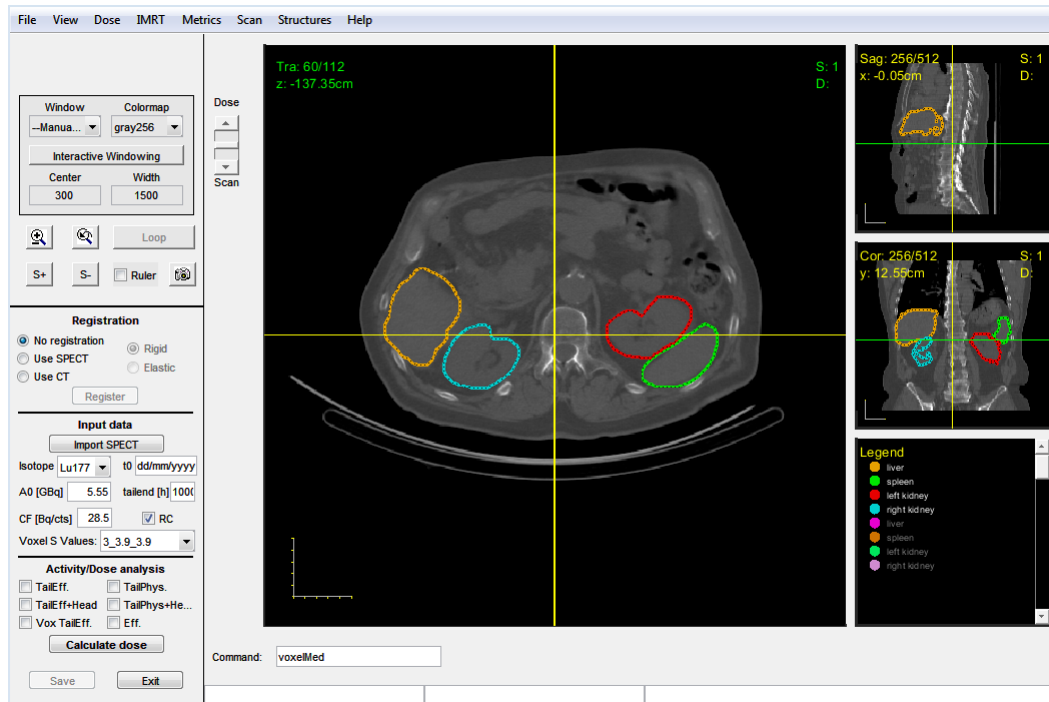


Figure 3.2: Screen capture of VoxelMed GUI. The user can enter the patient and treatment informations into the boxes on the left. The axial, coronal and sagittal slices of the fused images are shown.

Information about the radionuclide, the time of injection of radiopharmaceutical, the administered activity, the calibration factor, the SPECT voxel dimension and the limit of integration can be entered by means of the boxes and the drop down menu on the left in the main GUI.

### Fitting and Model selection

VoxelMed dose calculation is based on the voxel-level TIAC (Time Integrated Activity Curve), which is equals the area under the time-activity curve. In each voxel, the TIAC in the time interval between the first and the last acquisition is calculated using the trapezoidal method. The activity from the last time-point is extrapolated on the basis of the physical half-life (TailPhys) of the radionuclide or the effective half-life (TailEff). The effective half-life is obtained



### 3.2. VOXELMED: A HOME-MADE SOFTWARE FOR DOSIMETRY IN MRT81

using a bi-exponential curve to find the best fitting function the activity points of the VOI (i.e. organ or lesion). Optionally also the activity from the time of radiopharmaceutical injection to the first time point can be extrapolated on the basis of the physical (TailPhys + Head) or effective half-life. Hence, user can select four fitting modalities: TailEff, TailEff + Head, TailPhys, TailPhys + Head. Curve fitting is performed using the Matlab fitting tool. Constraints on the fitting parameters were included in the new version of VoxelMed to optimize the TIAC calculation.

#### **Image processing and dose calculation**

User can choose to apply PVE correction with the *RC* box (Figure 3.2). *RC* are based on the study shown in the paragraph 2.2. Compared to the previous version, VoxelMed2.0 includes the possibilities to create an excel file with main data reported (activities, volumes, calculated TIAC and absorbed dose), to export DVH (Dose Volume Histogram) in excel format and to visualize the fitted organ time-activity curves.

The voxel absorbed dose is determined by convolution of the cumulated activity and S values matrix. After calculations VoxelMed gives as a result the total residence time, the average voxel residence time and the mean absorbed dose for each of the fitting modality selected.

VoxelMed allows to provide dose calculations for  $^{177}\text{Lu}$  and  $^{90}\text{Y}$ . Since  $^{177}\text{Lu}$  is a  $\gamma$  emitter it is suitable to be used for imaging purpose. For that reason, VoxelMed allows to extrapolate dosimetry for  $^{90}\text{Y}$  based on the  $^{177}\text{Lu}$  dosimetry and the physical half-life of the isotopes.

The new version of VoxelMed also provide dose calculation at organ level. This possibility is particularly useful to provide residence time for calculation of absorbed dose in organ-level software (i.e. OLINDA1.1).

#### **Biological effective dose**

Since effects of radiation depends on biology factors like the capability of repair in the bombarded cells, VoxelMed2.0 allows to calculate the renal BED (Biological Effective Dose). A brief description of BED is reported in 5.1.1. BED calculation is based on the linear quadratic model, using the  $\alpha$ ,  $\beta$ , the repair

coefficients and the effective half-life of the kidneys activity curve. User can enter the values of administered activities using the *Patient Planning Treatment* GUI in Figure 3.3.

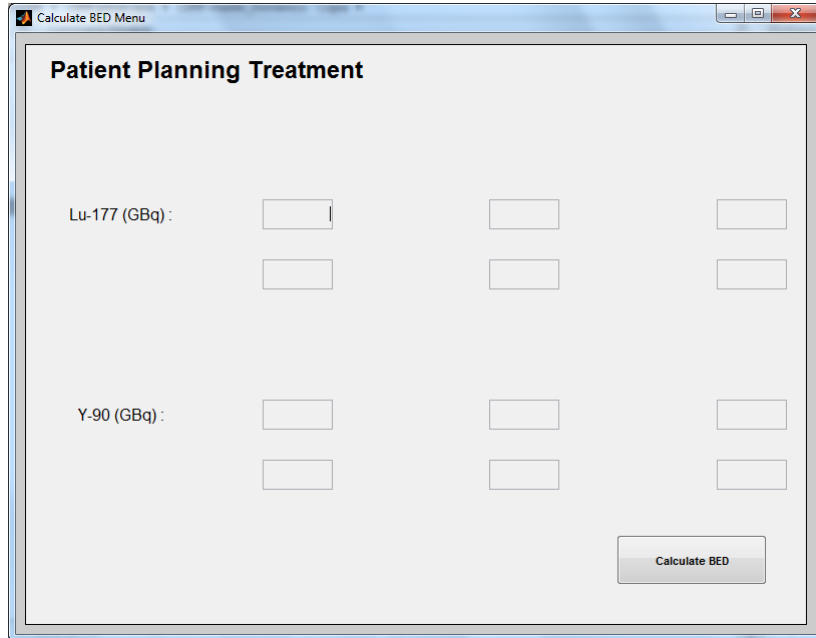


Figure 3.3: In the *Patient Planning Treatment* GUI user can enter the values of administered activities to calculate renal BED.

## Output

VoxelMed provides results of calculation both in terms of dose and BED maps and numerically. Numerical results are displayed into the Matlab Command Window. In the following it is reported, as an example, the full Command Window report for a dummy patient.

```

-----
Lu-177
-----

>>> Structure : Right kidney

VOI volume (ml):          184.300
VOI avg counts per vox: 1093.199 1084.561 906.510 767.648 552.809

Total Activity (Bq):      5.924498e+07    5.877686e+07    4.912756e+07    4.160202e+07    2.995904e+07
Total Activity (%):      1.6056          1.5929          1.3314          1.1274          0.8119
Mono-exp fit:            6.34e+07 * exp(-9.74e-03 t)
Bi-exp fit:              7.00e+07 * exp(-1.21e-02 t) + -7.00e+07 * exp(-1.57e+00 t)

```

### 3.2. VOXELMED: A HOME-MADE SOFTWARE FOR DOSIMETRY IN MRT83

Tau\_tot mono-exp (h): 1.77e+00  
Dose\_avg mono-exp (Gy/GBq): 7.16e-01  
Tau\_tot bi-exp (h): 1.56e+00  
Dose\_avg bi-exp (Gy/GBq): 6.31e-01

Tau\_tot trap (h): 8.439004e-01  
Tau\_avg\_voxel trap (h): 2.437610e-04  
Dose\_avg\_voxel trap (Gy/GBq): 3.502558e-01

TAIL\_EFF + HEAD:

Tau\_tot (h): 1.500042e+00  
Tau\_avg\_voxel (h): 4.332877e-04  
Dose\_avg\_voxel (Gy/GBq): 6.227063e-01

>>>> Structure : Left kidney

VOI volume (ml): 176.527  
VOI avg counts per vox: 962.962 924.857 785.405 640.994 469.797

Total Activity (Bq): 5.027579e+07 4.828635e+07 4.100562e+07 3.346600e+07 2.452786e+07  
Total Activity (%): 1.3625 1.3086 1.1113 0.9069 0.6647  
Mono-exp fit: 5.34e+07 \* exp(-1.04e-02 t)  
Bi-exp fit: 5.93e+07 \* exp(-1.30e-02 t) + -5.93e+07 \* exp(-1.58e+00 t)

Tau\_tot mono-exp (h): 1.39e+00  
Dose\_avg mono-exp (Gy/GBq): 5.89e-01  
Tau\_tot bi-exp (h): 1.23e+00  
Dose\_avg bi-exp (Gy/GBq): 5.21e-01

Tau\_tot trap (h): 6.948742e-01  
Tau\_avg\_voxel trap (h): 2.095519e-04  
Dose\_avg\_voxel trap (Gy/GBq): 3.003825e-01

TAIL\_EFF + HEAD:

Tau\_tot (h): 1.216351e+00  
Tau\_avg\_voxel (h): 3.668127e-04  
Dose\_avg\_voxel (Gy/GBq): 5.253673e-01

>>>> Structure : Liver

VOI volume (ml): 1672.058  
VOI avg counts per vox: 489.903 384.692 320.228 283.296 234.781

Total Activity (Bq): 2.110971e+08 1.657622e+08 1.379851e+08 1.220712e+08 1.011661e+08  
Total Activity (%): 5.7208 4.4922 3.7395 3.3082 2.7416  
Mono-exp fit: 2.06e+08 \* exp(-1.17e-02 t)

Bi-exp fit:  $2.19\text{e}+08 * \exp(-1.33\text{e}-02 t) + -2.18\text{e}+08 * \exp(-2.00\text{e}+00 t)$

Tau\_tot mono-exp (h): 4.76e+00  
 Dose\_avg mono-exp (Gy/GBq): 2.22e-01  
 Tau\_tot bi-exp (h): 4.44e+00  
 Dose\_avg bi-exp (Gy/GBq): 2.07e-01

Tau\_tot trap (h): 2.559013e+00  
 Tau\_avg\_voxel trap (h): 8.147388e-05  
 Dose\_avg\_voxel trap (Gy/GBq): 1.204771e-01

TAIL\_EFF + HEAD:

Tau\_tot (h): 4.660322e+00  
 Tau\_avg\_voxel (h): 1.483754e-04  
 Dose\_avg\_voxel (Gy/GBq): 2.193181e-01

>>>> Structure : Spleen

VOI volume (ml): 207.989  
 VOI avg counts per vox: 1475.840 1871.103 1523.280 1344.706 1016.795

Total Activity (Bq): 8.882619e+07 1.126158e+08 9.168149e+07 8.093365e+07 6.119772e+07  
 Total Activity (%): 2.4072 3.0519 2.4846 2.1933 1.6585  
 Mono-exp fit:  $1.04\text{e}+08 * \exp(-5.89\text{e}-03 t)$   
 Bi-exp fit:  $1.30\text{e}+08 * \exp(-1.10\text{e}-02 t) + -1.30\text{e}+08 * \exp(-9.42\text{e}-01 t)$

Tau\_tot mono-exp (h): 4.77e+00  
 Dose\_avg mono-exp (Gy/GBq): 1.73e+00  
 Tau\_tot bi-exp (h): 3.17e+00  
 Dose\_avg bi-exp (Gy/GBq): 1.15e+00

Tau\_tot trap (h): 1.570441e+00  
 Tau\_avg\_voxel trap (h): 4.019556e-04  
 Dose\_avg\_voxel trap (Gy/GBq): 5.835007e-01

TAIL\_EFF + HEAD:

Tau\_tot (h): 3.063383e+00  
 Tau\_avg\_voxel (h): 7.840756e-04  
 Dose\_avg\_voxel (Gy/GBq): 1.137795e+00

>>>> Structure : Kidneys

VOI volume (ml): 360.827  
 VOI avg counts per vox: 1028.0805 1004.7091 845.9577 704.3210 511.3031  
 Total Activity (Bq): 1.0952e+08 1.0706e+08 9.0133e+07 7.5068e+07 5.4487e+07  
 Total Activity (%): 2.9681 2.9015 2.4426 2.0344 1.4766  
 Effective decay constant (1/h): 1.274412e-02

### 3.2. VOXELMED: A HOME-MADE SOFTWARE FOR DOSIMETRY IN MRT85

Tau\_tot mono-exp (h): 3.16e+00  
Dose\_avg mono-exp (Gy/GBq): 6.53e-01  
Tau\_tot bi-exp (h): 2.79e+00  
Dose\_avg bi-exp (Gy/GBq): 5.76e-01

-----  
Y-90  
-----

>>>> Structure : Right kidney

Total Activity (Bq): 5.876077e+07 5.222141e+07 4.179886e+07 3.097569e+07 1.919360e+07  
Total Activity (%): 1.5924 1.4152 1.1328 0.8395 0.5202  
Mono-exp fit: 6.26e+07 \* exp(-1.56e-02 t)  
Bi-exp fit: 7.15e+07 \* exp(-1.92e-02 t) + -7.15e+07 \* exp(-1.48e+00 t)

Tau\_tot mono-exp (h): 1.09e+00  
Dose\_avg mono-exp (Gy/GBq): 2.65e+00  
Tau\_tot bi-exp (h): 9.98e-01  
Dose\_avg bi-exp (Gy/GBq): 2.43e+00

Tau\_tot trap (h): 6.983950e-01  
Tau\_avg\_voxel trap (h): 2.017317e-04  
Dose\_avg\_voxel trap (Gy/GBq): 1.780370e+00

TAIL\_EFF + HEAD:

Tau\_tot (h): 9.793505e-01  
Tau\_avg\_voxel (h): 2.828858e-04  
Dose\_avg\_voxel (Gy/GBq): 2.496874e+00

>>>> Structure : Left kidney

Total Activity (Bq): 4.986488e+07 4.290092e+07 3.488852e+07 2.491784e+07 1.571405e+07  
Total Activity (%): 1.3514 1.1626 0.9455 0.6753 0.4259  
Mono-exp fit: 5.28e+07 \* exp(-1.63e-02 t)  
Bi-exp fit: 5.95e+07 \* exp(-1.96e-02 t) + -5.95e+07 \* exp(-1.57e+00 t)

Tau\_tot mono-exp (h): 8.77e-01  
Dose\_avg mono-exp (Gy/GBq): 2.22e+00  
Tau\_tot bi-exp (h): 8.13e-01  
Dose\_avg bi-exp (Gy/GBq): 2.06e+00

Tau\_tot trap (h): 5.761212e-01  
Tau\_avg\_voxel trap (h): 1.737398e-04  
Dose\_avg\_voxel trap (Gy/GBq): 1.522256e+00

TAIL\_EFF + HEAD:

Tau\_tot (h): 8.016107e-01  
 Tau\_avg\_voxel (h): 2.417403e-04  
 Dose\_avg\_voxel (Gy/GBq): 2.115064e+00

>>>> Structure : Liver

Total Activity (Bq):	2.093718e+08	1.472745e+08	1.174009e+08	9.089080e+07	6.481319e+07
Total Activity (%):	5.6741	3.9912	3.1816	2.4632	1.7565
Mono-exp fit:	2.09e+08 * exp(-1.90e-02 t)				
Bi-exp fit:	2.24e+08 * exp(-2.12e-02 t) + -2.24e+08 * exp(-2.00e+00 t)				

Tau\_tot mono-exp (h): 2.98e+00  
 Dose\_avg mono-exp (Gy/GBq): 8.56e-01  
 Tau\_tot bi-exp (h): 2.84e+00  
 Dose\_avg bi-exp (Gy/GBq): 8.18e-01

Tau\_tot trap (h): 2.122224e+00  
 Tau\_avg\_voxel trap (h): 6.756738e-05  
 Dose\_avg\_voxel trap (Gy/GBq): 6.222427e-01

TAIL\_EFF + HEAD:

Tau\_tot (h): 2.988357e+00  
 Tau\_avg\_voxel (h): 9.514334e-05  
 Dose\_avg\_voxel (Gy/GBq): 8.756918e-01

>>>> Structure : Spleen

Total Activity (Bq):	8.810021e+07	1.000557e+08	7.800472e+07	6.026092e+07	3.920701e+07
Total Activity (%):	2.3876	2.7116	2.1140	1.6331	1.0625
Mono-exp fit:	1.01e+08 * exp(-1.11e-02 t)				
Bi-exp fit:	1.26e+08 * exp(-1.66e-02 t) + -1.26e+08 * exp(-1.01e+00 t)				

Tau\_tot mono-exp (h): 2.46e+00  
 Dose\_avg mono-exp (Gy/GBq): 5.39e+00  
 Tau\_tot bi-exp (h): 2.02e+00  
 Dose\_avg bi-exp (Gy/GBq): 4.43e+00

Tau\_tot trap (h): 1.287340e+00  
 Tau\_avg\_voxel trap (h): 3.294958e-04  
 Dose\_avg\_voxel trap (Gy/GBq): 2.961734e+00

TAIL\_EFF + HEAD:

Tau\_tot (h): 1.893639e+00  
 Tau\_avg\_voxel (h): 4.846786e-04  
 Dose\_avg\_voxel (Gy/GBq): 4.354166e+00

### 3.2. VOXELMED: A HOME-MADE SOFTWARE FOR DOSIMETRY IN MRT87

>>>> Structure : Kidneys

Total Activity (Bq):	1.0863e+08	9.5122e+07	7.6687e+07	5.5894e+07	3.4908e+07	
Total Activity (%):	2.9438	2.5779	2.0783	1.5147	0.9460	
Effective decay constant (1/h):	1.939244e-02					
Tau_tot mono-exp (h):	1.97e+00					
Dose_avg mono-exp (Gy/GBq):	2.44e+00					
Tau_tot bi-exp (h):	1.81e+00					
Dose_avg bi-exp (Gy/GBq):	2.24e+00					

-----  
BED  
-----

>>>> Structure : Right kidney

Lu-177 BED Trap (Gy) = 7.055373  
Y-90 BED Trap (Gy) = 2.018442  
BED Trap (Gy) = 9.073815

Lu-177 BED Head TailEff (Gy) = 13.519391  
Y-90 BED Head TailEff (Gy) = 2.887344  
BED Head TailEff (Gy) = 16.406735

>>>> Structure : Left kidney

Lu-177 BED Trap (Gy) = 5.959126  
Y-90 BED Trap (Gy) = 1.704082  
BED Trap (Gy) = 7.663208

Lu-177 BED Head TailEff (Gy) = 11.155578  
Y-90 BED Head TailEff (Gy) = 2.409607  
BED Head TailEff (Gy) = 13.565184

=====

The main window also display the absorbed dose and BED maps, as shown in Figure 3.4. VoxelMed also allows to create an excel file with a different sheet for each calculation modality chosen. This file displays the values of volume, activities, residence time and absorbed dose for each VOI. It is also possible to display a cumulative or differential dose volume histogram, and export each DVH in excel format.

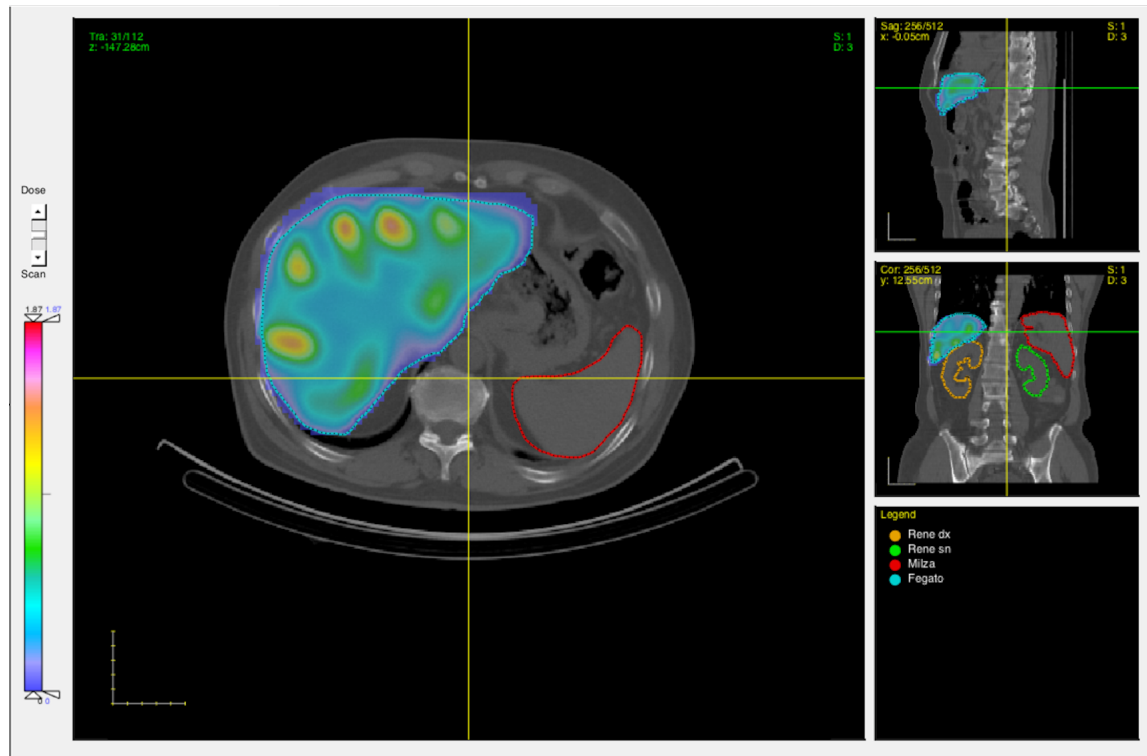


Figure 3.4: Liver absorbed dose map of a slice in axial, sagittal and coronal viewer. Using the colorbar in the left panel it is possible to set the dose-display range, colorbar display range and to adjust the scan contrast.

### 3.3 Comparison of different calculation techniques

Several methods of MRT dosimetry based on quantitative imaging (QI) were developed in the last years. Techniques based on standardized reference models (Paragraph 3.1.1) were first developed thanks to their simplicity of implementation and have been used for many years. These models assume uniform activity in the source region (i.e. organ/tumour) and uniform dose in the target (i.e. organ/tumour). However, evidence indicates that deterministic biological effects are not well predicted by the mean dose and may be significantly influenced by non-uniform dose distribution [58]. A non-uniform tumour absorbed dose may result in a under-treatment of certain parts of the tumour while over-treating other parts, and this might contribute to treatment failure by delivering sub-lethal doses to some clonogenic cells within the tumour. Hence, organ-level techniques may not be adequate to predict effects of therapy. For these reasons, voxel-level techniques were developed.



A number of clinical research centres have each developed in-house software packages [63]-[69]. In the last year, also some commercial software were developed [70]-[72]. However each of these software has taken considerable local expertise to develop, and there are no standard methods that can be readily taken up for routine clinical use. As a result, it is necessary to inter-compare the existing home-made software to provide a standard methodology for dosimetry in MRT.

In that context, the aim of this work is to inter-compare different modalities of absorbed dose calculation:

- Convolution based on organ-level standardized anthropomorphic reference models (such as OLINDA version 1.1 [73], which has been used for decades before the recent release of the new updated commercial version OLINDA version 2 [72]).
- Convolution based on pre-calculated voxel S-factors to perform voxel-level dosimetry (VoxelMed2.0 [37]).
- Monte Carlo (MC) simulations to perform voxel level dosimetry (RAYDOSE [74])

OLINDA1.1 was chosen because it was widely used for MRT dosimetry (OLINDA v2 had not yet been released when we performed this study). VoxelMed2.0 was chosen because it was designed to achieve a good compromise between calculation accuracy and easy applicability in clinical practice. RAYDOSE was considered because MC techniques are considered to provide the most accurate approach to dose estimate [75].

This study was performed both using phantoms and on clinical cases. This multi-approach method allowed to investigate the differences of performance between the calculation modalities (depending on the shape and the volume of the activity distribution) and to provide a valuable comparison based on a conspicuous number of clinical cases.

This work was carried out in collaboration with the Cardiff University (Cardiff, UK).

### 3.3.1 Material and methods

The following sections describe in detail the specific phantoms, the image set, the software and the data elaboration approach.

#### Preparation of phantoms

In order to compare the dosimetry approaches and to evaluate the impact of activity distribution, phantoms and inserts with different shapes and range of volume were considered as follows:

- The “Cylindrical phantom” filled with a homogeneous radioactive solution (Jaszczak, Data Spectrum Corporation; USA).
- The “Geometrical phantoms” described in 2.2.1. Each insert was filled with the same activity concentration and placed in a non-radioactive water background.
- The “Anthropomorphic phantom” described in 2.2.1. Every insert was filled with an activity concentration typical of real organs in clinical cases, and placed in a radioactive water background.

Inserts were filled with a solution containing  $^{177}\text{Lu}$  radio-labelled peptide left-over from clinics. Weight of empty and filled inserts was measured to obtain the filling volume. Filling volume was obtained by measuring the weight of the filled inserts and empty inserts, using a calibrated scale. An HCl (0.1 M) carrier solution was used to prevent inhomogeneities and sticking of peptides to the walls.

Each phantom was scanned once and physical decay was used to extrapolate the time-activity curve. Volumes of inserts and phantoms, insert activity and background activity are reported in Table 3.1.

#### Clinical data

A large number of patients was considered to compare results on clinical patterns. The sample of patients was divided in two groups: “Sample A” consisting of 50 patients (21 females, 29 males) and “Sample B” consisting of 20 patients

Table 3.1: Description of phantoms used to test the dosimetry tools.

Phantom	Phantom volume (ml)	Insert name	Insert volume (ml)	Insert activity concentration (MBq/ml)	Background activity concentration (MBq/ml)
Cylindrical	5640	N/A	N/A	0.25	N/A
		To17a	2.8		
		To26	9.7		
		E20	4.1		
		E30	14.8		
		E38	28.5		
Geometrical	6713	To17b	2.8	1.53	N/A
		P38	29.2		
		P39a	30.1		
		P39b	31.2		
		Tu38a	28.6		
		Tu38b	28.8		
		Anthropomorphic	11600	Lesion	2.0
Pancreas	92			0.99	
Left kidney	142			0.81	0.03
Right kidney	142			0.82	
Spleen	156			1.10	
Liver	1470			0.53	

(11 females, 9 males). All patients were enrolled in the PRRT clinical trial described in 1.7 (Trial A).

### Image acquisition and reconstruction

All phantoms and patients were acquired with a SPECT/CT scanner based on the standard clinical protocol for body studies described in section 2.2.1.

All cases of Sample A were rigidly registered to the first CT image of the sequence in Siemens E-soft workstation. Images of patients included in Sample B were registered using a deformable multi-pass algorithm with the Velocity Advanced Imaging workstation 3.2.0. The Volumes Of Interest (VOIs) for each phantom and each patient were manually drawn on the reference CT image.

### Software for image processing and dosimetry calculation

**VoxelMed:** VoxelMed version 2.0 was described in detail in section 3.2.

**RAYDOSE:** RAYDOSE was developed at Cardiff University (School of Engineering, Cardiff University, UK) and allows to calculate 3D patient-specific image-based dosimetry for MRT. In particular, RAYDOSE is based on Monte Carlo simulation on radiation transport based on the Geant4 MC toolkit (CERN, Switzerland). RAYDOSE generates voxel-level dose maps through by simulations of the transport of particle through matter joined with anatomical and physiological information from morphological and functional images [74]. RAYDOSE allows to calculate the area under the time-activity curve using different fitting modalities: mono-exponential decay, linear uptake plus mono-exponential decay or the trapezoidal method. In this study, for the dose calculation of the clinical cases, we used the trapezoidal method at the voxel level up to the last time acquisition point, while the time-activity curve beyond the last scan time was extrapolated from the mono-exponential curve fitting of the whole organ activities in the VOI. For dose calculation in phantoms, we used the physical half-life of the isotope to extrapolate the activity from the scan time upwards.

**OLINDA:** OLINDA version 1.1 [73] is an organ-level dosimetry software based on the MIRD methodology for internal dose estimation. OLINDA provides different models to perform dosimetry: human models (adult male, adult female, 10-years old, 5-years old, etc.) and sphere models. Human models are mathematical representations of the human body to represent organs and whole body, sphere models are mathematical representations of sphere to represent lesions.

In this study the number of decays of each VOI were calculated with Vox-elMed2.0 and were used for OLINDA dose calculations.

OLINDA sphere model was used for absorbed dose calculations of inserts in Geometrical phantom and for the dummy lesion housed in the anthropomorphic phantom, while OLINDA organ model (adult male) was used for the dummy organs placed in the anthropomorphic phantom. Real insert volumes were used for calculations. The human models (adult male or adult female) were used to calculate dosimetry of the cohort of patients. Doses were scaled using the true patient weight and the true organ masses.

Table 3.2: Summary of phantoms and patients studies performed.

Study type	Object of study	Image registration	Software
<b>Phantom</b>	Homogeneous phantom	No registration (only 1 scan)	OLINDA1.1 - VoxelMed - RAYDOSE
	Geometrical phantom	No registration (only 1 scan)	OLINDA1.1 - VoxelMed - RAYDOSE
	Anthropomorphic phantom	No registration (only 1 scan)	OLINDA1.1 - VoxelMed - RAYDOSE
<b>Clinical</b>	Sample A (50 patients)	Rigid registration	OLINDA1.1 - VoxelMed
	Sample B (20 patients)	Deformable registration	OLINDA1.1 - VoxelMed - VoxelMed <sup>(<math>\lambda</math> RD)</sup> - RAYDOSE

### Data analysis and statistics

Table 3.2 summarize the study type, the image registration and the software used for the dose calculations. Absorbed dose were calculated separately with OLINDA1.1, VoxelMed2.0 and RAYDOSE using the same set of images. As it is shown in Table 3.2, OLINDA and VoxelMed dose results were compared on patients of Sample A, while all of the three software were used on patients of Sample B. In order to highlight the intrinsic differences between MC and voxel convolution methods, calculations were repeated using the same effective decay constant for patients in Sample B. In particular, VoxelMed calculations were repeated using the same decay constant calculated by RAYDOSE (in the following this is called VoxelMed<sup>( $\lambda$  RD)</sup>).

While OLINDA results are limited to average organ absorbed doses, VoxelMed and RAYDOSE dosimetry offer the additional possibility of obtaining absorbed dose distributions. Dose-volume histograms (DVH) were considered to compare spatial dose distribution at voxel-level. Mean values of absorbed dose were used to compare organ level and voxel level techniques. Comparison between the different dosimetry methods was statistically evaluated using the Lin's concordance coefficient (LC) and the Bland-Altman plot [51]. The LC was calculated using the SAS software (SAS Institute, North Carolina State University, USA). The LC allows to evaluate the degree of concordance between two measures. A value of LC equal to +1 denotes perfect concordance, a value equal to -1 perfect discordance, while a value of 0 no correlation.

Table 3.3: Mean absorbed dose (Gy) calculated with OLINDA1.1, VoxelMed, and RAYDOSE for each phantom.

Phantom	Insert name	OLINDA 1.1	VoxelMed	RAYDOSE
<b>Cylindrical</b>	N/A	3.3	2.8	3.0
	To17a	3.3	2.8	3.0
<b>Geometrical</b>	To17a	6.3	3.0	4.0
	To17b	0.8	0.4	0.5
	To26	15.4	9.0	10.7
	E20	21.1	16.1	17.6
	E30	23.0	20.7	20.9
	P38	24.1	23.9	23.7
	P39a	2.5	2.0	2.1
	P29b	2.1	2.0	2.0
	Tu38a	2.5	2.0	1.9
	Tu39b	2.4	2.0	2.0
<b>Anthropomorphic</b>	Lesion	102.3	91.3	97.9
	Pancreas	13.6	11.9	12.2
	Kidneys	12.9	11.4	11.8
	Spleen	22.0	19.6	20.3
	Liver	10.4	9.3	9.8

### 3.3.2 Results

#### Phantom study

Table 3.3 shows the calculated absorbed doses in phantoms. The visual representation of the same data is provided in Figure 3.5.

Figures 3.6 and 3.7 show DVHs for the homogeneous phantom and for the Geometrical and the Anthropomorphic phantoms, respectively. Only some representative inserts (those with the greatest and the smallest difference of dose were chosen) were considered for the Geometrical and the Anthropomorphic phantoms. The shift toward low doses in VoxelMed DVHs reflects the VoxelMed underestimation of the average absorbed dose in comparison with RAYDOSE.

#### Clinical study

Table 3.4 shows the OLINDA1.1 and VoxelMed absorbed doses for the 50 patients (Sample A).

Table 3.4: Kidney, liver and spleen mean absorbed dose (Gy/GBq) calculated with OLINDA1.1 and VoxelMed for patients of Sample A

Cases	Kidneys		Liver		Spleen	
	OLINDA1.1	VoxelMed	OLINDA1.1	VoxelMed	OLINDA1.1	VoxelMed
1	0.84	0.99	0.13	0.11	1.34	1.26
2	0.69	0.83	0.08	0.09	0.57	0.70
3	0.42	0.52	0.15	0.16	0.28	0.30
4	0.44	0.46	N/A	N/A	0.21	0.25
5	0.56	0.67	0.38	0.42	0.06	0.07
6	0.33	0.39	1.11	1.47	0.24	0.27
7	0.57	0.59	0.13	0.12	0.88	0.80
8	0.42	0.52	0.05	0.05	0.20	0.22
9	0.79	0.79	0.06	0.07	0.48	0.52
10	1.30	1.63	0.23	0.27	0.91	1.14
11	0.76	0.91	0.40	0.33	0.59	0.96
12	0.55	0.80	0.15	0.16	0.27	0.30
13	0.43	0.49	0.04	0.04	0.15	0.14
14	0.33	0.40	0.08	0.09	N/A	N/A
15	0.66	0.75	0.17	0.18	1.08	1.18
16	0.27	0.31	0.03	0.03	0.17	0.18
17	1.89	2.26	0.45	0.51	1.26	1.44
18	0.78	0.90	0.18	0.21	0.98	1.12
19	0.90	1.03	0.15	0.17	1.09	1.13
20	0.68	0.80	0.08	0.09	0.76	0.89
21	0.47	0.55	0.20	0.22	0.41	0.45
22	0.55	0.66	0.24	0.26	0.73	0.85
23	0.57	0.53	0.22	0.25	1.14	1.33
24	0.53	0.61	0.11	0.12	0.45	0.50
25	1.04	1.01	0.14	0.15	0.65	0.72
26	0.54	0.65	0.11	0.11	0.54	0.59
27	0.27	0.31	0.08	0.09	N/A	N/A
28	0.37	0.43	0.11	0.13	0.57	0.65
29	0.50	0.49	0.06	0.07	0.50	0.48
30	1.00	1.08	0.10	0.10	0.67	0.68
31	0.38	0.40	0.22	0.22	0.16	0.17
32	0.34	0.40	1.00	1.13	0.44	0.54
33	0.31	0.35	0.12	0.12	0.22	0.24
34	0.48	0.39	0.13	0.13	0.28	0.23
35	0.26	0.30	0.02	0.02	0.08	0.09
36	0.64	0.75	0.11	0.12	0.73	0.84
37	0.62	0.71	0.34	0.37	1.76	1.94
38	0.50	0.56	0.11	0.12	0.55	0.62
39	0.85	0.99	0.14	0.16	1.24	1.40
40	0.59	0.67	0.06	0.07	0.51	0.56
41	0.29	0.33	0.79	0.91	0.24	0.26
42	0.52	0.60	0.13	0.14	0.43	0.47
43	0.27	0.30	0.03	0.03	0.12	0.13
44	0.18	0.20	0.23	0.25	0.45	0.50
45	0.86	1.09	0.05	0.06	0.35	0.41
46	0.50	0.58	0.08	0.09	0.29	0.33
47	0.40	0.45	0.05	0.06	0.70	0.76
48	0.69	0.78	0.11	0.12	1.11	1.24
49	0.60	0.55	0.07	0.08	1.45	1.34
50	0.65	0.76	0.03	0.02	0.23	0.26

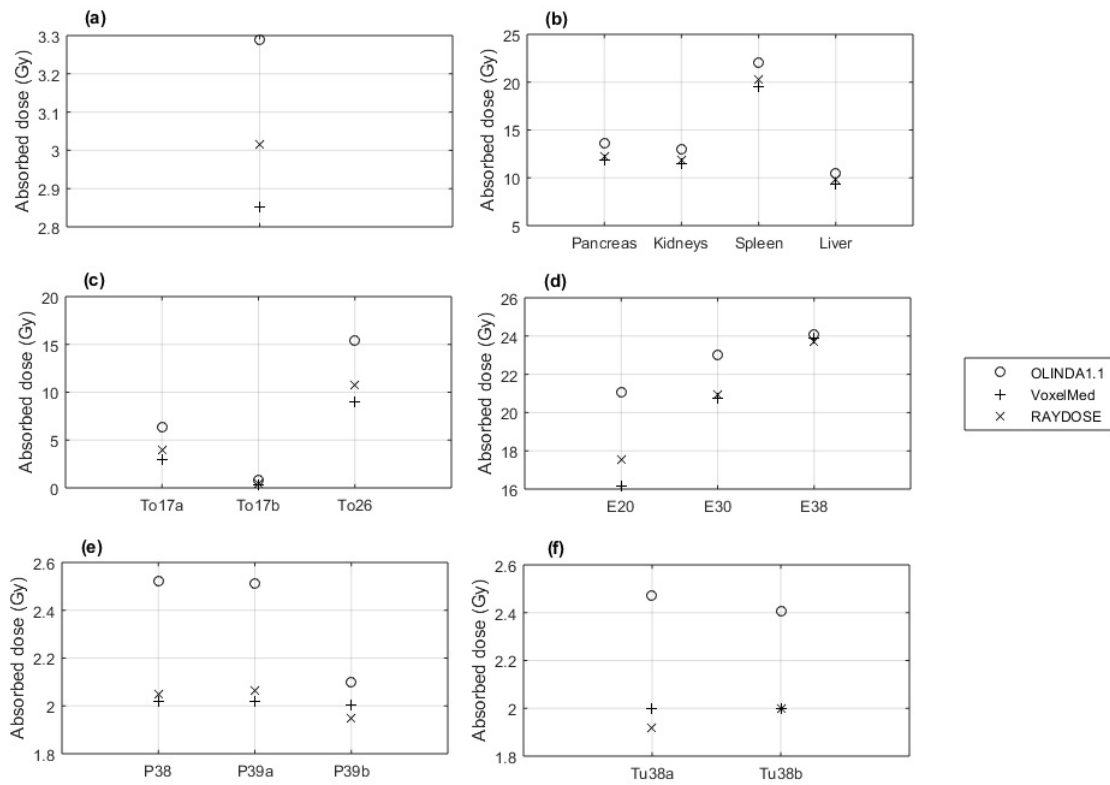


Figure 3.5: Comparison of mean absorbed dose (Gy) calculated using OLINDA1.1, VoxelMed and RAYDOSE.

OLINDA1.1 and VoxelMed absorbed dose resulted highly correlated for liver and spleen (Lin's coefficients:  $LC_{liver}=0.97$  and  $LC_{spleen}=0.85$  respectively), while lower correlation was obtained for kidneys ( $LC_{kidneys}=0.55$ ). Results were also compared by means of the Bland-Altman plot (Figure 3.8). Absorbed dose results calculated using OLINDA1.1, VoxelMed, VoxelMed<sup>(λ RD)</sup> and RAYDOSE for the 20 patients (Sample B) are shown in Table 3.5 and in Figure 3.9 for the Bland-Altman analysis. The absorbed dose calculated with VoxelMed and RAYDOSE were highly correlated ( $LC_{kidneys}=0.98$ ,  $LC_{liver}=0.99$  and  $LC_{spleen}=0.94$ ), and almost complete agreement was found between VoxelMed<sup>(λ RD)</sup> and RAYDOSE ( $LC_{kidneys}=0.99$ ,  $LC_{liver}=1$  and  $LC_{spleen}=1$ ).



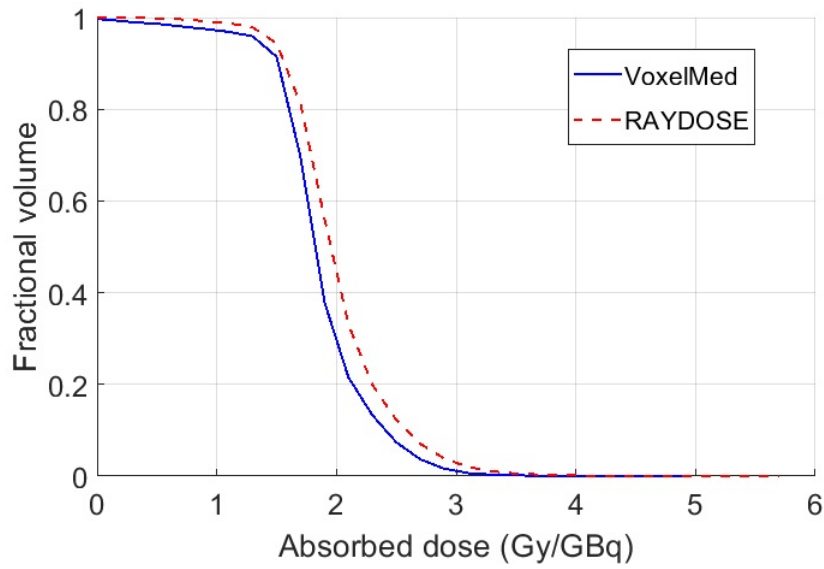


Figure 3.6: Comparison of DVHs calculated using VoxelMed (continuous line) and RAYDOSE (dotted line) for the Cylindrical phantom.

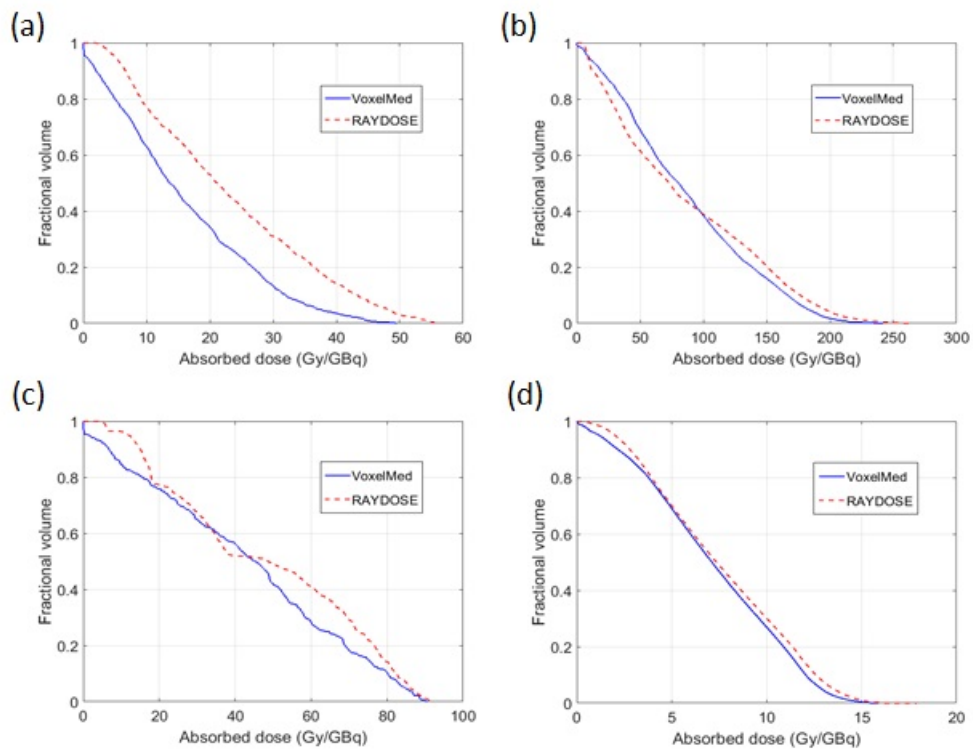


Figure 3.7: Comparison of DVHs calculated using VoxelMed (continuous line) and RAYDOSE (dotted line) for inserts of Geometrical phantom and Anthropomorphic phantom.

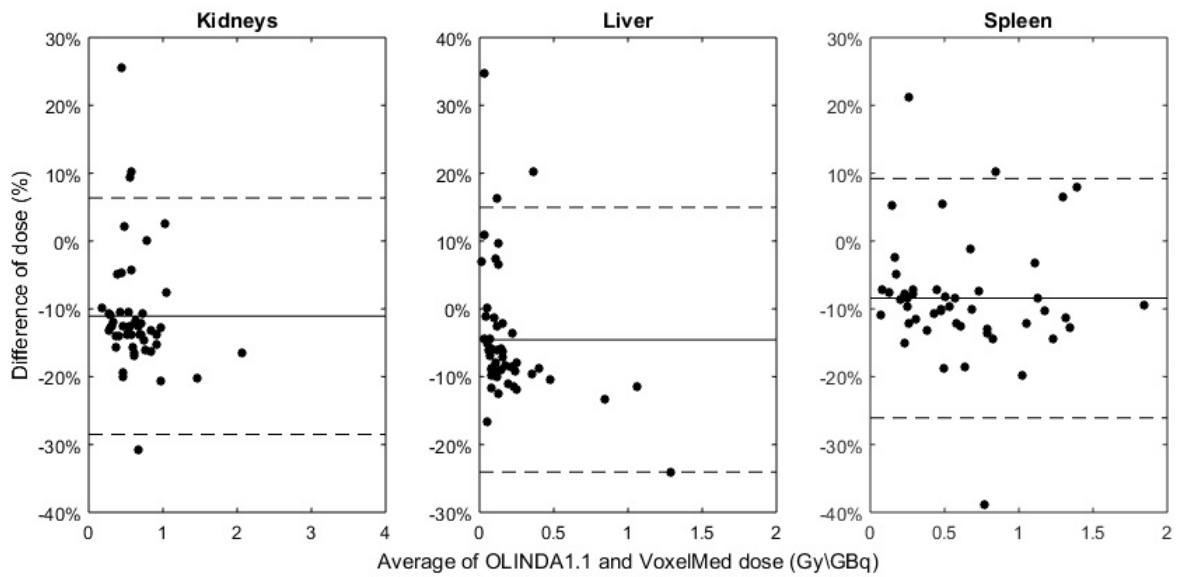


Figure 3.8: Comparison of OLINDA1.1 and VoxelMed calculated mean absorbed dose per unit of injected activity (Gy/GBq).

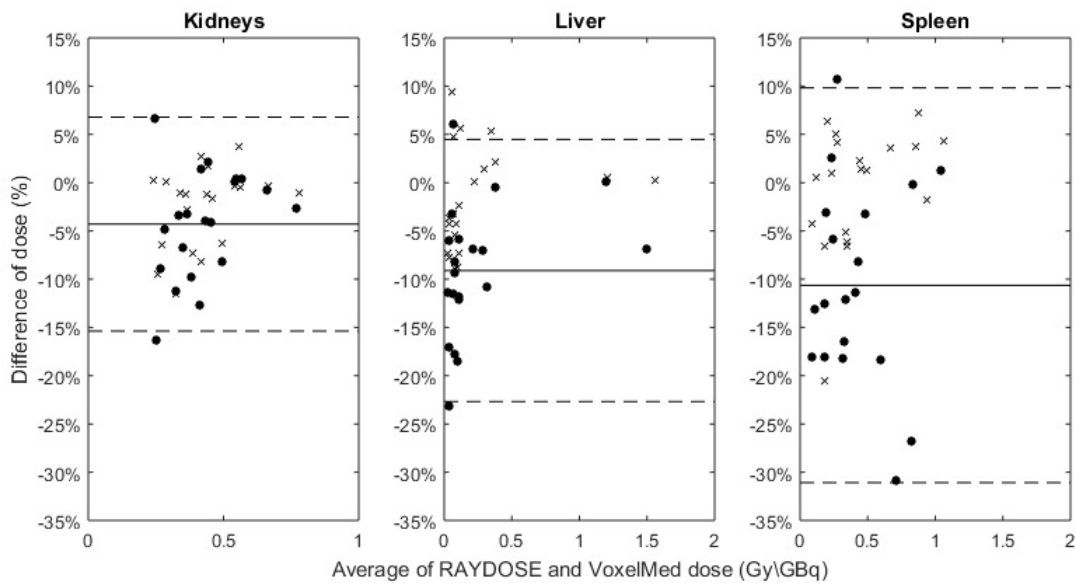


Figure 3.9: Comparison of RAYDOSE, VoxelMed and  $\text{VoxelMed}^{(\lambda RD)}$  calculated mean absorbed dose per unit of injected activity (Gy/GBq).

### 3.3.3 Discussion

Previous works investigated differences between dosimetry calculation techniques [67]-[69]. However, these studies were based on small groups of patients and the inter-patient variability cannot be investigated. In this study was, in-

Table 3.5: Kidney, liver and spleen mean absorbed dose (Gy/GBq) calculated with OLINDA1.1, VoxelMed, VoxelMed( $\lambda^{RD}$ ) and RAYDOSE for patients of Sample B

Cases	Kidneys				Liver				Spleen			
	OLINDA1.1	VoxelMed	VoxelMed( $\lambda^{RD}$ )	RAYDOSE	OLINDA1.1	VoxelMed	VoxelMed( $\lambda^{RD}$ )	RAYDOSE	OLINDA1.1	VoxelMed	VoxelMed( $\lambda^{RD}$ )	RAYDOSE
1	0.62	0.54	0.54	0.54	0.04	0.03	0.03	0.03	1.11	1.05	1.08	1.04
2	0.40	0.36	0.37	0.40	0.23	0.20	0.22	0.22	0.16	0.16	0.16	0.20
3	0.87	0.76	0.77	0.78	0.40	0.37	0.38	0.38	0.58	0.47	0.49	0.49
4	0.32	0.28	0.29	0.29	0.12	0.11	0.12	0.12	0.22	0.19	0.20	0.19
5	0.42	0.36	0.36	0.37	0.04	0.03	0.04	0.04	0.12	0.10	0.12	0.11
6	0.52	0.44	0.46	0.46	0.11	0.10	0.11	0.11	0.92	0.83	0.87	0.84
7	0.39	0.33	0.34	0.34	0.10	0.08	0.08	0.09	0.46	0.39	0.44	0.43
8	0.75	0.66	0.66	0.67	0.02	0.03	0.03	0.03	0.28	0.24	0.27	0.26
9	0.36	0.30	0.30	0.34	1.65	1.45	1.56	1.55	0.38	0.31	0.33	0.36
10	0.62	0.55	0.56	0.54	0.08	0.07	0.07	0.08	N/A	N/A	N/A	N/A
11	0.48	0.42	0.45	0.44	0.34	0.30	0.35	0.33	0.67	0.58	0.90	0.84
12	0.66	0.57	0.56	0.57	0.13	0.10	0.11	0.12	0.21	0.17	0.18	0.19
13	0.30	0.25	0.26	0.28	0.08	0.07	0.07	0.08	0.34	0.28	0.33	0.34
14	0.48	0.42	0.42	0.41	0.06	0.05	0.06	0.06	0.10	0.08	0.09	0.09
15	0.40	0.34	0.36	0.36	0.03	0.03	0.03	0.04	0.62	0.54	0.68	0.66
16	0.27	0.23	0.25	0.27	0.30	0.27	0.30	0.29	0.52	0.41	0.45	0.45
17	0.29	0.25	0.24	0.24	0.09	0.07	0.07	0.07	0.36	0.29	0.28	0.27
18	0.51	0.45	0.43	0.44	0.07	0.06	0.07	0.07	0.31	0.24	0.24	0.23
19	0.45	0.38	0.40	0.44	1.43	1.20	1.21	1.20	0.83	0.69	0.93	0.95
20	0.38	0.47	0.48	0.51	0.11	0.09	0.10	0.11	0.38	0.30	0.33	0.35

stead, considered a large sample of patients and a number of phantoms. This multi-approach method allowed to investigate the impact of activity distribution on the technique of calculation and to provide a valuable comparison on clinical patterns.

The simplest pattern that can be considered is a large homogeneous activity distribution. Inhomogeneities and irregular distribution of activity might differently affect results of calculation depending on the approach used. For that reason, a cylindrical Jaszczak phantom was firstly used in this study. Discrepancy around 5% was observed between VoxelMed and RAYDOSE, while larger differences between VoxelMed and OLINDA1.1 (13 %). Similar standard deviation across voxel (around 20%) and comparable slopes in DVHs were provided by VoxelMed and RAYDOSE (Figure 3.6).

In order to evaluate how accuracy of dose calculation depend on the activity distribution, the Geometrical phantom was acquired. Relative differences in absorbed dose depend on the shape and on the volume of the inserts, smaller is the volume and farer from a regular sphere is the shape, more the relative difference between modalities is higher. Toroids provided the greatest discordance

(relative difference with VoxelMed dose ranging from -52% to -41% for OLINDA and from -25% to -16% for RAYDOSE), while in the other inserts differences ranged between [-23%, 0%] for OLINDA1.1 and [-8%, +4%] for RAYDOSE. On one hand, the insert dose calculations in OLINDA1.1 were performed using the sphere model, since OLINDA1.1 only allows to perform dosimetry calculation for specified models (i.e. organs or spheres). This approximation might explain the huge discrepancies obtained with the voxel-based methods. On the other hand, a reason for the difference between RAYDOSE and VoxelMed is that the latter applies a mask before the convolution, while RAYDOSE does not. This contribution affects calculations in so far as the geometry and the volume of the insert may influence the activity distribution and leave empty spaces around or inside the objects. This effect is especially pronounced, for example, in the case of the toroid. The application of a mask also implies the lack of photon cross irradiation contribution between inserts, which has an impact on dose calculation (contribution around 5% [68]).

The Anthropomorphic phantom provided smaller discrepancies in comparison with the Geometrical phantom. Relative differences around 4% and 11% for RAYDOSE and OLINDA1.1, compared to VoxelMed dose. The larger volume of the inserts and the use of a more appropriate model in OLINDA1.1 is likely to have reduced the discrepancies. The tendency to underestimate the doses calculated with voxel dosimetry techniques in comparison to RADAR organ dosimetry (OLINDA) is shown also by other authors. Kletting et al [67] in their study obtained doses for their software NUKDOS around 1% to 2% lower than values obtained with OLINDA according to their workflow. However, NUKDOS performs voxel-dosimetry based on one SPECT/CT and on a series of planar images to determine the organ pharmacokinetics, making it much closer to organ-level dosimetry approach than VoxelMed. Hippeläinen et al [68] reported relative differences of 6%, 5%, 0% for left kidney, right kidney and spleen respectively when comparing their dosimetry software HIRD with an analytical dose calculation in the dynamic XCAT phantom study. These values were obtained in closer condition to our study than NUKDOS and can be compared to values around 11% collected in Table 3.3.

An advantage of voxel-based methods is the ability to calculate DVHs and to

show isodose lines. With reference to DVHs, VoxelMed and RAYDOSE for geometrical and anatomical inserts provide similar slopes, demonstrating a good accordance for the spatial distribution of the dose calculated with these two techniques. The shift toward low dose for VoxelMed DVHs also reflected the underestimation of the average absorbed dose.

The differences and the weak points in dose calculations pointed out on phantoms become essential to investigate and to explain the differences in clinical cases. Two different studies (Sample A and Sample B) were shown in this work. For a copious number of patients dosimetry was calculated with OLINDA1.1 (as in clinical trial) and VoxelMed (Sample A), while for a smaller number of patients all of the three software (Sample B) were considered. Similarly to the phantoms, also for patients it was observed the tendency of underestimation of absorbed dose calculated with voxel-level techniques in comparison with the organ-level technique. In Sample A, VoxelMed calculated dose was 8% lower than OLINDA1.1 calculated dose (for all patients and all organs). This value is smaller than the 11% obtained with phantoms. However, large variability was observed (Figure 3.8) and the discrepancy was 11% if the absolute percentage difference was considered. The large inter-patient variability is probably due to the inhomogeneity of activity and the use of a set of sequential images. These results were confirmed for patients in Sample B: VoxelMed doses were 13% lower than OLINDA1.1 doses (14% in absolute values) and 8% lower than RAYDOSE doses (9% in absolute values). Similarly to the phantoms, for patients differences were lower and correlations larger (0.79 against 0.97) between VoxelMed and RAYDOSE than OLINDA1.1. Furthermore, correlation was larger with liver than with kidney and spleen in both cases. This is probably due for kidneys to the smaller volume in comparison with liver and for spleen to the breathing artefacts that likely hugely affect the quality of the rigid registration of sequential images (and then of the dose calculation), as reported also by Hippeläinen et al. [68]. Finally, the importance of the activity integration technique in the dose calculation was pointed out: the smallest discrepancies and almost perfect correlation between VoxelMed and RAYDOSE results were obtained when the same decay constant was used.

As a result of the present work, it can be stated that in dosimetry calcula-

tions and in the harmonization process of different dosimetry software there are critical steps that may be summarized as: contouring of volumes of interest; matrices of S values and type of convolution used to calculate absorbed doses; calculation over the whole field or on a restricted region of the 3D image; time activity curve fitting and integral from the first to the last image time point; time activity curve extrapolated from the last time point to infinity; time required for calculations; degree of personalization of the technique. The use of different settings in these steps may provide very different results: all these steps should be deeply investigated on several real cases before implementing a new home-made or commercial system, based on voxel level or on organ level calculations.

# Chapter 4

## MRTDosimetry Project

This PhD project was funded by the European Metrology Programme for Innovation and Research (EMPIR), and, in particular, within the **Metrology for clinical implementation of dosimetry in molecular radiotherapy (MRTDosimetry)** project [76] which has received funding from the European Union.

The overall aim of the MRTDosimetry project was “to provide the metrology for the clinical implementation of absorbed dose calculations in Molecular Radiotherapy (MRT)”.

MRTDosimetry is a joint project that brings expertise in metrology and nuclear medicine with the aim of providing dosimetry standards, validated methods and clear guidance necessary for implementation of MRT dosimetry in every European clinic offering MRT. This project began on 1 June 2016 and run for three years, finishing on the 31 May 2019. It involved 6 European national metrology institutes, 13 clinical research institutions across European countries and a number of others collaborators and private companies (see Figure 4.1).

The project builds on the results and outputs from the preceding EMRP JRP HLT11 MetroMRT project [77], which occurred between June 2012 and May 2015. The MetroMRT researches identified the key needs to perform the dose measurements required to optimize clinical efficacy of MRT: measurements of the administered activity, quantitative imaging in the patients using tomographic functional imaging (i.e. SPECT or PET), integration of time-activity curve, calculation of dose from estimated cumulative activity and estimation

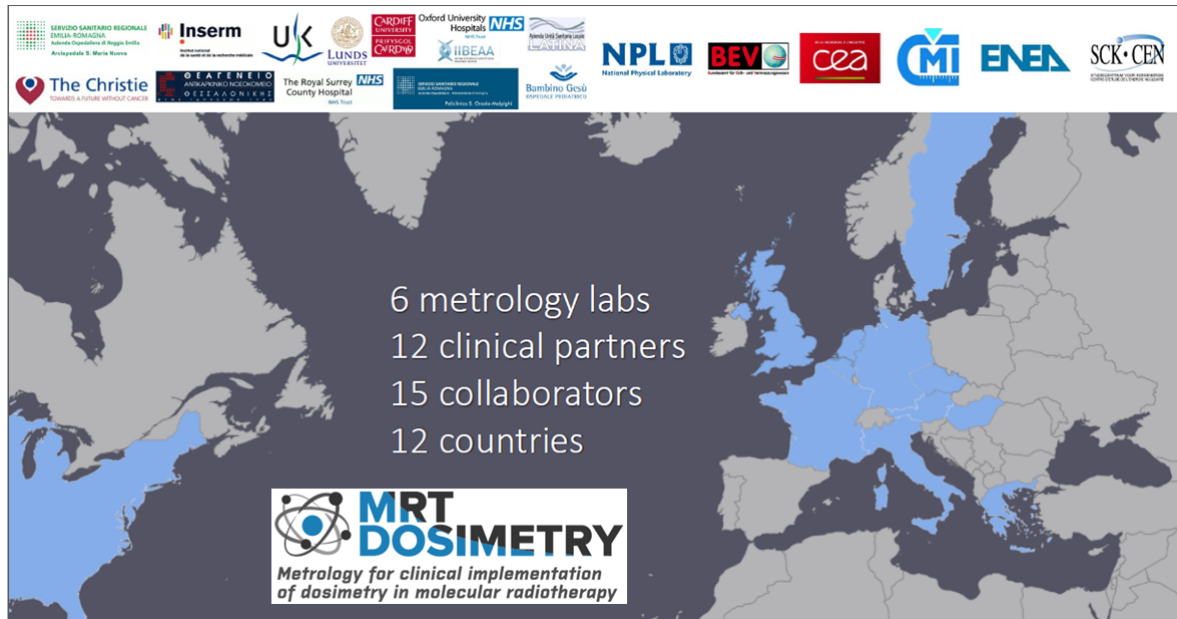


Figure 4.1: Countries directly or indirectly involved in the project. On the top of the picture the logos of the main partners.

of the overall uncertainty of the measurements and calculations. Each of these needs were addressed in the MRTDosimetry project, which established the following key objectives:

1. To determine branching ratios and emission probabilities for emerging beta-emitters ( $^{90}\text{Y}$  and  $^{166}\text{Ho}$ ), with the aim to improve quantitative imaging accuracy and dose estimations and developing new transfer instruments optimised for radiopharmaceuticals routinely used in MRT.
2. To develop 3D printing methods with the aim to generate a range of quasi-realistic anthropomorphic phantoms or sealed sources that can be used across the hospitals and research centres for calibration and validation of instrumentations.
3. To generate an open-access database of multimodal SPECT/CT and PET/CT images that can be used as reference data for commissioning and quality control.
4. To improve the accuracy in the calculation of absorbed dose by evaluating the optimal choice in term of acquisition time, measurement modality, dose calculation method and refinement of dose standards.



5. To determine uncertainties associated with each step of the dose measurement chain, from the primary standard to the dose calculation method. Moreover, uncertainty related to NTCP model were also evaluated.
6. To facilitate the dissemination of the results and technology developed by the project.

The AUSL di Reggio Emilia - IRCCS hospital was a clinical partner of the MRTDosimetry project. Therefore, this doctoral work was involved in several work-packages within the project and this took a consistent part of the PhD effort.

The main partners of the project met periodically every 9 months, rotating the location of the meetings among the partners. The meetings had the scope to review progress, discuss about the results and organize the future tasks of the project. Nine meetings totally took place. Where possible, conferences were held to follow the meetings to share the results of the project and to open discussion with the scientific community.

In the following paragraphs the workpackages which this PhD is involved to are described.

## 4.1 Validation of the Commissioning Protocol: Comparison Exercise

One of the main goals of the MRTDosimetry project was to define the standardization of quantitative SPECT/CT imaging. For this reason, a protocol for the commissioning and QC (Quality Control) of SPECT/CT scanner was developed by collaborators. The intention of this document was to fill the lack of standard guidelines for calibration, partial volume correction and validation of the imaging quantification system that can be applied for any acquisition system, regardless of manufacturer, location and other site-specific characteristics. The protocol was validated in a comparison exercise among 8 partners sites. A total of 9 SPECT/CT systems shown in Table 4.1 were included in this exercise. Each centre used its own gamma camera and meticulously followed the procedures described in the protocol.

Table 4.1: Participating systems for the Comparison Exercise.

	System 1	System 2	System 3	System 4	System 5	System 6	System 7	System 8	System 9
<b>Vendor</b>	Siemens	GE	GE	Mediso	GE	GE	GE	Siemens	Siemens
<b>Model</b>	Symbia T2	Discovery 670	Discovery 670	AnyScan SCP	Discovery 670	Optima 640	Optima 640	Intevo Bold	Symbia T2
<b>Year</b>	2009	2015	2015	2017	2011	2014	2015	2016	2006
<b>CT Rows</b>	2	16	16	16	16	4	4	2	
<b>Crystal</b>	3/8"	3/8"	3/8"	3/8"	3/8"	3/8"	3/8"	3/8"	5/8"
<b>Recon.</b>	Siemens e.soft	GE Xeleris	Hermes	Tera-Tomo SPECT	Ge Xeleris	Ge Xeleris	Ge Xeleris	Siemens e.soft	Siemens e.soft
<b>Algorithm</b>	OSEM	OSEM	OSEM	OSEM	OSEM	OSEM	OSEM	OSEM	OSEM
<b>AC</b>	CT-based	CT-based	CT-based	CT-based	CT-based	CT-based	CT-based	CT-based	CT-based
<b>SC</b>	TEW	TEW	TEW / MC	TEW	TEW	TEW	TEW	TEW	TEW
<b>RR</b>	Y	Y	Y	N	Y	Y	Y	Y	Y

The protocol was designed for the commissioning of SPECT/CT imaging with Lu-177 and I-131, even if it could theoretically be used for any radionuclide. This Paragraph describes and summarizes the results of this comparison exercise.

The set of measurements conducted by each site in the comparison exercise included:

1. Determination of the system specific Image Calibration Factor (ICF).
2. Assessment of the system specific partial volume effect.
3. Validation of the system SPECT-based activity quantification.

#### 4.1.1 Material and methods

##### Determination of the Image Calibration Factor (ICF)

Assessment of the ICF was obtained using a sufficiently large phantom (minimum height of 180 mm, minimum radius of 100 mm and maximum volume of 10000 mL). For example, Perspex Jaszczak cylinder without inserts [78] was suggested to be used.

Since the use of peptides or other labelling agents can lead to sticking to the walls of the phantom or syringe being used [79], non-carrier added radionuclides were used. In addition, in order to obtain homogeneous and stable

solutions, small quantities of inactive elements in a slightly acid solution were added to the solution.

Activities were measured, among the partners, using a radionuclide calibrator that has a traceable calibration (using a primary or secondary standard from a metrology institute [80]). In case this condition was not fulfilled, an aliquot was sent to a metrology institute for the activity concentration measurement. Activity and carrier solution quantity and chemistry are reported in Table 4.2.

Table 4.2: Activity and carrier solution for the commissioning and QC of SPECT.

Isotope	Activity (MBq)	Carrier Solution
Lu-177	400 (ICF)	Lutetium chloride (HCl [0.1 mol dm <sup>-3</sup> ] + Lu(iii)Cl <sub>3</sub> *6H <sub>2</sub> O [10 μg g <sup>-1</sup> ])
	122 (PVE)	
	400 (Validation)	

In order to check the peak position, peaking of the SPECT/CT system (without collimators) was performed before measurements (Figure 4.2). For this purpose, a point-source-like geometry with a small amount of activity was used (e.g. by using a 1 mL drop radioactive solution with ~5 MBq of <sup>177</sup>Lu).

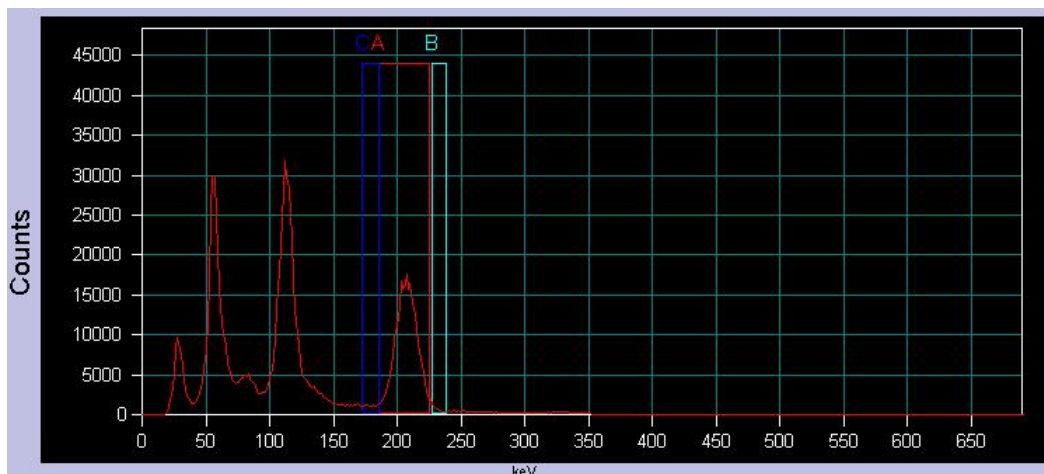


Figure 4.2: Siemens Symbia T2 (site: AUSL di Reggio Emilia) <sup>177</sup>Lu peaking.

SPECT/CT acquisitions and image reconstructions were performed according to the parameters in Table 4.3. AS, SC and RR were applied according to Table 4.1.

Table 4.3: SPECT/CT acquisition and reconstruction parameters for commissioning and QC.

<b>Lu-177</b>	
<b>Collimator</b>	Medium energy
<b>No. energy windows</b>	3
<b>Photopeak energy (keV)</b>	$208.4 \pm 10\%$
<b>Lower scatter energy (keV)</b>	$235.5 \pm 3\%$
<b>Higher scatter energy (keV)</b>	$235.5 \pm 3\%$
<b>Flood uniformity</b>	As per clinical imaging protocol for Lu-177
<b>Matrix</b>	128
<b>SPECT Movement</b>	Body contour
<b>No. projections</b>	120 (60 per detector)
<b>Time/projection</b>	60 s
<b>CT</b>	Standard low-dose
<b>Peaking Activity</b>	5 MBq
<b>Iterations</b>	5, 10, 15, 20, 25, 30, 35, 40, 45, 50
<b>Subsets</b>	2

A cylindrical VOI with a radius of 130% of the maximum phantom radius and a length of 120% of the phantom length was drawn in the SPECT images. For each number of iteration, the ICF was determined using Eq 4.1.

$$ICF = \frac{Counts}{\Delta t_{acq} \cdot A_{phantom}} \quad (4.1)$$

where  $\Delta t_{acq}$  is the acquisition duration,  $A_{phantom}$  is the activity in the phantom, and Counts the measured number of counts into the VOI.

### Assessment of partial volume effect

Assessment of the resolution and partial volume effect of the acquisition system and reconstruction setup were obtained using the IEC NEMA body phantom. This phantom consists of six sphere with increasing volumes and was already described in Paragraph 2.1.1. For that study the smallest sphere (volume equal to 0.52 mL) was excluded, while all six spheres were included in this study. Filling volume of each sphere was obtained by the difference between the weight of the filled sphere and the weight of the empty sphere.

A 60 mL of  $^{177}\text{Lu}$  radioactive stock solution with activity and chemistry as reported in Table 4.2 was prepared.

Peaking of SPECT/CT system was performed before measurements. The same acquisition and reconstruction parameters used to determine the ICF were set up. RC for each sphere and each parameter of acquisition was obtained using Eq. 2.6. The RC against the sphere volumes V points were fitted using the following curve:

$$f_{RC}(V) = \frac{\alpha}{1 + (\beta/V)^\gamma} \quad (4.2)$$

### Validation of the QI setup

The quantitative imaging (QI) setup was validated using a 3D printed 2-Organ anthropomorphic phantom, specifically designed as part of this project. The phantom is based on the ICRP Publication 110 (“Adult Reference Computational Phantoms”), and contains a spleen and a 2-compartment right kidney (with a internal substructure composed by cortex and medulla). The phantom was printed in polylactic acid, which has a CT number approximately 130 HU

which is similar to Perspex (110-130). Laser cut perspex baseplates and top plates were also produced to be easily attached to the holes in the base of the standard Jaszczak phantom. The computer-aided design and the assembled 3D printed phantom is shown in Figure 4.3.

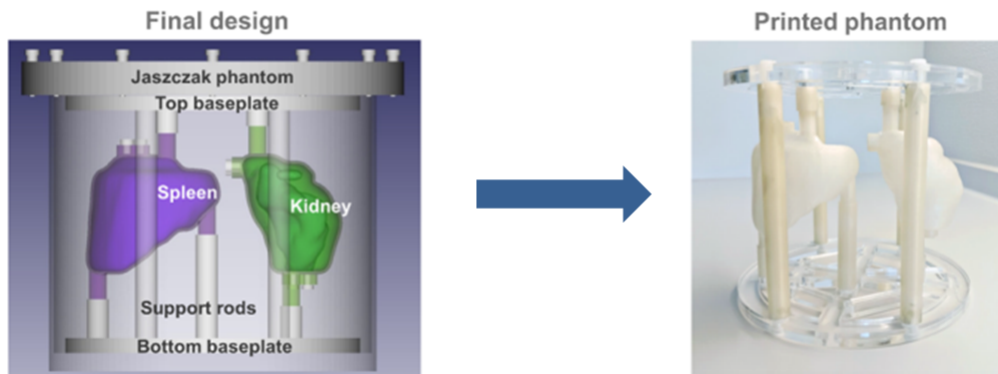


Figure 4.3: Design and 3D printed 2-organs anthropomorphic phantom. The baseplate for attachment is also included.

The needed equipment in term of Lu-177 activity and solution chemistry is reported in Table 4.2. Renal cortex and spleen had the same activity concentration, while it was different for the medulla. The radioactive solution was prepared in two different stock containers. Carrier solution was prepared following the chemistry in Table 4.2. Table 4.4 shows the volume of each insert-compartment, the desired activity concentration and the needed target volume and activity into the stock solution, assuming an 20% extra volume into the stock solution. In order to reduce the possibility of having air bubbles a long needle syringe and a clamp stand for holding inserts were used. The clamp stand was used to fix the insert and place it with the optimal angle for filling (e.g. for Medulla 10 mL of solution were drawn up with an angle of approximately 45°, and the remaining 25 mL positioning the clamp stand to have the Medulla filling holes pointing straight up).

After performing peaking, the SPECT/CT images were acquired according to Table 4.3. VOI were drawn using a threshold-based method so that the VOI volume matches the filling volume as closely as possible. SPECT-based partial

Table 4.4: Filling volume of the Two-Organ Phantom, target volume and activities for the stock solutions.

	Kidney Medulla	Kidney Cortex	Spleen
Filling volume (mL)	35	75	125
Activity concentration (MBq/mL)	0.5	1.5	
Target Volume (mL)	42	240	
Activity needed (MBq)	21	360	

volume corrected activities were calculated using Eq 4.3.

$$A_{SPECT,PVC} = \frac{Counts}{ICF \cdot \Delta t_{acquisition}} \cdot \frac{1}{RC(V_{insert})} = \frac{A_{SPECT}}{RC(V_{insert})} \quad (4.3)$$

Measured activity (in SPECT) and known activity (in dose calibrator) were compared to assess the accuracy of quantitative imaging setup.

#### 4.1.2 Results

An axial slice of the SPECT/CT image of the three phantoms acquired is reported in Figure 4.4.

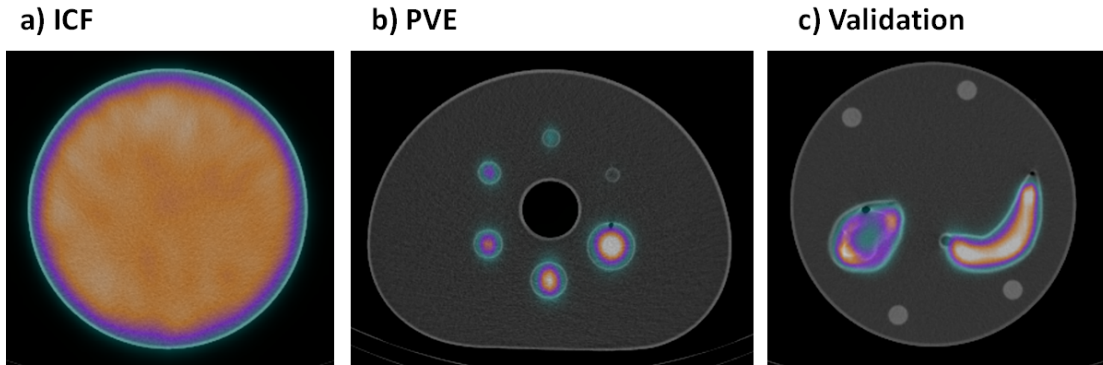


Figure 4.4: Siemens Symbia T2 (site: AUSL di Reggio Emilia) SPECT/CT fusion images for a) the homogeneous cylindrical Jaszczak phantom, b) the IEC NEMA body phantom and c) the MRTDosimetry 2-Organ anthropomorphic phantom.

**Determination of the ICF:** The ICF measurements were performed on all available systems. The ICF values for all systems and applied reconstructions (with 25 Iterations and 2 Subsets) are shown in Figure 4.5. The error

bars are also reported in the graph. Uncertainty associated with the ICF was estimated applying the law of propagation of uncertainty. As some sites did not submit an estimate for the uncertainty of the radionuclide calibrator, it was assumed to be 4% for all measurements.

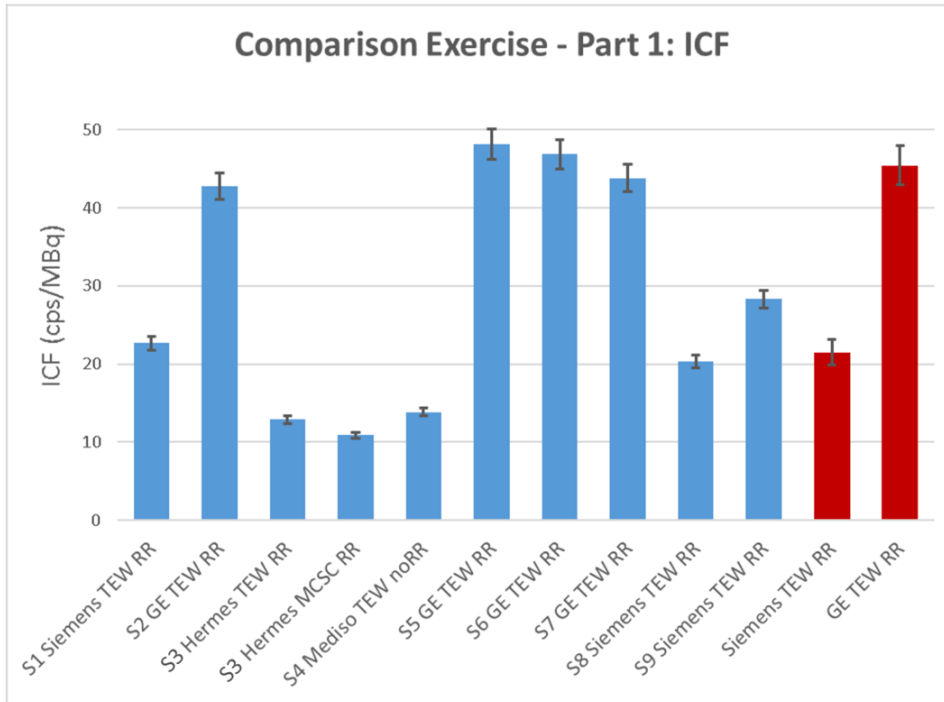


Figure 4.5: ICF values for each system and reconstruction. The red bars shows the mean and standard deviation over all 2 Siemens TEW RR and all 4 GE TEW RR reconstructions (only 3/8" crystals).

The same combination of imaging system and reconstruction generally leads to the same ICF: all Siemens-based TEW RR reconstructions lead to a mean value of  $21.5 \pm 1.6$  cps/MBq, all GE-based TEW RR reconstructions average at  $45.4 \pm 2.5$  cps/MBq. For Hermes, the two different scatter correction methods (TEW against Monte Carlo) result in an 18.5% difference in ICF.

**Assessment of partial volume effect:** The recovery curves of all systems (reconstruction with 25 Iterations and 2 Subsets) are shown in Figure 4.6.

Uncertainty analysis was based on the law of propagation of uncertainty. Likewise observed for ICF, the same combination of imaging system and reconstruction generally leads to the similar RC. For Siemens, the two older systems



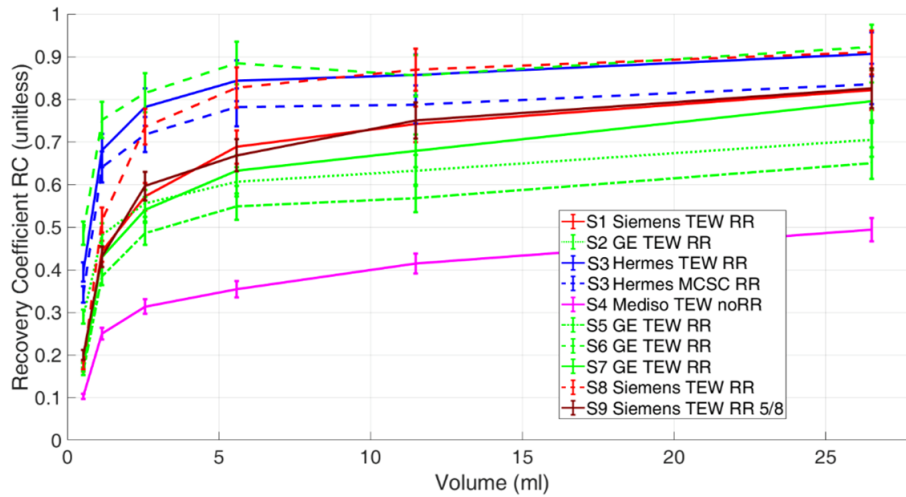


Figure 4.6: Lu-177 RC curves for each system and reconstruction. The Siemens systems are indicated in red, the GE systems in green and the Mediso system is in blue.

(S1 and S9) had comparable RCs, while the newer system (S8) featured a 12% mean higher recovery. Interestingly, one GE TEW RR reconstruction (S6) yielded considerable better recovery than the three sites with the same imaging setup (S2, S5 and S7). The only reconstruction without resolution recovery (S4) had a considerable lower RC value than all other reconstructions.

The fitted curves for each reconstruction are shown in Figure 4.7. A non-weighted and a weighted (based on the uncertainty of each RC value) fit were performed and the 95% confidence interval is given for each fit.

**Validation of the QI setup:** The ratio between SPECT-based and radionuclide calibrator-based activity was calculated. Results are shown in Figure 4.8. Error bars were estimated applying the uncertainty propagation law (including radionuclide calibrator measured activity, counts, acquisition duration, ICF and RC errors).

### 4.1.3 Discussion

All reconstructions gave comparable ICF values for equivalent combinations of imaging system and protocol (acquisition and reconstruction). While the two Siemens-based TEW RR reconstructions led to values of  $21.5 \pm 1.6$  cps/MBq,

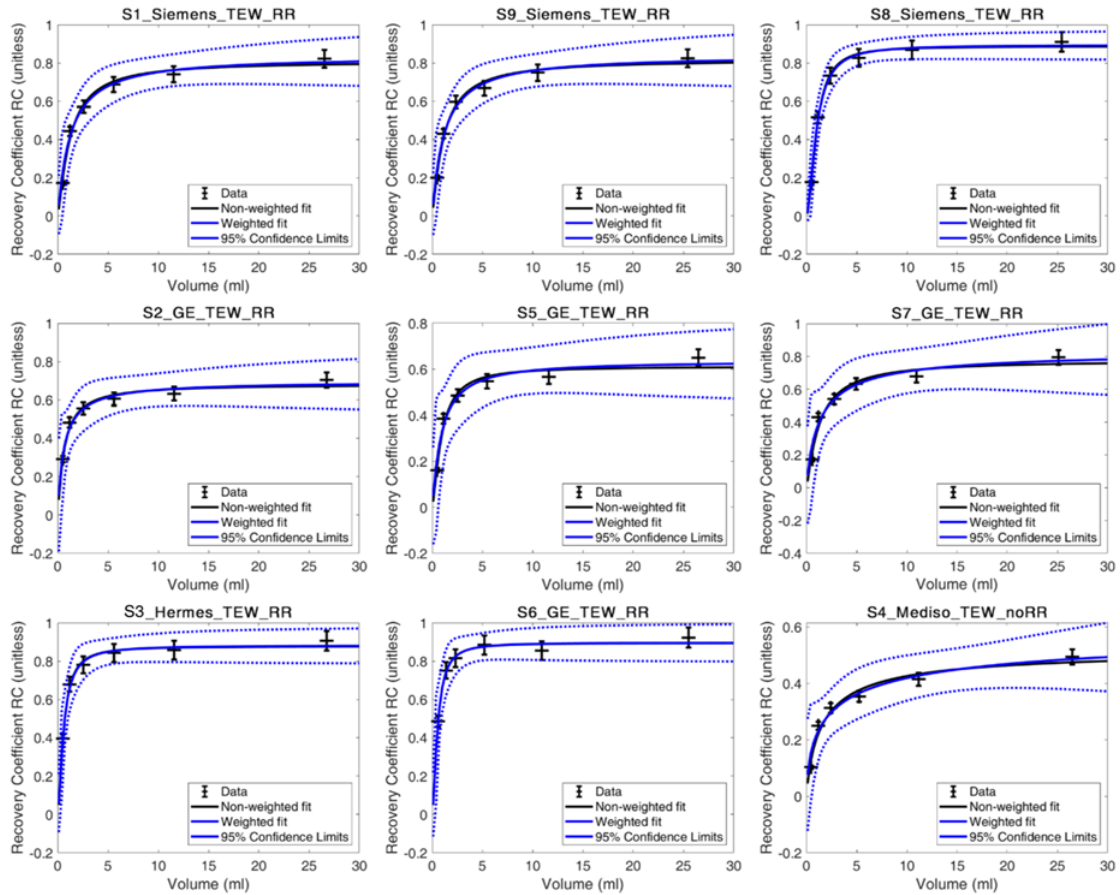


Figure 4.7: Lu-177 RCs and fitted curves for each participating system. The black crosses are the RCs, the solid blue lines are the non-weighted fits, the dotted blue lines the 95% confidence intervals and the dashed black lines the non-weighted fits.

the four GE-based TEW RR reconstructions averaged to  $45.4 \pm 2.5$  cps/MBq. Mean uncertainty of ICF was about 4%. Activity error was the dominating factor in the final uncertainty of ICF.

RCs were considerably lower in case of reconstruction without resolution recovery (System 4). This suggests that RR should be applied whenever available.

One limitation of this exercise is the use of relatively small spheres for the partial volume effect evaluation. More specifically, the spheres (all volumes  $< 30$  mL) were considerably smaller than the spleen and the right kidney inserts (volumes of 125 and 110 mL, respectively). This results in a large uncertainty of the fitted recovery curves for volumes  $\gg 30$  mL (i.e. the spleen and right kidney inserts). Nevertheless, average high accuracy of activity quantification

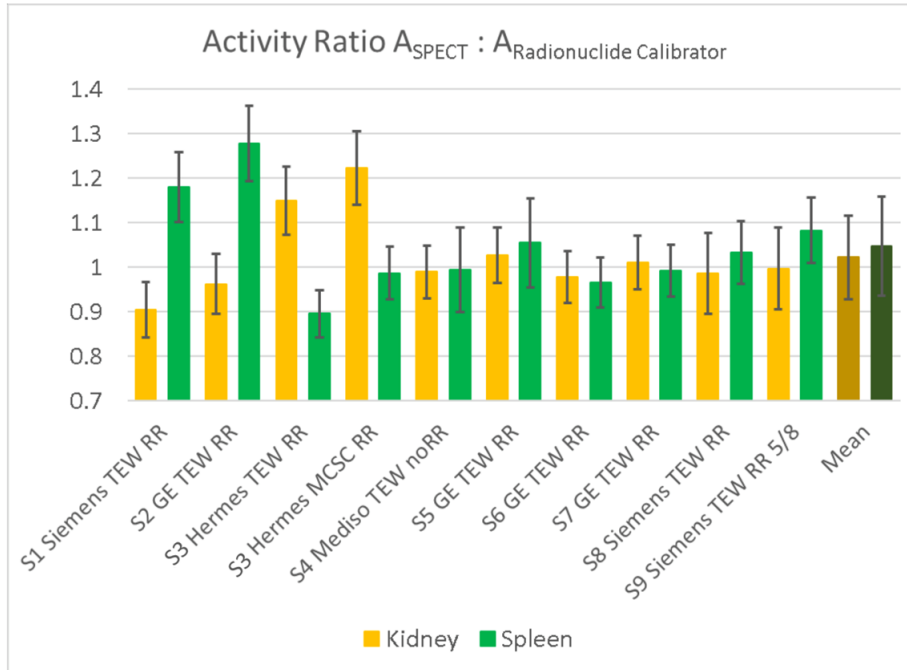


Figure 4.8: Ratio between SPECT-based activity and radionuclide calibrator-based activity for the 2-Organ phantom. In orange the kidney's results and in green the spleen's results. The mean and standard deviation is indicated by a darker color.

was obtained (average ratios between the estimated and known activities were 1.02 and 1.05 for kidneys and spleen, respectively).

## 4.2 Surrogate sources for QI

In nuclear medicine imaging, commissioning and quality control (QC) is usually performed based on hollow, fillable containers, which are usually filled with in-loco prepared radio-active solutions. However, this leads to a multitude of problems, such as ensuring that the filling volume and activity concentration are determined with an acceptably small error and that similar activities are used for repeated measurements to be comparable in terms of counting and statistics. Routine QC can be significantly simplified by the use of sealed test sources as an alternative to using phantoms. In particular, radioactive sources containing radionuclides of comparable energies and emission probabilities to the ones to be used for imaging (e.g.  $^{57}\text{Co}$  for  $^{99m}\text{Tc}$  or  $^{133}\text{Ba}$  for  $^{131}\text{I}$ ) can be used.

The aim of this study was to investigate the feasibility of using solid  $^{133}\text{Ba}$  source as a surrogate of  $^{131}\text{I}$  solution for SPECT/CT QC.

### 4.2.1 Material and methods

Two sets of traceable  $^{133}\text{Ba}$  sources were produced at CEA (Commissariat à l'énergie atomique et aux énergies alternatives) and CMI (Czech Metrology Institute), both participating in the project. Both sets were encapsulated in 3D-printed cylinders. To assess the feasibility of using the solid sources as surrogates, identical containers to be filled with liquid  $^{131}\text{I}$  were sent to the partner sites for a quantitative SPECT/CT imaging comparison exercise between 8 sites.

In order to assess the potential of solid  $^{133}\text{Ba}$  as surrogate for liquid  $^{131}\text{I}$ , a set of radioactive sources were acquired in the participating sites and results were compared.

#### I-131 phantom preparation and acquisition

Four cylindrical 3D-printed fillable inserts (Figure 4.9a) were specifically designed and produced as part of the project and were shipped to the participating partners. The cylinders were attached, using a baseplate, to the Jaszczak phantom. Cylinders had an increasing volumes (1.7, 6.7, 26.9 and 107.4 mL). The height of the cylinder was set to 38 mm in all cases, while the diameter was changed (7.5 mm, 15 mm, 30 mm, 60 mm). Volumes and positions were specifically chosen to have negligible overlapping counts arising from different sources (taking into account the partial volume effect). For each cylinder a cap was provided. Two types of cylinder cap were designed, one for containing a resin and one for injection of solution (through a small hole).

Each cylinder was filled with a 187.5 kBq/mL activity concentration of pure  $^{131}\text{I}$  radioactive solution. Small quantities of inactive iodine ( $\text{KI } 10 \mu\text{g g}^{-1}$ ) in a slightly basic solution ( $\text{NaOH } 0.1 \text{ mol dm}^{-3}$ ) were added, in order to obtain homogeneous and stable solutions. The phantom was filled with tap water. Activities were measured, among the partners, using a radionuclide calibrator that has a traceable calibration (using a primary or secondary standard from a metrology institute). Because of this condition was not fulfilled in AUSL di

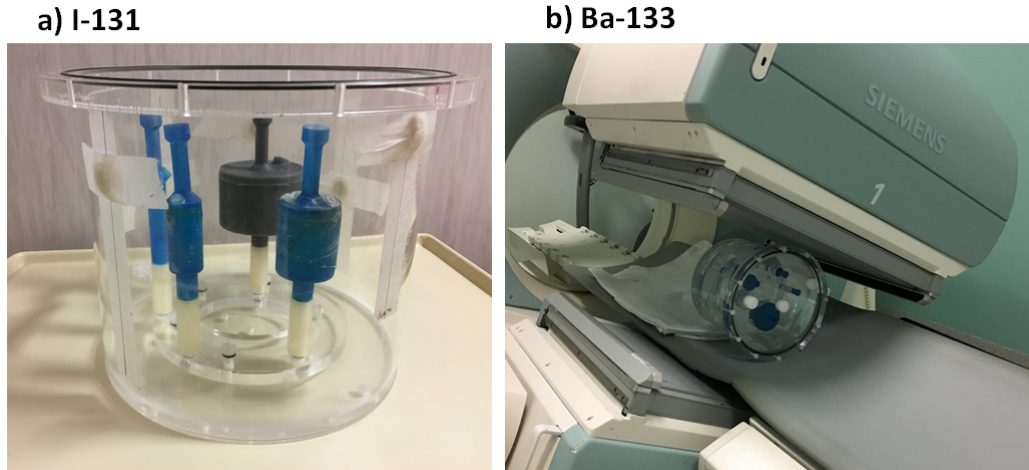


Figure 4.9: Captures of (a) phantom with  $^{131}\text{I}$  cylinders during assembly and (b) phantom with  $^{133}\text{Ba}$  during the SPECT/CT acquisition.

Reggio Emilia hospital, an aliquot with  $\sim 1$  mL of solution was sent to the UK national metrological institute (the National Physical Laboratory, Teddington, UK).

SPECT/CT acquisitions and reconstructions were performed according to Table 4.5. In order to check the peak position, peaking of the SPECT/CT system (without collimators) was performed before measurements (Figure 4.10a) using a point-source like geometry with  $\sim 1$  MBq of  $^{131}\text{I}$ .

### Ba-133 phantom preparation and acquisition

In each site, the two sets of 4  $^{133}\text{Ba}$  were mounted in a water-filled Jaszczak cylinder (Figure 4.9b), in the same order and position as in the  $^{131}\text{I}$  phantom. Activities of CEA sources were about 2-fold the activities of the CMI sources. Details on the geometry of the sources and the respectively activities are provided in Table 4.6.

SPECT/CT acquisition and reconstruction parameters are reported in Table 4.5. Peaking of the  $^{133}\text{Ba}$  setup is shown in Figure 4.10.

In order to compare the differences between the  $^{131}\text{I}$  cylinders and the  $^{133}\text{Ba}$  surrogates, the “pseudo-ICFs” were calculated using Eq. 4.1. The prefix “pseudo-” was added because it was not a calibration (the pseudo-ICFs were calculated for each cylinder). To find a cross-calibration factor between  $^{133}\text{Ba}$  and  $^{131}\text{I}$ , a regression analysis was performed once with intercept set to zero,

Table 4.5: SPECT/CT acquisition and reconstruction parameters for  $^{131}\text{I}$  and  $^{133}\text{Ba}$  sources.

	<b>Ba-133</b>	<b>I-131</b>
<b>Collimator</b>	High energy	High energy
<b>No. energy windows</b>	3	3
<b>Photopeak energy (keV)</b>	$356 \pm 7.5\%$	$364.5 \pm 10\%$
<b>Lower scatter energy (keV)</b>	$321 \pm 2.5\%$	$317.1 \pm 3\%$
<b>Higher scatter energy (keV)</b>	$403 \pm 5\%$	$411.9 \pm 3\%$
<b>Flood uniformity</b>	As per clinical imaging protocol for I-131	As per clinical imaging protocol for I-131
<b>Matrix</b>	128	128
<b>SPECT Movement</b>	Body contour	Body contour
<b>No. projections</b>	120 (60 per detector)	120 (60 per detector)
<b>Time/projection</b>	30 s	30 s
<b>CT</b>	Standard low-dose	Standard low-dose
<b>Peaking Activity</b>	1 MBq	1 MBq
<b>Iterations</b>	30	30
<b>Subsets</b>	2	2

Table 4.6: Specifications of the cylindrical solid  $^{133}\text{Ba}$  sources.

<b>Diameter (mm)</b>	<b>Length (mm)</b>	<b>Volume (cm<sup>3</sup>)</b>	<b>CMI Activity (kBq) at 37/7/2018</b>	<b>CEA Activity (kBq) at 15/05/2018</b>
7.5	38.0	1.68	$161.9 \pm 1.8$	$341.8 \pm 8.9$
15.0	38.0	6.72	$674.2 \pm 7.4$	$1377.0 \pm 35.8$
30.0	38.0	26.9	$2685 \pm 30$	$5280 \pm 137$
60.0	38.0	107.4	$10710 \pm 118$	$20860 \pm 542$

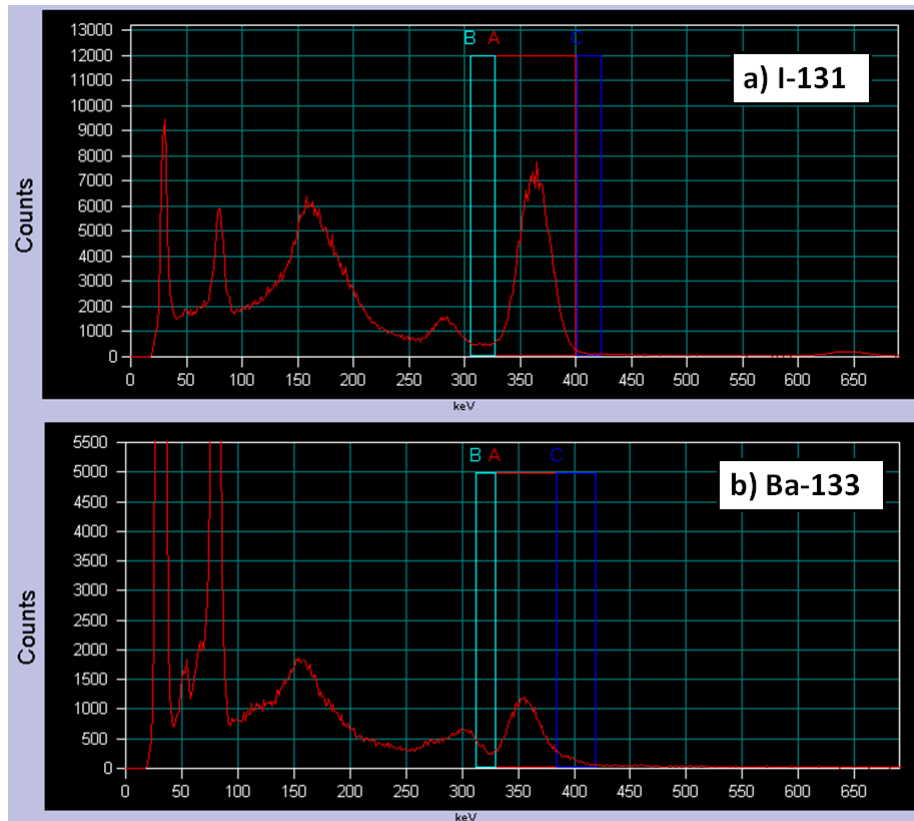


Figure 4.10: Siemens Symbia T2 (site: AUSL di Reggio Emilia) peaking of a)  $^{131}\text{I}$  point-like source and b)  $^{133}\text{Ba}$  small source.

and one with open intercept.

## 4.2.2 Results

An axial slice of the SPECT/CT image of the  $^{131}\text{I}$  and  $^{133}\text{Ba}$  cylindrical inserts is shown in Figure 4.11.

For  $^{133}\text{Ba}$ , the mean pseudo-ICFs between CMI and CEA sources were calculated. Figure 4.12 shows the pseudo-ICFs of  $^{131}\text{I}$  and  $^{133}\text{Ba}$  for each system.

The pseudo-ICFs of  $^{131}\text{I}$  are higher than those of  $^{133}\text{Ba}$  for all reconstructions and systems. As in the previous study 4.1, equivalent setups yield comparable pseudo-ICFs (e.g. GE TEW RR and Siemens TEW RR). To quantify this difference, the ratio between  $^{133}\text{Ba}$  and  $^{131}\text{I}$  based ICF for each imaging setup and source was calculated. For each imaging setup, the mean value of the ratio of all sources are shown in Figure 4.13. The ratios range between 0.6 and 0.9, the overall mean ratio lies at  $0.74 \pm 0.12$ .

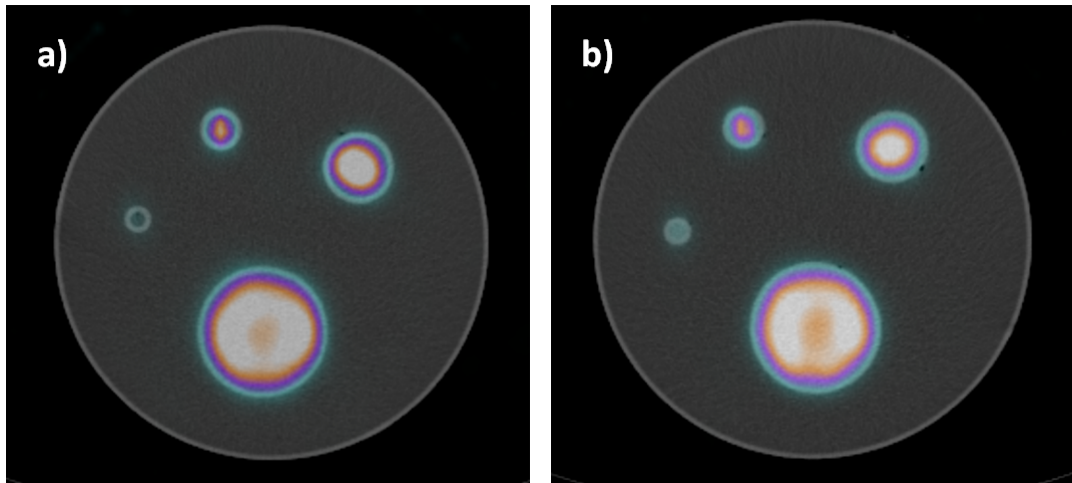


Figure 4.11: Siemens Symbia T2 (site: AUSL di Reggio Emilia) SPECT/CT fusion of a)  $^{131}\text{I}$  cylinders and b)  $^{133}\text{Ba}$  sources.

Figure 4.14a shows the regression analysis with intercept set to zero, while Figure 4.14b the regression analysis with intercept be fitted.



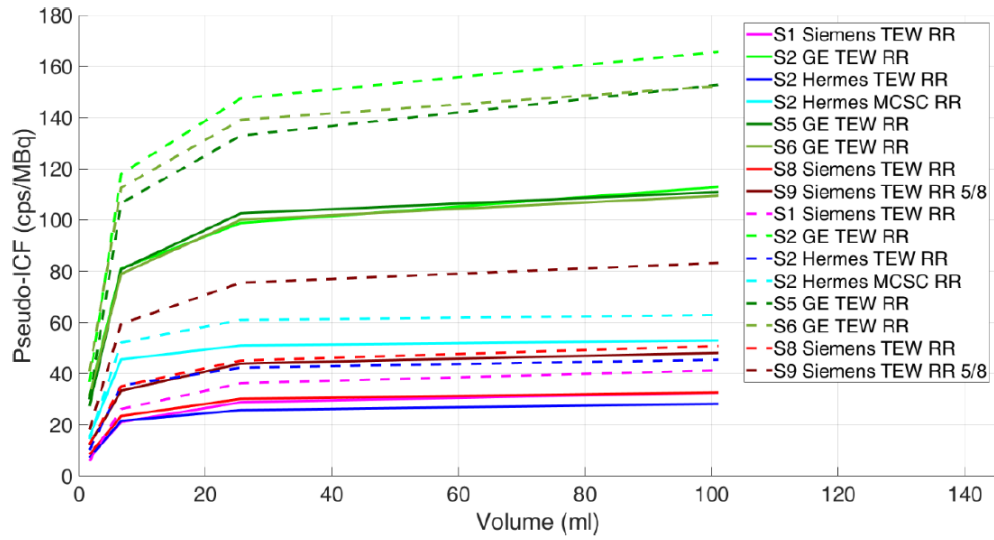


Figure 4.12: Pseudo-ICF of  $^{131}\text{I}$  (dashed lines) and  $^{133}\text{Ba}$  (solid lines). Color shades indicate different systems and reconstructions (Green: GE TEW RR; Red: Siemens TEW RR; Blue: Hermes)

### 4.2.3 Discussion

In this study, a mean value of  $0.74 \pm 0.12$  was found for the ratio between the ICFs for both radionuclides. In contrast, the regression analysis yielded values of  $0.71 \pm 0.01$  (with intercept zero) and  $0.70 \pm 0.02$  (with intercept fitted). Interestingly, this value is in good agreement with the ratio of the emission probabilities, which are 62.1% for the 356.0 keV peak of  $^{133}\text{Ba}$  and 81.2% for the 364.5 keV peak of  $^{131}\text{I}$ , leading to a ratio of 0.764.

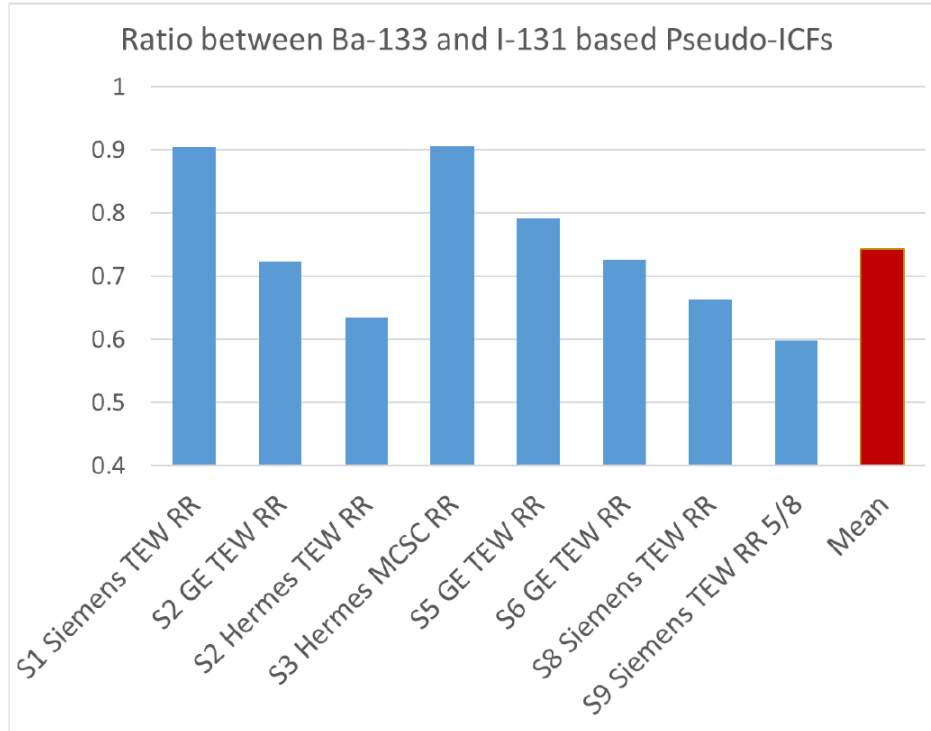


Figure 4.13: Mean value of the ratios between  $^{133}\text{Ba}$  and  $^{131}\text{I}$  based ICFs of all sources, for each imaging setup. The red bar is the overall average value.

### 4.3 Cross comparison of dosimetry calculations

Dosimetry calculations in MRT can be described theoretically in a relative straightforward manner by the MIRDO schema (see Paragraph 1.6). However, in reality dosimetry calculations are a complex series of functions governed by practical considerations which vary between centres that may use different imaging systems, calibration systems, analysis software and dosimetry systems. As such it has proven very challenging for the project to compare dosimetry techniques in MRT dosimetry.

A cross-comparison exercise based on real clinical functional images was performed in order to compare the accuracy and uncertainty of dosimetry calculations among several clinical groups within the project.

The aim of this comparison was to improve the accuracy in the calculation of dose. For this purpose, differences of the time-activity curve integration between different software solutions were evaluated and how error propagation of the integration of the TAC is handled by different software solutions was investigated.

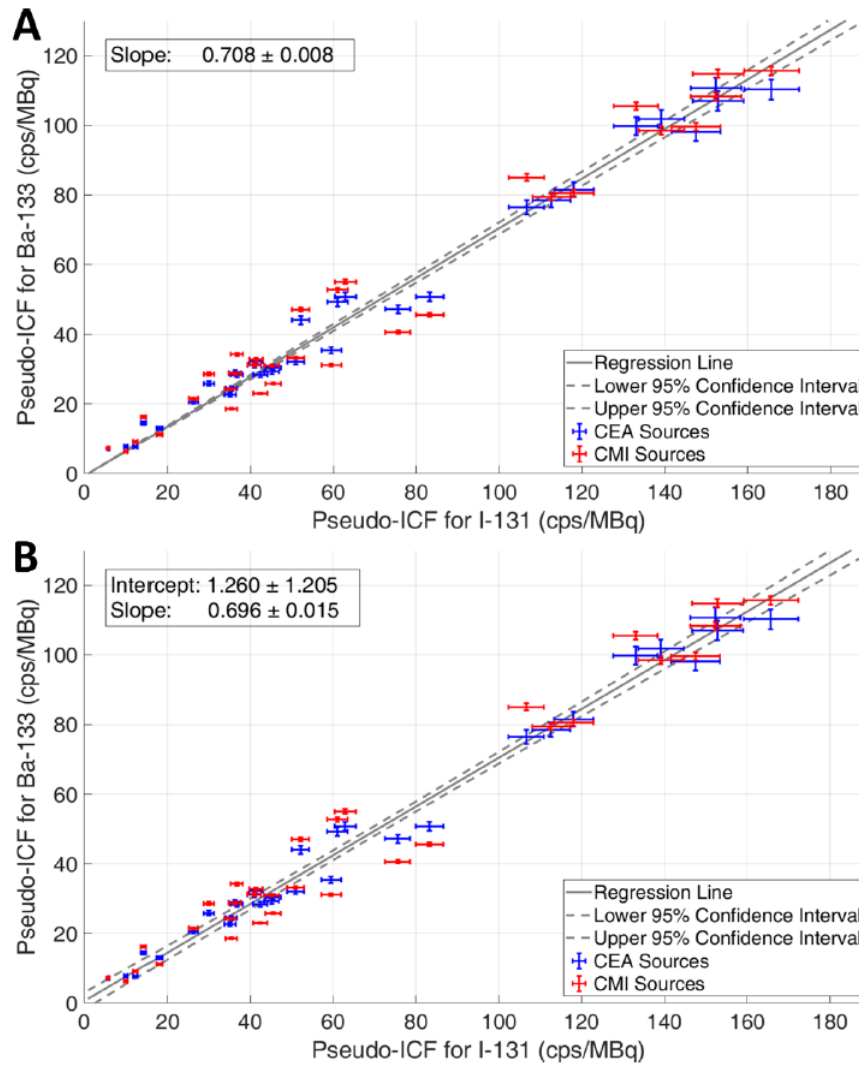


Figure 4.14: Regression analysis of the pseudo ICFs of  $^{133}\text{Ba}$  and  $^{131}\text{I}$ , with a) intercept set to zero and b) intercept fitted.

### 4.3.1 Material and methods

For this study, two patient dataset with multiple post-therapeutic SPECT/CT images were distributed to project partners. Patients were enrolled at AUSL di Reggio Emilia hospital. Commercial project partners were excluded from this exercise due to restrictions with respect to patient data protection and each site had to agree to the terms and conditions set by the AUSL di Reggio Emilia IRB. Initially, 10 sites were considered in the exercise. Table 4.7 shows the characteristics in term of input images and outputs of all the software solutions used by the partners involved in this exercise. Only software 1-6 took part in this comparison. S8 and S9 were not able to correctly “read” the SPECT/CT

Table 4.7: Input image type and calculation modality of the software used by partners.

Software	Type	Input images	Output TIAC
S1	In-House	Multi-SPECT	Voxel-wise
S2	In-House	Multi-SPECT	Voxel-wise
S3	In-House	Multi-SPECT	Organ-wise
S4	In-House	Multi-SPECT	Voxel-wise
S5	Commercial	Multi-SPECT	Organ-wise
S6	In-House	Multi-SPECT	Organ-wise
S7	In-House	1 SPECT + multi-planar	Organ-wise
S8	Commercial	Multi-SPECT	Organ-wise
S9	Commercial	Multi-SPECT	Organ-wise
S10	In-House	1 SPECT + multi-planar	Organ-wise

images provided, while S7 and S10 were excluded because of they needed planar images to perform dosimetry.

Patients were already enrolled in a clinical trial, as described in 1.7. Each datasets consisted of the reconstructed SPECT images, the reconstructed SPECT images registered to the first SPECT/CT time point, the VOI outlines (drawn in AUSL di Reggio Emilia), low dose CT acquired for attenuation correction and the calibration factor (28.5 Bq/Counts). Each of the 5 sequential SPECT/CT images were included in the datasets. Axial slice capture of the SPECT/CT fusion for the 24 h p.i. time-points are shown in Figure 4.15.

Analysis was performed on kidneys, liver (both health and tumours) and spleen.

According to the ability of each software to correctly read the pre-registration of the fusion images or to output a voxel-based or organ-based integration, results were labelled in four categories:

- 1A: In-house registration + voxel-wise TAC fitting
- 1B: Pre-registered dataset + voxel-wise TAC fitting

- 2A: In-house registration + organ-wise TAC fitting
- 2B: Pre-registered dataset + organ-wise TAC fitting

In this exercise only the TIACs were evaluated and compared.

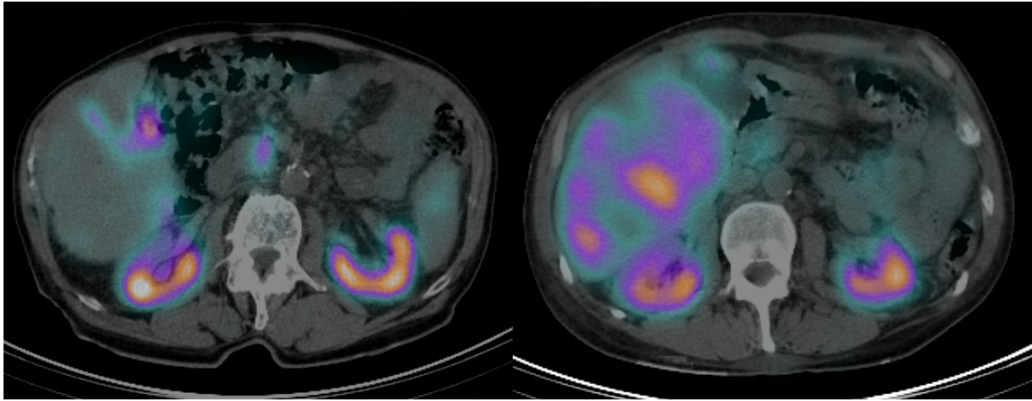


Figure 4.15: Image captures of hybrid SPECT/CT axial slices of patients for the cross comparison of dosimetry calculation systems.

### 4.3.2 Results

A survey among all participating sites to get an overview on how each software performed integration of the time-activity curves was conducted:

- S1: The site provides only voxel-based TIACs. The TIACs in each voxel were obtained using the effective tail calculated with a bi-exponential fit of the organ activities. TIACs were calculated, for each voxel, using the trapezoidal method up to the last time-point and analytically beyond this time-point. The site performed one calculation using the pre-registered dataset with a recovery coefficient based partial volume correction. In addition, the site used the original VOIs.
- S2: The site performed TAC integration using their in-house solution based on the Geant4 Monte Carlo code. Registration of NM data was performed using a non-rigid algorithm. The best fit function (linear uptake + mono-exponential or mono-exponential only) was automatically chosen by the software. An effective exponential tail was calculated with

a mono-exponential fit of the last two points of the time activity curve. The provided VOIs were used.

- S3: The site provided two organ-based datasets (self-registered and pre-registered) per patient. The provided VOIs were used for the analysis. Integration was performed using either a mono- or bi-exponential function chosen by the user, with a linear uptake assumed if appropriate.
- S4: The site provided two voxel-based datasets (self-registered and pre-registered) per patient. Trapezoidal integration was performed up to the maximum value and a mono-exponential fit was applied to the remaining data points. If the first time point was the highest value, then a monoexponential fit was applied only.
- S5: The site performed both voxel-based and organ-based dosimetry. Two voxel-based datasets (self-registered and pre-registered) were calculated, using PLANETDose (DOSIsoft, France) per patient. Two organ-based datasets (self-registered and pre-registered) per patient were also calculated. Manual segmentation was performed on the CT data with each organ being registered independently prior to the dosimetry calculation. No detailed explanation on the fitting was provided by the vendor.
- S6: The site provided two organ-based datasets (self-registered and pre-registered) per patient. The site performed manual segmentation on the CT data with each organ being registered independently. Curve fitting and integration was performed using bi-exponential function.

The results of the TIACs are shown in Figures 4.16-4.18 (separately for kidneys, liver and spleen).

### 4.3.3 Discussion

All software solutions in this exercise used a different methodology of TIAC calculations. These heterogeneity of methods might explain the considerable differences observed among the software. Deviations up to 50% were observed for the mean value of the TIAC in the same organ. Different registrations and

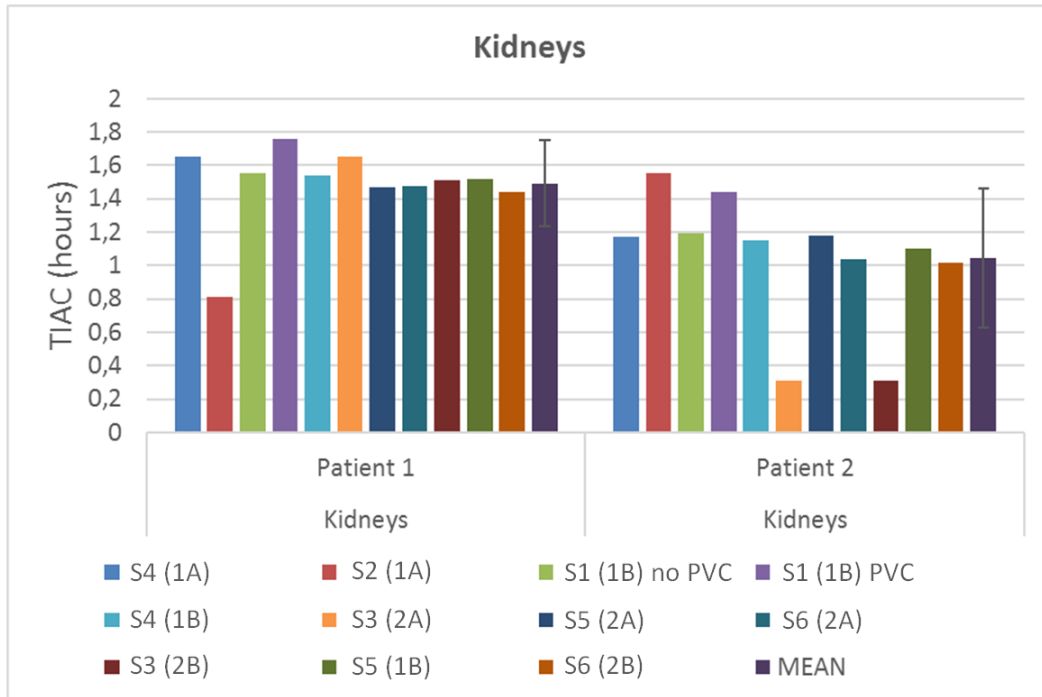


Figure 4.16: Results for each software of TIACs (h) for kidneys (sum of both kidneys) in the 2 patients. In bracket the integration and registration: 1. Voxel-based TAC fitting. 2. Organ-based TAC fitting. A: SPECR registration by the site. B: Pre-registered data were used. The mean data and the standard deviations are shown in the last columns.

VOIs were also used among the sites, which makes comparison even more challenging. In addition, a calculation of the error propagation is not implemented, thus making it even more difficult to check the validity of the results.

The necessity of standardization, especially in voxel-level calculations, is probably the main conclusion of this study. The lack of a generally accepted VOI format is also something that need to be managed to, especially to perform multi-sites comparisons.

Uncertainty of calculated dose should be provided to evaluate the accuracy of calculations. However, most of the software are not still able to provide them. Effort to fill these gaps needs to be performed.

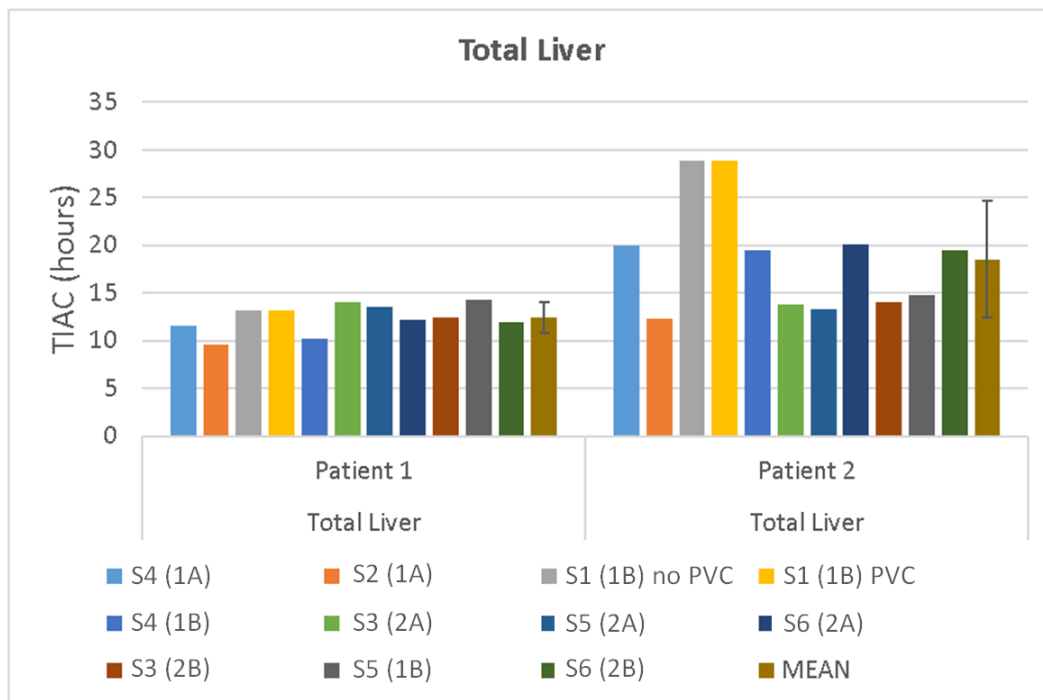


Figure 4.17: Results for each software of TIACs (h) for total liver (both health and tumours) in the 2 patients. In bracket the integration method and image registration: 1. Voxel-based TAC fitting. 2. Organ-based TAC fitting. A: Image registration provided by the site. B: Pre-registered images were used. The mean data and the standard deviations are shown in the last columns.



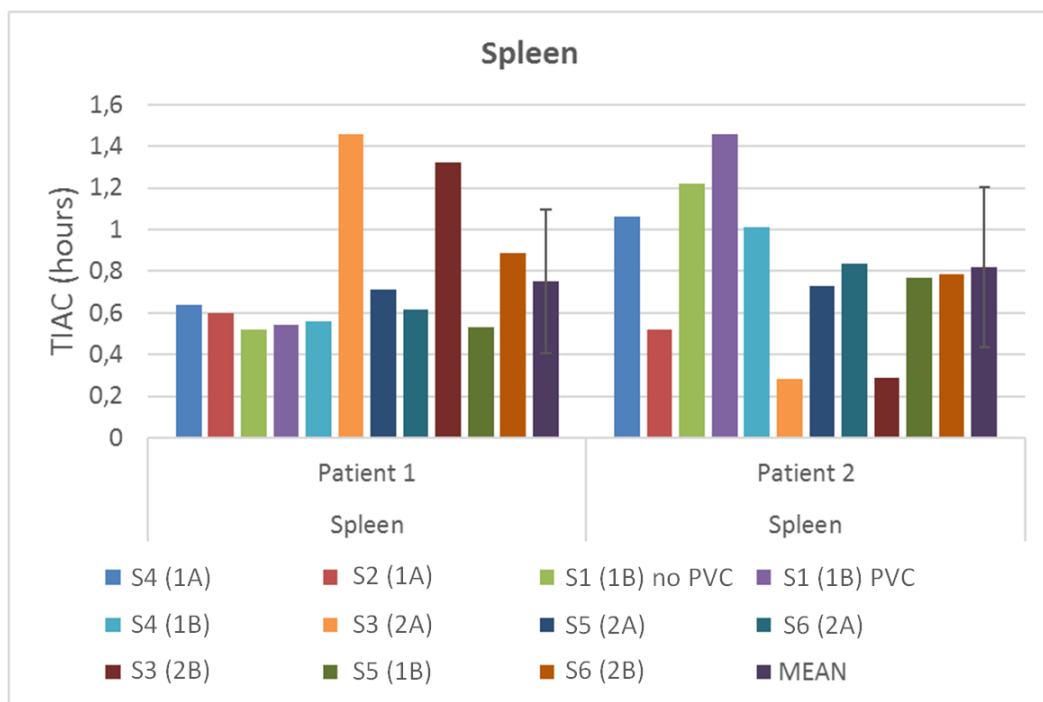


Figure 4.18: Results for each software of TIACs (h) for spleen in the 2 patients. In bracket the integration and registration: 1. Voxel-based TAC fitting. 2. Organ-based TAC fitting. A: Image registration provided by the site. B: Pre-registered images were used. The mean data and the standard deviations are shown in the last columns.



## Chapter 5

# Correlation of dose with organ toxicity in PRRT

As previously stated, the aim of any radiotherapy is to deliver a high dose of radiation to the tumour while keeping the absorbed dose to normal tissues within acceptable limits. In this setting, dosimetry plays a role of particular importance since absorbed dose is the main physical quantity able to estimate the effect of the treatment. In case of PRRT, treatment is generally well tolerated by patients even if adverse effects may occur. The more serious side effect in PRRT is the renal radio-toxicity. The radiopharmaceutical is eliminated by renal excretion, but renal retention of the radioactivity occurs. Haematological toxicity is another important side effect of PRRT. A transient decrease in platelet and leukocyte count is often observed, but patients usually recover between treatment fractions. In some patients more severe bone marrow depression has to be managed.

For that reason, it is very important to be able to predict the tolerance in critical organs at risk from the administered radioactivity. This relies on a well established understanding of the behaviour of radiation beams in organs and tissues. Furthermore, several results showed that absorbed dose alone may not predict response to treatment, and that radiobiological quantities should be utilised.

This work was carried out in collaboration with the Istituto Europeo di Oncologia (Milan, Italy).

## 5.1 Background

### 5.1.1 Radiobiology aspects

Radiobiology investigates the interactions between ionizing radiation and living systems, and the consequences of these interactions. Ionizing radiation deposits energy into a material as it passes through it. Although all molecules can be damaged by radiation, DNA molecules that carry genetic information are the most probable targets. Radiation may damage a part of the DNA molecule and can cause cell death or malign transformation. Dead cells are normally eliminated by the organism. However, if the number of cell deaths exceeds a certain limit, they will affect the proper functioning of the organism and can kill it.

The interaction of radiation with cells can be considered as either direct or indirect. In the first case, the radiation directly affects DNA molecules via the photoelectric effect and Compton interactions. In the case of indirect interaction, the radiation will ionise other atoms or molecules within a cell (i.e. water) leading to the formation of free radicals and the resulting molecular damage caused by their interactions with the chemical bonds along the DNA chain. Free radicals do not occur solely as a result of irradiation, but their formation occurs continuously in the cells. It has been estimated that between 10,000 and 150,000 oxidative interactions occur between DNA and free radicals per human cell per day, as a result of the normal metabolic processes.

#### **Linear Quadratic Model (LQM)**

In describing the response of cells to radiation, a number of different models have been proposed. Of these, the Linear Quadratic Model (LQM) developed by Douglas and Fowler in 1972, is the most widely established. This model assumes that the DNA can be damaged by a single interaction or two double strand breaks in the same DNA strand. While a single double strand break can usually be repaired by a cell, two double strand breaks can cause the cell to die. Lethal damage caused by single interactions, such as mutations of vital genes, are assumed to be linearly related to the dose  $D$  via  $\alpha D$ , whereas lethal damage caused by two double strand breaks show a quadratic relationship with dose

$\beta D^2$ . Thus, the basic equation describing the relation between the surviving fraction (SF) and the radiation dose D is expressed as:

$$SF = e^{-\alpha D - \beta D^2} \quad (5.1)$$

The  $\alpha$  and  $\beta$  coefficients are tissue specific. The term  $\alpha$  is called intrinsic cell radio-sensitivity and the term  $\beta$  cell repair capability. The  $\alpha/\beta$  ratio is the dose for which the number of acutely responding cell deaths is equal to the number of late-responding cell deaths (the dose for which the linear and quadratic components of cell death are equal). Figure 5.1 shows the linear and the quadratic components of a typical survival curve for an irradiated population cell.

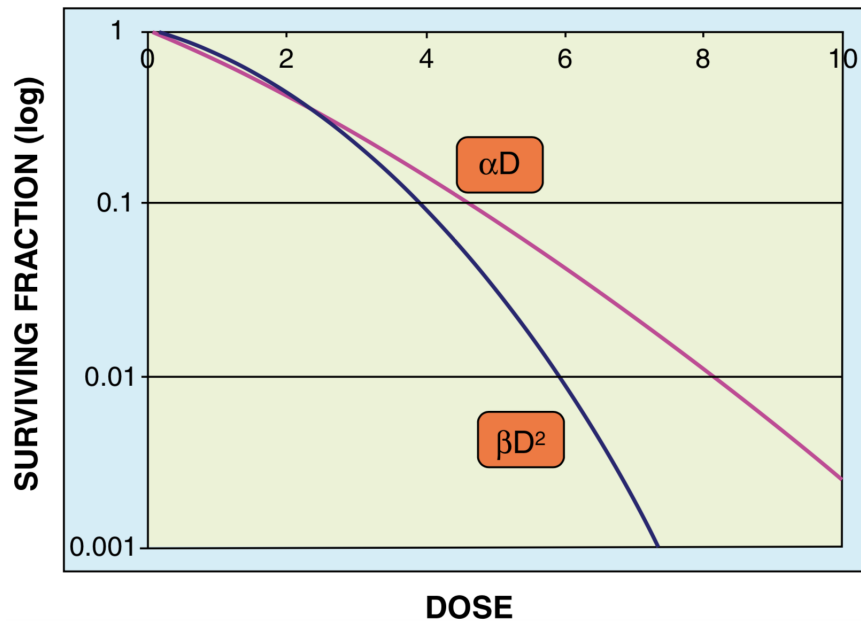


Figure 5.1: Linear and quadratic components of the survival fraction as a function of absorbed dose. Source: Basic Radiation Oncology, Springer-Verlag Berlin Heidelberg 2010.

Tissues with high  $\alpha/\beta$  ratio show a fast-acting response to the radiation, while tissues with low  $\alpha/\beta$  ratio have a longer time of repair leading to accumulate sub-lethal damages. The  $\alpha/\beta$  ratio is generally higher for tumours (typical range 5-25 Gy) than for late-responding normal tissues (typical range 2-5 Gy).

If the absorbed dose D is delivered over a time T equal or longer than the time

of repair  $T_{rep}$ , in Eq 5.1 an additional parameter associated with the quadratic component is introduced to include the repair of non lethal damages:

$$S = e^{-\alpha D - g(T) \cdot \beta D^2} \quad (5.2)$$

where  $g(T)$  is a function of the time that ranges between 0 and 1. When the duration  $T$  of the protracted dose  $D$  become significantly long compared with the repair half-time, then  $g(T)$  can be approximated by the expression:

$$g(T \gg T_{rep}) = \frac{\lambda_e}{\lambda_e + \mu} = \frac{T_{rep}}{T_{rep} + T_{eff}} \quad (5.3)$$

where  $\mu$  is the rate of repair of sublethal damage ( $\mu = \log(2)/T_{rep}$ ) and  $\lambda_e$  is the effective decay rate in the tissue ( $\lambda_e = \log(2)/T_{eff}$ ).

### Biological Effective Dose (BED)

The total absorbed dose alone is not enough to predict the response. For example dose-rate, fractionation scheme or tissue radiosensitivity will all play a part in determining the response to radiation. Thus, a number of further parameters, as the Biological Effective Dose (BED) [81] are introduced to quantify the impact of radiation of the tissue or tumour. The BED is defined by the following expression:

$$SF = e^{-\alpha BED} \quad (5.4)$$

BED represents the dose producing the same biological effect obtained under different irradiation condition, thus it allows to inter-compare different treatment types.

Using Eq. 5.2 BED can be expressed as:

$$BED = D \left( 1 + \frac{g(T)}{\alpha/\beta} D \right) \quad (5.5)$$

Hence, BED depends on the radiobiological parameters  $\alpha$  and  $\beta$  that are specific of the tissue and are related to the repair mechanisms, as it is shown in Figure 5.2.

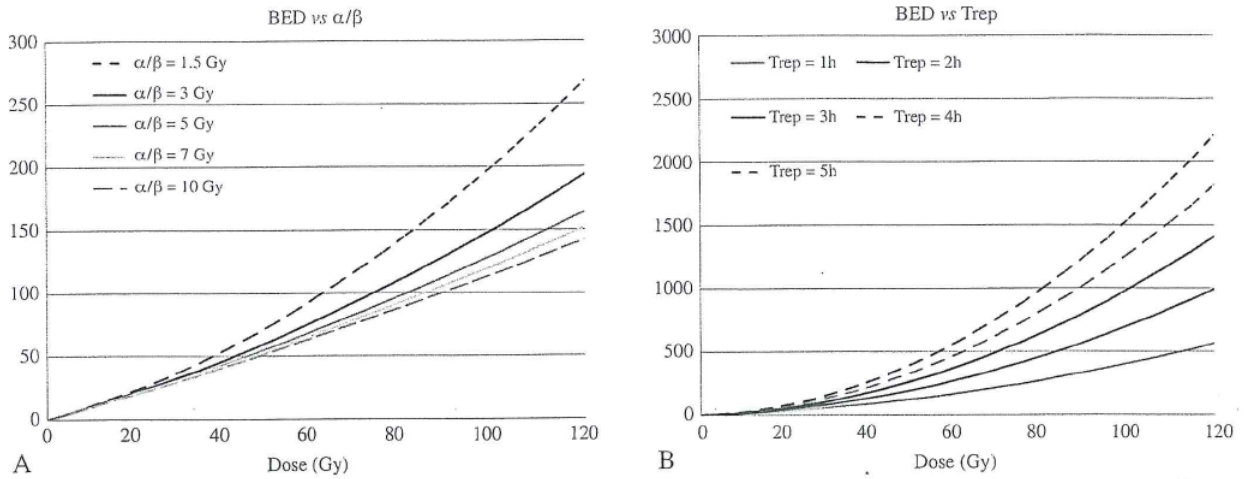


Figure 5.2: BED for different values of  $\alpha/\beta$  ratio (A) and  $T_{rep}$  (B).

Using Eq 5.3 and in the general case of multiple cycles, BED can be expressed as:

$$BED = \sum_i D_i + \frac{\beta}{\alpha} \cdot \frac{T_{rep}}{T_{rep} + T_{eff}} \cdot \sum_i D_i^2 \quad (5.6)$$

where  $D_i$  is the absorbed dose in the  $i$ -th cycle.

### 5.1.2 Evaluation of toxicity

As mentioned above, PRRT with  $^{90}\text{Y}$  and  $^{177}\text{Lu}$  provides acceptable renal and haematological toxicity in the majority of patients. However, cases of serious kidney injury have been reported, especially after treatment with  $^{90}\text{Y}$ .

Toxicities and adverse side effects are generally evaluated according to Common Terminology Criteria for Adverse Events (CTCAE) version 4.03.

**Kidneys** Radiation may damage nephrons, the basic structural and functional units of the kidney. Nephrons consist of glomeruli and tubuli, which are responsible for filtration and reabsorption, respectively. Renal uptake of radiopeptides in kidneys can be reduced using positively charged amino acids, such as L-lysine and/or L-arginine, which inhibit the proximal tubular reabsorption of the radiopeptide. Despite the co-administration of these amino acids leads to a significant reduction in the renal absorbed dose up to 40-60%, kidneys remain the principal organ at risk for PRRT, and their functionality

Table 5.1: CTCAE Common Terminology Criteria for Adverse Event versions 4.03 for acute and chronic renal disorders after PRRT.

Renal and urinary disorders					
Adverse Event	Grade				
	1	2	3	4	5
<b>Acute kidney injury</b>	Creatinine (Cr) level increase of > 0.3 mg/dL; Cr 1.5 - 2.0 × above baseline	Cr 2 - 3 × above baseline	Cr > 3 × baseline or > 4.0 mg/dL; hospitalization indicated	Life-threatening consequences; dialysis indicated	Death
Definition: a disorder characterized by the acute loss of renal function and is traditionally classified as pre-renal (low blood flow into kidney), renal (kidney damage) and post-renal causes (ureteral or bladder outflow obstruction).					
<b>Chronic kidney disease</b>	eGFR (estimated Glomerular Filtration Rate) or CrCl (creatinine clearance) < LLN-60 ml/min/1.73 m <sup>2</sup> or proteinuria 2 <sup>+</sup> present; urine protein/creatinine > 0.5	eGFR or CrCl 59-30 ml/min/1.73 m <sup>2</sup>	eGFR or CrCl 29-15 ml/min/1.73 m <sup>2</sup>	eGFR or CrCl < 15 ml/min/1.73 m <sup>2</sup> ; dialysis or renal transplant indicated	Death
Definition: a disease was defined based on the presence of kidney damage or glomerular filtration rate (GFR < 60 ml/min per 1.73 m <sup>2</sup> ) for 3 months, irrespective of cause, and was classified into five stages based on the level of GFR.					

need to be monitored during the treatment. Renal function is usually assessed by means of laboratory tests (creatinine) or calculation of creatinine clearance, which is the main parameter to estimate the glomerular filtration. Table 5.1 shows CTCAE 4.03 criteria.

In particular, the creatinine (Cr) is used to evaluate the acute toxicity, while the creatinine clearance (CrCl) the chronic toxicity. CrCl can be assessed according to the Cockcroft-Gault formula [86]:

$$CrCl(ml/min) = \frac{(140 - age(y)) \cdot weight(kg)}{72 \cdot sCr(mg/dL)} \cdot [0.85 \text{ if female}] \quad (5.7)$$

where sCr is the serum creatinine concentration in urine samples.

Several studies have published results about renal toxicity. Cremonesi et al. [87] reviewed the main results in the literature. Figure 5.3 summarizes the toxicity rates related to PRRT with <sup>90</sup>Y-DOTATOC, <sup>90</sup>Y-DOTATATE and <sup>177</sup>Lu-DOTATATE and the combination of <sup>90</sup>Y-DOTATOC and <sup>177</sup>Lu-DOTATATE. Yellow, orange and red bars indicate grades I-II, III, and IV-V, respectively. Serious kidney toxicity was observed mainly in patients treated with <sup>90</sup>Y alone



and  $^{90}\text{Y}+^{177}\text{Lu}$ , while severe nephrotoxicity was virtually absent after treatment with  $^{177}\text{Lu}$ -labelled peptides.

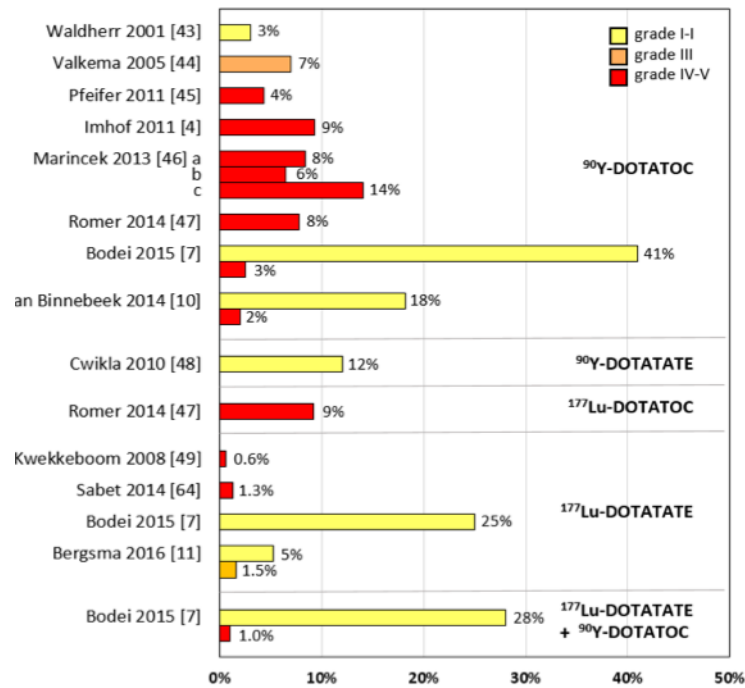


Figure 5.3: Renal toxicity rates reported in several studies of PRRT with  $^{90}\text{Y}$ -DOTATOC,  $^{90}\text{Y}$ -DOTATATE,  $^{177}\text{Lu}$ -DOTATATE and the combination of  $^{90}\text{Y}$ -DOTATOC and  $^{177}\text{Lu}$ -DOTATATE. Source: Cremonesi et al. Eur J Nucl Med Mol Imaging. 2018

**Red Marrow** Although kidneys are the main dose-limiting organ in PRRT, side effects on red marrow were reported and must to be taken into account. Red marrow toxicity results from damage to haematopoietic tissue. Different grades of toxicity can be evaluated monitoring the variation of hemoglobin, platelet and leukocyte according to CTCAE criteria in Table 5.2. Severe bone marrow toxicity, mostly reversible, is observed in less than 10–13% of treatment cycles with  $^{90}\text{Y}$ -DOTATOC and in 2–3% of cycles with  $^{177}\text{Lu}$ -DOTATATE [88]. However, relationship between red marrow toxicity and absorbed dose are difficult to be evaluated, because of doses are very low and differences in absorbed dose among individual radioresistance prevails over differences in irradiation effects. Red marrow dosimetry estimates are generally based on the blood activity measurements, assuming the same activity concen-

Table 5.2: CTCAE Common Terminology Criteria for Adverse Event versions 4.03 for bone marrow disorders after PRRT.

Blood and lymphatic system disorders					
Adverse Event	Grade				
	1	2	3	4	5
<b>Anemia</b>	Hemoglobin (Hgb) < LLN – 10.0 g/dL; < LLN – 6.2 mmol/L; < LLN - 100 g/L.	Hgb < 10.0-8.0 g/dL; < 6.2-4.9 mmol/L; < 100-80 g/L.	Hgb < 8.0 g/dL; < 4.9 mmol/L; < 80 g/L; transfusion indicated.	Life- threatening consequences; urgent intervention indicated.	Death
Definition: a disorder characterized by a reduction in the amount of hemoglobin in 100 ml of blood. Signs and symptoms of anemia may include pallor of the skin and mucous membranes, shortness of breath, palpitation of the heart, soft systolic murmurs, lethargy and fatigability.					
<b>Platelet count decreased</b>	< LLN – 75.000/ mm <sup>3</sup> ; < LLN – 75.0 × 10 <sup>9</sup> /L.	< 75.000 – 50.000/ mm <sup>3</sup> ; < 75.0 – 50.0 × 10 <sup>9</sup> /L.	< 50.000 – 25.000/ mm <sup>3</sup> ; < 50.0 – 25.0 × 10 <sup>9</sup> /L.	< 25.000/ mm <sup>3</sup> ; < 25.0 × 10 <sup>9</sup> /L.	
Definition: a finding based on a laboratory test results that indicate a decrease in number of platelets in a blood specimen.					
<b>Leukocytosis</b>	-	-	> 100.000/mm <sup>3</sup>	Clinical manifestation of leukocytosis; urgent intervention indicated.	Death
Definition: a disorder characterized by laboratory test results that an increased number of white blood cells in the blood.					

tration in blood and marrow.

The first study about this relationship was published by Ferrer et al. [89], who found association between activity concentrations in the blood and red marrow aspirates. Del Prete et al [90] reported a moderate association between the red marrow absorbed dose and the variation of platelet 4 weeks after the therapy. However, no correlation between red marrow absorbed dose and acute haematological toxicity has been reported so far.

### Normal Tissue Complication Probability (NTCP) model

The LQM allows to calculate the surviving fraction of a collection of cells and, using BED, to include information regarding the radiobiological response of the cells. In this pattern, it is very useful while treatment planning to estimate the probability of rising side effects in organ at risk. NTCP assigns a probability of a certain complication associated with a treatment plan derived from data and outcome of a large population.

One of the first NTCP model was proposed by Lyman in 1985 and extended by Kutcher and Burman in the 1980s and 1990s. The NTCP is a function of the total dose, fraction dose, fraction number and the volume of tissue exposed

to the radiation. The following expression was proposed in EBRT for uniform irradiation, with a total absorbed dose  $D$  delivered at 2 Gy/fraction:

$$NTCP(t) = \frac{1}{\sqrt{2\pi}} \cdot \int_{-\infty}^t e^{-\frac{s^2}{2}} ds \quad (5.8)$$

with

$$t = \frac{D - TD^{50,5(v)}}{m TD_{50,5(v)}} \quad (5.9)$$

and

$$TD^{50,5(v)} = TD^{50,5(1)} v^{-n} \quad (5.10)$$

where  $m$  is the steepness of the dose-effect curve,  $TD^{50,5(1)}$  is the dose value where 50% of the population exhibited renal complication within 5 years for a uniform whole-organ irradiation,  $n$  is the volume-effect parameter. In order to successfully use NTCP models in the clinic, the model parameters have to be determined by fitting the results obtained from a large patient population.

NTCP models have been largely used in EBRT and, in recent years, these models were also applied in PRRT. Despite a number of evaluations of the correlation between absorbed dose and response has been performed, there are no established dose limits for bone marrow and kidneys for PRRT, so such data has to be extrapolated from EBRT. However, data from EBRT cannot be directly applied to PRRT due to the intrinsic differences between external and internal radiotherapy: different dose rates and fractionation schemes, an inhomogeneous absorbed dose distribution and possibly different radiobiological mechanisms of cytotoxicity resulting in varying biological effects. For that reason, BED was used in lieu of the absorbed dose to extrapolate the dose limit established with EBRT for PRRT. The first study suggesting a dose-effect relationship for kidney in PRRT was performed in 2005 by Barone et al. [82]. This study suggested to use the BED in lieu of the absorbed dose to achieve a stronger dose-effect relationship. According to the literature data in EBRT, a dose in the range of 23-27 Gy causes toxicity effect in 5% of patients [91][92]. However, due to the intrinsic differences between EBRT and PRRT, the BED was used. Therefore, the limit value of BED were 40 Gy (which corresponds to 23 Gy of dose)[93] and 46 Gy (which corresponds to 27 Gy of dose)[94].

MIRD pamphlet No. 20 [83] showed the NTCP for kidney extrapolated from a sample of 20 patient undergone to  $^{90}\text{Y}$  PRRT. This curve was compared with the one derived for EBRT. The two curves for EBRT and  $^{90}\text{Y}$ -DOTATOC nearly coincided when BED was used, while they were shifted when dose was used.

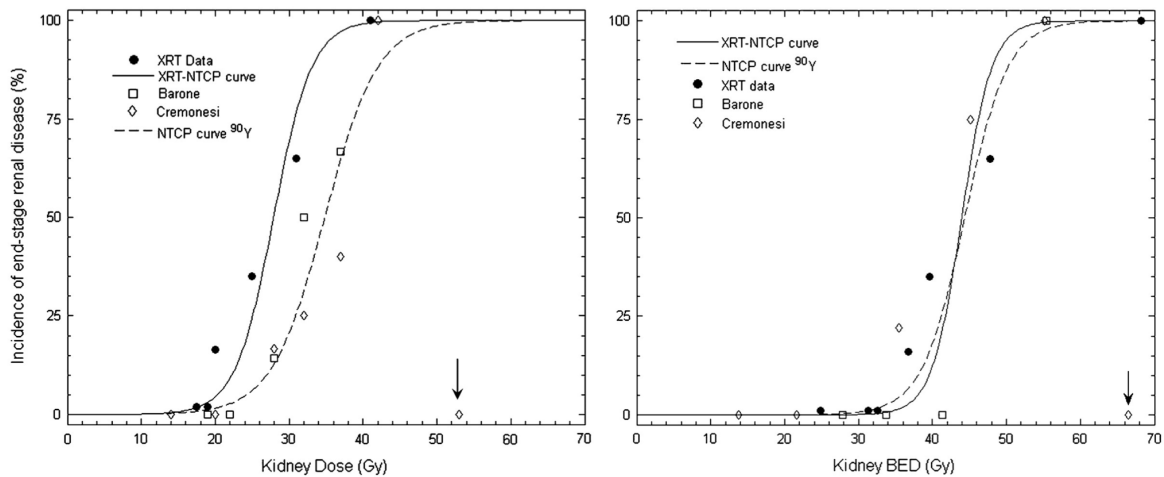


Figure 5.4: Dose–response curve for kidneys after ERBT and  $^{90}\text{Y}$  PRRT, as a function of the absorbed dose on the left and the BED on the right. Adapted from MIRD No. 20, J Nucl Med 2008.

## 5.2 Material and methods

### 5.2.1 Clinical trial

This study was conducted on a sample of 64 patients enrolled in the PRRT clinical trial described in Paragraph 1.7 (Trial A).

### 5.2.2 Image acquisition and dose calculation

Multi-modal images were acquired using the dual head Symbis T2 camera (Siemens Medical Solutions, Germany). For more details about the acquisition settings, see Paragraph 3.3. According to the trial design, absorbed doses for liver, spleen and kidneys were calculated using the organ level dosimetry software OLINDA/EXM 1.1. Red marrow absorbed dose calculation was based on the blood measurements. In particular, blood samples were drawn at 0.16,

0.67, 2, 4, 8, 20 and 40 h after the administration at the first cycle. Activity in the blood samples were measured using a HPGe detector (Camberra Industries, USA). The mean absorbed dose to the red marrow was calculated based on the blood model, therefore assuming equal activity concentration in marrow and in the blood, as discussed above (Paragraph 5.1.2) and according to the formula:

$$TIAC_{RM} = \frac{m_{RM}}{m_{blood}} \cdot TIAC_{blood} \quad (5.11)$$

### 5.2.3 Assessment of toxicity

In order to evaluate the functionality of organs at risk (kidneys and red marrow) patient blood samples were analysed every two weeks during PRRT and every month up to at least 6 months after the last injection. The grade of possible side effects were estimated based on the CTCAE 4.03 criteria reported in Paragraph 5.1.2.

### 5.2.4 Data analysis and statistics

Mean and median values, standard deviation and range were used to visualize distribution of data. The t-test was used to statistically compare different groups of patients. Box-plots were used to visualize data distributions. The statistical analysis was performed in Matlab.

## 5.3 Results

In the majority of patients, 2 cycles of  $^{90}\text{Y}$ -DOTATOC and 3 cycles of  $^{177}\text{Lu}$ -DOTATOC were used. Table 5.3 shows the mean value, standard deviation, median and range of administered activities and number of cycles.

Table 5.3: Treatment administered activities and number of cycles.

	Isotope	Mean $\pm$ SD	Median	Range
Administered activity	$^{177}\text{Lu}$	$7.1 \pm 7.8$	5.6	0 - 33.5
	$^{90}\text{Y}$	$2.9 \pm 3.9$	1.7	0 - 16.6
No. of cycles	$^{177}\text{Lu}$	$2.8 \pm 1.3$	3	1 - 7
	$^{90}\text{Y}$	$2.6 \pm 1.2$	2	1 - 5

Average patient age was  $61 \pm 12$  y, with median = 62 y and range = 26-84 y.

Table 5.4: Patients characteristics concerning the kidneys risk factors.

Characteristics	no. of pts
Gender	
Male	31 (48%)
Female	33 (52%)
No Risk Factors	37 (58%)
Risk Factors	23 (36%)
Hypertension	23 (36%)
Diabetes	2 (3%)
Previous chemotherapies	10 (16%)
LLC	1 (2%)
Previous radiotherapies	1 (2%)
Hyperglycemia	1 (2%)
Age > 80 y	1 (2%)

The cohort of patient were labelled and differentiated between patient with No Risk Factors (No-RF) and Patient with Risk Factors (RF).

Table 5.4 summarizes patients characteristics concerning renal risk factors. In particular, 37 patients were in the group of No-RF, 23 patients in the group of RF, 2 patients were excluded because of the lack of follow-up and 2 patients were excluded because of outlier in the relation dose-toxicity. Different administrations were planned depending on the presence risk factor: the renal BED

limit was 46 Gy for patients with No-RF, and 28 Gy for patients with RF.

### 5.3.1 Evaluation of toxicity

Evaluation of toxicity was performed as described in 5.1.2. As an example, a representative case for each biological parameter was reported.

Based on Hgb, Case A (Figure 5.5) showed no red marrow toxicity up to the third cycle. From the third cycle onward, Hgb decreased leading to a grade 1 toxicity. Hgb continued to decrease after the end of the therapy, involving toxicity of grade 2.

Blood samples in Case B (Figure 5.6) showed a progressive decrease in the number of platelets. However, PLTs levels stay within the normal values ( $150-400 \cdot 10^3/\text{mm}^3$ ) up to the last cycle. After the end of the therapy, the PLTs level fell below the limit of ordinary values in two measurements. The number

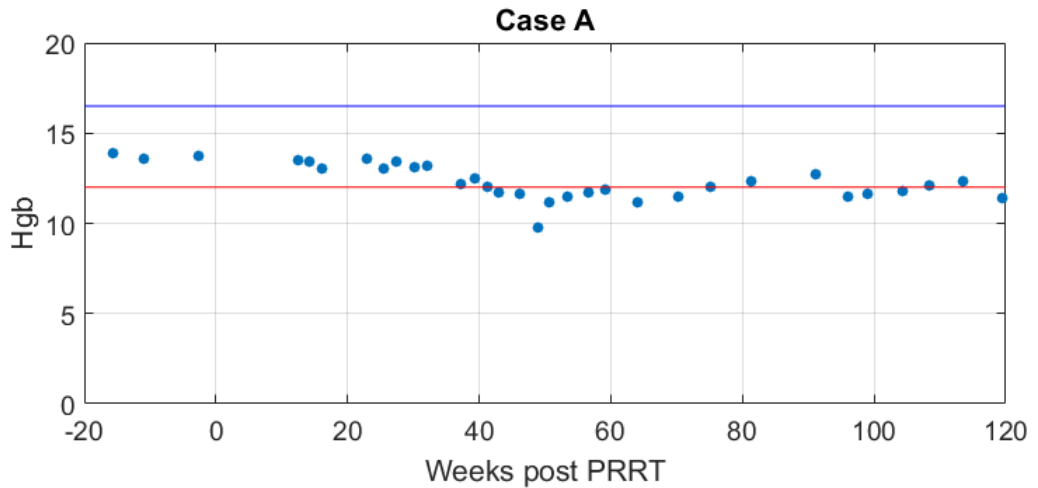


Figure 5.5: Hemoglobin level as a function of time after injection in a representative patient (Case A). The red and blue lines are the minimum and maximum interval of ordinary values (i.e. no toxicity).

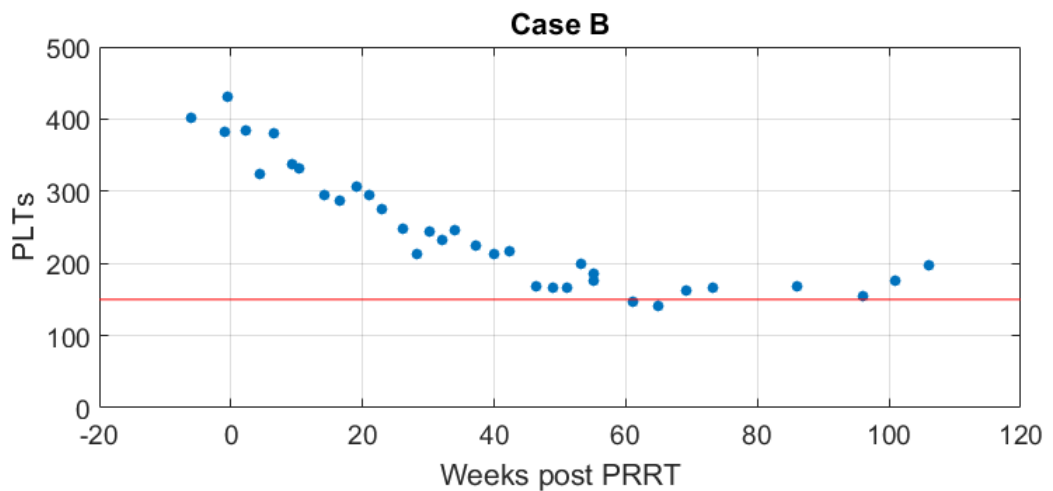


Figure 5.6: Platelets level as a function of time after injection in a representative patient (Case B). The red line is the minimum level of ordinary values (i.e. no toxicity).

of PLTs slowly increased later on. The overall PLTs toxicity assigned was grade 1.

Renal toxicity was evaluated monitoring creatinine (Cr) and creatinine clearance (ClCr) levels, according to Table 5.1. Cr measures the acute toxicity, while CrCL the chronic toxicity. As an example, evaluations of Cr for Case C is shown in Figure 5.7. During the entire time of evaluation, the Cr

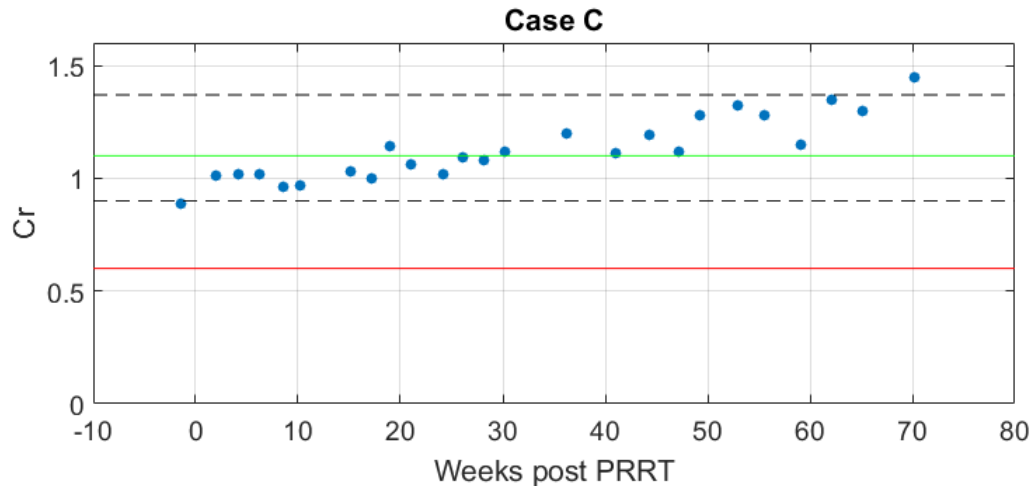


Figure 5.7: Creatinine level as a function of time after injection in a representative patient (Case C). The red and green lines are the minimum and maximum interval of ordinary values (i.e. no toxicity). Dotted lines indicate the interval corresponding to toxicity effect with grade 1.

level progressively increased. After the third cycle, an acute kidney toxicity of grade 1 was observed (Cr level is between 1.2 and 1.45 mg/dL). Cr exceeded the latter value after the 60<sup>th</sup> week, leading to a grade 2 acute toxicity.

### 5.3.2 Correlation between dose and red marrow toxicity

In this paragraph the relation between absorbed dose and red marrow toxicity is shown. As discussed above, red marrow toxicity was evaluated according to either PLTs or Hgbs. The ratios between each value of PLT (as well as Hgb) and the baseline value were calculated. Figure 5.8 shows the relation between PTLs toxicity and red marrow absorbed dose, while Figure 5.9 shows the relation between PTLs toxicity and red marrow absorbed dose.

### 5.3.3 Correlation between dose and renal toxicity

Figure 5.10 shows relation between renal BED and creatinine variation. An increase of the creatinine value is indicative of renal impairment, since the Cr is a substance to be eliminated by kidney. Therefore, a creatinine increase is indicative of renal toxicity. However, association between BED and creatinine variation was not statistically significance (p-value = 0.815).



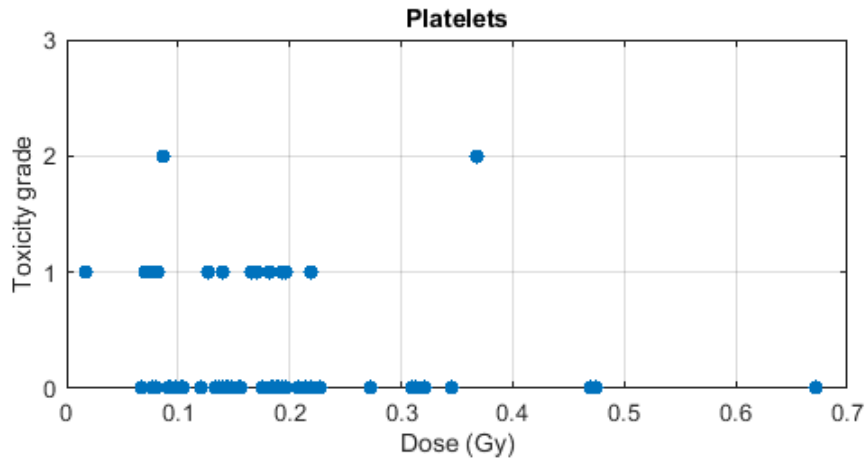


Figure 5.8: PLTs toxicity grade as a function of red marrow absorbed dose.

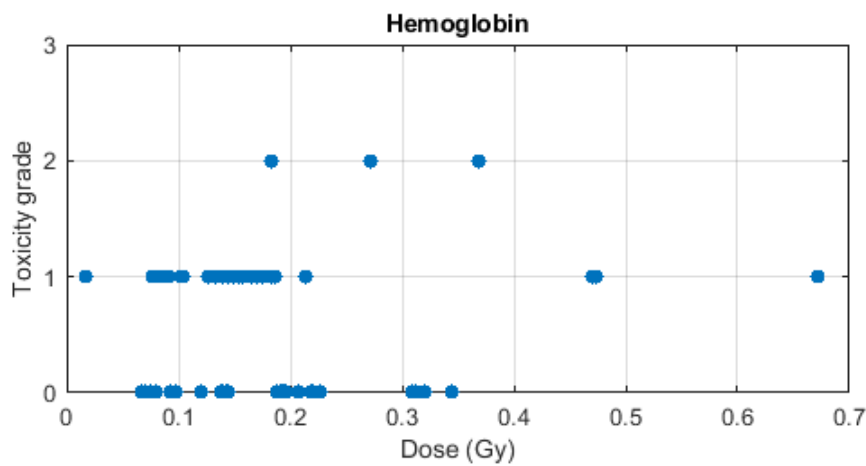


Figure 5.9: Hgb toxicity grade as a function of red marrow absorbed dose.

A decrease of the CrCl is indicative of renal impairment, since the CrCl evaluates the renal filtration capacity. Therefore, a CrCl decrease is indicative of renal toxicity. Creatinine clearance loss (CCL) was monitored as a function of time. Different CCL curves were observed for patients with risk factors and patients with no risk factors, as shown in Figure 5.11.

CCL was approximately the same 6 months after the therapy for patients with RF and patients with No-RF. However, CCL is progressively higher for patient with RF and after 24 months of follow-up there is a consistent increase of CCL for patient with RF, while there is a recovery of CrCl for patients with No-RF.

Figure 5.12 shows the frequency of chronic renal toxicity in the sample of patients.

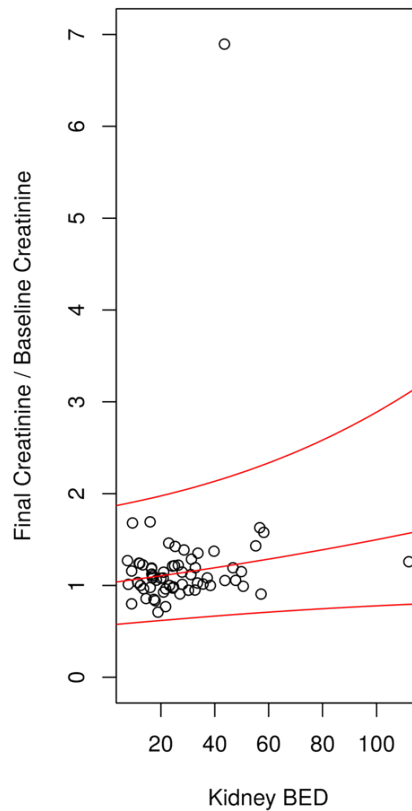


Figure 5.10: Final/basal Cr ratio as a function of renal BED.

Figure 5.13 shows the probability of developing chronic renal toxicity with grade 0 (No toxicity), 1 or  $\geq 2$  during the whole treatment as a function of absorbed dose. Two different analysis were performed for patients with RF and patients with No-RF. There is not a significantly distinct trend between the two groups of patients.

Probability of chronic renal radio-toxicity was calculated for each class of patients (RF and No-RF). However, no statistically differences were observed. Probably, the limited number of patients, in particular at high absorbed doses, and the presence of few cases without toxicity despite the high absorbed dose and the presence of risk factors could influence the absence of such distinction. For that reason, NTCP was derived including all patients. NTCP curve is shown in Figure 5.14.

Box-plots in Figure 5.15 show distribution of dose and BED between patients who developed toxicity and patient who did not. Differences between median values were statistically compared with a t-test. The test resulted

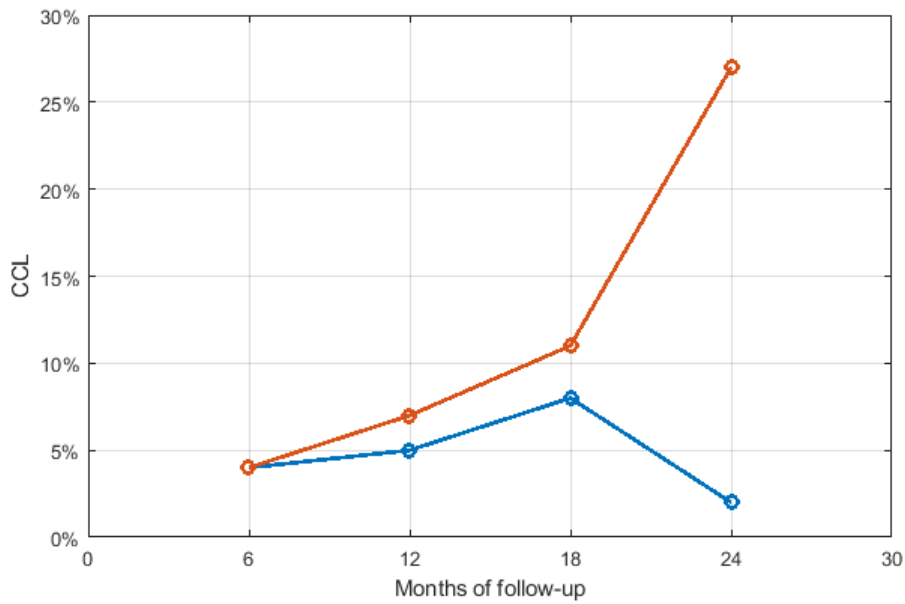


Figure 5.11: CrCl loss (CCL) as a function of months after the end of the treatment. Patients with RF (red line) and patients with No-RF (blue line) were separately considered.

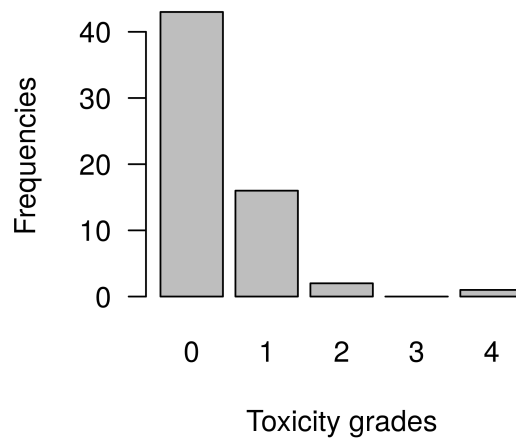


Figure 5.12: Frequencies of chronic renal toxicity grades.

statistically significant for each case analysed (all patients, RF, No-RF). This result indicates that the mean absorbed doses and BED of the patients who developed toxicity were always significantly higher than the absorbed doses of the patients who did not develop toxicity.

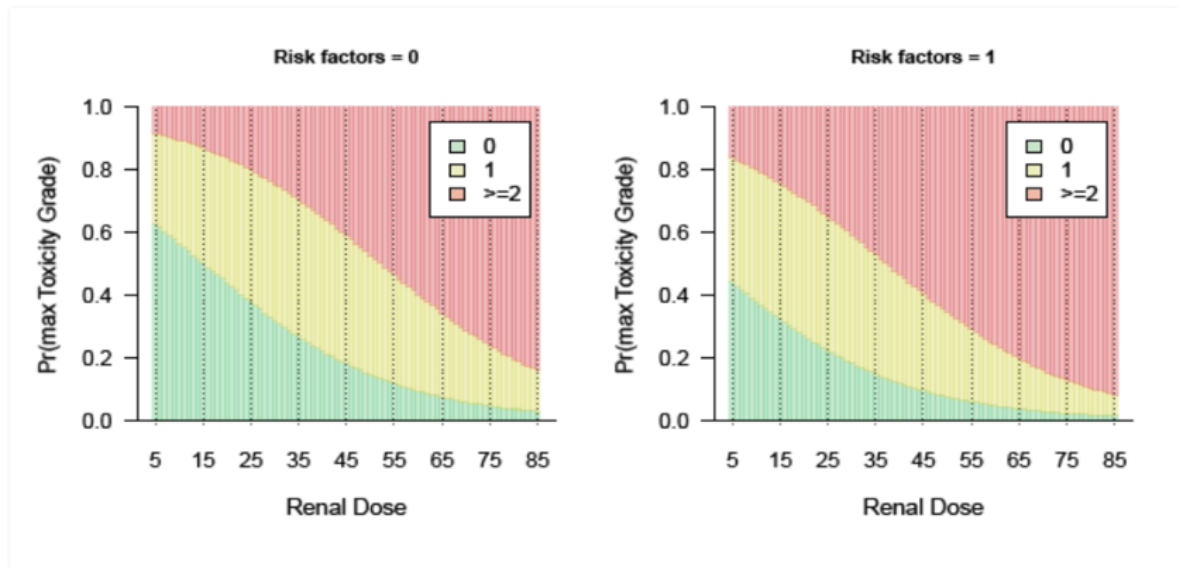


Figure 5.13: Probability of developing chronic renal toxicity during the treatment as a function of renal absorbed dose. No-RF on the left and RF on the right. The green area indicates the grade 0 of toxicity, yellow area grade 1 and red area grade 2 or higher.

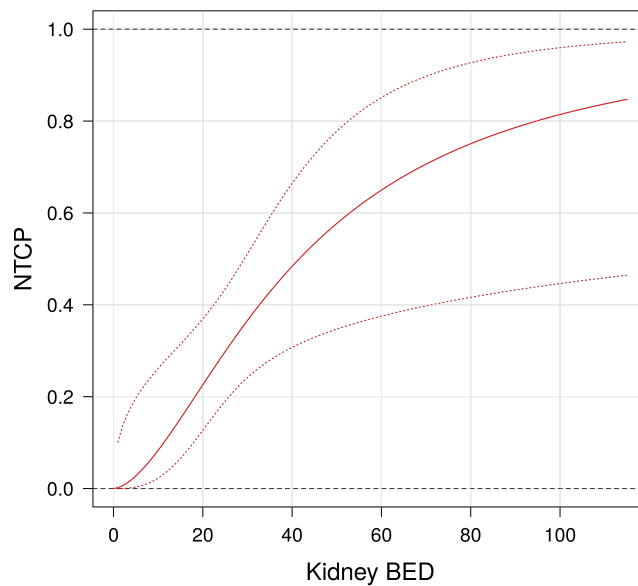


Figure 5.14: Normal Tissue Complication Probability as a function of renal BED. Dotted lines indicate the confidence intervals.

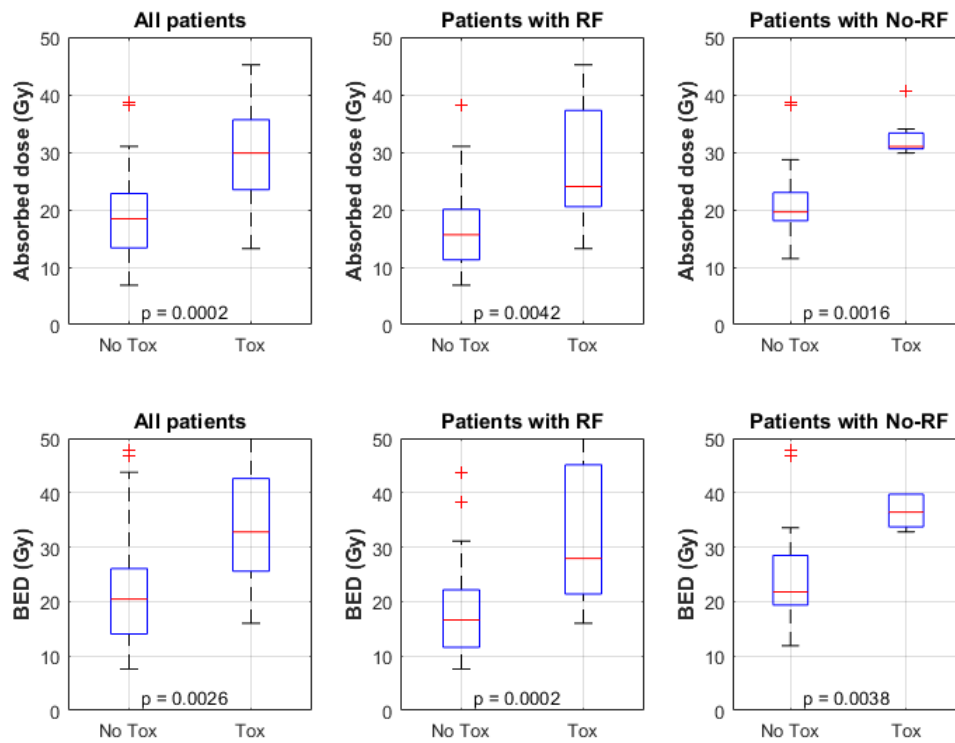


Figure 5.15: Distribution of absorbed dose and BED in patients who developed toxicity and patients who did not. Patients with RF, all patients and patient with No-RF were separately considered. A t-test was used to compare the median values of the distribution (p-values below the box-plots).

## 5.4 Discussion

Data in this retrospective study indicate that PRRT with  $^{90}\text{Y}$  and  $^{177}\text{Lu}$ -peptides is safe and promising approach for the treatment of patients affected by NETs. The results obtained reveals that this therapy can be safely applied because no serious adverse effects were observed among the 64 patients analysed. However, due to their radio-sensitivity, kidneys remain the main critical organs in PRRT and their functionality need to be monitored. Assessment of risk factors is essential in evaluating renal toxicity, as kidney side effects may be more probable in patients in whom these factors coexist. Correlation between kidney toxicity and absorbed dose was investigated, with the aim of determine a relation that allows to predict possible side effects for different treatment schemes. In this framework, the LQ model was considered to evaluate the

effect of the treatment schema.

Concerning red marrow, no correlation between hematological toxicity and absorbed dose was found. Both platelets and hemoglobin were used for evaluation of red marrow toxicity. The lack of correlation might be due to the inappropriateness of the blood model for calculation of red marrow absorbed dose. Bone marrow dosimetry is difficult and find the best dose calculation method is still an open problem. Another explanation for the lack of correlation might be that bone marrow doses are very low and difference in dose among individuals prevails over difference in irradiation effects.

As regards renal toxicity, correlations with absorbed dose were found. Patients with RF had wider reductions of creatinine clearance than did patient with No-RF, especially 24 months after the end of the therapy. Patient with No-RF instead showed a tendency towards recovery after 18 months. However, the probability of showing side effects did not result higher for patient who had RF than others. The limited number of patients, in particular at high absorbed doses, and the presence of few cases without toxicity and presence of risk factors might have been influenced the results.

The NTCP curve for kidney was successfully extrapolated to analytically associate renal toxicity and absorbed dose. Since no significant distinction were observed between patients with RF and patients without them, NTCP including the whole sample of patients was used to obtain an higher statistical significance.

The results of this study have shown that calculation of absorbed dose in PRRT can be used to predict the probability of side effects induced by the therapy.

## Chapter 6

# Tumour Control Probability

Assessment of response is an important target that, together with with assessment of toxicity, can be decisive in the success of the therapy. Prediction of treatment efficacy before therapy allows to identify patients with high probability of response and to reject the ones who would be most likely non-responders. Evaluation of response over time during the therapy can lead to the optimization of the initial plan, by intensification of treatment in those patients who are responding and eventual interruption or modification in those patients with clear disease progression. Evaluation of response at the end of the treatment might allow to outline the best strategy to apply after therapy. Thus, TCP (Tumour Control Probability) curves, along with NTCP models, are the key elements to improve efficacy of therapy.

The evaluation of response to PRRT is an important clinical problem, especially for the lack of reliable markers that can predict and evaluate therapeutic response. Conventionally, tumour response is evaluated by means of morphological criteria, by measuring the tumour diameter. However, studies showed that despite a clear improvement in symptoms for most patients treated with PRRT, only a small percentage showed a significant decline in tumor size as measured by CT [95][96]. Furthermore, improved quality of life after PRRT was not clearly associated with a visible morphologic response to therapy [97]. Internal radiation therapy with high-energy  $\beta$ -emitters induces damage to tumour cells during a relatively long period of time. Consequently, some degree of necrosis will continuously accumulate, and on subsequent examination the presence of necrotic and fibrotic tissue may cause the size of lesions to ap-

pear unchanged. For these reasons, imaging methods of superior sensitivity for monitoring the response to treatment among NET patients are necessary. PET with  $^{18}\text{F}$ -FDG has become established as an indispensable tool for diagnostics and therapy-monitoring of various tumour types [98]-[100]. However, NETs showed low metabolic activity with  $^{18}\text{F}$ -FDG, and treatment response is difficult to assess [101]. Most NETs typically express high levels of somatostatin receptors, therefore making the somatostatin receptor imaging a useful tool for the diagnosis and staging of the disease in these patients. Some studies have confirmed a possible role of SSTR (somatostatine receptor) based functional imaging, such as the  $^{68}\text{Ga}$ -SST PET/CT, for imaging and quantitative assessment of response, but to date this method is not used except in the experimental clinical protocols [102][103].

TCP prediction models have conventionally focused on using “dosimetric” predictors alone. The term “predictor” indicates a measurable datum that can be used to predict an outcome. Thus, dosimetric predictors are those variables that relate specifically to the delivery of radiation. “Non-dosimetric” or “clinical” predictors include all other variables, such as age, sex or histology. As radiation treatment outcomes are determined by complex interactions among treatment, anatomical, and patient-related variables [104], recent approaches have utilized increasingly data-driven models incorporating Machine Learning tools in which both dose and other patients- or disease-based prognostic factors are included to improve outcomes prediction. Many researchers [105]-[110] have investigated the application of Machine Learning in radiotherapy treatment response and outcome predictions, however studies about PRRT are still missing.

In this Chapter the relation between  $^{68}\text{Ga}$ -DOTATATE PET/CT and absorbed dose was evaluated with the aim to assess feasibility of using  $^{68}\text{Ga}$ -SST PET/CT for monitoring and evaluation of treatment response. A statistical approach based on Machine Learning was chosen to examine feasibility of predicting response by means of dosimetric and clinical variables.



## 6.1 Background

Despite some evidences [95]-[97] indicate tumour size is not the optimal parameter for response evaluation in NETs, to date radiologic imaging techniques are the best established criteria for tumour response evaluation in imaging studies. For solid tumours, assessment of therapy response is based on the Response Evaluation Criteria in Solid Tumours (RECIST). RECIST 1.0 criteria were initially published in 2000 and updated in 2009 (RECIST version 1.1) [111].

Pauwels et al. [112] presented the first correlation between absorbed dose and tumour reduction in a study of 13 patients affected by gastroenteropancreatic NET and treated with  $^{90}\text{Y}$ -DOTATOC PRRT. Relationship ( $R^2=0.496$ ) between tumour volume reduction assessed by CT and absorbed dose was reported.

One of the most relevant and cited study was published by Ilan et al. [113] in 2015. This group reported correlation between absorbed dose and tumour reduction for patients treated with  $^{177}\text{Lu}$ -DOTATATE. Tumour diameters were evaluated according to RECIST. Patients were monitored at intervals of 6 months after the end of the therapy until disease progression/recurrence. Figure 6.1 shows the relation between the absorbed dose until best response and tumour response, for tumour larger than 2.2 and 4.0 cm in diameter, respectively.

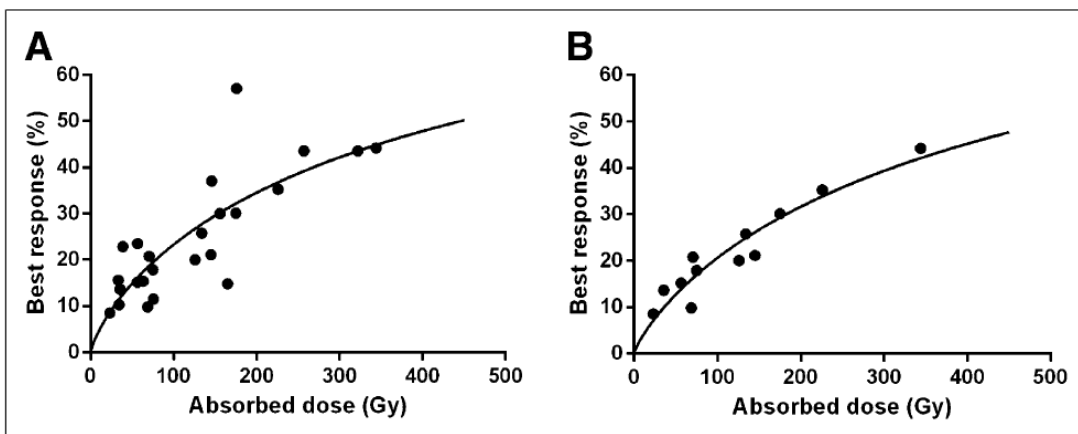


Figure 6.1: Tumour response in relation to tumour absorbed dose (A) for lesions with a diameter larger than 2.2 cm and (B) for lesions with a diameter larger than 4.0 cm. Source: Ilan et al. 2015.

In contrast with these results, Del Prete et al. [90] found no correlation between the relative lesion size variation and the cumulative lesion absorbed dose in 36 measurable NET lesions in 15 patients. However, in 12 assessable patients, a strong inverse correlation was found between the biochemical response (relative chromogranin A variation) at 3 months and the cumulative maximum tumour absorbed dose (Figure 6.2).

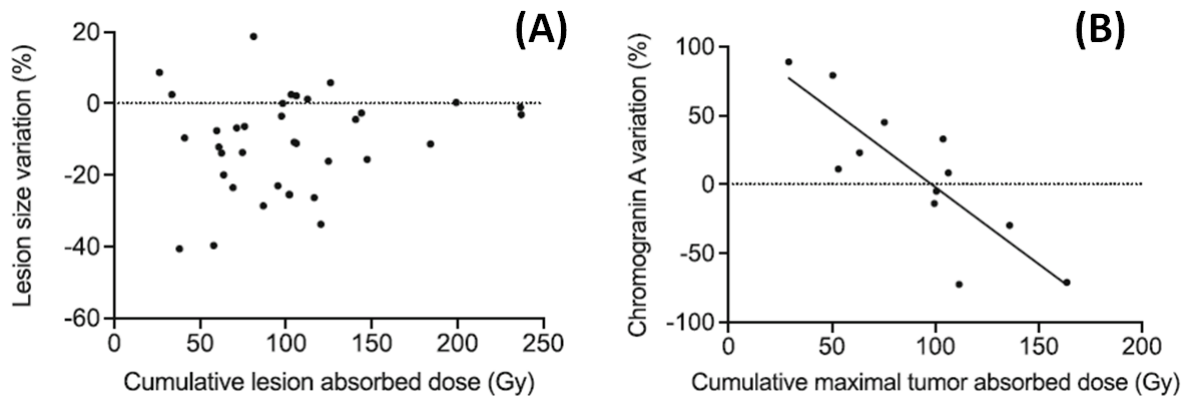


Figure 6.2: Relationship between (A) cumulative lesion absorbed dose and radiological response (i.e. relative lesion size variation) and (B) cumulative maximum tumour absorbed dose and relative chromogranin A variation on the right. Source: Del Prete et al. 2017.

RECIST 1.1 has also been validated for NET patients within the NETTER-1 trial [25].

Several studies investigate the feasibility of  $^{68}\text{Ga}$  PET/CT to predict the treatment response [103][114]-[116], however, only a few studies examine relation between absorbed dose and treatment response. Gabriel et al. [117] reported no clear correlation between change in SUV and outcome parameters, but they also affirmed  $^{68}\text{Ga}$ -PET to be useful as early predictor of progressive disease by detecting new metastases. Gâlne et al. [118] found significant changes in tumour SUVmax for lesions characterized as in progression, stable disease or in regression. Hence they depicted SUVmax as a valid marker for monitoring the disease status.

## 6.2 Material and methods

### 6.2.1 Patients and therapy

This study was conducted on a sample of 45 patients enrolled in the PRRT clinical trial described in Paragraph 1.7 (Trial B). A total of 129 tumours were considered. Only lesions with a volume larger than 2 mL were included. Table 6.1 shows the number of cycles and the administered activities of  $^{177}\text{Lu}$ - and  $^{90}\text{Y}$ -DOTATATE for the patient cohort.

Table 6.1: Administered activities and number of cycles of  $^{177}\text{Lu}$ - and  $^{90}\text{Y}$ -DOTATATE for the patient cohort.

	n cycles $^{177}\text{Lu}$	n cycles $^{90}\text{Y}$	Admin. Activity $^{177}\text{Lu}$ (MBq)	Admin. Activity $^{90}\text{Y}$ (MBq)
<b>Mean</b>	4.07	1.75	18.24	2.85
<b>25<sup>th</sup> perc</b>	4	1	14.93	1.85
<b>75<sup>th</sup> perc</b>	5	2	20.20	3.69

### 6.2.2 Image acquisition and Dosimetry

SPECT/CT acquisitions of abdomen, and also of thorax if necessary, were performed as described in Paragraph 3.3.

Lesions were manually segmented on the fused SPECT/CT image acquired 24h p.i. by a nuclear medicine physician in the Velocity Workstation. Then contours were duplicated and manually translated to match them with the lesion volume on the other SPECT/CT images.

Fitting of the time-activity curves was performed using MATLAB Curve Fitting Toolbox, TIACs were calculated analytically and absorbed doses were calculated using the OLINDA1.1 sphere model. Activities were corrected for PVE using the RCs derived from phantom measurements, as described in Paragraph 2.2.

### 6.2.3 Evaluation of response

Each patient underwent  $^{68}\text{Ga}$ -DOTATATE PET scans before and at the end of the therapy, according to the study protocol (Paragraph 1.7). Whole-body

Table 6.2: PERCIST-derived criteria adopted to evaluate therapy response for each tumour by  $^{68}\text{Ga}$ -DOTATATE PET/CT images.

Response	MTV	Other markers
Complete Response (CR)	Disappearance of the lesion	Disappearance of the lesion
Partial Response (PR)	$\Delta\text{MTV} \leq -48.8\%$	$\Delta\text{Marker} \leq -30\%$
Stable Disease (SD)	$-48.8\% < \Delta\text{MTV} < +119.7\%$	$-30\% < \Delta\text{Marker} < +30\%$
Progressive Disease (PD)	$\Delta\text{MTV} \geq +119.7\%$	$\Delta\text{Marker} \geq +30\%$

$^{68}\text{Ga}$ -DOTATATE PET/CT were acquired within 2 months preceding initial therapy for baseline evaluation. After 3 months after the last therapy cycle, each patient underwent follow-up with whole-body  $^{68}\text{Ga}$ -DOTATATE.

For each patient, a maximum of 5 lesions with the largest SUVmax and volume larger than 2 mL at the PET/CT exam at baseline were selected. The same lesions were evaluated at follow-up for assessment of response. Irregular isocontour regions of interest were drawn over the target lesion at 40% [120] of maximum pixel value within the tumour.

For each tumour, four markers were monitored at baseline and follow-up: MTV (Metabolic Tumour Volume) - i.e. volume of the isocontour region, SUVmax - i.e. maximum value of SUV in the isocontour region, SUVmean - i.e. average value of SUV in the isocontour region and TLSR (Total Lesion Somatostatine Receptor) - i.e. product between MTV and SUVmean.

Percentage variations of these markers between basal and follow up values were calculated. The  $^{68}\text{Ga}$ -DOTATATE PET/CT findings were categorized as Complete Response, Partial Response, Stable Disease or Progressive Disease based on the criteria in Table 6.2. Criteria for assessment using MTV were derived from RECIST1.1. Criteria for assessment using the other markers were derived from PERCIST 1.0 [119]. RECIST 1.1 and PERCIST 1.0 describe in detail the methods for assessment of the overall patient response to therapy with CT and  $^{18}\text{F}$ -FDG PET, respectively. In this study, however, the variations of the markers reported in Table 6.2 were used to categorize the response for each lesion individually.

Finally, therapy outcome for each lesion was dichotomized as ‘‘Response’’ in case of CR, PR or SD and ‘‘Non-Response’’ in case of PD.

Table 6.3: Indicators used for Machine Learning classifiers.

Indicator	Range
Grade	G1, G2, G3
Primary site	Gastric, Lungs, Pancreatic, Paraganglioma, Rectal, Renal, Small intestinal
Number of $^{90}\text{Y}$ cycles	1 - 3
Number of $^{177}\text{Lu}$ cycles	1 - 5
Cumulative $^{90}\text{Y}$ injected activity	0 - 8.1 GBq
Cumulative $^{177}\text{Lu}$ injected activity	10.9 - 31.5 GBq
Site	Bone, Liver, Lung, Lymph node, Pancreas
Volume in SPECT/CT outline	1.5 - 274.8 mL
Cumulative absorbed dose	5.3 - 810.4 Gy
Basal SUVmax	5.5 - 190

#### 6.2.4 Machine Learning analysis

Machine learning algorithms were used to build model of tumour response prediction. The model combines 10 indicators (including both therapeutic and biological markers) and classifies the tumour as responder or non-responder. Table 6.3 shows all the indicators included in the model.

Sixteen supervised classifiers were included in the analysis. Each classifier learned on a pre-labelled dataset of 129 tumours. Response was based on the SUVmax variation, since SUVmax had shown the highest association between marker variation and absorbed dose, compared to the other markers. The prediction models were evaluated through a 5-fold cross-validation [121]. The original sample was randomly partitioned into 5 equal sized subsamples, a single subsample was retained as the validation data for testing the model, and the remaining 4 subsamples were used as training data. The cross-validation process was repeated 5 times, with each of the 5 subsamples used exactly once as the validation data. The 5 results were averaged to produce a single estimation. Performance of classification, for each classifier, were assessed in terms of Accuracy, AUC (Area Under the Curve) of ROC (Receiver Operating Characteristics) curve, Sensitivity (or True Positive Rate), Specificity (or True Negative Rate) and BAR (Balanced Accuracy Rate). Accuracy and AUC are commonly the most established methods for assessment of predictor perfor-

mance. However, these parameters may not provide a reliable indicator when classifiers are trained using imbalanced dataset. A dataset is called unbalanced if it contains many more samples from one class than from the rest of the classes or, in other words, one class is presented by only a small number of training examples while other classes represent the majority. Hence, sensitivity and specificity were preferred as a performance measure because the interest is in classifying correctly both labels (Response and Non-response). BAR, defined as the average between sensitivity and specificity, was used to synthetically assess the performances. See Appendix A for more details about the methods for testing classifiers.

### 6.2.5 Data analysis and statistics

Data were log-transformed before analysis. LRT test was used to evaluate association between variables (absorbed dose per unit of injected activity and marker value at baseline or cumulative absorbed dose and marker percentage variation). The difference in absorbed dose between responder and non-responder lesions was tested with the Wilcoxon Rank Sum Test. LRT and Wilcoxon test results were described as significant at  $p < 0.05$ .

Absorbed doses were divided into 5 intervals with the same length (log scale), and probability of response in each interval was estimated. TCP curves from data were derived.

LRT and TCP curves were derived using the SAS software. All Machine Learning analyses and the Wilcoxon Rank Sum Test were performed using Matlab v2019a.

## 6.3 Results

### Patient characteristics and tumour dosimetry

Table 6.4: Patients characteristics.

<b>Number of patients</b>	<b>45</b>
<b>Gender</b>	
Male (%)	21 (47%)
Female (%)	24 (53%)
<b>Age (y)</b>	
median (range)	61.5 (36-79)
<b>Primary Tumour</b>	
Small intestinal (%)	15 (33.3%)
Pancreatic (%)	13 (28.9%)
Lungs (%)	6 (13.3%)
Paraganglioma (%)	2 (4.4%)
Rectal (%)	2 (4.4%)
Gastric (%)	1 (2.2%)
Renal (%)	1 (2.2%)
Unknown (%)	5 (11.1%)

Forty-five patients (21 male, 24 female; median age 61.5 years, range 36-79 years) were treated with PRRT. Detailed information about patient characteristics is given in Table 6.4. Most of primary tumours were located in small intestine or pancreas, while other ones were located in lungs, rectus, stomach. Five patients had cancer of unknown primary and two patients paraganglioma.

Figure 6.3 shows the distribution of MTV and cumulative absorbed dose for all

the lesions. The median value (interquartile range) of MTV and absorbed dose were 8.8 (5.0-17.3) mL and 59.6 (28.2-114.5) Gy, respectively.

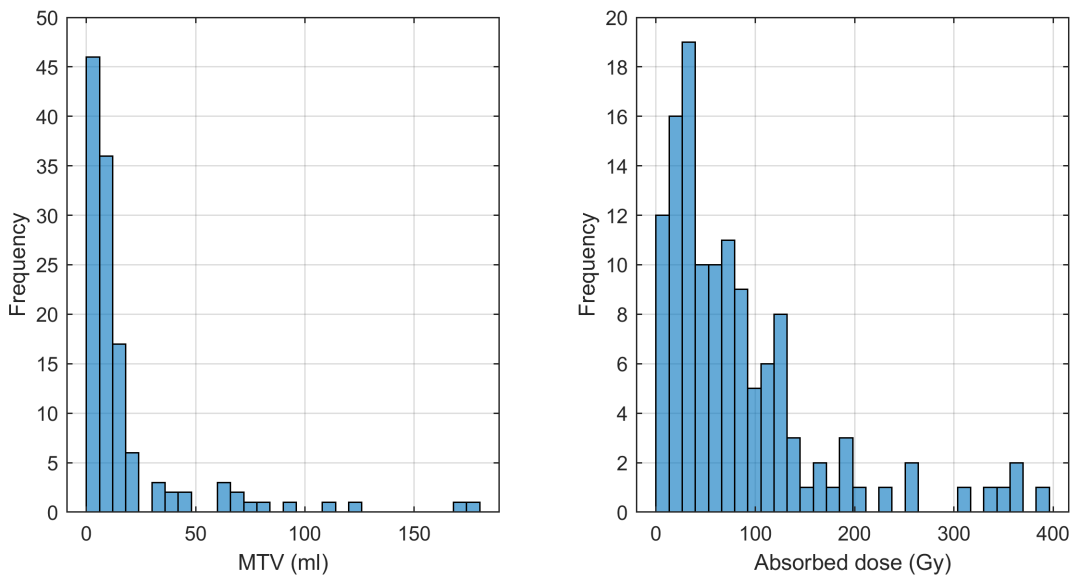


Figure 6.3: Frequency distribution of MTV (on the left) and absorbed dose (on the right) for all tumours.

Table 6.5: Association between absorbed dose and marker percentage variation by LRT.

	<b>Estimate</b>	<b>lower ci</b>	<b>upper ci</b>	<b>p</b>
<b>MTV</b>	0.91	0.67	1.25	0.533
<b>SUVmax</b>	1.10	0.82	1.46	0.528
<b>SUVmean</b>	1.28	0.89	1.84	0.190
<b>TLSR</b>	0.67	0.40	1.12	0.124

### 6.3.1 $^{68}\text{Ga}$ -PET for assessment of response

#### Association between markers variation and dose

Results of the LRT are shown in Table 6.5 (log-log scale was used). Estimate is a coefficient indicating a positive relation between outcome and covariate when higher than 1, and negative relation when lower than 1. For example, a value of the parameter Estimate equal to 1.10 (for SUVmax in the Table 6.5) means that an increase of 10% (c.i. -18% - 46%) of SUVmax is associated to an increase of one order of magnitude of dose. No significant statistical association was found for any marker.

Figure 6.4 shows the response rate for each PET marker, evaluated according to the PERCIST-like criteria. Most of lesions showed a stable response, regardless of the marker used for evaluation. Similar response rates were obtained for SUVmax and SUVmean.

Box-plots in Figure 6.5 show significant differences of the distribution of absorbed dose across Responder and Non-Responder lesions only if response was evaluated with SUVmax or SUVmean. Box-plots show range from first to third quartiles as box and median as horizontal line. Whiskers denote data range. Outliers are denoted using the “+” symbol. Wilcoxon Sum-Rank Test showed significant different absorbed doses between responder and non-responder lesions if response was evaluated through MTV, SUVmax or SUVmean (p-values 0.0017,  $3.99 \cdot 10^{-6}$ ,  $4.32 \cdot 10^{-5}$ , respectively), while the difference of doses was not statistically significant in case of MTV (p-value 0.579).



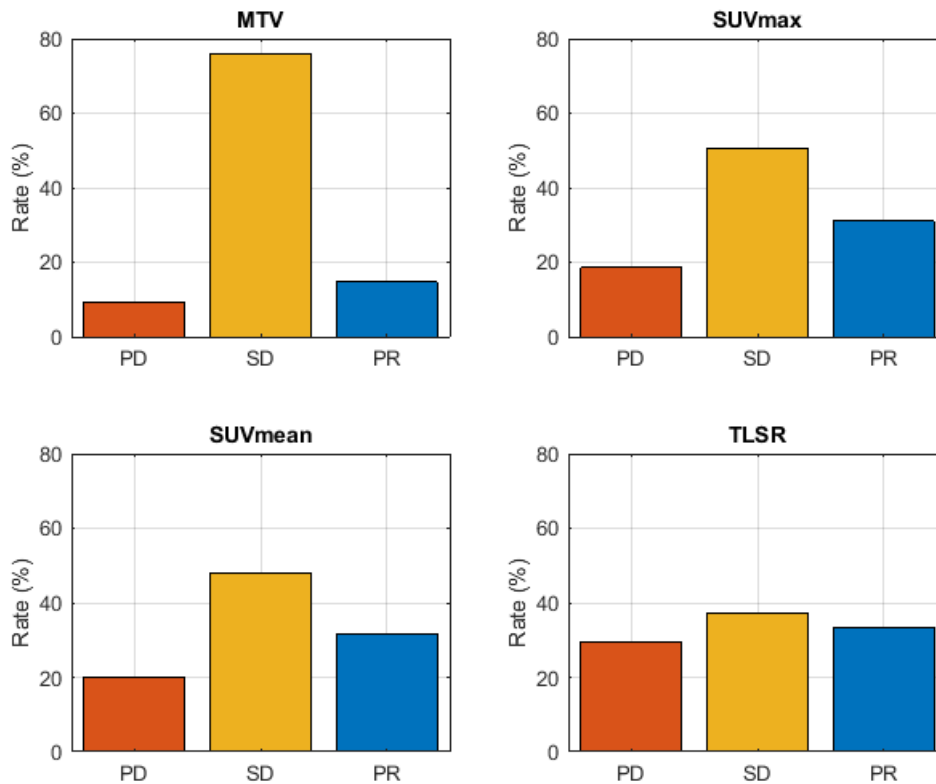


Figure 6.4: Response rate (%) based on the PERCIST-like criteria for MTV, SUVmax, SUVmean and TLSR.

## TCP

Probability of tumour response within five intervals of absorbed dose are shown in Figure 6.6. Probability of response is basically higher for larger absorbed dose, but different patterns were observed among the markers. Associations were statistically evaluated by means of a LRT, results are shown in Table 6.6. Odds ratios confirmed the increase of response probability against the dose. However, only in case of SUVmax and SUVmean association was statistically significant.

### 6.3.2 Prediction of response: a Machine Learning approach

Table 6.7 shows accuracy, AUC, TPR and FPR for each classifier.

The Ensemble RUSBoosted tree classifier showed the best performances,

Table 6.6: Association between absorbed dose and response.

	<b>Estimate</b>	<b>lower ci</b>	<b>upper ci</b>	<b>p</b>
<b>MTV</b>	1.96	0.62	6.19	0.274
<b>SUVmax</b>	24.45	3.17	188.32	0.002
<b>SUVmean</b>	20.54	2.51	168.16	0.009
<b>TLSR</b>	5.38	0.87	33.37	0.099

Table 6.7: Performance of classification for several supervised classifiers.

<b>Classifier type</b>	<b>Algorithm</b>	<b>Accuracy (%)</b>	<b>AUC</b>	<b>Sensitivity</b>	<b>Specificity</b>	<b>BAR</b>
Decision Trees	Fine Tree	85.3	0.72	0.93	0.5	0.71
	Medium Tree	85.3	0.72	0.93	0.5	0.71
	Coarse Tree	86.8	0.77	0.94	0.54	0.74
Logistic Regression	Logistic Regression	78.3	0.63	0.87	0.32	0.59
Naive Bayes	Gaussian Naive Bayes	66.7	0.63	0.73	0.37	0.55
	Kernel Naive Bayes	79.8	0.66	0.92	0.25	0.58
Support Vector Machine	Linear SVM	79.8	0.76	0.96	0.08	0.52
	Quadratic SVM	80.6	0.8	0.92	0.29	0.60
	Cubic SVM	80.6	0.79	0.91	0.33	0.62
	Fine Gaussian SVM	81.4	0.68	0.98	0.08	0.53
	Medium Gaussian SVM	81.4	0.81	0.98	0.08	0.53
	Coarse Gaussian SVM	81.4	0.77	1	0	0.5
Ensemble Classifiers	Boosted Trees	85.3	0.77	0.94	0.46	0.7
	Bagged Trees	79.8	0.76	0.92	0.25	0.58
	RUSBoosted Tree	83.7	0.81	0.87	0.71	0.79

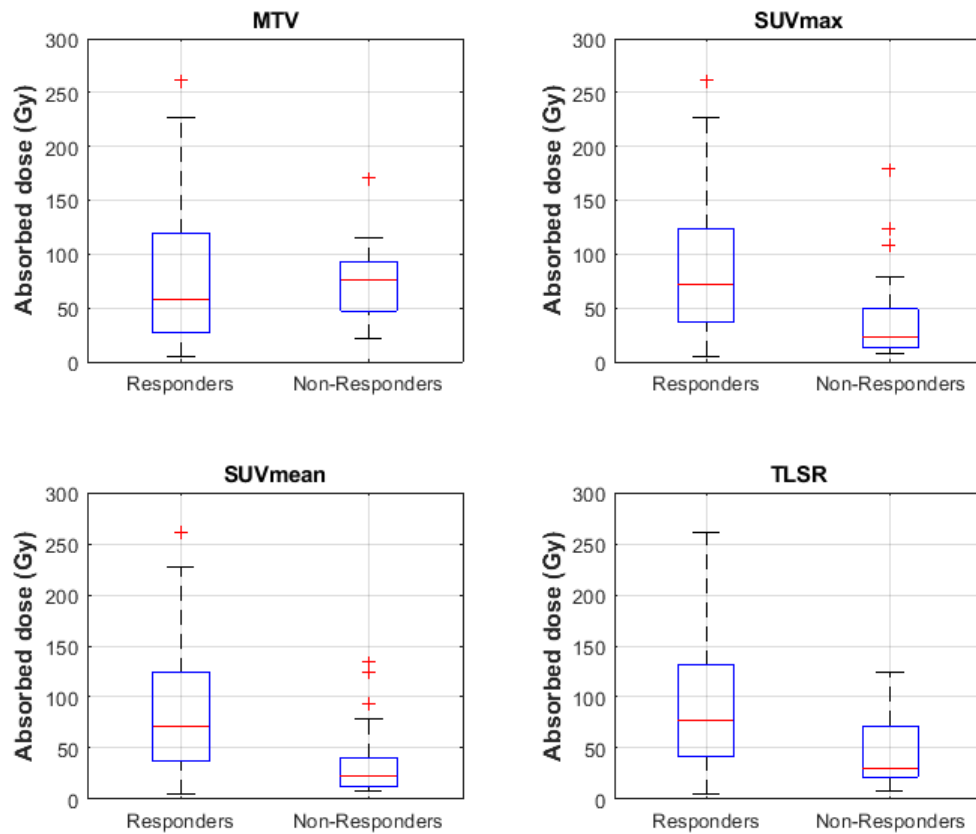


Figure 6.5: Box-plot analysis of the cumulative absorbed dose for “Responder” and “Non-Responder” lesions according to MTV, SUVmax, SUVmean and TLSR variations.

based on the BAR parameter. It is evident that Accuracy and AUC are not appropriate for evaluating the performance of the classifiers. For example, the Coarse Gaussian SVM seems to have good classification performance even if it simply assigns all lesions to the class “Responder”.

Figures 6.8 and 6.9 show the Confusion Matrix and the ROC curve of the Ensemble RUSBoosted classifier in the prediction of response.

## 6.4 Discussion

In this study, a total of 129 tumours from a sample of 45 patients were analysed in order to assess feasibility of using  $^{68}\text{Ga}$ -DOTATATE PET imaging for both response evaluation and response prediction in PRRT. While several stud-

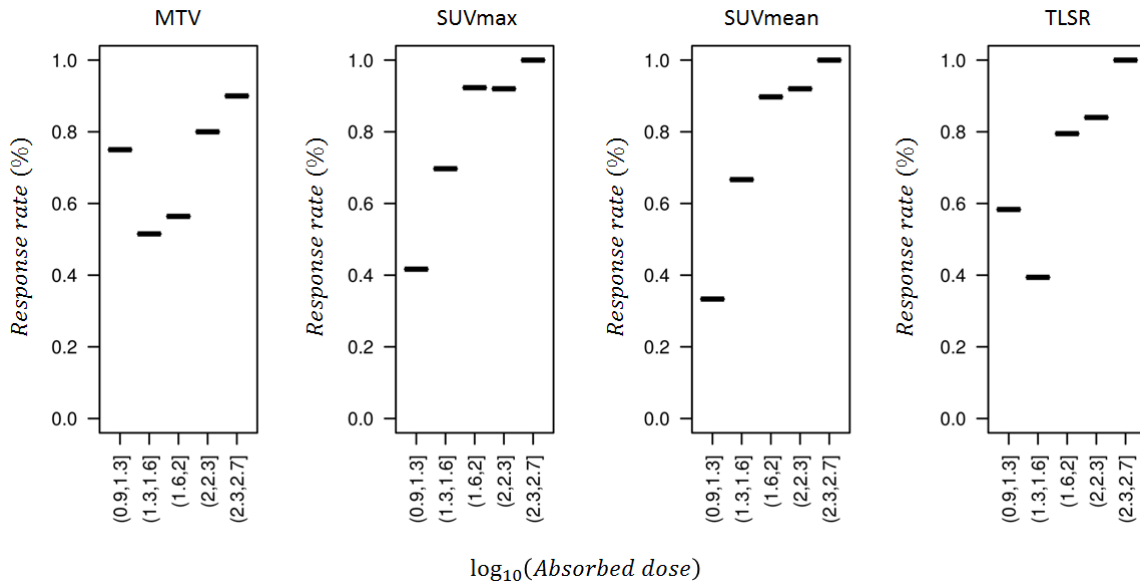


Figure 6.6: Rate of response (%) for each marker within intervals of absorbed dose.

ies demonstrated the role of  $^{68}\text{Ga}$ -PET to assess eligibility of patients to the treatment, there are not so many works about evaluation of the response after therapy.

As expected we found a large inter-patient variability in tumour absorbed dose [123]. Despite no statistically significant association was obtained between tumour absorbed dose and marker variation, findings indicate that SUVmax and SUVmean might be good indicators for assessment of response. Responding tumours had higher absorbed doses than non responding tumours, if response was evaluated using SUVmax, SUVmean or TLG. A significant association was found between absorbed dose and tumour response, if response was assessed using SUVmax or SUVmean. The graphs (Figures 6.6 and 6.7) confirmed the typical expected trend of increasing probability against the dose.

On the other hand, this study had some limitations. Uncertainty of dose calculation, which may also be larger than 50% for tumours, affects results of this analysis. The tumour volume is strictly related to the final dose accuracy. For that reason, only lesions with volume larger than 2 mL were included in this study. Other works reported more stricter inclusion criteria, for example Ilan et al. excluded tumours with diameter smaller than 2.2 cm (volume 5.6 mL). However, since no significant difference in terms of association was

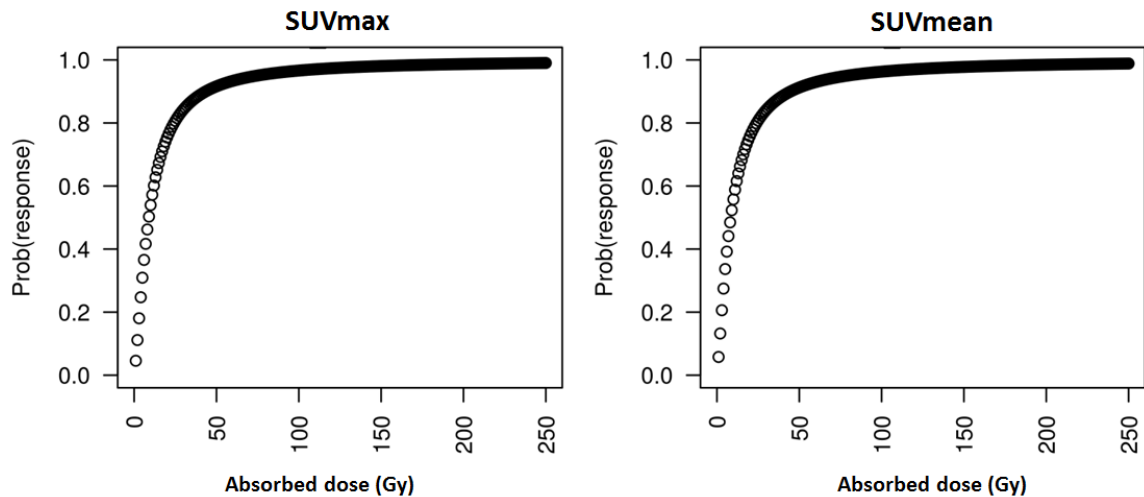


Figure 6.7: Predicted TCP (Tumour Control Probability) against absorbed dose.

obtained when smaller lesions were excluded, the value of 2 mL was used in order to have sufficient statistical significance. Moreover, absorbed dose was only evaluated after the first therapeutical administration. In the following treatment cycles, absorbed dose per unit of injected activity was assumed to be unchanged. Since tumour volume and effective half-life may change during the course of the therapy, this assumption may not be true and absorbed dose be either overestimated or underestimated. However, because complete dosimetric evaluation at each therapy cycle is resource-demanding, this approach is commonly applied in clinical practice [124]. A number of factors affect image quantification. Results from Chapter 2 were used to improve accuracy of quantification, but error in SPECT image quantification remains. In order to compensate for PVE we applied RCs as determined from phantom measurements (see Paragraph 2.2). However, PVE compensation using RC is not complete. For example, it is not ideal for non-spherical tumours or if uptake is not homogeneous. In this study, lesions were outlined in the PET images using a 40% threshold of the maximum pixel value. This allowed to automatically contour lesions, however, lesions with low tumour-to-background contrast, were excluded from the study. In future works, a variable threshold based on the tumour-to-backgraond contrast can be used to include more lesions in the analysis.

One of the main drawback of this study is that only lesions selected at the

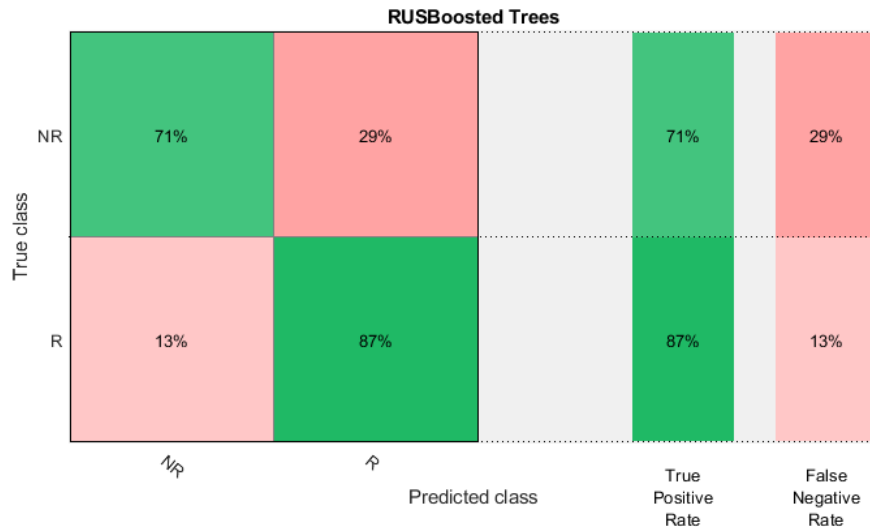


Figure 6.8: Confusion Matrix showing the performance of the Ensemble RUS-Boosted classifier in the prediction of response to PRRT.

beginning of the therapy were monitored for the evaluation of individual response. However, tumour response is not independent with the overall patient response. A change in the SUV of the lesion may be related to growing or shrinking of other lesions.

Machine Learning allowed to include both therapeutic and dosimetric parameters to build a model for predicting therapeutic tumour response. Several classifiers were tested and the Ensemble RUSBoosted tree provided the best performance in term of classification. This result was not surprising, as the RUSBoost is one of the methods that eliminate the data distribution imbalances between the classes and improve the classification performance. RUSBoost applies random undersampling (RUS), a technique which randomly removes examples from the majority class. This model predicted well the response for 83.7% of the lesions (87% of responding and 71% of non-responding lesions). A 5-fold-cross validation was performed to avoid overfitting.

To the best of our knowledge, this is the first study to establish a response predictive model in PRRT. However, although this study provides promising results, there are some limitations. First, the assessment of response was based on the SUVmax variation. However, there are not studies which demonstrated

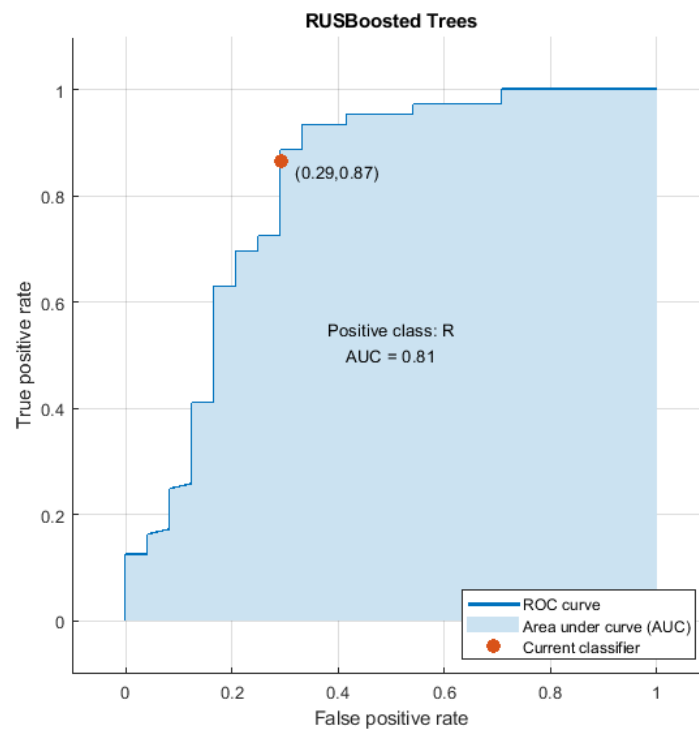


Figure 6.9: ROC curve showing the performance of the Ensemble RUSBoosted classifier in the prediction of response to PRRT.

SUVmax to be good predictor of the response. Second, because of the limited number of patients, we adopted a cross validation procedure to assess the performances of classifiers, instead of using independent training and test sets. Future work would benefit from training with larger and, possibly, multicenter dataset. For these reason, this study is to be considered only preliminary and these promising results necessitate further investigations to be confirmed.





# Chapter 7

## Evaluation of dose uncertainty on clinical cases

The importance of performing absorbed dose calculations to optimize PRRT was extensively discussed in the previous chapters. In Chapter 3 three different calculation techniques were compared and considerable differences in term of dose results were pointed out. The necessity of including estimation of uncertainty combined with the dosimetric result was highlighted in Chapter 4. Indeed, most of the software included in the inter-comparison exercise within the MRTDosimetry project were not able to provide accuracy of dose calculations. Later on, in Chapter 5 and 6, relationship between absorbed dose and organ side effects/tumour response was investigated, pointing out once again the importance of the absorbed dose calculation in PRRT.

Calculation of dosimetry needs to be accomplished with the estimation of uncertainty to be adequately weighted in the planning of treatment. Especially in the case of dosimetry to tumour in MRT, for which published studies reported very high rate of uncertainty. Recently, EANM published a practical guidance on the uncertainty analysis for molecular radiotherapy absorbed dose calculations [125].

This chapter reports results of uncertainties associated to tumour absorbed dose on a sample of clinical cases. The aim of this study is to give an indication of the typical uncertainty which is expected when performing dosimetry on clinical patterns and to determine parameters which more affect accuracy of calculations.

This work was carried out in collaboration with the Royal Marsden NHS Foundation Trust (Downs Road, Sutton SM2 5PT, UK).

## 7.1 Background

Previous studies to assess accuracy of absorbed dose calculations were mainly based on phantom measurements [126][127] or only investigated specific steps of the dose calculation schema [128][129]. Only recently a paper to practically evaluate uncertainty of dose calculations in MRT was published by Gear et al. [125]. This guide provided a detailed methodology to determine uncertainties based on the application of the law of propagation of uncertainty (LPU). The full MRT dose measurement chain from imaging quantification to absorbed dose calculation was examined. Flow diagram in Figure 7.1 shows chronological sequence of the dosimetry schema and how uncertainty propagate between each step. As a result uncertainty and covariance associated with all concerned quantities should be considered.

A patient example was also provided in the paper to facilitate application of the guidelines. However, to date no data were published regarding the application of the EANM practical guidance on uncertainty for MRT dose calculations on a large clinical sample.

## 7.2 Material and methods

This study was conducted on a sample of 49 patients enrolled in a PRRT clinical trial described in Paragraph 1.7 (Trial B). A total of 154 lesions were considered.

A mean value of  $4.2 \pm 0.9$  GBq of  $^{177}\text{Lu}$ -DOTATATE was administered to patients. Sequential SPECT/CT scans were acquired in order to perform dosimetry of each lesion. Four scans at (average  $\pm$  SD)  $1.5 \pm 0.62$ ,  $23.5 \pm 1.2$ ,  $44.0 \pm 1.0$ ,  $67.2 \pm 0.9$  h p.i. were performed for lesions in the abdomen, while three scans at  $2.7 \pm 1.13$ ,  $24.4 \pm 1.0$  and  $67.7 \pm 0.9$  h p.i. for lesions in the thorax. A total of 141 lesions were placed in the abdomen, while a total of 13 lesions were in the thorax. Acquisition imaging setup was described in detail

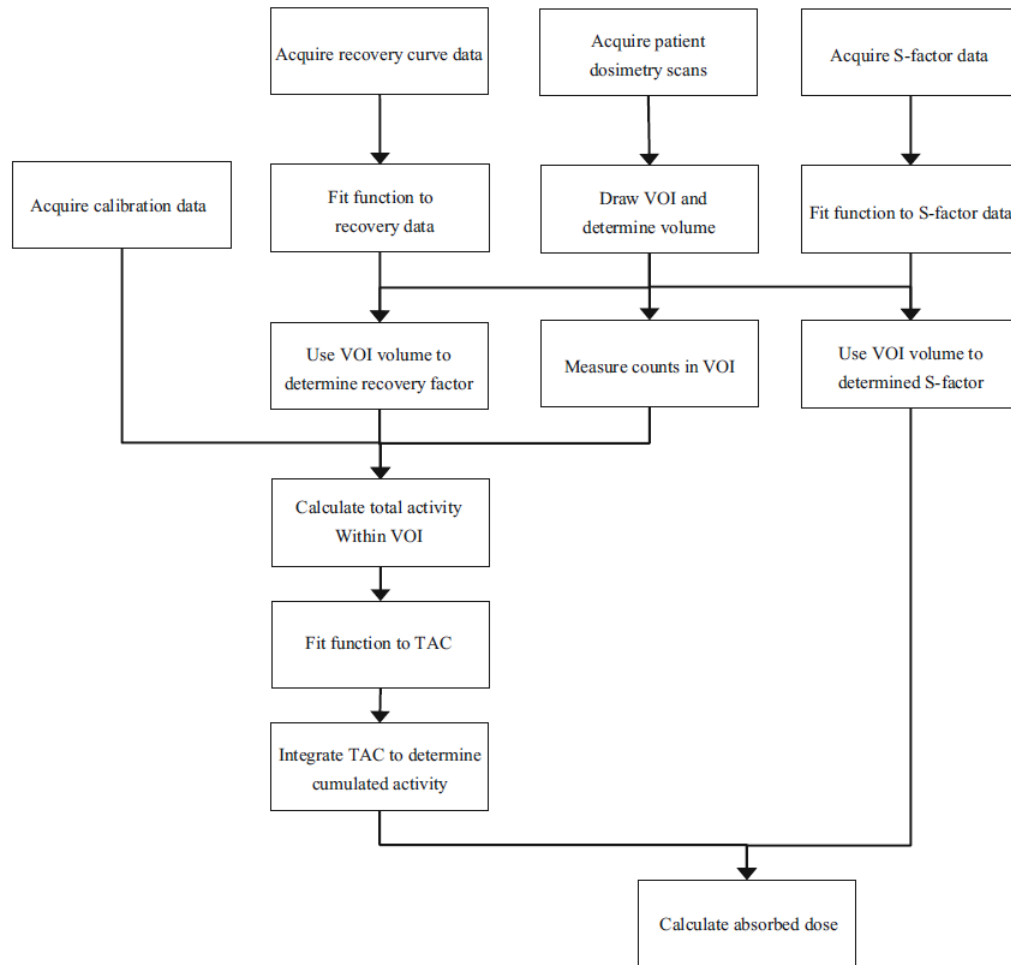


Figure 7.1: Chronological sequence of the dosimetry schema. Source: Gear et al., Eur J Nucl Med Mol Imaging 2018.

in Paragraph 2.2.1.

A maximum of 5 lesions were considered for each patient. VOIs were manually drawn on the fused SPECT/CT image acquired 24h p.i. by a nuclear medicine physician in the Velocity Workstation. Then, contours were duplicated and manually translated to match them with the lesion volume on the other SPECT/CT images.

All dose and uncertainty calculations were performed in MATLAB version R2019a.

### 7.2.1 Dose and uncertainty calculation

Appendix B shows how to apply LPU to determine uncertainty in MRT absorbed dose calculation. Uncertainties were calculated, step by step, for each of the nine following quantities:

**Volume:** The tumour volume was obtained from the VOI manually outlined on the functional images. Thus, volume error depends on the operator ability to define the VOI. However, in this thesis, the operator variability was not analysed and volume uncertainty was determined analytically. Contribution to the uncertainty due to voxelization process and spatial resolution were included. SPECT voxel width was 0.478 cm, while FWHM was 1.041 cm.

**Recovery Coefficient:** Activities were corrected for PVE using the RCs derived from phantom measurements, as described in Paragraph 2.2. Empirical RC points were fitted with an exponential curve (Eq 2.10). Volume uncertainty was combined with the RC uncertainty as described in Appendix B.

**Counts:** Uncertainty of measured counts within the VOI included the limited spatial resolution of the measuring system, the volume uncertainty and the RC.

**CF:** Calibration factor uncertainty was determined by error propagation of measured activity and counts. Uncertainty associated to measured activity (with a radionuclide activity meter) was 1.8% , while standard deviation of counts (from multiple measurements) was 5.4%.

**Activity:** Uncertainty of administered activity was assumed to be negligible. Uncertainty of activity was determined by error propagation of calibration factor, recovery coefficient and counts.

**Fitting:** Two different exponential curves were used to fit the time-activity points:

$$f_1(t) = A \cdot \exp(-B \cdot t) \quad (7.1)$$

$$f_2(t) = A \cdot \exp(-B \cdot t) \cdot [1 - \exp(-C \cdot t)] \quad (7.2)$$

where A, B and C are the fitting parameters and t (time) is the independent variable. Eq. 7.1 was used in case time-activity points had a monotonically decreasing trend or if only 3 time-activity points were available. Otherwise, Eq. 7.2 was used.

**CA:** Cumulated activity was calculated analytically, based on the fitting parameters. Uncertainty included a random component (from TAC fitting parameters) and systematic component (from activity).

**S-factor:** S-factors were derived from OLINDA1.1 sphere model. As OLINDA only provides S-factors for limited sampled values of volumes, S-factors were fitted against the mass using a mono-exponential curve.

**Absorbed dose:** Absorbed dose was calculated by multiplying cumulated activity and S-factor.

### 7.2.2 Data analysis

Distribution of uncertainties for each one of nine variables were analysed using box-plots. Relationships between the variable and the dose uncertainties were visually assessed using graphs. Absorbed dose uncertainty curve against lesion volume was determined by least squared fitting. A Power function of Eq. 7.3 was used to fit the empirical data points:

$$f(x) = ax^b + c \quad (7.3)$$

where a, b, and c are the fitting parameters and x is the independent variable.

In order to evaluate how accuracy of calculations depends on the spatial resolution, uncertainty were calculated assuming different values of spatial resolution.

All analysis and graphs were obtained using MATLAB v2019a.

### 7.3 Results

Median value of the contoured volumes on SPECT images were 6.9 mL, the interquartile range was 4.68-17.24 mL.

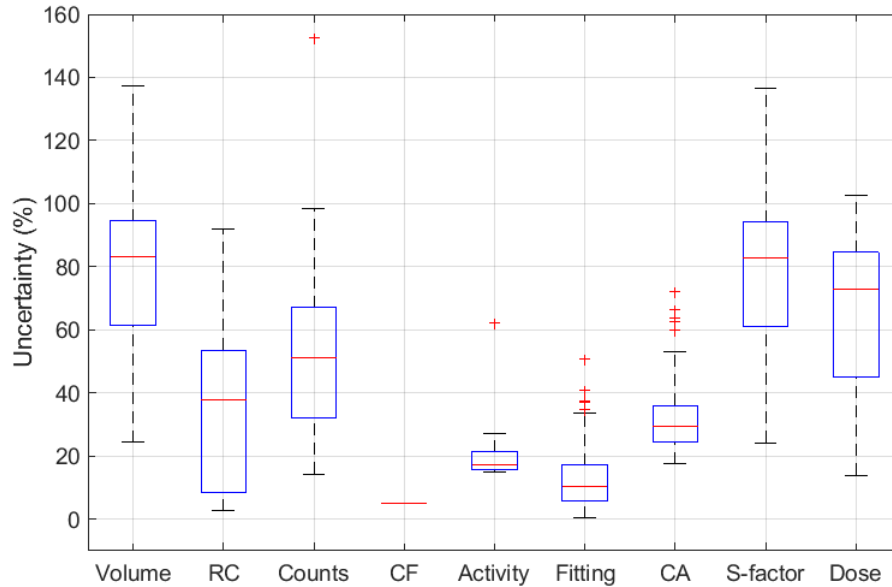


Figure 7.2: Distribution of uncertainty (%) for each step of the dose calculation schema.

High average dose uncertainty was obtained (mean 64.6%, median value 72.8%) and a wide distribution of values (interquartile range 45.4-84.5%, minimum and maximum values were 14.0 and 102.4%, respectively). Figure 7.2 shows the distribution of the relative uncertainty for each quantity of the dose calculation chain. Volume and S-factors were the quantities with the highest relative uncertainties. Different distributions were observed, hence relationship between each quantity and the final absorbed dose uncertainty may not be simple. In order to investigate how uncertainty ( $u(\%)$ ) of each quantity is related to the final dose uncertainty, Figure 7.3 plots each quantity against the dose uncertainty (%).

Clear relationship was observed between dose uncertainty and volume uncertainty, and as a consequence between dose uncertainty and RC, Counts and S-factors uncertainty, which are strictly dependent on the volume uncertainty.

Power curve of Eq. 7.3 fitted well the dose uncertainty vs volume points,

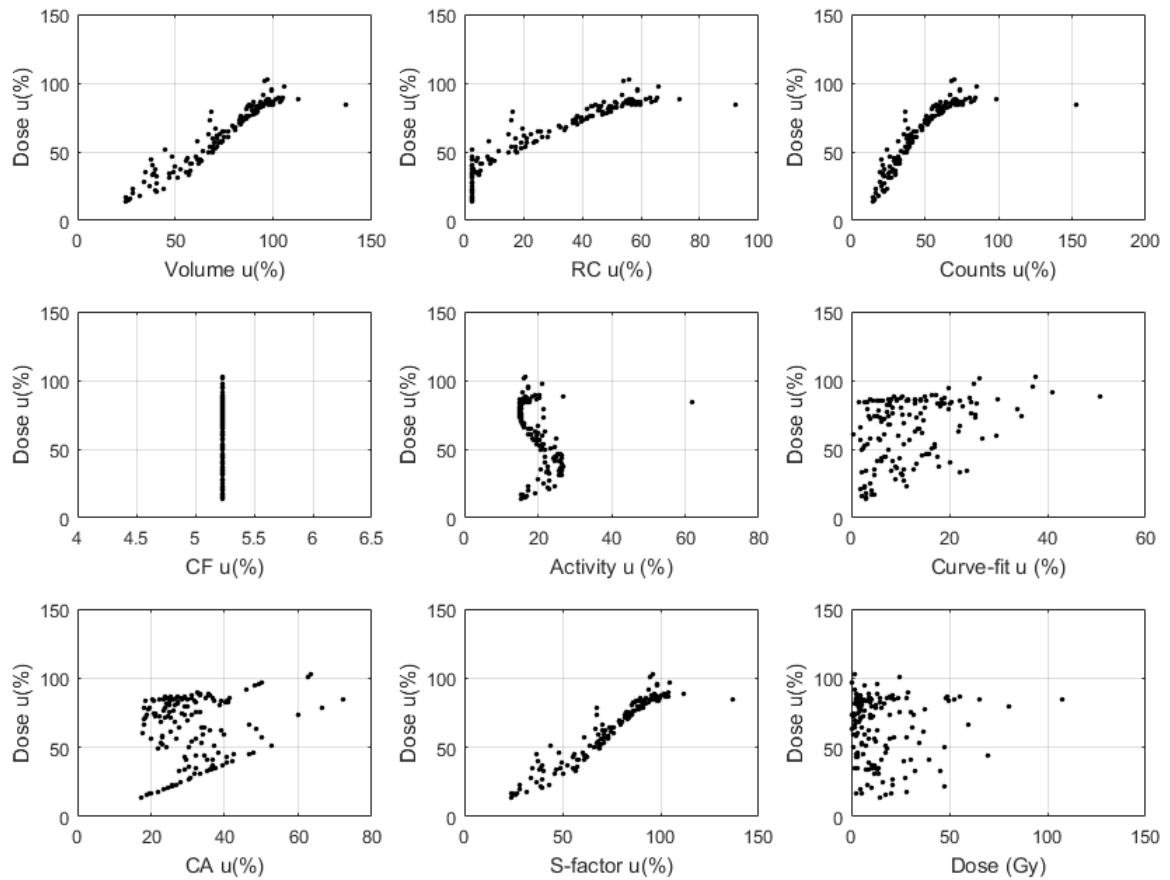


Figure 7.3: Relationship between dose uncertainty (y-axis) and volume, RC, counts, CF, activity, curve fitting, cumulated activity and S-factor uncertainty (x-axis). The graph at the bottom right shows absorbed dose (Gy) against the dose uncertainty.

as shown in Figure 7.4.

Using different values of spatial resolution, the curves in Figure 7.5 and 7.6 were generated. Figure 7.5 shows the relative dose uncertainty re-calculated for all the lesions, assuming four different values (0.1, 0.5, 1 and 2 cm) of FWHM (note: the actual FWHM of the acquisition system was 1.041 cm). In Figure 7.6 four lesions with very different volumes were considered and dose uncertainty was calculated as a function of the system spatial resolution.

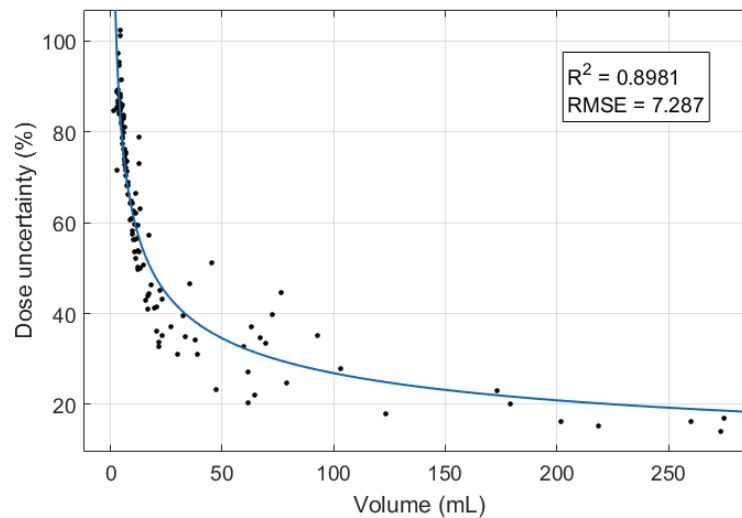


Figure 7.4: Dose uncertainty (%) against Volume (mL). Points were fitted with a Power function,  $R^2$  and RMSE are reported into the graph.

## 7.4 Discussion

Lack of standard methodologies for estimation of uncertainty in MRT dose calculations has been one of the weak points towards the widespread of dosimetry in clinical routine. In a personalized medicine prospective, which yields treatment to be optimized based on the dosimetry outcome, calculation of dosimetry needs to be accomplished with the estimation of uncertainty to be adequately weighted in the planning of treatment.

The EAMN guidelines published in August 2018 firstly provided the schema of uncertainty propagation to evaluate the standard uncertainty in absorbed dose to a target. This schema was based on the recommendations described within the GUM [130] and necessarily involves formation of covariance matrices for several steps of the dosimetry process.

In this work, we have applied the EANM guidelines to evaluate uncertainty of tumour dosimetry calculations. This study carried out, for the first time, the uncertainty analysis of the entire process of dosimetry calculation on a large sample of clinical cases.

Figure 7.2 gives an idea of the typical range of uncertainty it is expected from performing dosimetry. The relative uncertainty associated with the quantities examined was very widespread around the median value, therefore a high



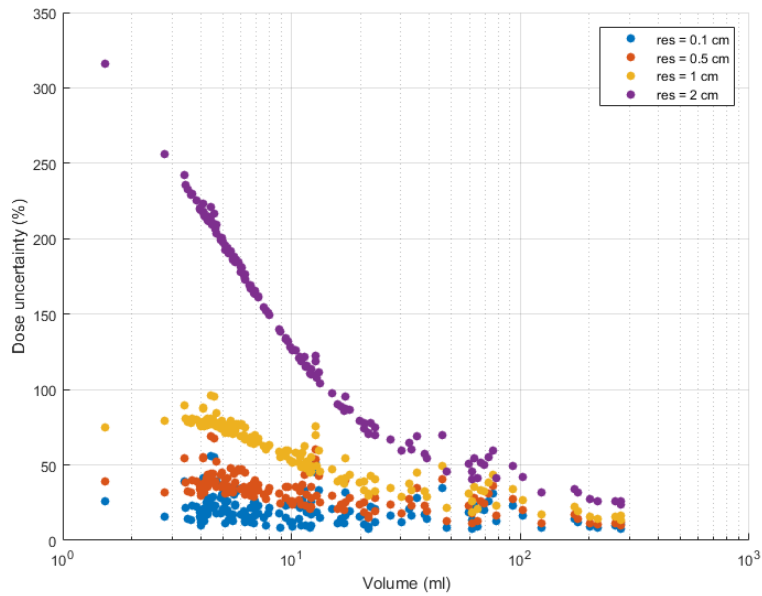


Figure 7.5: Dose uncertainty (%) against Volume (mL) calculated for all the lesions, assuming four different spatial resolution values of the imaging system (FWHM: 0.1, 0.5, 1 and 2 cm).

inter-lesion variability is present. For that reason, the relationship between variables was investigated. Analytical model in Figure 7.4 fitted well the empirical data points and it would be useful, in clinical practice, for a quick estimate when protocols are being drafted. These results confirmed that the major factor affecting uncertainty in the absorbed dose originates from the uncertainty in the delineation of the VOI. As a further demonstration of this, Figure 7.7 shows the uncertainty in dose (black points) and the volume uncertainty (blue line) on the same axis. This shows how the volume uncertainty impacts the final uncertainty in absorbed dose. The final uncertainty is smaller than the uncertainty associated to the volume. This is due to the covariance between parameters, which tends to reduce the effect of propagation. The “spread” of the data from an exact line described the effect of random uncertainty elements, that are not part of the volume model and are presumably derived from the TAC fit. For larger lesions uncertainty of volume delineation is less significant and the fit to the TAC begins to dominate. This is evident from the vertical distribution of the points, which is narrower for larger volumes.

Impact of spatial resolution of final uncertainty was evaluated by postu-

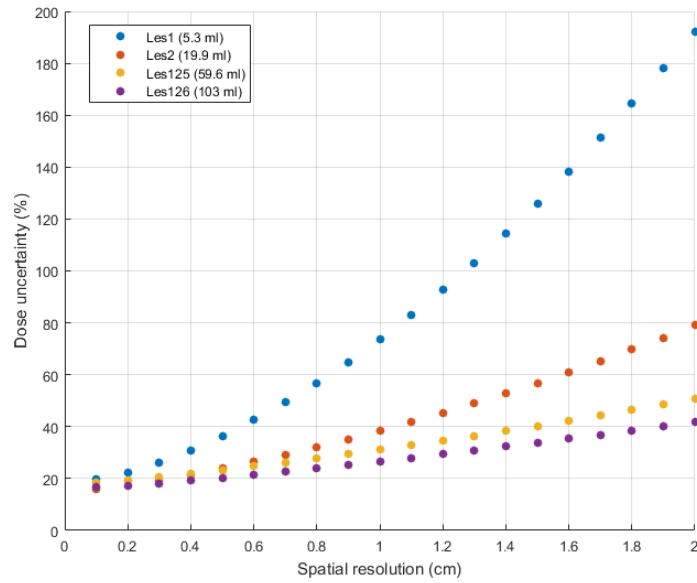


Figure 7.6: Dose uncertainty (%) as a function of the imaging system spatial resolution (cm) in four lesions. Lesions were chosen to fill a range of different values of volume.

lating different FWHM of the imaging system. Results in Figures 7.5 and 7.6 pointed out that uncertainty would be significantly reduced by increasing the spatial resolution. This effect would be particularly significant in the case of small volumes. Hence, a minimal acceptable volume cut-off might be set, depending on the spatial resolution of the system available in the site.

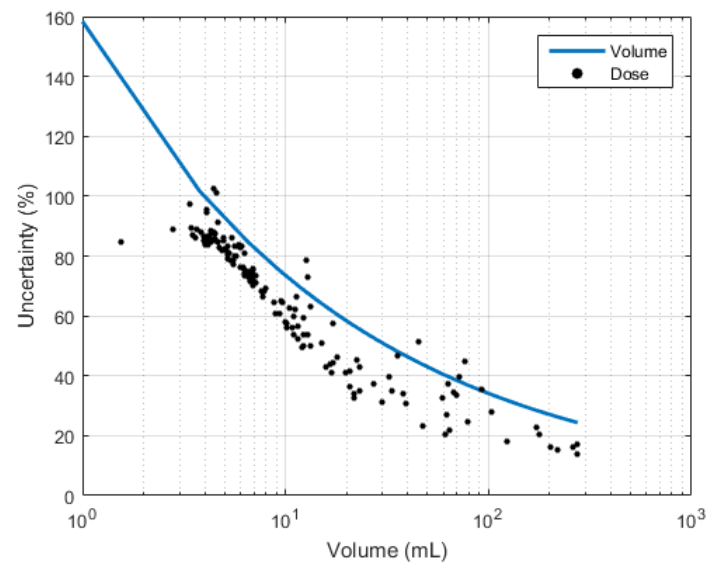


Figure 7.7: Dose uncertainty (black points) and the volume uncertainty (blue line) as a function of the delineated VOI volume.



## Conclusion and future perspectives

Neuroendocrine tumors are rare neoplasms with an incidence of about 5.25 cases per year out of 100,000 inhabitants. When a NET is diagnosed, in the majority of cases it has already metastasized and surgery, which is the only curative treatment option nowadays, is no longer an option available. Approximately 80% of NETs express somatostatin receptors (SSTRs) on cell surface, both in primary and in related metastases [131]. The idea of using radiolabelled somatostatine analogues to vehicle radioactivity on cancer tissues was first introduced by Klenning et al. [132]. PRRT has been used for decades in the treatment of NETs. Numerous single-centre Phase I and Phase II trials have indicated in the last decades that PRRT with  $^{90}\text{Y}$  and  $^{177}\text{Lu}$  is a valid and promising therapeutic option. In 2017, results of the first Phase III multicenter randomized controlled clinical trial (the NETTER-1 trial) were published. Participants randomized to the experimental arm received four doses of 7.4 GBq of  $^{177}\text{Lu}$ -DOTATATE once every 2 months. Participants randomized to the control arm received high dose (60 mg) of the “cold” somatostatin analog octreotide alone. The objective response rate was significantly different between the two arms. Subjects receiving  $^{177}\text{Lu}$ -DOTATATE had a 79% reduction in risk of progression ( $p < 0.001$ ) with an estimated PFS (Progression Free Survival) of 40 months, compared with 8.4 months for high-dose octreotide therapy. The overall survival improvement was associated with a significant benefit in terms of quality of life compared with high-dose octreotide. Following this publication, the therapy has been approved by the Food and Drug Administration (FDA) and the European Medicines Agency (EMA). Administration of  $^{177}\text{Lu}$ -DOTATATE has been approved for the treatment of SSTR-positive NET, at a recommended fixed dosage of 7.4 GBq every 8 weeks (considered as a safe dosage for toxicities), for a total of four cycles. Although clinical approval of

$^{177}\text{Lu}$ -DOTATATE has been an important milestone in the field of MRT, there are still number of challenges to be addressed, especially regarding dosimetry and treatment efficacy.

In PRRT, as in every radiation therapy, the goal is to deliver an effective radiation dose to the tumour without causing undesired effects in healthy tissues. Improvements in the success of radionuclide therapy also depend on the optimization of radiation doses to tumour versus normal organs in individual patients. Since many studies showed marked inter-patient variability in peptide pharmacokinetics, personalized treatment planning based on dosimetry outcome is likely to improve the efficacy of the radionuclide therapy. For example, Ulrike et al [133] demonstrated, in a prospective observational study, that a cut-off defined by four cycles of 7.4 GBq will exclude patients who might benefit from further therapy. They found higher progression-free survival and overall survival for patients who reached 23 Gy in renal dose than patients who did not, but only 66% of patients treated with four cycles reached this value, with the risk to undertreat this portion of patients.

In this framework, this thesis investigated several aspects concerning PRRT, from the imaging SPECT quantification to the biological effect of radiation. The overall aim of these studies was to provide the metrology for the clinical implementation of absorbed dose calculations in MRT and to modelize the biological response to radiation in PRRT in order to optimize the treatment efficacy and to improve the clinical outcome.

**Chapter 1** provided a general introduction on molecular radiotherapy, PRRT and NETs. The MIRD formalism, which is the basis for the absorbed dose assessment and can be applied both at organ- and voxel-scale, was described. Also, a typical treatment planning protocol and the AUSL-IRCCS of Reggio Emilia hospital PRRT clinical trials were reported in this chapter.

**Chapter 2** dealt with quantitative SPECT/CT assessment of radioactivity. In particular, three different points were studied: the best choice for the num-

bers of iterations and subsets of iterative reconstruction algorithms, a practical solution for partial volume effects and the impact of two non-rigid registration algorithms.

The first study found there is not a single configuration which is the best in every situation, but the OSEM updates should be chosen depending on the object dimension being scanned. The importance of these results rely on their impact on clinics: small objects, for example lesions, may be not correctly detected if the OSEM updates are not optimally set. We also determined, for our scanner, the best compromise in abdominal exam focused on lesion and organ dosimetry if multiple image reconstructions are not a feasible option (as it may happen in clinical routine). In the case of small lesions, the effect of partial volume is predominant and it becomes necessary to apply corrections for the PVE regardless of the OSEM updates.

Two models of PVE correction were determined based on phantom measurements. One model is suitable to be used for lesion activity quantification, while the other one is suitable to be used for organ activity quantification. Methods based on RC derived from phantom measurements did not provide a full correction for PVE, however they are appreciated for their simplicity and can be easily applied in clinics. The PVC models were also tested using inserts with different volume and shapes to represent various clinical scenarios. These measurements allowed to assess accuracy of compensation and dependence of PVE on the asphericity, which is a parameter that should be taken into account in clinical practice.

Misregistration represents one of the main source of error in MRT dose calculations schema. Non-rigid registrations algorithms are preferred to rigid registration because they allow to capture anatomical change of organs, on the contrary of only roto-translations techniques which do not. Commonly, dose maps are calculated on the basis of the activities from the registered images. In this study a novel image registration workflow is considered. Time-point dose maps were first generated. Then, the dose maps were registered and the cumulative dose was calculated. The two workflows provided no statistically significant difference in term of absorbed dose, hence the usual workflow was suggested to be used.

In **Chapter 3** different calculation dose modalities were compared. One of the reasons for a reluctance to perform dosimetry in clinical routine is that the process is complicated and there are no standard methods for the calculation of dose. Over the last decades, plenty of non-commercial tools and a few of commercial tools have been developed. A home-made software (VoxelMed) developed at the Reggio Emilia hospital and optimized to the novel version VoxelMed2.0 during the course of the PhD was included in the comparison. Three main approaches are commonly used to perform dosimetry: organ-convolution, voxel-convolution and MC based approach. The motivation for this comparison was to identify differences in the methods of dose calculation and to assess the feasibility for absorbed dose calculations in MRT clinical daily practice. Both phantoms and clinical dataset were used to derive more general conclusions. Values obtained with the organ-level approach were generally higher in comparison to the other modalities. Voxel-based convolution provided more similar results with the MC simulations and allowed fast processing of calculations. Also, the importance of activity integration techniques were pointed out in this work: differences of results were considerably reduced when software used the same decay constant. Standardization of the procedures would improve accuracy of dosimetry and would make the multi-center scientific collaborations easier to be performed.

**Chapter 4** describes the main results obtained in collaboration with other institutes within the MRTDosimetry project. International collaboration between metrological institutes, research centres and hospitals is of foremost importance at this stage of the MRT development to encourage clinics to adopt dosimetry as a routine part of patient treatment and to assist them into the transition from the nominal treatment to the personalized one, as required by the EC Directive 2013/59/EURATOM. The MRTDosimetry project has been one of the most important international collaborations in the field of the radionuclide therapy. It brought together expertise in metrology and nuclear medicine research from 12 different countries.

A series of phantoms, including a quasi-realistic anthropomorphic phantom,



were used to perform a multi-site inter-comparison exercise (covering 8 clinical sites in 5 countries) in order to develop a protocol for the commissioning and QC of SPECT/CT systems. As different SPECT/CT systems were included, this protocol allows to achieve harmonization of imaging quantification across multiple centres, systems and countries, this represents a major step towards personalised therapies.

Feasibility of using  $^{133}\text{Ba}$  sources as surrogate of  $^{131}\text{I}$  solutions for SPECT/CT QC was investigated. Iodine-131 is not used in PRRT, but it is widely employed in Nuclear Medicine. Major uses of  $^{131}\text{I}$  include the treatment of thyrotoxicosis (hyperthyroidism) and treatment of thyroid cancer. Using sealed long-lived test sources instead of hollow fillable containers will significantly simplify routine QC procedures. Two sets of traceable  $^{133}\text{Ba}$  sources and a set of identical containers to be filled with liquid  $^{131}\text{I}$  were sent around 8 different sites of the MRTDosimetry partners to perform this exercise. A regression analysis yielded a cross-calibration factor of  $0.70 \pm 0.02$ , which can be explained by the emission probabilities.

A cross-comparison exercise based on real clinical functional images was performed in order to compare the dosimetry tools used across different clinical partners. Each site applied image registration and VOI delineation as it routinely performed them in order to include the entire process of dose calculation. Comparison was based on the TIACs provided by each participant. The results differed considerably, with deviations from the mean value of up to 50%. The lack of standardization in MRT is one of the main limitation to the development of dosimetry in clinics and still need to be addressed.

In **Chapter 5**, the incidence of renal radio-toxicity, associated risk factors (like hypertension, diabetes, previous chemo- or radio-therapies) and renal function during follow-up was analysed in 64 patients treated with  $^{177}\text{Lu}$ - and  $^{90}\text{Y}$ -DOTATOC. Results of this study indicate that PRRT with  $^{177}\text{Lu}$ - and  $^{90}\text{Y}$ -peptides is safe and promising approach for the treatment of patients affected by NETs. Only two cases (about 3%) among the treated patients had a grade 2 renal toxicity and one patient had grade 4 renal toxicity. Patients with risk factors had wider reductions of creatinine clearance than patient with no risk

factors. However, the probability of showing side effects was not significantly different between the two groups of patients. Probably, the limited number of patients and the presence of few cases without toxicity and risk factors might have influenced the results. These results also highlight the importance of performing dosimetry to keep patient at safety level of radiation exposure. The renal mean absorbed dose of the patients who developed toxicity were significantly higher than the absorbed doses of the patients who did not develop toxicity. It is very important to be able to predict the tolerance in critical organs at risk from the administered radioactivity while treatment planning or patient recruitment to therapy. The NTCP models allow to estimate the probability of radio-toxicity effects as a function of absorbed dose, hence they can be used to determine the dose limits to guarantee a safe treatment within a certain probability. Currently, the cut-off for renal absorbed dose to guarantee a safe treatment is assumed to be between 23 and 27 Gy. However, these values have been derived from external beam radiation therapy and in PRRT the limit values are probably higher due to the intrinsic differences between the modality of radiation exposure. This PRRT protocol (average 7.1 GBq of  $^{177}\text{Lu}$  and 2.9 GBq of  $^{90}\text{Y}$  fractioned in 5 cycles) preserved the patient safety. Only a few cases of renal toxicity with grade 2 or more were observed, hence the number of data is not sufficient to derive a safe BED cut-off. Chronic NTCP of 50% was associated with a BED value of 42 Gy.

In this study also the red marrow radio-toxicity was monitored. Serious haematological toxicity is rare. No high haematological toxicity grade (3-4) was observed among the monitored patients. Nevertheless, no correlation between bone marrow absorbed dose and the development of haematological toxicity was found. The lack of correlation might be due to the inappropriateness of the blood model for calculation of red marrow absorbed dose. Recently, some authors proposed a method for red marrow absorbed dose calculation based on functional images. However, finding the best dose calculation method is still an open problem. Moreover, bone marrow absorbed doses are usually quite low and difference in dose among individuals may prevail over difference in irradiation effects.

Assessment of tumour response was examined in **Chapter 6**. Similarly to the organs at risk, the effectiveness of PRRT might probably be improved if information about absorbed dose to tumours was included in defining treatment strategy. However, the radiation sensitivity of neuroendocrine tumors has not been established and the reliable markers for tumour assessment still need to be determined.

A total of 129 tumours from a sample of 45 patients were analysed in order to assess feasibility of using  $^{68}\text{Ga}$ -DOTATATE PET for response evaluation. This study found significant association between absorbed dose and tumour response based on SUVmax and SUVmean variation in a volume of interest. Although obtained in a limited number of patients, the dose–response relationship suggests the potential usefulness of tumour dosimetry in the management of patients with NETs. The derived TCP curves based on SUVmax and SUVmean variations showed the typical shape expected from the theoretical models. The importance of these models relies on the possibility to derive the lower threshold of tumour dose which provides response to therapy. This may help clinicians to determine patients who are likely responding the therapy. Based on these results, a tumour absorbed dose of 50 Gy is associated with a 0.9 probability of stable disease or partial response. However, some issue still need to be addressed: feasibility of using SUVmax for tumour response evaluation need to be confirmed, response criteria for  $^{68}\text{Ga}$ -DOTATATE PET/CT are missing and there is a lack of standard methods for tumour volume delineation. The main conclusion of this study is that tumour dosimetry is feasible on clinical routine and it may become an important tool for patient recruitment and treatment planning.

Absorbed dose based on SPECT/CT and tumour uptake based on  $^{68}\text{Ga}$ -PET are the main physical quantities to assess eligibility of patients to PRRT. However, effect of radiation on lesions depend on a number of variables such as the grade of the neoplasm, the administered activity, the radiopharmaceutical or the tumour dimensions. In recent years, Machine Learning has emerged as an incisive tool capable to statistically handle relationships between copious number of variables. A model which includes ten variable as input and classifies each lesion between responder or not responder was built using the Ensemble

RUSBoosted Three algorithm. To the best of our knowledge, this is the first study to establish a model based on Machine Learning analysis for response assessment in PRRT. High performance of classification were obtained (83.7% of lesions were correctly classified). Hence this study gave promising results and further investigations may confirm the role of Machine Learning for PRRT response evaluation.

In **Chapter 7** uncertainty of absorbed dose calculation in MRT is investigated. In particular, the uncertainties in relation to the full MRT dose measurement chain, ranging from the image acquisition system calibration to the absorbed dose calculation were assessed based on the recently published EANM practical guidelines. The aim of this study is to provide an indication of the typical uncertainty associated to the dose on clinical patterns and to determine the parameters which most affect accuracy of dose calculations. In a prospective in which dosimetry is routinely performed for therapy optimization, assessment of dose uncertainty is of primary importance to adequately weight the impact of the calculated dose and eventually improve the dose estimations. Moreover, lack of standard methodologies for assessment of uncertainty in MRT has been one of the limiting factor to the widespread of dosimetry in clinics.

This study carried out, for the first time, the uncertainty analysis of the entire process of absorbed dose calculation on a large sample of patients. On a total of 154 lesions, uncertainties ranged between 14% and 102%. A quarter of all the lesions showed an uncertainty lower than 45%, while half of the lesions lower than 65%. Also, results showed uncertainty of dose is strongly related to the lesion dimensions. A model was derived to analytically express dose uncertainty as a function of the tumour volume. This model might be used by clinicians to fast check the accuracy of calculations if it were implemented in the dosimetry calculation software. Impact of spatial resolution on the dose uncertainty was assess by postulating spurious values of FWHM of the imaging system. This results highlight the importance of improving spatial resolution to achieve accurate dosimetry and can be used to set a cut-off volume in relation with the spatial resolution.

In future studies, assessment of dose uncertainty may help to improve results

in dose-response analysis. Noise may be reduced by means of excluding data-points with uncertainty lower than a fixed threshold and weighing the fit based on the accuracy of absorbed dose calculation.



# Appendices





# Appendix A

## Machine Learning

Machine Learning (ML) is a branch of artificial intelligence that relies on automated analytical model building. ML uses input data to achieve the desired task without being literally programmed to produce a particular outcome. These algorithms automatically “learn” based on a training dataset so that they become better and better at achieving the desired task. Then, the trained model is used for predicting the results for new data. Machine learning algorithms can be largely classified into three categories: supervised learning, unsupervised learning and reinforcement learning. Supervised learning systems make use of labelled datasets, i.e. each input data-point is associated to the corresponding true known class. Unsupervised learning systems use unlabelled datasets to train the system. Unsupervised learning algorithm investigates the similarity between pairs of objects to develop new skills. Reinforcement learning systems do not experience a fixed dataset, but a feedback loop between the system and its experiences.

### A.1 Decision Tree

Decision tree learning is a method commonly used in Machine Learning. Decision trees are constructed via an algorithmic approach that categorize data by splitting them in a flowchart-like structure (or tree-like structure). Every node in the tree depicts a feature that has to be classified, and the branches depict an outcome of the node. These algorithms are very common because they can handle heterogeneous data (ordered, categorical, or a mix of both),

they intrinsically implement variable selection, they are robust to outliers and they can easily be visualized in a tree structured format, which is easy interpretable. However, they are prone to overfit the training data, i.e. the model no longer generalizes well, and they also can be unstable, i.e. small variations in the data might result in a completely different tree being generated. These limitations can be partially solved by using “ensemble”.

## A.2 Ensemble RUSBoosted Tree

Ensemble methods combine multiple learning algorithms in order to obtain a classifier with superior performance to individual classifiers. Three methods can be used for constructing ensembles of decision tree: boosting, bagging and random subspace. Boosting, which is the most popular method, consists by repeatedly running a weak learner on various distribution training data. These classifiers are then weighted and a boosted classifier is generated by weighting the weak classifiers with linear combination of other classifiers. Boosting methods are resistant against overfitting and instability. The RUSBoost (Random Under Sampling Boosting) randomly deletes data from the training dataset until the intended balanced class distribution is achieved. The RUSBoost is one of the methods that address the data distribution imbalances between the classes and improve the performance of classification.

## A.3 Performance of classification

Machine Learning algorithms usually work by splitting the dataset into a training dataset and a test dataset. The machine learning algorithm is then trained on the first one, while the test dataset is used to assess performance of classification. A common problem for machine learning algorithms is overfitting, which means the model describes well the training data but it does not generalize well to to an independent dataset. In order to address this problem, a common approach is to use an k-Fold Cross Validation. Cross Validation describes the process of splitting the whole dataset into k subsets and using each one of them sequentially as the test dataset while combining the others

to the training data. Afterwards, the performance indicators are averaged over all test subsets.

The prediction results are divided into four categories: true positive (TP), false positive (FP), true negative (TN), and false negative (FN). The description of these four types of results are shown in Table A.1.

Table A.1: Confusion Matrix.

		True Class	
		True Positive (TP)	False Positive (FP)
Predicted Class	True Positive (TP)	True Positive (TP)	False Positive (FP)
	False Negative (FN)	False Negative (FN)	True Negative (TN)

In order to quantify the quality of a machine learning model, different performance measures can be computed using the predicted labels. The right metric for evaluating ML models should be chosen based on the type of dataset. In the following TP, FP, TN and FN are intended as the number of observations for each category.

- **Accuracy** is a ratio between the correctly predicted observations to the total observations. Accuracy is one of the most common performance measure to evaluate any ML algorithm or model. However, accuracy might not be appropriate when data is imbalanced. For example, accuracy of the model might be high, but in reality the model is predicting only the majority class which contains almost all the data.

$$Accuracy = \frac{TP + TN}{TP + FP + FN + TN} \quad (\text{A.1})$$

- **AUC** stands for Area Under the Receiver Operating Characteristics (ROC) Curve. ROC curve is created by plotting the true positive rate (which is same as Sensitivity) against the false positive rate (which is same as 1-Specificity) at different threshold settings. AUC represents degree or measure of separability. Similarly to accuracy, AUC is not a good metric to assess performance of a classifier in case of imbalanced dataset. Sensitivity and Specificity provide, in these cases, reliable results.
- **Sensitivity**, also called true positive rate (TPR), measures the proportion of actual positives which are correctly identified as such from the

total amount of positives:

$$\textit{Sensitivity} = \frac{TP}{TP + FN} \quad (\text{A.2})$$

- **Specificity**, also called true negative rate (TNP), measures the proportion of actual negatives which are correctly identified as such from the total amount of negatives:

$$\textit{Specificity} = \frac{TN}{TN + FP} \quad (\text{A.3})$$

- **BAR** stands for Balanced accuracy rate (BAR) and it is the average between sensitivity and specificity:

$$\textit{BAR} = \frac{\textit{Sensitivity} + \textit{Specificity}}{2} \quad (\text{A.4})$$

# Appendix B

## Calculation of uncertainty

This Appendix reports methods and formula used to evaluate uncertainties in Chapter 7. Uncertainties were calculated based on the EANM practical guidance on uncertainty analysis for molecular radiotherapy absorbed dose calculations (Gear et al [125]).

### B.1 The law of propagation of uncertainty (LPU)

In this section, terminology and nomenclature adopted to apply LPU is presented.

Given the generic multivariate measurement model:

$$\mathbf{Y} = \mathbf{f}(\mathbf{X}) \quad (\text{B.1})$$

where

$$\mathbf{X} = [X_1, \dots, X_n]^T \quad (\text{B.2})$$

is a vector measured of  $n$  generic input quantities  $X_1, \dots, X_n$  and

$$\mathbf{Y} = [Y_1, \dots, Y_m]^T \quad (\text{B.3})$$

is a vector measurand of  $m$  output quantities  $Y_1, \dots, Y_m$ . The output covariance matrix associated with the estimate of  $\mathbf{Y}$  -  $\mathbf{y}$  - is:

$$\mathbf{V}_y = \mathbf{G}_x \mathbf{V}_x \mathbf{G}_x^T \quad (\text{B.4})$$

where  $\mathbf{V}_x$  is the output covariance matrix associated with the estimate of  $\mathbf{Y} - \mathbf{y}$ .  $\mathbf{V}_x$  is the input covariance matrix

$$\mathbf{V}_x = \begin{bmatrix} u^2(x_1) & \dots & u(x_1, x_n) \\ \vdots & \ddots & \vdots \\ u(x_n, x_1) & \dots & u^2(x_n) \end{bmatrix} \quad (\text{B.5})$$

associated with the vector  $\mathbf{x} = [x_1, \dots, x_n]^T$  - estimate of  $\mathbf{X}$ , and  $G_x$  is the sensitivity matrix associated with  $\mathbf{x}$ , defined as:

$$\mathbf{G}_x = \begin{bmatrix} \frac{\partial f_1}{\partial x_1} & \dots & \frac{\partial f_1}{\partial x_n} \\ \vdots & \ddots & \vdots \\ \frac{\partial f_m}{\partial x_1} & \dots & \frac{\partial f_m}{\partial x_n} \end{bmatrix} \quad (\text{B.6})$$

where  $\partial f_i / \partial x_j$  denotes  $\partial f_i / \partial X_j$  evaluated at  $\mathbf{X} = \mathbf{x}$ .  $u(x_i, x_j)$  of  $V_x$  is the covariance associated with  $x_i$  and  $x_j$ , and  $u(x_i, x_i)$  is equal to  $u^2(x_i)$ , the squared uncertainty associated with  $x_i$ .

For a generic scalar measurement model, Eq B.1 become  $\mathbf{Y} = \mathbf{f}(\mathbf{X})$ , where  $\mathbf{Y}$  is a scalar quantity and  $\mathbf{f}$  is a scalar function. Propagation of uncertainty for the estimate  $y$  of  $\mathbf{Y}$  can be achieved using the matrix form of the LPU:

$$u^2(y) = \mathbf{g}_x^T \mathbf{V}_x \mathbf{g}_x \quad (\text{B.7})$$

where  $u^2(y)$  is the variance (squared standard uncertainty) associated with the estimate  $y$ , and

$$\mathbf{g}_x = \begin{bmatrix} \frac{\partial f_1}{\partial x_1} \\ \vdots \\ \frac{\partial f_m}{\partial x_n} \end{bmatrix} \quad (\text{B.8})$$

is the gradient matrix in which the  $i^{\text{th}}$  element denotes the partial derivative of  $\mathbf{f}$  with respect to the quantity  $X_i$  evaluated at  $\mathbf{x}$ .

## B.2 Application of LPU

### Volume uncertainty

The volume or mass of an organ or tumour is generally obtained from a volume of interest (VOI) outlined on anatomical or functional imaging data. Accuracy of contouring depends on the operator ability and on the method to define the VOI. Operator variability can be assessed using historical datasets. However, as historical datasets were not available, uncertainty was determined analytically. Accuracy of volume determination is mainly affected by voxelization of outlined VOI and limited spatial resolution of the system. Application of LPU yields relative volume uncertainty to be:

$$\left[\frac{u(v)}{v}\right]^2 = \left[3\frac{u_{vox}(d)}{d}\right]^2 + \left[3\frac{u_{res}(d)}{d}\right]^2 \quad (\text{B.9})$$

where  $v$  is the delineated volume and  $d$  the equivalent diameter. Diametric uncertainty due to voxelization can be expressed as:

$$u_{vox}^2 = \frac{a^2}{6} \quad (\text{B.10})$$

where  $a$  is one voxel width. Diametric uncertainty due to the spatial resolution is:

$$u_{res}^2 = \frac{(FWHM)^2}{4\ln 2} \quad (\text{B.11})$$

### Count rate

The total reconstructed count rate  $C$  within a VOI depends on the VOI delineation. Assuming a Gaussian profile of the count density due to the limited spatial resolution of the measuring system, propagation of volume uncertainty into the measurement of counts yields to:

$$\frac{u(C)}{C} = \frac{\varphi}{2RC} \frac{u(v)}{v} \quad (\text{B.12})$$

where

$$\varphi = \text{erf}\left(\frac{2r}{\sigma\sqrt{2}}\right) - \frac{2\sigma}{r\sqrt{2\pi}} \left[1 - e^{-\frac{2r^2}{\sigma^2}}\right] \quad (\text{B.13})$$

RC is the PVE recovery coefficient,  $r$  is the equivalent radius and  $\sigma = \frac{FWHM}{2\sqrt{2\ln 2}}$ .

### Recovery coefficient

Counts were corrected for partial volume effects using recovery coefficients:

$$RC = \frac{C_{measured}}{C_{true}} \quad (\text{B.14})$$

where  $C_{measured}$  are the measured counts and  $C_{true}$  are the true counts. RCs were calculated using spherical inserts with various volumes. RC points against volume were plotted and fitted by a mono-exponential function with three adjustable parameters  $\mathbf{b} = [b_1, \dots, b_3]^T$ , determined by least squared fitting. The squared standard uncertainty associated with RC is:

$$u^2(RC) = \mathbf{g}_{\mathbf{b}+1}^T \mathbf{V}_{[\mathbf{b},v]} \mathbf{g}_{\mathbf{b}+1} \quad (\text{B.15})$$

where

$$\mathbf{g}_{\mathbf{b}+1} = \begin{bmatrix} \mathbf{g}_{\mathbf{b}} \\ \frac{\partial RC}{\partial v} \end{bmatrix}, \quad (\text{B.16})$$

$$\mathbf{V}_{[\mathbf{b},v]} = \begin{bmatrix} \mathbf{V}_{\mathbf{b}} & \mathbf{0} \\ \mathbf{0} & u^2(v) \end{bmatrix} \quad (\text{B.17})$$

$\mathbf{g}_{\mathbf{b}}$  is the matrix of dimension  $3 \times 1$  containing the partial derivatives of first order of RC with respect to  $\mathbf{b}$ ,  $\mathbf{V}_{\mathbf{b}}$  is the covariance matrix of dimension  $3 \times 3$ .  $\mathbf{B}_{\mathbf{b}}$  can be determined as a by-product of the least squares fitting process and  $\mathbf{0}$  is a matrix of zeros of dimension  $3 \times 1$ .

### Calibration factor

Calibration factor was determined by the ratio between the measured total counts  $C_{measured}$  and the known activity  $A_{known}$  of a source. Application of LPU yield:

$$\left[ \frac{u(CF)}{CF} \right]^2 = \left[ \frac{u(A_{known})}{A_{known}} \right]^2 + \left[ \frac{u(C_{measured})}{C_{measured}} \right]^2 \quad (\text{B.18})$$



$u(A_{known})$  depends on the dose calibrator accuracy, while  $u(C_{measured})$  was derived from multiple measurements.

### Activity

It was assumed negligible uncertainty in the administered activities.

Activities were determined from the measured counts  $C_i$  in a target VOI, the calibration factor CF and the recovery coefficient RC:

$$\mathbf{A} = \begin{bmatrix} A_1 \\ \vdots \\ A_n \end{bmatrix} = \frac{CF}{RC} \begin{bmatrix} C_1 \\ \vdots \\ C_n \end{bmatrix} \quad (\text{B.19})$$

$\mathbf{A}$  is a vector with  $n = 3$  or  $4$  (depending on whether it is an abdominal or thoracic lesion).  $A_i$  is the activity corresponding to the acquisitions at the time  $t_i$ . Eq. B.19 is a multivariate model with  $n + 2$  input quantities (CF, RC,  $C_1, \dots, C_n$ ) and  $n$  output quantities  $\mathbf{A} = [A_1, \dots, A_n]^T$ . LPU yields the relative uncertainty to be:

$$\left[ \frac{u(A_i)}{A_i} \right]^2 = \left[ \frac{u(CF)}{CF} \right]^2 + \left[ \frac{u(RC)}{RC} \right]^2 + \left[ \frac{u(C_i)}{C_i} \right]^2 - \frac{\varphi}{(RC)^2 v} \frac{\partial(RC)}{\partial v} u^2(v) \quad (\text{B.20})$$

where  $\varphi$  was expressed in Eq. B.13.

### TAC fitting

Image noise, patient motion, registration and other imperfect post-acquisition operations such as image reconstruction, including scatter and attenuation corrections contribute to the uncertainty of time-activity curve fitting. However, due to the complexity of these operations, it is assumed that these factors are negligible. Uncertainty derived from the fit parameters of the TAC was assumed to be the main source of error.

Either one of the exponential model in Eq. 7.1 and 7.2 were chosen to be fitted to the data. The Trust-Region algorithm was used to minimize the

objective function:

$$\chi^2 = \sum_i [A_i - f(t_i)]^2 \quad (\text{B.21})$$

where the  $t_i$  denote the image acquisition times and  $A_i$  the corresponding measured activities ( $i = 1, \dots, n$ , where  $n$  is the number of sequential images). The vector  $\mathbf{p} = [p_1, \dots, p_q]^T$  denotes the fit parameters ( $q = 2$  or  $3$  depending on the fitting model chosen). Uncertainties of the fit parameters are estimated using:

$$\mathbf{V}_{\mathbf{p}} = \frac{\chi^2}{n - q} [\mathbf{J}_{\mathbf{p}}^T \mathbf{J}_{\mathbf{p}}]^{-1} \quad (\text{B.22})$$

where  $\mathbf{J}_{\mathbf{p}}$  is the Jacobian matrix, i.e. the matrix of first-order partial derivatives of the TAC model with respect to  $\mathbf{p}$ , evaluated at  $\mathbf{A}$ :

$$\mathbf{J}_{\mathbf{p}} = \begin{bmatrix} \frac{\partial A_1}{\partial p_1} & \cdots & \frac{\partial A_1}{\partial p_q} \\ \vdots & \ddots & \vdots \\ \frac{\partial A_n}{\partial p_1} & \cdots & \frac{\partial A_n}{\partial p_q} \end{bmatrix} \quad (\text{B.23})$$

Diagonal of the  $\mathbf{V}_{\mathbf{p}}$  matrix provides the variance of the  $\mathbf{p}$  parameters.

### Cumulated activity

The cumulated activity was determined as the integral of the TAC from  $t = 0$  to  $\infty$ :

$$\tilde{A} = \int_0^{\infty} f_j(t) dt \quad (\text{B.24})$$

where  $j = 1$  or  $2$  denotes either one of the model equations 7.1 or 7.2. Uncertainty of the cumulated activity depends both on the uncertainty of the fit parameters (random component) and the uncertainty of the activities (systematic component). Application of LPU yield the random standard component:

$$u_r^2(\tilde{A}) = \mathbf{g}_{\mathbf{p}}^T \mathbf{V}_{\mathbf{p}} \mathbf{g}_{\mathbf{p}} \quad (\text{B.25})$$

where  $\mathbf{g}_p$  is the gradient matrix and  $\mathbf{V}_p$  the covariance matrix.

The systematic relative uncertainty is given by:

$$\left[ \frac{u_s(\tilde{A})}{\tilde{A}} \right]^2 = \left[ \frac{u(A_i)}{A_i} \right]^2 \quad (\text{B.26})$$

### S-factors

S-factors for spheres of various size were derived from OLINDA1.1. As OLINDA only provides S-factors for limited sampled values of volumes, S-factor versus were fitted by the Power function:

$$S = c_1 m^{-c_2} \quad (\text{B.27})$$

where  $m$  is the mass and  $c_1$  and  $c_2$  the fitting parameters. Figure B.1 shows, on a log-log scale, the S-factors data points and the fitted curve.

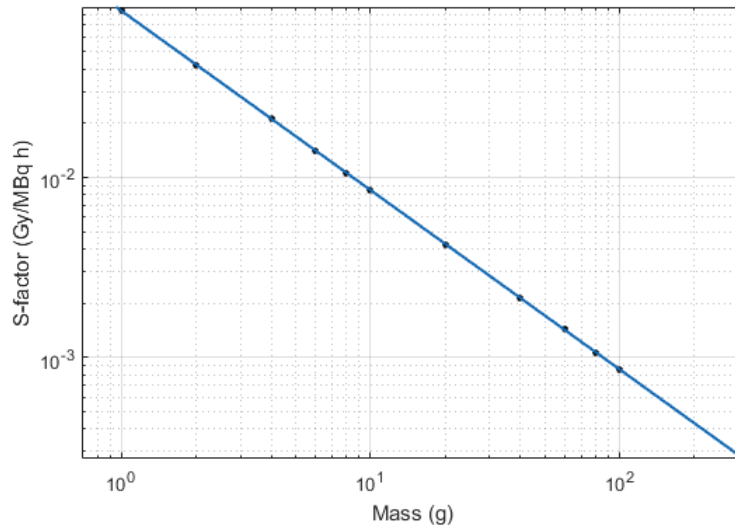


Figure B.1: S-factors for unit density spheres versus mass fitted by power model.

Uncertainties associated with S-factors are predominantly influenced by the uncertainty associated with the volume. For that reason, uncertainties associated with the fit parameters were ignored. Given that mass is proportional to volume, and assuming a known tissue density with negligible uncertainty, the

fractional standard uncertainty associated with  $S$  can be expressed, applying the from the LPU, as:

$$\frac{u(S)}{S} = |c_2| \frac{u(v)}{v} \quad (\text{B.28})$$

### Absorbed dose

Mean absorbed dose was determined as the product of the cumulated activity and the  $S$ -factor, following the MIRD equation:

$$D = \tilde{A}S \quad (\text{B.29})$$

Hence, LPU gives the relative uncertainty:

$$\left[ \frac{u(D)}{D} \right]^2 = \left[ \frac{u(\tilde{A})}{\tilde{A}} \right]^2 + \left[ \frac{u(S)}{S} \right]^2 + 2 \frac{u(\tilde{A}, S)}{\tilde{A}S} \quad (\text{B.30})$$

where the covariance  $u(\tilde{A}, S)$  can be expressed as:

$$u(\tilde{A}, S) = -\frac{c_2}{RC \cdot v} \tilde{A}S \left( \frac{\varphi}{2v} - \frac{\partial RC}{\partial v} \right) u^2(v) \quad (\text{B.31})$$

# Bibliography

- [1] Kostylev VA. *Medical physics: yesterday, today, and tomorrow*. Biomed eng, 2000. 34(2):106-112.
- [2] Stabin M. *Nuclear medicine dosimetry*. Physics in medicine and biology v.51, R187-202, 2006.
- [3] Tischler AS. *The dispersed neuroendocrine cells: the structure, function, regulation and effects of xenobiotics on this system*. Toxicologic pathology. 1989;17(2):307-16.
- [4] Yao JC, Hassan M, Phan A et al. *One hundred years after "carcinoid": epidemiology of and prognostic factors for neuroendocrine tumors in 35,825 cases in the United States*. J Clin Oncol. 2008 Jun 20;26(18):3063-72.
- [5] Bajetta E, Ferrari L, Martinetti A et al. *Chromogranin A, neuron specific enolase, carcinoembryonic antigen, and hydroxyindole acetic acid evaluation in patients with neuroendocrine tumors*. Cancer. 1999 Sep 1;86(5):858-65.
- [6] Hallet J et al. *Exploring the rising incidence of neuroendocrine tumours: a population-based analysis of epidemiology, metastatic presentation, and outcomes*. Cancer, 2015. 121(4):p. 589-97.
- [7] Modlin IM et al. *Gastroenteropancreatic neuroendocrine tumours*. The Lancet Oncology, 2008. 9(1):p. 61-72.
- [8] Oberg K et al. *Neuroendocrine gastro-etero-pancreatic tumors: ESMO Clinical Practice Guidelines for diagnosis, treatment and follow-up*. Ann Oncol, 2012. 23 Suppl 7:p. 124-30.

- [9] <https://www.cancer.net/cancer-types/neuroendocrine-tumor/statistics>
- [10] Bison SM, Konijnenberg MW, Melis M et al. *Peptide receptor radionuclide therapy using radiolabeled somatostatin analogs: focus on future developments*. Clin Transl Imaging. 2014; 2(1): 55–66.
- [11] Bodei L, Mueller-Brand J, Baum RP et al. *The joint IAEA, EANM, and SNMMI practical guidance on peptide receptor radionuclide therapy (PRRNT) in neuroendocrine tumours*. Eur J Nucl Med Mol Imaging. 2013 May;40(5):800-16.
- [12] Oberg K, Norheim I, Lundqvist G et al. *Cytotoxic treatment in patients with malignant carcinoid tumors. Response to streptozocin – alone or in combination with 5-FU*. Acta Oncol 26: 429-432, 1987.
- [13] Higgins GA, Recant L and Fishman AB. *The glucagonoma syndrome: surgically curable diabetes*. Am J Surg. 1979 Jan;137(1):142-8.
- [14] Prinz RA, Dorsch TR and Lawrence AM. *Clinical aspects of glucagon-producing islet cell tumors*. Am J Gastroenterol. 1981 Aug;76(2):125-31.
- [15] Otte A, Jermann E, Behe M et al. *DOTATOC: a powerful new tool for receptor-mediated radionuclide therapy*. Eur J Nucl Med 24: 792-795, 1997.
- [16] Otte A, Mueller-Brand J, Dellas S et al. *Yttrium-90-labelled somatostatin-analogue for cancer treatment*. Lancet 351: 417-418, 1998.
- [17] de Jong M, Kwekkeboom D, Valkema R et al. *Radiolabelled peptides for tumour therapy: current status and future directions*. Plenary lecture at the EANM 2002. Eur J Nucl Med Mol Imag 30: 463-469, 2003.

- [18] Bodei L, Cremonesi M, Grana C et al. *Receptor radionuclide therapy with  $^{90}\text{Y}$ -[DOTA]0-Tyr3 octreotide ( $^{90}\text{Y}$ -DOTATOC) in neuroendocrine tumours.* Eur J Nucl Med Mol Imag 31:1038-46, 2004.
- [19] Valkema R, De Jong M, Bakker WH et al. *Phase I study of peptide receptor radionuclide therapy with [In-DTPA]octreotide: the Rotterdam experience.* Semin Nucl Med. 2002 Apr;32(2):110-22.
- [20] Kwekkeboom DJ, de Herder WW, Kam BL, et al. *Treatment with the radiolabeled somatostatin analog [ $^{177}\text{Lu}$ -DOTA 0, Tyr3]octreotate: toxicity, efficacy, and survival.* J Clin Oncol. 2008 May 1;26(13):2124-30.
- [21] Bodei L, Cremonesi M, Grana CM, et al. *Peptide receptor radionuclide therapy with  $^{177}\text{Lu}$ -DOTATATE: the IEO phase I-II study.* Eur J Nucl Med Mol Imaging. 2011 Dec;38(12):2125-35.
- [22] Hörsch D, Ezziddin S, Haug A, et al. *Effectiveness and side-effects of peptide receptor radionuclide therapy for neuroendocrine neoplasms in Germany: A multi-institutional registry study with prospective follow-up.* Eur J Cancer. 2016 May;58:41-51.
- [23] Imhof A, Brunner P, Marincek N, et al. *Response, survival, and long-term toxicity after therapy with the radiolabeled somatostatin analogue [ $^{90}\text{Y}$ -DOTA]-TOC in metastasized neuroendocrine cancers.* J Clin Oncol. 2011 Jun 10;29(17):2416-23.
- [24] Strosberg J, El-Haddad G, Wolin E, et al. *Phase 3 Trial of  $^{177}\text{Lu}$ -Dotatate for Midgut Neuroendocrine Tumors.* N Engl J Med. 2017 Jan 12;376(2):125-135.
- [25] Kupitz D, Wetz C, Wissel H et al. *Software-assisted dosimetry in peptide receptor radionuclide therapy with  $^{177}\text{Lu}$ -DOTATATE for various imaging scenarios.* PLoS One. 2017 Nov 6;12(11):e0187570.
- [26] Nuclear medicine physics : a handbook for students and teachers. — Vienna : International Atomic Energy Agency, 2014.

- [27] Bolch WE, Eckerman EF, Sgouros G et al. *A generalized schema for radiopharmaceutical dosimetry — standardization of nomenclature, MIRDPamphlet No. 21*. J. Nucl. Med. 50 (2009) 477–484.
- [28] Ritt P, Vija H, Hornegger J et al. *Absolute quantification in SPECT*. Eur J Nucl Med Mol Imaging. 2011 May;38 Suppl 1:S69-77.
- [29] Vandenberghe S, D’Asseler Y, Van de Walle R et al. *Iterative reconstruction algorithms in nuclear medicine*. Comput Med Imaging Graph. 2001 Mar-Apr;25(2):105-11.
- [30] Hudson HM, Larkin RS. *Accelerated image reconstruction using ordered subsets of projection data*. IEEE Trans Med Imaging. 1994;13(4):601-9.
- [31] Hutton BF, Hudson HM, Beekman FJ. *A clinical perspective of accelerated statistical reconstruction*. Eur J Nucl Med. 1997 Jul;24(7):797-808.
- [32] Kadrmas DJ. *Statistically regulated and adaptive EM reconstruction for emission computed tomography*. IEEE Trans Nucl Sci. 2001 Jun; 48(3):790-98.
- [33] Morey AM1, Kadrmas DJ. *Effect of varying number of OSEM subsets on PET lesion detectability*. J Nucl Med Technol. 2013 Dec;41(4):268-73.
- [34] National Electrical Manufacturers Association (2007) Performance measurements of gamma camera. NEMA NU 1-2007. Rosslyn, VA.
- [35] Soret M, Bacharach SL, Buvat I. *Partial-volume effect in PET tumor imaging*. J Nucl Med. 2007 Jun;48(6):932-45.
- [36] Deasy JO, Blanco AI, Clark VH. *CERR: a computational environment for radiotherapy research*. Med Phys. 2003 May;30(5):979-85.
- [37] Grassi E, Fioroni F, Ferri V et al. *Quantitative comparison between the commercial software STRATOS by Philips and a home-made software for voxel-dosimetry in radiopeptide therapy*. Phys Med. 2015 Feb;31(1):72-9.



- [38] Berthon B, Marshall C, Evans M et al. *Evaluation of advanced automatic PET segmentation methods using nonspherical thin-wall inserts*. Med Phys. 2014 Feb;41(2):022502.
- [39] Apostolova I, Steffen IG, Wedel F et al. *Asphericity of pretherapeutic tumour FDG uptake provides independent prognostic value in head-and-neck cancer*. Eur Radiol. 2014 Sep;24(9):2077-87.
- [40] Tran-Gia J, Lassmann M. *Optimizing Image Quantification for  $^{177}\text{Lu}$  SPECT/CT Based on a 3D Printed 2-Compartment Kidney Phantom*. J Nucl Med. 2018 Apr;59(4):616-624.
- [41] Robinson AP, Tipping J, Cullen DM et al. *Organ-specific SPECT activity calibration using 3D printed phantoms for molecular radiotherapy dosimetry*. EJNMMI Phys. 2016 Dec;3(1):12.
- [42] Srinivas SM, Dhurairaj T, Basu S et al. *A recovery coefficient method for partial volume correction of PET images*. Ann Nucl Med. 2009 Jun;23(4):341-8.
- [43] Willowson K. P., Ryu H., Jackson P., et al. *A Comparison of 2D and 3D Kidney Absorbed Dose Measures in Patients Receiving  $^{177}\text{Lu}$ -DOTATATE*. Asia Ocean J Nucl Med Biol. 2018 Spring; 6(2): 113–119.
- [44] Guerra L, De Ponti E, Elisei F, et al. *Respiratory gated PET/CT in a European multicentre retrospective study: added diagnostic value in detection and characterization of lung lesions*. Eur J Nucl Med Mol Imaging 2012;39(9):1381–90.
- [45] Fortin D, Basran PS, Berrang T, Peterson D, Wai ES. *Deformable versus rigid registration of PET/CT images for radiation treatment planning of head and neck and lung cancer patients: A retrospective dosimetric comparison*. Radiat Oncol. 2014 Feb 10;9(1):50.
- [46] Ao ECI, Wu NY, Wang SJ, Song N, Mok GSP. *Improved dosimetry for targeted radionuclide therapy using nonrigid registration on sequential SPECT images*. Med Phys. 2015 Jan 29;42(2):1060–70.

- [47] Ward G, Ramasamy S, Sykes JR, et al. *Superiority of Deformable Image Co-registration in the Integration of Diagnostic Positron Emission Tomography-Computed Tomography to the Radiotherapy Treatment Planning Pathway for Oesophageal Carcinoma*. Clin Oncol. 2016 Oct;28(10):655–62.
- [48] Grassi E, Fioroni F, Berenato S, et al. *Effect of image registration on 3D absorbed dose calculations in  $^{177}\text{Lu}$ -DOTATOC peptide receptor radionuclide therapy*. Phys Medica. 2018 Jan 1;45:177–85.
- [49] Collamati F, Bellini F, Bocci V, et al. *Time Evolution of DOTA-TOC Uptake in Neuroendocrine Tumors in View of a Possible Application of Radioguided Surgery with  $\beta$ -Decay*. J Nucl Med. 2015 Oct;56(10):1501-6.
- [50] Brock KK, Mutic S, McNutt TR, et al. *Use of image registration and fusion algorithms and techniques in radiotherapy: Report of the AAPM Radiation Therapy Committee Task Group No. 132*. Med Phys. 2017 Jul;44(7):e43–76.
- [51] Giavarina D. *Understanding Bland Altman analysis*. Biochem Med (Zagreb). 2015 Jun 5;25(2):141-51.
- [52] Strigari L, Konijnenberg M, Chiesa C, et al. *The evidence base for the use of internal dosimetry in the clinical practice of molecular radiotherapy*. Eur J Nucl Med Mol Imaging 2014;41(10):1976–88.
- [53] Ilan E, Sandström M, Wassberg C, et al. *Dose response of pancreatic neuroendocrine tumors treated with peptide receptor radionuclide therapy using  $^{177}\text{Lu}$ -DOTATATE*. J Nucl Med. 2015 Feb;56(2):177-82.
- [54] Council Directive 2013/59/Euratom. Off J Eur Union. 2014;57.
- [55] Snyder W, Ford M, Warner G, et al. *MIRD Pamphlet No 5 - Estimates of absorbed fractions for monoenergetic photon sources uniformly distributed in various organs of a heterogeneous phantom*. J Nucl Med, Suppl No 3, 5; 1969.

- [56] Cristy M. and Eckerman K. *Specific absorbed fractions of energy at various ages from internal photons sources*. ORNL/TM-8381 V1-V7. Oak Ridge National Laboratory, Oak Ridge, TN; 1987.
- [57] International Commission on Radiological Protection. ICRP Publication 89: Basic Anatomical and Physiological Data for Use in Radiological Protection: Reference Values, Elsevier Health, 2003.
- [58] Dewaraja YK1, Frey EC, Sgouros G et al. *MIRD pamphlet No. 23: quantitative SPECT for patient-specific 3-dimensional dosimetry in internal radionuclide therapy*. J Nucl Med. 2012 Aug;53(8):1310-25.
- [59] Amato E, Italiano A, Minutoli F et al. *Use of the GEANT4 Monte Carlo to determine three-dimensional dose factors for radionuclide dosimetry*. Nucl Inst Meth Phys Res. 2013; A 708 15-18.
- [60] Lanconelli N, Pacilio M, Lo Meo S et al *A free database of radionuclide voxel S values for the dosimetry of nonuniform activity distributions*. Phys Med Biol. 2012 Jan 21;57(2):517-33.
- [61] [www.cerr.info](http://www.cerr.info)
- [62] Finocchiaro D (2016). *Ottimizzazione di un sistema di calcolo Voxel Dosimetry e implementazione di grandezze radiobiologiche per MRT*. (Master dissertation). Available on AlmaDL University of Bologna Digital Library.
- [63] Grimes J, Uribe C, Celler A. *JADA: a graphical user interface for comprehensive internal dose assessment in nuclear medicine*. Med Phys. 2013 Jul;40(7):072501.
- [64] Jackson PA, Beauregard JM, Hofman MS, et al. *An automated voxelized dosimetry tool for radionuclide therapy based on serial quantitative SPECT/CT imaging*. Med Phys. 2013 Nov;40(11):112503.
- [65] McKay E. *A software tool for specifying voxel models for dosimetry estimation*. Cancer Biother Radiopharm. 2003 Jun;18(3):379-92.

- [66] Gardin I, Bouchet LG, Assié K, et al. *Voxeldoes: a computer program for 3-D dose calculation in therapeutic nuclear medicine*. Cancer Biother Radiopharm. 2003 Feb;18(1):109-15.
- [67] Kletting P, Schimmel S, Hänscheid H, et al. *The NUKDOS software for treatment planning in molecular radiotherapy*. Z Med Phys. 2015 Sep;25(3):264-74.
- [68] Hippeläinen ET, Tenhunen MJ, Mäenpää HO, et al. *Dosimetry software Hermes Internal Radiation Dosimetry: from quantitative image reconstruction to voxel-level absorbed dose distribution*. Nucl Med Commun. 2017 May;38(5):357-365.
- [69] Kost SD, Dewaraja YK, Abramson RG, et al. *VIDA: a voxel-based dosimetry method for targeted radionuclide therapy using Geant4*. Cancer Biother Radiopharm. 2015 Feb;30(1):16-26.
- [70] <https://www.dosisoft.com/products/planet-dose/>
- [71] [https://www.mimsoftware.com/mim\\_sureplan\\_mrt](https://www.mimsoftware.com/mim_sureplan_mrt)
- [72] Stabin MG, Siegel JA. *RADAR Dose Estimate Report: A Compendium of Radiopharmaceutical Dose Estimates Based on OLINDA/EXM Version 2.0*. J Nucl Med. 2018 Jan;59(1):154-160.
- [73] Stabin MG, Sparks RB, Crowe E. *OLINDA/EXM: the second-generation personal computer software for internal dose assessment in nuclear medicine*. J Nucl Med. 2005 Jun;46(6):1023-7.
- [74] Marcatili S, Pettinato C, Daniels S, et al. *Development and validation of RAYDOSE: a Geant4-based application for molecular radiotherapy*. Phys Med Biol. 2013 Apr 21;58(8):2491-508.
- [75] Spezi E, Lewis G. *An overview of Monte Carlo treatment planning for radiotherapy*. Radiat Prot Dosimetry. 2008;131(1):123-9.
- [76] <http://mrt-dosimetry-empir.eu/>
- [77] <http://projects.npl.co.uk/metromrt/>

- [78] [http://www.spect.com/pub/Flanged\\_Jaszczak\\_Phantom.pdf](http://www.spect.com/pub/Flanged_Jaszczak_Phantom.pdf)
- [79] Park MA, Mahmood A, Zimmerman RE, et al. *Adsorption of metallic radionuclides on plastic phantom walls*. Med Phys. 2008 Apr;35(4):1606-10.
- [80] NPL Good Practice Guide #93 [Available from: <http://training.npl.co.uk/course/radionuclide-calibrator/>].
- [81] Kalogianni E, Flux GD, Malaroda A, *The Use of BED and EUD Concepts in Heterogeneous Radioactivity Distributions on a Multicellular Scale for Targeted Radionuclide Therapy*, Cancer Biother Radiopharm, 2007.
- [82] Barone R, Borson-Chazot F, Valkema R, et al. *Patient-specific dosimetry in predicting renal toxicity with (90)Y-DOTATOC: relevance of kidney volume and dose rate in finding a dose-effect relationship*. J Nucl Med. 2005 Jan;46 Suppl 1:99S-106S.
- [83] Wessels BW, Konijnenberg MW, Dale RG, et al. *MIRD pamphlet No. 20: the effect of model assumptions on kidney dosimetry and response—implications for radionuclide therapy*. J Nucl Med. 2008 Nov;49(11):1884-99.
- [84] Dawson LA, Kavanagh BD, Paulino AC, et al. *Radiation-associated kidney injury*. Int J Radiat Oncol Biol Phys. 2010 Mar 1;76(3 Suppl):S108-15.
- [85] Marks LB, Yorke ED, Jackson A, et al. *Use of normal tissue complication probability models in the clinic*. Int J Radiat Oncol Biol Phys. 2010 Mar 1;76(3 Suppl):S10-9.
- [86] Cockcroft DW, Gault MH. *Prediction of creatinine clearance from serum creatinine*. Nephron. 1976;16(1):31-41.
- [87] Cremonesi M, Ferrari ME, Bodei L, et al. *Correlation of dose with toxicity and tumour response to 90Y- and 177Lu-PRRT provides the basis for optimization through individualized treatment planning*. Eur J Nucl Med Mol Imaging. 2018 Dec;45(13):2426-2441.

- [88] Bodei L, Ferone D, Grana CM, et al. *Peptide receptor therapies in neuroendocrine tumors*. J Endocrinol Invest. 2009 Apr;32(4):360-9.
- [89] Forrer F, Krenning EP, Kooij PP, et al. *Bone marrow dosimetry in peptide receptor radionuclide therapy with [ $^{177}\text{Lu}$ -DOTA(0),Tyr(3)]octreotate*. Eur J Nucl Med Mol Imaging. 2009 Jul;36(7):1138-46.
- [90] Del Prete M, Buteau FA, Beauregard JM. *Personalized  $^{177}\text{Lu}$ -octreotate peptide receptor radionuclide therapy of neuroendocrine tumours: a simulation study*. Eur J Nucl Med Mol Imaging. 2017 Aug;44(9):1490-1500.
- [91] National Council on Radiation Protection and Measurements. *Misadministration of radioactive material in medicine-scientific background*. Bethesda, MD, 1991:27.
- [92] Cassady JR. *Clinical radiation nephropathy*. Int J Radiat Oncol Biol Phys.
- [93] Bodei L, Cremonesi M, Ferrari M, et al. *Long-term evaluation of renal toxicity after peptide receptor radionuclide therapy with  $^{90}\text{Y}$ -DOTATOC and  $^{177}\text{Lu}$ -DOTATATE: the role of associated risk factors*. Eur J Nucl Med Mol Imaging. 2008 Oct;35(10):1847-56.
- [94] Forrer F, Mueller-Brand J, Maecke H. *Pre-therapeutic dosimetry with radiolabelled somatostatin analogues in patients with advanced neuroendocrine tumours*. Eur J Nucl Med Mol Imaging. 2005 Apr;32(4):511-2.
- [95] Valkema R, Pauwels S, Kvols LK, et al. *Survival and response after peptide receptor radionuclide therapy with [ $^{90}\text{Y}$ -DOTA0,Tyr3]octreotide in patients with advanced gastroenteropancreatic neuroendocrine tumors*. Semin Nucl Med. 2006 Apr;36(2):147-56.

- [96] Waldherr C, Pless M, Maecke HR, et al. *Tumor response and clinical benefit in neuroendocrine tumors after 7.4 GBq (90)Y-DOTATOC.* J Nucl Med. 2002 May;43(5):610-6.
- [97] Teunissen JJ, Kwekkeboom DJ, Krenning EP. *Quality of life in patients with gastroenteropancreatic tumors treated with [177Lu-DOTA0,Tyr3]octreotate.* J Clin Oncol. 2004 Jul 1;22(13):2724-9.
- [98] Juweid ME, Cheson BD. *Positron-emission tomography and assessment of cancer therapy.* N Engl J Med. 2006 Feb 2;354(5):496-507.
- [99] Eschmann SM, Friedel G, Paulsen F, et al. *18F-FDG PET for assessment of therapy response and preoperative re-evaluation after neoadjuvant radio-chemotherapy in stage III non-small cell lung cancer.* Eur J Nucl Med Mol Imaging. 2007 Apr;34(4):463-71.
- [100] Nishiyama Y, Yamamoto Y, Kanenishi K, et al. *Monitoring the neoadjuvant therapy response in gynecological cancer patients using FDG PET.* Eur J Nucl Med Mol Imaging. 2008 Feb;35(2):287-95.
- [101] Belhocine T, Foidart J, Rigo P, et al. *Fluorodeoxyglucose positron emission tomography and somatostatin receptor scintigraphy for diagnosing and staging carcinoid tumours: correlations with the pathological indexes p53 and Ki-67.* Nucl Med Commun. 2002 Aug;23(8):727-34.
- [102] Haug A, Auernhammer CJ, Wängler B, et al. *Intraindividual comparison of 68Ga-DOTA-TATE and 18F-DOPA PET in patients with well-differentiated metastatic neuroendocrine tumours.* Eur J Nucl Med Mol Imaging. 2009 May;36(5):765-70.
- [103] Haug AR, Auernhammer CJ, Wängler B, et al. *68Ga-DOTATATE PET/CT for the early prediction of response to somatostatin receptor-mediated radionuclide therapy in patients with well-differentiated neuroendocrine tumors.* J Nucl Med. 2010 Sep;51(9):1349-56.

- [104] El Naqa I, Li R, Murphy M. *Machine Learning in Radiation Oncology: Theory and Applications*. Cham: Springer; 2015. 336 p. DOI: 10.1007/978-3-319-18305-3.
- [105] Zhang HH, D'Souza WD, Shi L, et al. *Modeling plan-related clinical complications using machine learning tools in a multiplan IMRT framework*. Int J Radiat Oncol Biol Phys. 2009 Aug 1;74(5):1617-26.
- [106] Naqa IE1, Deasy JO, Mu Y, et al. *Datamining approaches for modeling tumor control probability*. Acta Oncol. 2010 Nov;49(8):1363-73.
- [107] Lee S, Ybarra N, Jeyaseelan K, et al. *Bayesian network ensemble as a multivariate strategy to predict radiation pneumonitis risk*. Med Phys. 2015 May;42(5):2421-30.
- [108] Kang J, Schwartz R, Flickinger J, et al. *Machine Learning Approaches for Predicting Radiation Therapy Outcomes: A Clinician's Perspective*. Int J Radiat Oncol Biol Phys. 2015 Dec 1;93(5):1127-35.
- [109] Yahya N, Ebert MA, Bulsara M, et al. *Statistical-learning strategies generate only modestly performing predictive models for urinary symptoms following external beam radiotherapy of the prostate: A comparison of conventional and machine-learning methods*. Med Phys. 2016 May;43(5):2040.
- [110] Deist TM, Dankers FJWM, Valdes G, et al. *Machine learning algorithms for outcome prediction in (chemo)radiotherapy: An empirical comparison of classifiers*. Med Phys. 2018 Jul;45(7):3449-3459.
- [111] Eisenhauer EA, Therasse P, Bogaerts J, et al. *New response evaluation criteria in solid tumours: revised RECIST guideline (version 1.1)*. Eur J Cancer. 2009 Jan;45(2):228-47.
- [112] Pauwels S, Barone R, Walrand S, et al. *Practical dosimetry of peptide receptor radionuclide therapy with (90)Y-labeled somatostatin analogs*. J Nucl Med. 2005 Jan;46 Suppl 1:92S-8S.
- [113] Ilan E1, Sandström M2, Wassberg C, et al. *Dose response of pancreatic neuroendocrine tumors treated with peptide receptor radionuclide*



- therapy using 177Lu-DOTATATE*. J Nucl Med. 2015 Feb;56(2):177-82.
- [114] Ezziddin S, Lohmar J, Yong-Hing CJ, et al. *Does the pretherapeutic tumor SUV in 68Ga DOTATOC PET predict the absorbed dose of 177Lu octreotate?* Clin Nucl Med. 2012 Jun;37(6):e141-7.
- [115] Öksüz MÖ, Winter L, Pfannenberg C, et al. *Peptide receptor radionuclide therapy of neuroendocrine tumors with (90)Y-DOTATOC: is treatment response predictable by pre-therapeutic uptake of (68)Ga-DOTATOC?* Diagn Interv Imaging. 2014 Mar;95(3):289-300.
- [116] Kratochwil C, Stefanova M, Mavriopoulou E, et al. *SUV of [68Ga]DOTATOC-PET/CT Predicts Response Probability of PRRT in Neuroendocrine Tumors*. Mol Imaging Biol. 2015 Jun;17(3):313-8.
- [117] Gabriel M, Oberauer A, Dobrozemsky G, et al. *<sup>68</sup>Ga-DOTA-Tyr3-octreotide PET for assessing response to somatostatin-receptor-mediated radionuclide therapy*. J Nucl Med. 2009 Sep;50(9):1427-34.
- [118] Gälne A, Almquist H, Almquist M, et al. *A prospective observational study to evaluate the effects of long-acting somatostatin analogs on <sup>68</sup>Ga-DOTATATE uptake in patients with neuroendocrine tumors*. J Nucl Med. 2019 Apr 18.
- [119] Wahl RL, Jacene H, Kasamon Y, et al. *From RECIST to PERCIST: Evolving Considerations for PET response criteria in solid tumors*. J Nucl Med. 2009 May;50 Suppl 1:122S-50S.
- [120] Moon SH, Hyun SH, Choi JY. *Prognostic significance of volume-based PET parameters in cancer patients*. Korean J Radiol. 2013 Jan-Feb;14(1):1-12.
- [121] Kim J-H. *Estimating classification error rate: Repeated cross-validation, repeated hold-out and bootstrap*. Comput Stat Data Anal. 2009;53:3735-45.

- [122] Mounce SR, Ellis K, Edwards JM et al. *Ensemble Decision Tree Models Using RUSBoost for Estimating Risk of Iron Failure in Drinking Water Distribution Systems* Water Resour Manage (2017) 31: 1575.
- [123] Cremonesi M, Ferrari M, Di Dia A, et al. *Recent issues on dosimetry and radiobiology for peptide receptor radionuclide therapy*. Q J Nucl Med Mol Imaging. 2011;55:155–67.
- [124] Eberlein U, Cremonesi M, Lassmann M. *Individualized Dosimetry for Theranostics: Necessary, Nice to Have, or Counterproductive?* J Nucl Med. 2017 Sep;58(Suppl 2):97S-103S.
- [125] Gear JJ, Cox MG, Gustafsson J, et al. *EANM practical guidance on uncertainty analysis for molecular radiotherapy absorbed dose calculations*. Eur J Nucl Med Mol Imaging. 2018 Dec;45(13):2456-2474.
- [126] Dewaraja YK, Wilderman SJ, Ljungberg M et al. *Accurate Dosimetry in  $^{131}\text{I}$  Radionuclide Therapy Using Patient-Specific, 3-Dimensional Methods for SPECT Reconstruction and Absorbed Dose Calculation* J Nucl Med. 2005 May; 46(5): 840–849.
- [127] Gear JJ, Charles-Edwards E, Partridge M, et al. *A quality-control method for SPECT-based dosimetry in targeted radionuclide therapy*. Cancer Biother Radiopharm. 2007 Feb;22(1):166-74.
- [128] Uribe CF, Esquinas PL, Tanguay J, et al. *Accuracy of  $^{177}\text{Lu}$  activity quantification in SPECT imaging: a phantom study*. EJNMMI Phys. 2017 Dec;4(1):2.
- [129] Marin G, Vanderlinden B, Karfis I, et al. *Accuracy and precision assessment for activity quantification in individualized dosimetry of  $^{177}\text{Lu}$ -DOTATATE therapy* EJNMMI Phys. 2017 Dec; 4: 7.
- [130] Joint Committee for Guides in Metrology. JCGM 102. *Evaluation of measurement data - Guide to the expression of uncertainty in measurement*. Sèvres: BIPM; 2011.

- [131] Maccauro M, Capozza A, Seregni E. *Peptide receptor radionuclide therapy after NETTER-1 clinical trial: what should not be left behind*. Clinical and Translational Imaging (2019) 7:155-157.
- [132] Levine R, Krenning EP. *Clinical History of the Theranostic Radionuclide Approach to Neuroendocrine Tumors and Other Types of Cancer: Historical Review Based on an Interview of Eric P. Krenning by Rachel Levine*. J Nucl Med. 2017 Sep;58(Suppl 2):3S-9S.
- [133] Garske-Román U, Sandström M, Fröss Baron K, et al. *Prospective observational study of  $^{177}\text{Lu}$ -DOTA-octreotate therapy in 200 patients with advanced metastasized neuroendocrine tumours (NETs): feasibility and impact of a dosimetry-guided study protocol on outcome and toxicity*. Eur J Nucl Med Mol Imaging. 2018 Jun;45(6):970-988.



# Ringraziamenti

Al termine di questi tre anni di dottorato desidero ringraziare molte persone che ne hanno reso possibile la sua realizzazione. Innanzitutto, ringrazio vivamente il mio supervisore, la Dott.ssa Elisa Grassi, per il suo costante e fondamentale supporto, ed il mio co-supervisore, il Prof. Gastone Castellani, per avermi guidato durante questo percorso. Ringrazio il direttore della struttura di Fisica Medica dell’Arcispedale Santa Maria Nuova di Reggio Emilia, il Dott. Mauro Iori, per avermi permesso di lavorare qui. Un sentito ringraziamento va anche alla Dott.ssa Federica Fioroni per essersi sempre dimostrata pronta ad aiutarmi e consigliarmi. Ringrazio poi tutta la S.C. di Fisica Medica dell’Arcispedale Santa Maria Nuova di Reggio Emilia, il Dott. Marco Bertolini, Alfredo Palmieri, Simona Cola e il Dott. Annibale Versari, primario della S.C. di Medicina Nucleare, per l’ambiente professionale e sereno dove ho potuto svolgere il mio lavoro.

Ringrazio le persone con cui ho collaborato per le mie ricerche scientifiche durante questi tre anni: le Dott.sse Marta Cremonesi e Mahila Ferrari dell’Istituto Europeo di Oncologia di Milano, il Dott. Salvatore Berenato e il Dott. Emiliano Spezi della Cardiff University ed i Dott.ri Glenn Flux, Jonathan Gear e Iain Murray del Royal Marsden NHS Foundation Trust del Sutton.

Grazie alla mia famiglia, che mi ha permesso di arrivare fin qui. Un grazie particolare sento di darlo a mia nonna “Tuaccia”, alla quale devo moltissimo per ciò che sono oggi. Ringrazio poi tutti i miei colleghi del corso di studio che mi hanno accompagnato durante questa esperienza e “gli amici di sempre” Dario, Peppe e Paolo, che mi hanno seguito durante l’intero percorso.

Infine uno ringraziamento speciale va a Letizia, che è stata il mio punto di riferimento in questi tre anni.